Applied Physics Reviews

REVIEW ARTICLE | OCTOBER 28 2024

Energy conversion and transport in molecular-scale junctions ✓

Haixin Zhang ; Yunxuan Zhu ; Ping Duan; Mehrdad Shiri; Sai Chandra Yelishala ; Shaocheng Shen ; Ziqi Song; Chuancheng Jia ✉; Xuefeng Guo ✉ ; Longji Cui ✉ ; Kun Wang ✉

Appl. Phys. Rev. 11, 041312 (2024)
https://doi.org/10.1063/5.0225756

AIP Publishing

Applied Physics Reviews REVIEW pubs.aip.org/aip/are

Energy conversion and transport in molecular-scale junctions

Cite as: Appl. Phys. Rev. **11**, 041312 (2024); doi: 10.1063/5.0225756
Submitted: 26 June 2024 · Accepted: 19 September 2024 ·
Published Online: 28 October 2024

Haixin Zhang,[1] Yunxuan Zhu,[2] Ping Duan,[3] Mehrdad Shiri,[1] Sai Chandra Yelishala,[2] Shaocheng Shen,[4] Ziqi Song,[3] Chuancheng Jia,[3,a)] Xuefeng Guo,[3,5,a)] Longji Cui,[2,6,a)] and Kun Wang[1,4,a)]

AFFILIATIONS

[1]Department of Physics, University of Miami, Coral Gables, Florida 33146, USA
[2]Department of Mechanical Engineering, University of Colorado Boulder, Boulder, Colorado 80309, USA
[3]Center of Single-Molecule Sciences, Institute of Modern Optics, Frontiers Science Center for New Organic Matter, Tianjin Key Laboratory of Micro-Scale Optical Information Science and Technology, College of Electronic Information and Optical Engineering, Nankai University, Tianjin 300350, People's Republic of China
[4]Department of Chemistry, University of Miami, Coral Gables, Florida 33146, USA
[5]Beijing National Laboratory for Molecular Sciences, National Biomedical Imaging Center, College of Chemistry and Molecular Engineering, Peking University, Beijing 100871, People's Republic of China
[6]Materials Science and Engineering Program and Center for Experiments on Quantum Materials (CEQM), University of Colorado Boulder, Boulder, Colorado 80309, USA

[a)]**Authors to whom correspondence should be addressed:** jiacc@nankai.edu.cn; guoxf@pku.edu.cn; longji.cui@colorado.edu; and kunwang@miami.edu

ABSTRACT

Molecular-scale junctions (MSJs) have been considered the ideal testbed for probing physical and chemical processes at the molecular scale. Due to nanometric confinement, charge and energy transport in MSJs are governed by quantum mechanically dictated energy profiles, which can be tuned chemically or physically with atomic precision, offering rich possibilities beyond conventional semiconductor devices. While charge transport in MSJs has been extensively studied over the past two decades, understanding energy conversion and transport in MSJs has only become experimentally attainable in recent years. As demonstrated recently, by tuning the quantum interplay between the electrodes, the molecular core, and the contact interfaces, energy processes can be manipulated to achieve desired functionalities, opening new avenues for molecular electronics, energy harvesting, and sensing applications. This Review provides a comprehensive overview and critical analysis of various forms of energy conversion and transport processes in MSJs and their associated applications. We elaborate on energy-related processes mediated by the interaction between the core molecular structure in MSJs and different external stimuli, such as light, heat, electric field, magnetic field, force, and other environmental cues. Key topics covered include photovoltaics, electroluminescence, thermoelectricity, heat conduction, catalysis, spin-mediated phenomena, and vibrational effects. The review concludes with a discussion of existing challenges and future opportunities, aiming to facilitate in-depth future investigation of promising experimental platforms, molecular design principles, control strategies, and new application scenarios.

TABLE OF CONTENTS

I. INTRODUCTION

Downscaling electronic and sensing devices to the molecular scale represents one of the central missions in modern nanotechnology and quantum sciences. Beyond their nanometric confinement, molecules offer unique advantages: structural tunability, self-assembly capabilities, mechanical flexibility, and fabrication-free nature, all of which expand device functionality and tunability beyond solid state-based semiconductor devices. Additionally, intriguing quantum effects arise from the discrete distribution of energy levels (i.e., molecular orbitals) at the molecular scale, making single molecules ideal designer quantum materials. In these systems, charge and energy transport are governed by quantum mechanically dictated energy profiles, which can be tuned chemically or physically with atomic precision. Catalyzed initially by the seminal theoretical work of Aviram and Ratner in 1974,[1] and further propelled by continuous experimental advancements, molecular electronics (ME) has become a rapidly growing field at the intersection of physics, chemistry, biology, nanoengineering, and quantum sciences.

To interrogate charge transport and energy conversion processes at the molecular scale, a straightforward device structure should feature an individual molecule or a monolayer of molecules as the main transport backbone that is reliably connected to the source and drain electrodes. Thanks to the remarkable progress in developing suitable experimental platforms, such a device structure, now named as molecular-scale junction (MSJ), can be realized using multiple techniques, including scanning tunneling microscope break junction (STMBJ),[2–5] mechanically controlled break junction (MCBJ),[6–8] conductive atomic force microscope break junction (CAFMBJ),[9,10] electromigration break junction (EBJ),[11–15] and graphene–molecule–graphene junction (GMGJ).[16–18] Adopting these techniques, research efforts over the past two decades have primarily focused on understanding the structure–property relations of various molecules via probing charge transport through MSJs. Insights from these recent studies have enabled the design of molecular-scale diodes,[19] transistors,[20] and switches[21] and led to the discovery of emerging quantum phenomena that have no analogy in conventional semiconductor devices, such as quantum interference[22] and quantum entanglement.[23]

Charge transport across an MSJ involves multiple sequential steps: under an applied bias, electron injection occurs first from the source electrode within a specific energy window,[24] followed by physical or chemical perturbations and scattering on the molecular core.[25] Subsequently, electron ejection takes place toward the drain electrode, leading to equilibration with the electron reservoir at the measurement temperature. These steps are often accompanied by energy transformations, especially under external stimuli.[26] A MSJ typically consists of three primary segments: the electrodes, the molecular core, and two molecule–electrode interfaces.[27,28] Energy conversion and transport can occur at one or multiple sites within a MSJ. By manipulating the characteristics of the electrodes, the molecular core, or the interfaces, energy conversion processes can be tailored to achieve desired functionalities.[29] This flexibility affords possibilities for optimizing the performance and efficiency of future molecular-scale devices.[30] MSJ therefore serves as an excellent testing ground for understanding energy conversion and transport for molecular-scale quantum systems. However, while charge transport properties have been extensively studied experimentally, energy conversion and transport in MSJs have only become experimentally attainable in recent years, primarily due to the previous lack of appropriate experimental tools.

In an MSJ, energy can manifest in various forms, such as optical, electrical, thermal, magnetic, chemical, and vibrational forms. As demonstrated in recent studies, the importance of examining how one form of energy is converted to another or transported across a MSJ is multi-folds. On the one hand, such process can significantly alter the resulting electrical behavior of the MSJ, facilitating direct device applications.[31] For instance, the efficient conversion between light and electricity, as observed in photoelectricity and electroluminescence effects, makes carefully designed molecules promising photosensor,[32] photo switch,[33] and light-emitting diode (LED).[34] Thermoelectric effects in MSJs, including the Seebeck effect and the Peltier effect, underpin the potential of creating efficient thermal management and harvesting devices, such as molecular Peltier coolers,[35] heat engine,[36] and energy filter.[37,38] On the other hand, probing energy conversion and transport in MSJs enable one to gain deeper insights into the fundamental transport mechanisms. For example, the sign and amplitude of the Seebeck coefficient of a MSJ inform critical transport information, such as the nature of charge carriers (electron vs hole) and the transmission profile at the electrode Fermi energy.[39] Thus, it is both fundamentally and practically crucial to expand our understanding of and ultimately harness energy conversion and transport processes in MSJs.

In this Review, we provide a comprehensive overview and critical analysis of various forms of energy conversion and transport processes in MSJs. From an energy perspective, we focus on promising experimental approaches, key discoveries, and underlying mechanisms in representative MSJ systems. Figure 1 provides a schematic summary of the representative energy conversion processes covered and the corresponding experimental platforms. The article is structured as follows: In Sec. II, we discuss light-induced energy conversion in MSJs, including photoisomerization, exciton formation, photoelectric effect, molecular-scale nano-optics, and electroluminescence. Section III delves into heat-mediated energy conversion and transport processes from both theoretical and experimental perspectives, including thermal transport and thermoelectricity in MSJs. In Sec. IV, we present energy conversion occurring in chemical catalysis driven by different stimuli, including stress, electrostatic, and heat. Section V highlights recent advances of spin-mediated effects in MSJs, encompassing spin Seebeck, Kondo,

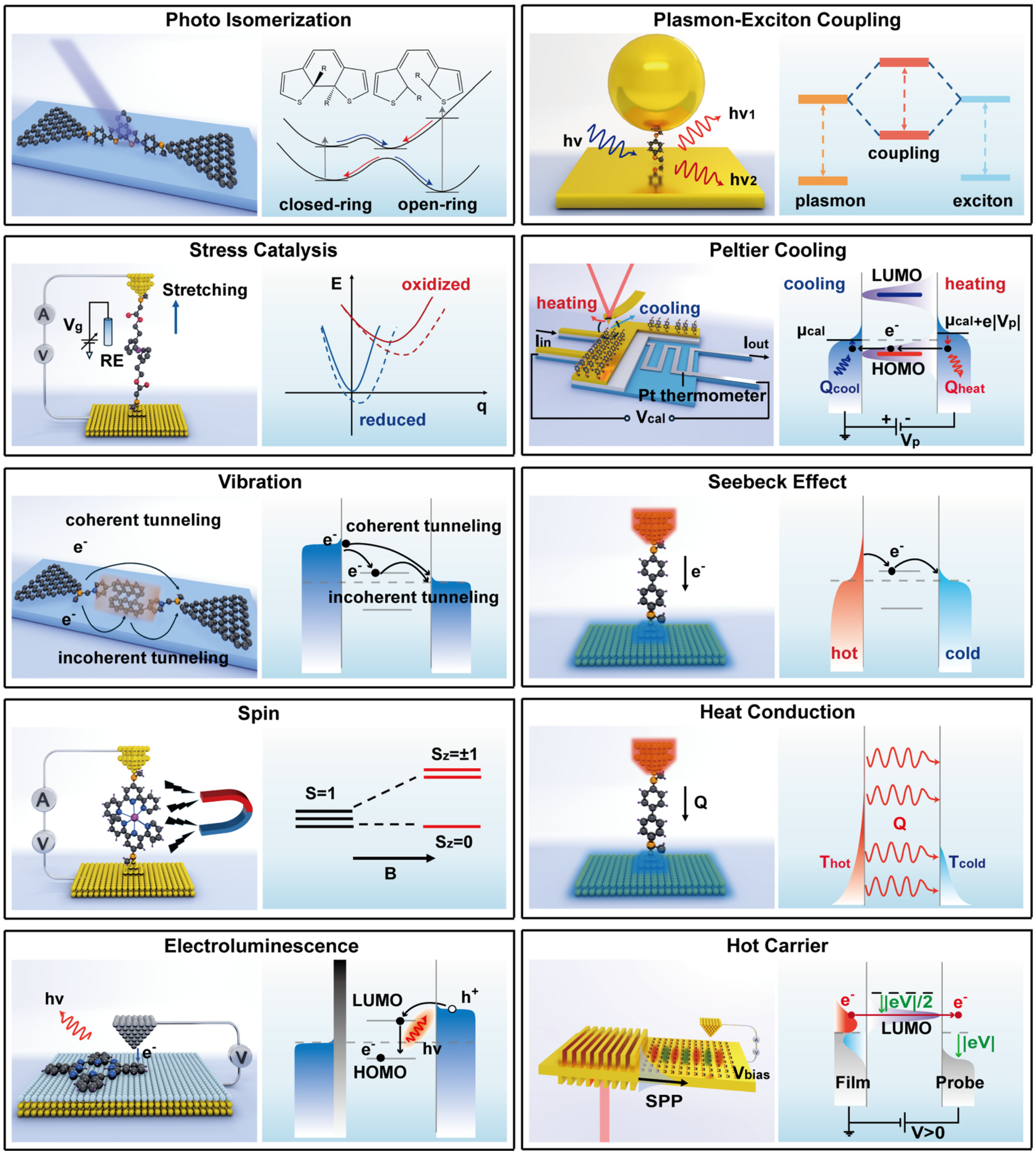

FIG. 1. Schematic summary of representative energy conversion processes observed in MSJs. The left (right) panel in each frame displays the schematic of experimental setup (associated energy diagram).

chirality-induced spin selectivity (CISS), and magnetoresistance effects. In Sec. VI, we survey experimental advancements in studying vibration effects in MSJs, which are induced by electrons, heat, and light. Finally, in Sec. VII, we conclude the article by discussing existing challenges, emerging opportunities, and potential future directions of the field.

II. LIGHT-DRIVEN ENERGY CONVERSION IN MSJs

A. Light-induced charge transport

The precise modulation of conductance in single molecules is of fundamental importance for their integration into next-generation optoelectronic devices,[40] computational components,[41] and sensing technologies applications.[42] Demonstrations of conductance change in MSJs have been achieved through diverse external stimuli, including electric fields,[43–45] mechanical forces,[46–49] chemical interactions,[50,51] and light exposure.[33,52] This section concentrates on the intricate interplay between light and molecular properties, the resulting photo-induced conductance change, and the associated energy conversion processes, highlighting their potential for advancing molecular-scale optoelectronic technologies. Energy conversion in this section mainly contains the transition from photon energy to chemical energy of different states, finally resulting in the variation of electrical conductance of MSJ, i.e., electrical energy.

1. Photoisomerization

Energy storage based on photo-induced isomerization can be achieved by rearranging the molecular structure and bonds of photosensitive molecules. Under illumination conditions, stable photosensitive molecules absorb energy from incident photons and is subsequently transformed to a metastable state, storing energy in chemical bonds. Under proper environmental cues, molecules in the metastable state (or excited state) return to its most stable state (or ground state), releasing the stored energy, typically in the form of heat, thereby enabling efficient and controllable energy storage and release processes. In such process, the cyclic stability is crucial as it lays the foundation for the reliability of energy storage and release processes. Moreover, at the single-molecule level, the photoisomerization of molecules with multiple stable states has been utilized not only for energy storage but also to facilitate conductance switching effects.

As one of the representative photochromic molecules, diarylethene and its derivatives undergo 6π electrocyclization upon ultraviolet (UV) light, isomerizing from a colorless open-ring form to a colored close-ring form.[53,54] The energy diagram of the transition process is shown Fig. 2(a). The open-ring isomer under UV irradiation can be excited to the S_1 state (purple arrow) and then decay to the ground state S_0 of the close-ring isomer through the conical intersection indicated by the red arrow. Similarly, under visible (Vis) light, the close-ring isomer follows the excitation (light blue arrow), transiting to the open-ring isomer by the same conical intersection. From energy point of view, the transition between open-ring and closed-ring isomers enables the conversion of optical energy into chemical energy. Owing to this isomerization property, diarylethene derivatives have been widely used in molecular optoelectronics. For instance, at the molecular scale, Jia *et al.*[55] used the GMGJ technique with the molecule containing

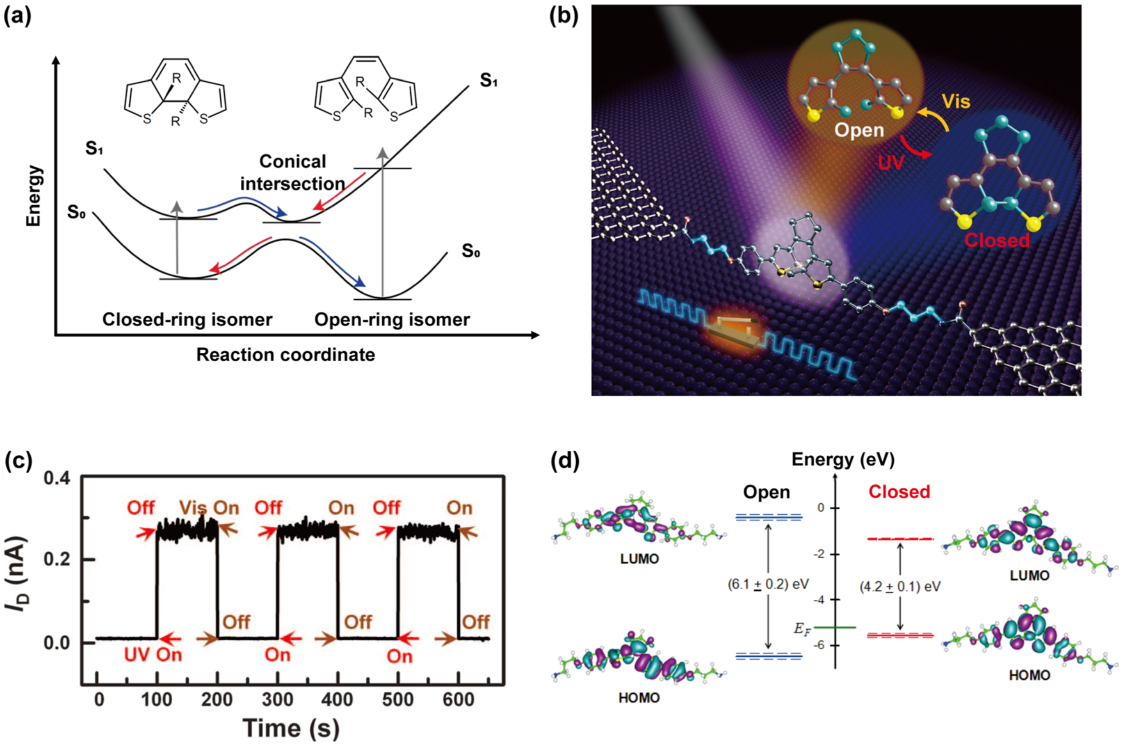

FIG. 2. (a) The energy diagram of the transition process of diarylethene isomerization. (b) Experimental setup of GMGJ with diarylethene molecule. (c) Current signal switching based on UV and Vis light irradiation. (d) Molecular orbitals of open and closed states. Reproduced with permission from Jia *et al.*, Science. **352**, 1443 (2016). Copyright 2016 American Association for the Advancement of Science.

diarylethene as the core, constructing a single-molecule optoelectrical device [Fig. 2(b)]. Due to the structural change based on the photochromic property of diarylethene, the single-molecule junction (SMJ) had a switchable conductance under UV and Vis light illumination. Under 100 mV bias between the two graphene electrodes, the close-ring form presented a higher tunneling current ("On" state) than the near-zero current performance of the open-ring form under Vis-light ("Off" state), as illustrated in Fig. 2(c). The two conduction states were reversible with a remarkably high On/Off ratio of $\sim 10^7$. The conductance change was attributed to the drastic reduction of the energy gap between the highest occupied molecular orbital (HOMO) and the lowest unoccupied molecular orbital (LUMO) of the closed state [Fig. 2(d)]. The HOMO, i.e., the frontier molecular orbital (FMO), has an upward shift toward the electrode Fermi energy (E_F) when diarylethene isomerizes from open state to closed state, greatly enhancing electron transmission through the molecule.

Azobenzene derivatives represent another prominent type of photochromic molecules with wide availability and chemical resilience.[56–59] Similarly to diarylethene, azobenzene has two stable isomers, *trans* and *cis*, while the *trans* isomer is more stable than the *cis* isomer in ambient conditions.[60] Azobenzene photoswitches can store energy by isomerizing from their thermodynamically stable *trans* isomer to the higher-energy metastable *cis* isomer.[61,62] As shown in Fig. 3(a), the *trans* conformation is nearly planar, while the *cis* form has two twisted phenyl rings angled ∼60°.[63] To switch between two isomer configurations, photoexcitation of azobenzene to the first excited state S_1 is needed, with UV and Vis lights for *trans* (B to B_1) and *cis* (A to A_1), respectively. Using GMGJ featuring 2′-p-tolyldiazenyl-1,1′:4,4′-terphenyl-4,4″-dicarboxylic acid (TTDA) containing an azobenzene side group, Meng *et al.* developed a reversible photoelectric molecular switch that can be turned "On" and "Off" optically [Figs. 3(b) and 3(c)].[64] The conductance enhancement under the "On" state was attributed to a narrowed energy gap between HOMO of *cis* isomer and E_F. In addition, by changing the applied bias, the stability of these two isomer states was altered. As shown in Fig. 3(d), $\triangle E$ is the transition energy required to switch from *trans* to *cis*. When the bias is below the critical point −0.21 V, the transition energy is negative, indicating that the *cis* is more stable than *trans*. The energy diagram for this phenomenon is illustrated in Fig. 3(e). Due to the fixed spatial orientation of azobenzene side group, the energy levels of *trans* and *cis* are influenced by external applied bias. Therefore, with more negative bias voltage, the *cis* form becomes progressively more stable relative to the *trans* state. This unique photo-switching property opens up prospects for the storage and conversion of optical energy. In the azobenzene system, light stimuli ingeniously facilitate the conversion of light energy into chemical energy, while electrical stimuli further convert the stored chemical energy into other forms of energy, thus enabling efficient energy storage and tunable conversion.

Additionally, other photoswitching compounds, such as dimethyldihydropyrene and spiropyran derivatives, are also adopted as charge transport mediums in single-molecule optoelectronics. Similar to diarylethene and azobenzene, these molecules also exhibit conductance changes under optical stimulation. For instance, the rapid and reversible switching between low- and high-conductance states in single-molecule devices was achieved through the photon-induced isomerization [SP and MC in Fig. 3(f)] of bifunctional spiropyran derivatives.[65] Similarly, employing the MCBJ approach, single-molecule junctions incorporating dimethyldihydropyrene isomers [DHP and CPD in Fig. 3(g)] have been successfully constructed, demonstrating a fairly high On/Off conductance ratio (exceeding 10^4) alongside reversibility.[66] These investigations underscore the versatile applicability of these photochromic molecules in the realm of single-molecular-scale optoelectronics.

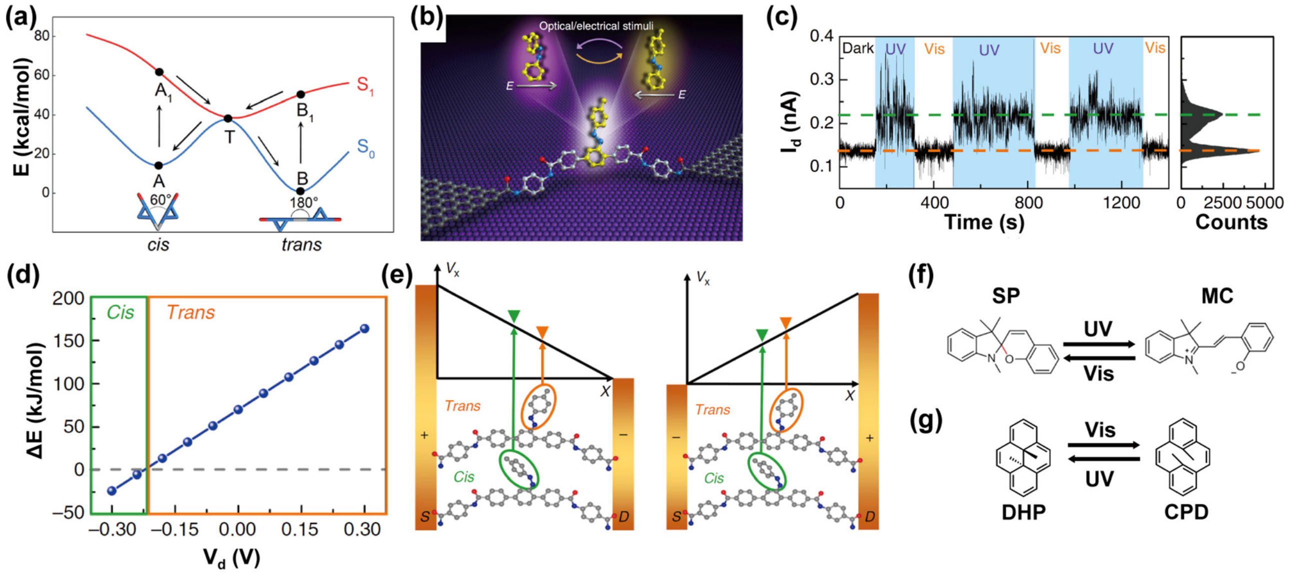

FIG. 3. (a) Energy schematic of azobenzene in between *trans* and *cis*. Reproduced with permission from Li *et al.*, Soft. Matter. **10**, 8758 (2014). Copyright 2014 Royal Society of Chemistry. (b) GMGJ setup with azobenzene derivative. (c) Current signal with photoswitching behavior; (d) Energy diagram of isomerization depending on voltage. (e) schematic of *Cis* and *Trans* potential under positive and negative bias. (f) SP and MC structures. (g) DHP and CPD structures. Reproduced with permission from Meng *et al.*, Nat. Commun. **10**, 1450 (2019). Copyright 2019 Authors, licensed under a Creative Commons Attribution (CC BY) license.

2. Exciton formation

The performance and efficiency of organic optoelectronic devices, such as Organic Light-Emitting Diodes (OLEDs), rely on the light emission owing to radiative recombination of electron–hole pairs, known as excitons. In semiconductor materials, the photon excites the electron from the valence band to the conduction band upon light illumination, creating an electrically neutral quasiparticle whose energy lies slightly less than the unbound electron and hole. Understanding the light–matter interaction in atoms, ions, and molecules, as well as the formation, dynamic, and annihilation of excitons, is of fundamental importance to modern optoelectronics and display technologies. Once a molecule absorbs the quantum of energy, it can be excited from HOMO to LUMO within the same molecular manifold forming a tightly bound exciton with energy in the range of 0.1–1 eV. Scanning tunneling microscopy (STM) can resolve light emission and/or transmission changes due to excitons within a short lifetime of nanoseconds. In a single-molecule junction, the alignment of excitonic binding energies with Fermi energies of metal terminals can give rise to photoconductance. Different mechanisms have been proposed for photoconductance for molecules under illumination. Light absorption can induce structural change that favors or opposes charge transport. As an example, under UV irradiation, the azobenzene molecule transforms from planar *trans* to the curved *cis* conformation with a higher HOMO–LUMO gap.[59,67] A large degree of molecular asymmetry in molecular junctions leads to the opening of an additional conduction channel analogous to a semiconducting donor–acceptor system. Finally, the creation of photoinduced conduction sidebands upon light absorption is known as adiabatic photo-assisted tunneling.[68–71] In perfectly symmetric molecular moiety, and without any structural change, Zhou *et al.* showed that the exciton formation would manipulate the energy alignments, leading to enhanced charge transport at a single-molecule junction.[72] To validate this theory, they performed the photoconductance measurement using STMBJ with perylene tetracarboxylic diamide (PTCDI) attached to the gold electrode, as shown in Fig. 4(a). Electrons in the photoactive PTCDI, under resonant illumination, are excited from the HOMO level to the LUMO, making it partially filled. Therefore, HOMO shifts toward the Fermi energy of the gold due to the Coulombic interaction [Fig. 4(b)]. This implies that the transmission can be progressively enhanced as the exciton binding energy increases. The results suggest that the photoconductance is mediated by the formation of bound exciton, which causes a shift in the local energy of frontier orbitals. Consequently, as depicted in Fig. 4(c), the conductance in the dark mode is lower than that of the illuminated mode, yielding a photoconductance with an On/Off ratio of 40%, which is perfectly reversible. This work hinted

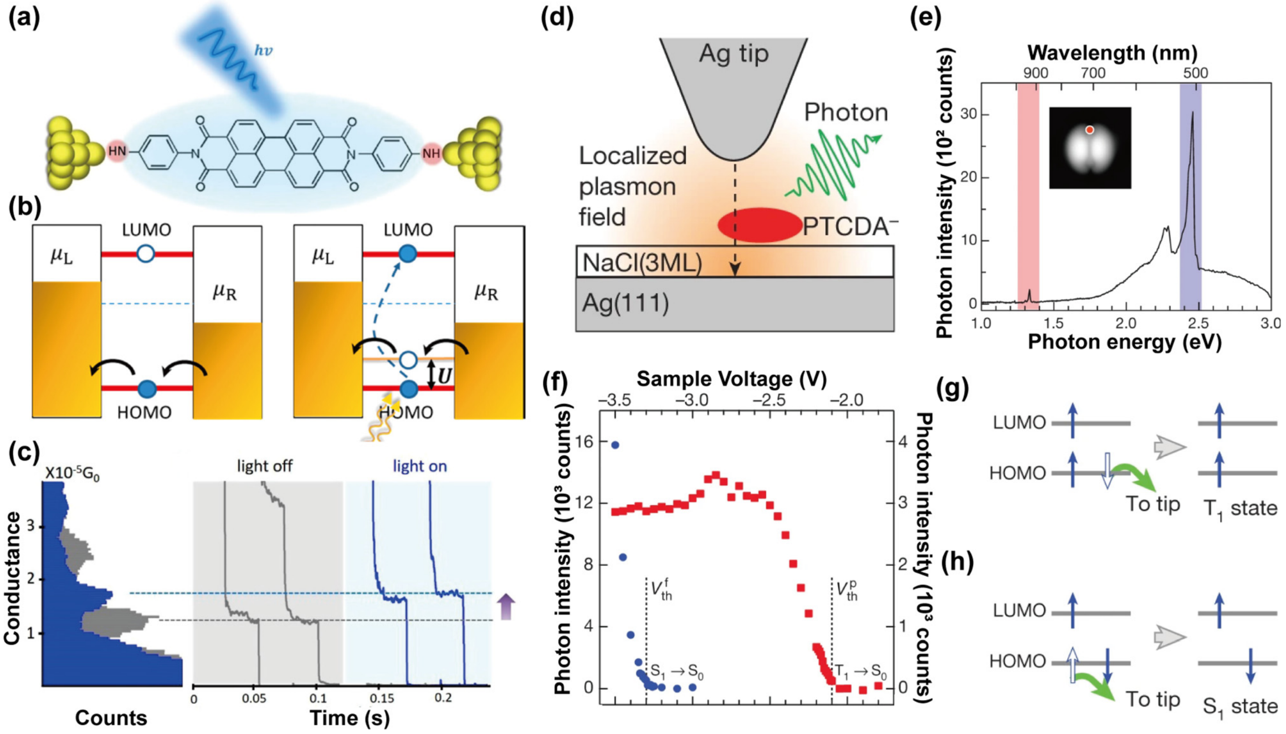

FIG. 4. (a) Schematic representation of molecular junction incorporating NH2-PTCDI-NH2 molecule in an STMBJ setup. (b) Energy diagram of the molecular junction with two electrodes held at a voltage difference (left). In the dark mode, the charge transport is dominantly through the HOMO energy level, while (right) for molecule under illumination, the LUMO is half filled leading to a shift in the HOMO level toward Fermi level enhancing the conductance. (c) 1D histogram and representative conductance traces when the light is off (gray) and on (blue). Reproduced with permission from Zhou *et al.*, J. Am. Chem. Soc. **140**, 70 (2018). Copyright 2018 Authors, licensed under a Creative Commons Attribution (CC BY) license. (d) Schematic of STML measurement. (e) Luminescence spectrum captured from a single PTCDA molecule. The blue and red labeled regions are where S_1 -> S_0 and T_1 -> S_0 transition occurs. The STM image is shown in the 4 nm by 4 nm inset. (f) The photon intensity as a function of bias voltage (blue circles and red squares represent fluorescence and phosphorescence intensities, respectively). Schematic of exciton generation mechanism at sample voltage of (g) $V_s < -2.1$ and (h) $V_s < -3.3$. Reproduced with permission from Kimura *et al.*, Nature. **570**, 210 (2019). Copyright 2019 Springer Nature.

that if the energy gap between the Frontier molecular orbital (FMO) and electrode E_F is designed to be comparable to the exciton energy, the photoconductance can be enhanced to several orders of magnitude.

To further enhance the energy conversion in OLEDs, the formation and recombination of excitons play a crucial role. The advantage of the spin-triplet (T_1) exciton decay was demonstrated in efficient OLED based on phosphorescence. Owing to the lower energy of T_1 compared to spin-singlet (S_1), selectively employing the T_1 exciton decay as the light emission source enables the device to operate at lower voltages. To elucidate the physics of exciton in a single molecular system, Kimura *et al.*[73] employed STM combined with optical spectroscopy. They proposed a method of selective formation of T_1 exciton using the charged molecule of 3,4,9,10-erylenetetracarboxylicdianhydride (PTCDA), adsorbed on NaCl film over Ag(111). The electron transport was obtained by measuring the differential conductance spectrum. Observing the double-lobed structure, similar to the LUMO spatial distribution, at both voltage polarities indicates that the charge transport is LUMO-dominated at both polarities. As shown in Figs. 4(d) and 4(e), as the charge is injected into the specified location of the charged molecule, immobilized on NaCl, two types of transitions occur upon exciton decay. The primary peak at 2.45 eV was attributed to the 0–0 transition between the vibrational ground state S_1 exciton state and the S_0 ground state. The other less prominent peak at 1.33 eV was assigned to the T_1-S_1 phosphorescence transition. It is worth noting that the coupling of tip-induced localized plasmon with exciton is responsible for the enhanced luminescence of the system. To selectively form the T_1, they investigated the correlation of sample voltage and the STM luminescence (STML) spectra. Figure 4(f) shows that the phosphorescence occurs at the voltages between −2.1 and −3.3 V. The high voltage threshold for phosphorescence is smaller than 2.45 V, which corresponds to the S_1, which suggests the direct formation of T_1 at low voltages. The proposed mechanism for the selective formation of the T_1 exciton is depicted in Figs. 4(g) and 4(h). As the applied bias goes below $V s < -0.5$ V, the charged PTCDA transits to the neutral ground state S_0 under resonant tunneling conditions. On the basis of exchange interaction, the novel experimental techniques of monitoring the spin-transition at the single-atom and single-molecule level pave the way for the development of more energy-efficient spintronic and optoelectronic devices.

Advancement in tip-enhanced spectrometry techniques, primarily by means of STM, has provided insights into enhanced light–matter interaction and dynamics of optical excitations at the single molecule level, which are crucial in quantum emitters and quantum computing.[74–76] For instance, in the realm of nanoscale, STML has enabled researchers to unmask the underlying mechanisms of generation and dynamics of singlet, doublet, and triplet molecular Frankel excitons.[77–79] After the discovery of charged exciton, known as trions, resolving the ultrafast dynamic of exciton and trion at the molecular level has remained a challenging task, although the STML time resolution is comparable to exciton and trion lifetime. Using the STML and redirecting the charge-induced emitted photons to a picosecond single-photon counter, Doležal *et al.*[80] resolved the combined dynamics of exciton and trion of a single ZnPc molecule. The response of the system in terms of radio frequency phase shift was interpreted from the phase shift of electrical modulation and delayed optical response, which was linked to the finite decay rate of the molecular exciton. The experimental setup is schematically depicted in Fig. 5(a), where the ZnPc single molecule lies on the three layers of NaCl deposited on Ag (111). Upon injection of electrons and holes in the molecule, optical excitation occurs due to exciton recombination. The peaks on the electroluminescence spectra, shown in Fig. 5(b), correspond to the emission of neutral exciton (X) at 1.89 eV and the charged exciton (X^+) at 1.52 eV. The measured phase shift associated with the observed peaks is shown in Fig. 5(c). Images captured from the single molecule elucidated that X emission is more pronounced at porphyrazine macrocycle at higher bias voltages, and the X^+ map appears on the periphery of the molecule. In this study, the high temporal resolution of the STML with high yield provided useful information about the exciton–trion dynamics and also the particularly, ultrafast trion lifetime that suggests the potential use of trions as single photon electro-optical transducers in the GHz regime.

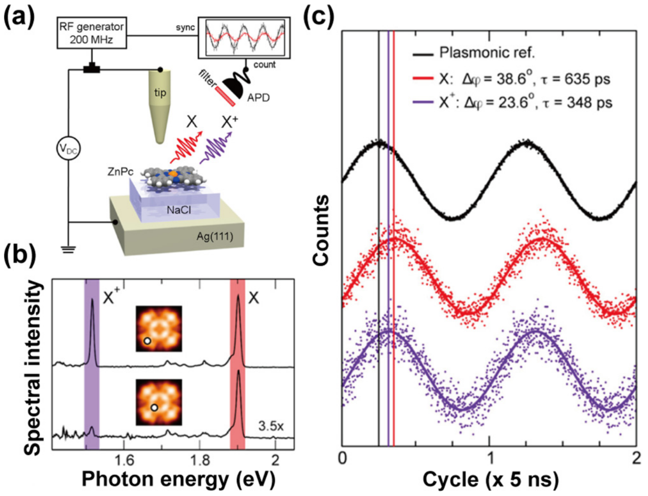

FIG. 5. (a) Schematic illustration of the experimental setup. (b) STML spectra extracted from a lobe and a point close to the center of ZnPc while V_{DC} and tunneling current are held at −3.0 V and 100 pA, respectively. The insets show the position of the charge injection. (c) Radio-frequency phase-shifted waves collected for a (black) plasmonic reference at $V_{DC} = 2.0$ and tunneling current of 70 pA and $V_{AC} = 100$ mV, (red) neutral exciton at $V_{DC} = 2.2$ and tunneling current of 70 pA and $V_{AC} = 100$ mV, and (purple) trion X^+ at $V_{DC} = 3.2$ and tunneling current of 120 pA and $V_{AC} = 100$ mV. Reproduced with permission from Doležal *et al.*, ACS. Nano **15**, 7694 (2021). Copyright 2021 Authors, licensed under a Creative Commons Attribution (CC BY) license.

The high spectral and temporal resolution of tip-enhanced scanning probe spectrometers has successfully mapped the eigenstates and characterized the excitonic state and energy transfer mechanisms of charged and neutral excitons. Moreover, thanks to the precise local spectro-microscopy techniques, the coupling between molecular clusters can be controlled, which leads to the generation of a delocalized excitonic state. Carefully controlling the local entanglement between molecular excited states can be utilized in quantum computing, where quantum information is encoded by molecular coupling in an aggregate. Doležal *et al.*[81] showed that the exciton delocalization across the small clusters of PTCDA anions. They spatially and temporally resolved the eigenmodes employing the STML and atomic force microscope (AFM), which were used to transduce electric current to the well-defined optical transitions in the dye molecule. For the sufficiently decoupled single molecule, the molecule becomes anion radical on the surface with a total spin of ½ (D_0-); therefore, chromophores have the predominant optical decay from D_1- to D_0-., known as longitudinal mode. As seen in Figs. 6(a) and 6(b) for the nonlinear parallel dimer configuration, the two longitudinal modes are efficiently coupled, leading to two exited states, T_1^{2-} and T_2^{2-}. This can be understood by the dominant peak at 1.333 eV, which was assigned to the two excited states of the assembly T_1^{2-} and T_2^{2-}. On the other hand, the perpendicular mode favors the coupling between longitudinal and transversal modes, leading to a dominant contribution from higher energy state T_3^{2-} (Figs. 6(c) and 6(d)). These results imply that engineering the excitonic properties in organic dye assemblies offers advanced functionalities and the ability to control photon emission and energy conversion at the nanoscale precisely.

The exciton dynamics and the degree of its delocalization are significantly affected by the conjugation length of the molecule. In a π-conjugated cyclic oligothiophenes, Park *et al.*[82] investigated the size-dependent of the excited-state dynamic planarization processes employing the femtosecond upconversion technique. In this process, delocalization of exciton occurs as a consequence of dynamic planarization, which reduces the torsional angles and enhances the π-orbital overlap between chromonic units. As schematically shown in Figs. 6(e) and 6(f) for two extreme cases of dynamic planarization of cyclic oligothiophene composed of six (C-6T) and twelve (C-12T) thiophene units, the system size increases the higher degree of conformational disorder of cyclic oligothiophene inhibit the complete delocalization of exciton over carbon chain. These results suggest that properly designed molecular materials can be tailored to have controllable delocalization of exciton for different applications.

B. Photocurrent and photovoltaic effects in MSJs

Photovoltaic effect is a fundamentally critical physical phenomenon in which electrical energy is generated by a semiconductor or semiconductor-like material when it absorbs photon energy. It is worth clarifying the difference between photovoltaic and photoelectric effect here. Photoelectric effect involves the ejection of electrons from a material (often metals) when it is exposed to light of energy greater than the work function of the material. Photovoltaic phenomenon concerns the generation of electrical power by converting light directly into electricity. In a photovoltaic device, when photons are absorbed by a semiconductor material, they excite electrons from the valence band to the conduction band, creating electron–hole pairs. Subsequently, electrons and holes are driven by the built-in electric field toward opposite directions, generating a flow of electric current (also known as photocurrent) when an external circuit is connected. In contrast to macroscopic materials where energy landscape are largely continuous, molecular-scale materials possess quantized energy levels that are defined by molecular structures, which can be tuned with atomic precision,[83] allowing one to control the resulting photocurrent.[84]

Photocurrent from a MSJ can inform critical energy information of the molecule.[85] To obtain comprehensive details on the charge transport dynamics of molecular materials and devices, the ability to map out transmission spectrum, namely, transmission as a function of energy, of MSJs is central.[83] To achieve this, several experimental techniques have been developed to quantify the electron transmission at different energies via gauging the alignment of electrode E_F and the frontier molecular orbital (FMO) at ambient condition, such as transition voltage spectroscopy,[86] thermopower measurements,[87,88] and gating techniques.[89] However, challenge remains in accessing and understanding transmission properties in the regime beyond the HOMO–LUMO gap. To overcome this challenge, Liu *et al.*[90] recently developed a STM-based single-molecule photoelectron tunneling spectroscopy capable of accessing the LUMO + 1 and LUMO + 2 molecular orbitals above the HOMO–LUMO gap. This was achieved through monitoring the excessive electrical current produced by the resonant tunneling of photoexcited electrons from one of MSJ electrodes. As shown in Fig. 7(a), a regular current amplifier was used to measure the static conductance of

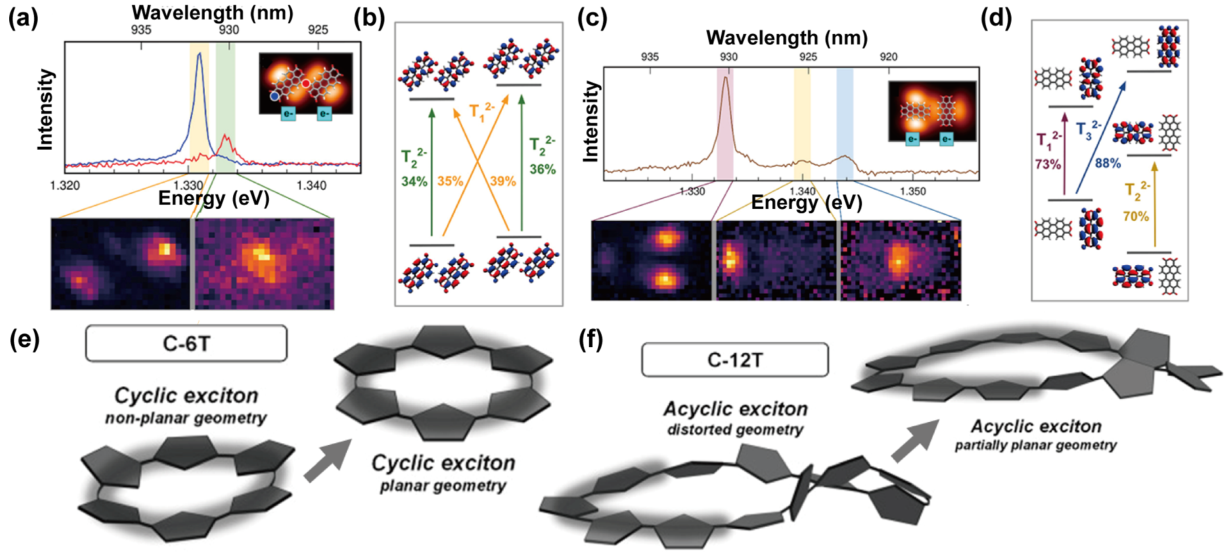

FIG. 6. (a) and (b) STML spectra of parallel and perpendicular dimers and the experimental photon map extracted from the shaded region. Insets show the constant-height tunneling current image marked by the representative location of where the spectra with the corresponding color are obtained. (c) and (d) Excitations with the primary contributions to the ground state (weight in percent). Reproduced with permission from Doležal *et al.*, ACS. Nano. **16**, 1082 (2022). Copyright 2022 Authors, licensed under a Creative Commons Attribution (CC BY) license. Planarization process of (e) C-6T, and (f) C-12T. Reproduced with permission from Park *et al.*, Angew. Chem., Int. Ed. **54**, 12711 (2015). Copyright 2015 Wiley.

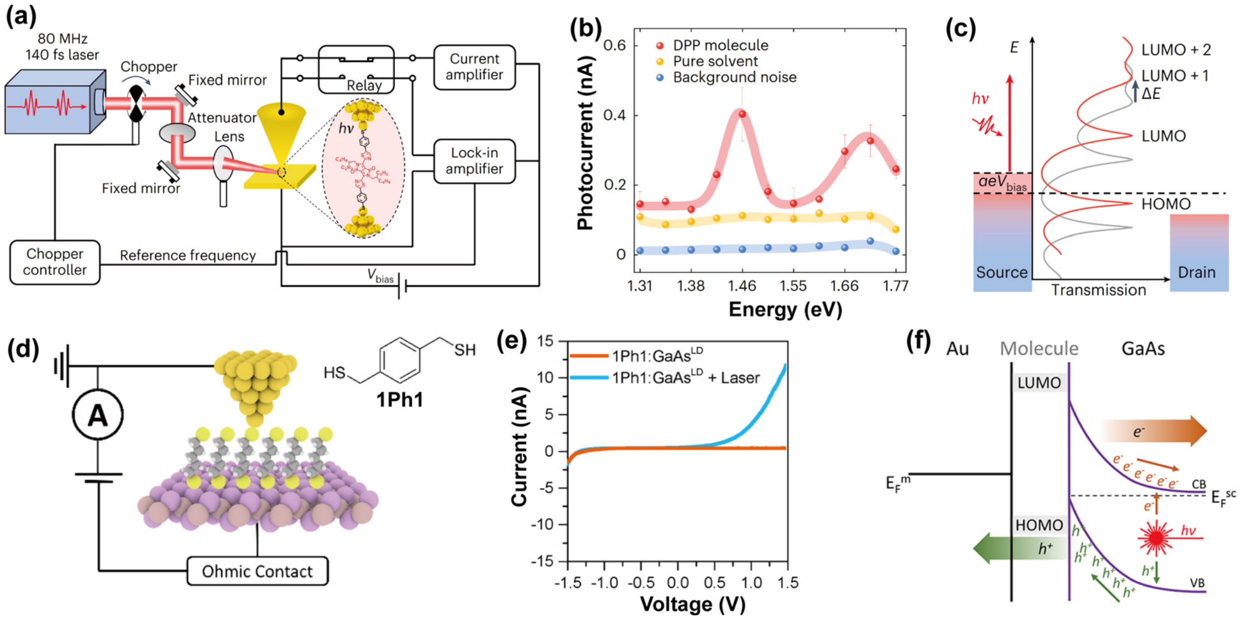

FIG. 7. (a) Schematic of STMBJ setup and DPP molecular structure. (b) Photocurrent spectrum indicating the molecular orbital for charge transport. (c) Energy diagram of molecular orbitals with light irradiation. Reproduced with permission from Liu *et al.*, Nat. Mater. **22**, 1007 (2023). Copyright 2023 Springer Nature. (d) Schematic of MMS setup and molecular structures 1Ph1. (e) IV curves with and without the laser. (f) Energy diagram of the charge transport through the junction. Reproduced with permission from Vezzoli *et al.*, Nano. Lett. **17**, 6702 (2017). Copyright 2017 Authors, licensed under a Creative Commons Attribution (CC BY) license.

a single diketopyrrolopyrrole (DPP) molecule using STMBJ technique. Upon creating a mechanically stabilized DPP junction, a 1 kHz ultrafast laser pulse irradiation was applied, and the resulting photocurrent was measured with a lock-in amplifier. During laser irradiation, the external bias across the tip and substrate was zeroed to suppress static current. To avoid light absorption by the molecule, the laser energy smaller than the HOMO–LUMO gap of the molecule was chosen. By measuring the photocurrent under different laser energies, the transmission profile at higher energies can be directly accessed and mapped out. In Fig. 7(b), the two photocurrent peaks indicate the resonant transport of photo-induced electrons tunneling through two distinct transmission resonances LUMO + 1 and LUMO + 2. During the process of photo-induced tunneling, electrons on the source electrode are first excited to higher energies due to laser illumination. Then, these photoexcited electrons migrate through perfectly aligned molecular orbitals via coherent resonant tunneling, facilitating the energy conversion from light to electricity. In this case, the light-electric energy conversion is leveraged as a tool to gain insights into MSJ energy landscape, which is essential for understanding the transport properties of MSJs.

In addition to widely used noble-metal electrodes (e.g., Au, Pt, and Ag) in MSJs, utilization of semiconductors as electrode materials offers opportunities to introduce photovoltaic effect in the junction. In this regard, Vezzoli *et al.*[91] adopted GaAs as one of the electrodes to form a metal–molecule–semiconductor (MMS) junction in a STMBJ setup. The MMS junction comprised of conjugated molecule 1,4-Phenylene(dimethanethiol) (1Ph1) yields a higher photocurrent [Figs. 7(d) and 6(e)] attributed to a smaller HOMO–LUMO gap. As shown in Fig. 7(f), when the GaAs electrode is illuminated, electron–hole pairs are first generated on GaAs and then swept into the molecular junction by the electric field in the space charge region. Thus, the HOMO level of 1Ph1 opens the transmission channel for holes, resulting in the observed photocurrent. Despite that the photovoltaic effect originates from the semiconductor electrode rather than the molecular core, the molecular structure plays a deterministic role in engineering the alignment between and excited charge carriers and, in this case, leads to a strong current rectification effect.

C. Nano-optics in MSJs

Metallic MSJs allow strong spatial confinement of electromagnetic fields to dimensions much smaller than the free-space wavelength of light, resulting in localized surface plasmon resonances (LSPR) at wavelengths determined by the junction material, shape, and size.[92–95] Specifically, LSPRs refer to the collective and coherent oscillations of conduction electrons confined to the surface of the metallic nanostructures and are typically excited upon optical illumination or electrical excitations such as inelastic electron tunneling through the molecular junctions. Through the manipulation of size, shape, and material composition of the nanostructure, LSPR can be finely tuned across a broad spectral range, spanning from the infrared to ultraviolet wavelengths, and thus opens up a wide array of potential applications across various fields.[96–99] The extremely small effective volume of MSJ has provided a means for significantly amplified interactions between light and electronic excitations, as well as phonons, facilitating efficient energy transfer and conversion.[100–102] In this section, advances in plasmon-induced processes at the molecular scale are reviewed, including quantum plasmonics, molecular-scale photon emission, strong coupling-enabled molecular nanophotonics, and optomechanics.

1. Quantum plasmonics

Classical electrodynamics are commonly applied to understand the plasmonic behavior of metal nanostructures. These methods predict a monotonic increase in electric field enhancements as the gap distance decreases, achieved through a frequency- and position-dependent linear dielectric function.[103–105] However, when the two nanostructures are coupled to form an ultrathin gap structure, which could contain a molecular junction, such coupled nanosystems, described by the single-digit nanometer or sub-nanometer-sized gaps, can support quantum plasmonic effects due to non-local screening and electron tunneling, for which classical electrodynamics is no longer valid [Fig. 8(a)].[106–108] The spatial localization of surface charges can be quantified by the frequency-dependent distance parameter called the Feibelman parameter, defined as the position of the centroid of the induced surface charge density relative to the geometrical boundaries and is typically within the sub-nanometer range.[109] Due to the shift of the surface charges with respect to the geometrical boundaries induced by the nonlocal screening, the Feibelman parameter can be modified accordingly and thus lead to an "effective" nano-gap size. The non-local screening leads to deviations of quantum plasmon resonances from the classical description. Furthermore, electron tunneling at optical frequencies represents another major quantum feature that cannot be captured by classical theories. The electron densities associated with the two metal surfaces begin to overlap when the gap distance is comparable to the length scale of the electron spill-out, resulting in the tunneling of electrons through the potential barrier. Electron tunneling is crucial for elucidating the observed quantum plasmonic responses when the nanostructure geometry varies at the sub-nanometer scale, corresponding to the length scale of a typical molecular junction. Typically, it has been reported that the plasmon resonance associated with a tunneling gap undergoes significant influence from the electrons tunneling across the junction, leading to a gradual emergence of the blue-shifted charge-transfer plasmon (CTP) mode [Fig. 8(b)].[110]

a. Non-local effects. Savage *et al.*[111] investigated the quantum regime of plasmonics by concurrently measuring the electrical and optical properties of two coupled gold nanostructures with controllable sub-nanometer separation [Fig. 8(c)]. Dark-field scattering spectra were recorded for two gold-nanoparticle-terminated AFM tips in a tip-to-tip configuration. When the distance is 0.3 nm, tunneling-induced quantum plasmonics start to dominate, leading to the formation of CTP modes, which limits the optical field confinement in the gap due to non-local screening. Similar experiments were performed by Scholl *et al.*,[112] in which coupled metallic nanoparticles with varying gap sizes were employed for electron energy-loss spectroscopy. It was found that when the gap size reduced to < 0.5 nm, the bonding dipolar mode vanished and was replaced by a dipolar CTP mode.

When a molecular dielectric layer is applied inside the gap, the peak wavelength of the plasmonic resonance was observed to diverge from the predictions of the local classical plasmonic model for gap distances of approximately < 3 nm, which agrees well with the hydrodynamic model [Fig. 8(d)].[113] Zhu *et al.*[114] performed surface-enhanced Raman scattering on molecules embedded in plasmonic dimers with a gap size of 0.2 nm to probe the quantum mechanical effects on the plasmonic enhancement. By correlating the structural characterization of each individual dimer with its SERS spectra, they illustrated that the maximum achievable plasmonic enhancement is constrained by electron tunneling effects at optical frequencies.

b. Inelastic electron tunneling: Below- and above-threshold light emission. When a tunneling junction is electrically biased, electrons can tunnel through the barrier. As the gap distance approaches the nanometer and sub-nanometer scale, inelastically tunneled electrons can go through radiative decay channels and generate photons mediated by the plasmons. In this section, inelastic tunneling-induced photon conversion will be presented, with an emphasis on how different mechanisms are affected by the gap size (tunneling regime) and plasmonic characteristics.

The phenomenon of light emission from electrically biased tunnel junctions has been well-known since the seminal work by Lambe and McCarthy.[115] The underlying mechanism involves the excitation of LSPR near the tunneling junction through inelastic interaction with tunneling electrons, followed by rapid radiative decay, resulting in far-field photon emission. One important characteristic of this photon emission is the energy cutoff of the emitted photon ($\hbar\omega < V_b$, also called below-threshold photon emission), where V_b is the electrical bias. The emission spectrum of electrically driven tunnel junctions and ultra-thin plasmonic gaps is determined by considering the detailed atomic-scale local geometry and the specific conditions of inelastic electron tunneling. In general, it can be understood as an antenna effect, where the surface plasmon mode of the tunnel junction is scattered by the fluctuating tunneling current, which can be described by the shot noise spectra, into the far-field photons.[116] The energy cutoff is therefore imposed by the current noise spectral density. This below-threshold light emission is often observed in STM-based tunnel junctions at relatively small tunneling current ($\sim$100 nA).[117,118]

Above-threshold light emission occurs when the tunneling current is increased to the point that the higher-order electron tunneling events become possible. Briefly, instead of tunneling individually through the barrier, two or more electrons can coherently tunnel through the junction, resulting in the excitation of a higher energy plasmon. This phenomenon leads to the emission of so-called "2e" and "3e" emissions, which surpass the energy cutoff mentioned above. Several theoretical models have been developed to explain multielectron coherent tunneling, each offering variations in the detailed depiction of the tunneling process.[119–121]

More recently, Peters *et al.* conducted a measurement of light emission from an STM-based junction structure, revealing kink-like features at respective energies corresponding to 1e, 2e, and 3e, indicating the emission resulting from the quantized multielectron tunneling process.[122,123] This emission pattern agrees well with their developed multielectron coherent scattering model. This model was later generalized to a finite temperature scenario [Fig. 8(e)].[123]

Plasmonic processes, such as the generation of hot carriers, can play an important role in the emission of above-threshold photons. Under this scenario, the LSPR excited by the inelastic tunneling electrons initially undergo a nonradiative damping process, generating hot electrons and hot holes above and below the Fermi surface. A steady-state distribution of hot carriers can be sustained if the rate of tunneling electrons surpasses the rate of hot carrier relaxation, with its specific form influenced by the time interval between successive electron tunneling events and the lifetime of hot carriers. These hot carrier pairs subsequently undergo radiative decay via plasmon-mediated recombination. This process results in broadband photon emission that can exceed the energy threshold limited by the voltage bias [Fig. 8(f)].[124,125]

2. Molecular-scale strong-coupling effect

Molecular quantum emitters positioned within the intensified fields of these metallic plasmonic junctions undergo alterations in

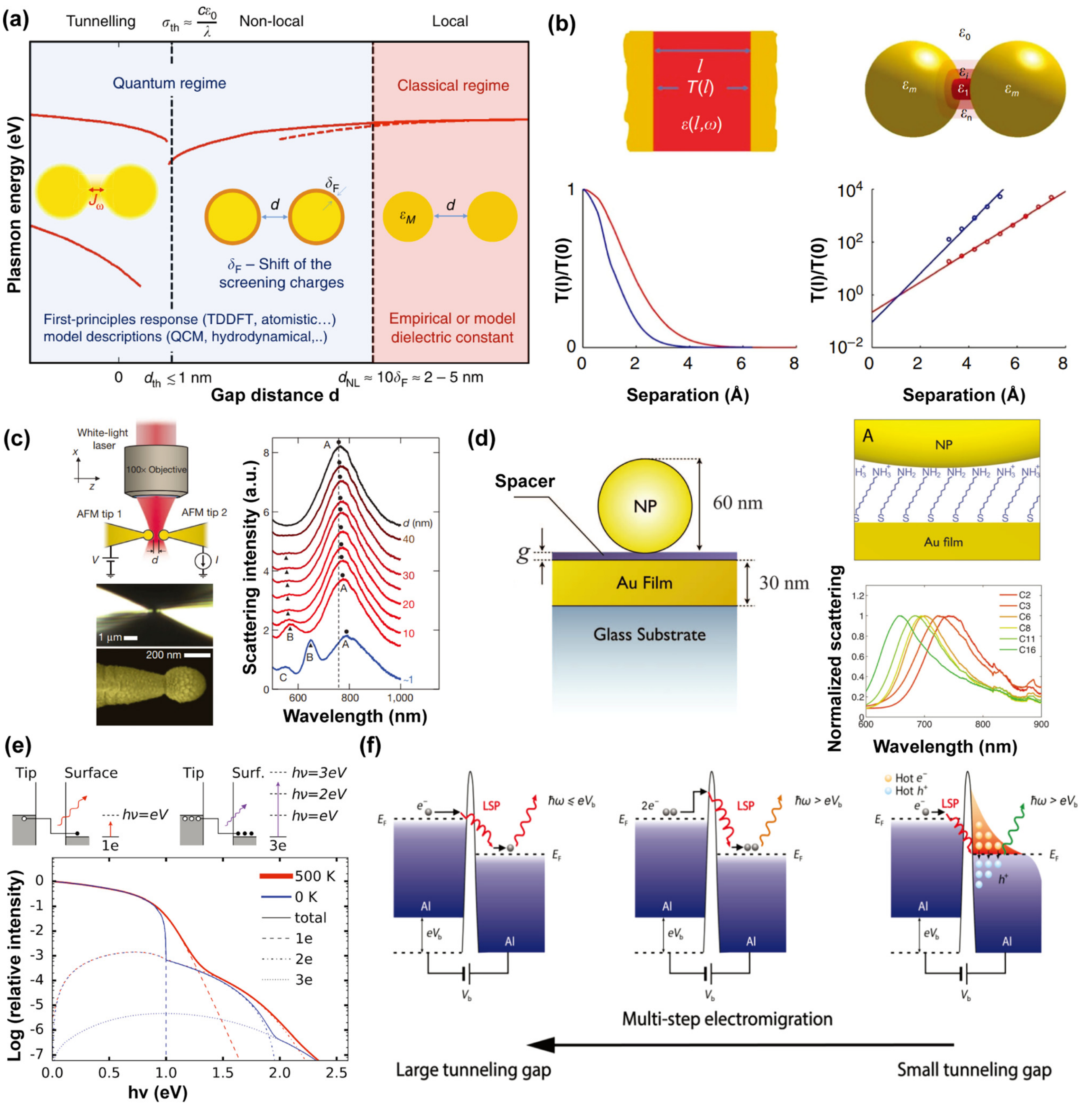

FIG. 8. (a) Different regimes for the plasmon resonances of a sphere-dimer in a vacuum identified as a function of the gap distance *d*. Reproduced with permission from Zhu *et al.*, Nat. Commun. **7**, 11495 (2016). Copyright 2016 Authors, licensed under a Creative Commons Attribution (CC BY) license. (b) Geometries and parameters involved in the quantum-corrected model as well as calculated optical response. Reproduced with permission from Esteban *et al.*, Nat. Commun. **3**, 825 (2012). Copyright 2012 Authors, licensed under a Creative Commons Attribution (CC BY) license. (c) Formation and characterization of a nanoscale plasmonic cavity, with measured dark-field scattering spectra from one inter-tip cavity at different cavity widths. Reproduced with permission from Savage *et al.*, Nature **491**, 574 (2012). Copyright 2012 Springer Nature. (d) Geometry of the film-coupled nanoparticle and normalized dark-field measured spectra of ensembles of film-coupled nanoparticles for SAM spacer layers of different numbers of carbon atoms. Reproduced with permission from Ciracì *et al.*, Science. **337**, 1072 (2012). Copyright 2012 American Association for the Advancement of Science. (e) Energy diagrams for single- and multielectron photon emission processes from an STM junction comprising a tip and a surface as well as Calculated emission intensity of multielectron processes at T = 0 and 500 K. Reproduced with permission from Peters *et al.*, Phys. Rev. Lett. **119**, 066803 (2017). Copyright 2017 American Physical Society. (f) Schematics for various light emission mechanisms and electromigration process. Reproduced with permission from Zhu *et al.*, Nano. Lett. **22**, 8068 (2022). Copyright 2022 Authors, licensed under a Creative Commons Attribution (CC BY) license.

absorption and emission rates, quantum efficiencies, and radiation patterns, resulting in strong light–matter interaction and thus strong coupling effects. A wide variety of materials incorporating well-defined energy transition levels can be employed, including quantum dots,[126,127] few layer transition metal dichalcogenides (TMD),[124,128–130] and fluorescent dyes.[131,132] The precise nanoscale positioning of the molecular quantum emitter and the orientation of its dipole moment play a crucial role, as the local fields of nanogap structures can vary significantly over a few nanometers and preferentially align to specific orientations.

In the weak coupling regime, the modification of the molecular fluorescence rate becomes significant. Emitters in close proximity to a plasmonic gap or tunnel junction can either improve the fluorescence through the high local field intensity[133] or quench the fluorescence via non-radiative decay channels from the metal. Fluorescence changes stem from several factors, including altered radiative quantum yields, excitation efficiency, collection efficiency, and spontaneous emission rate due to the presence of the plasmonic gap. The intrinsic dipole moment of an emitter, along with its controllable electromagnetic environment, determines its spontaneous emission rate [Figs. 9(a) and 9(b)],[134,135] which can be substantially enhanced through the Purcell effect by employing plasmonic nanogaps characterized by high-quality factors and ultra-small effective mode volumes. The radiative decay rate, on the other hand, can also be improved.[136] Appropriately balancing between high-field enhancements and non-radiative decay rate enables significant radiative-rate enhancements, reaching approximately three orders of magnitude for dye molecules positioned within a 10-nm gap between a metal film and silver nanocubes or nanowires, or in a nanoparticle on mirror structure (NPoM) encapsulated with DNA origami.[137,138] The ability to tune the spontaneous emission rate of emitters by combining them within cavities holds the potential for realizing ultrafast, low-power light sources, modulators, and single-photon sources.

When molecules with significant oscillator strengths are utilized, where the radiative decay rate is comparable to the plasmon decay rate, it results in efficient energy exchange between the emitter and the cavity mode, leading to the formation of hybridized states. This can be realized for ensembles of many molecular emitters, such as molecular aggregates. J-aggregates constitute a class of fluorophore aggregates that arise from the structured assembly of organic dyes, representing narrowly confined and red-shifted absorption and emission bands. Strong plexciton coupling and giant Rabi splitting are observed for J-aggregates when embedded in single plasmonic gold dimers, which is also the first experimental observation of strong coupling in individual nanostructures.[139] Similar single-emitter level strong coupling had also been realized by using host-guest chemistry to align one to ten protectively isolated methylene-blue molecules into the NPoM structure with an effective mode volume of less than 40 cubic nanometers.[140] Strong plasmonic coupling with molecules has also been observed in nanohole arrays, grating structures, nanovoids, and nanorods.[141–143]

3. Surface/tip-enhanced Raman spectroscopy and optomechanics

Plasmonic nanojunctions can locate enhanced optical field distributions in an ultra-small mode volume and anchor molecules or layers of interest in predetermined positions and orientations. Such characteristics hold significant promise for applications such as real-time chemical interrogation of small quantities of molecules or ultrathin materials. The significant field enhancements facilitate surface or tip-enhanced Raman spectroscopy (SERS or TERS) signals from samples situated within the gap, enabling localized detection and fingerprinting for chemical information down to the single molecule level. SERS or TERS involves the inelastic scattering of light with nanoconstrictions or nanogaps. An excitation photon induces a dipole in the molecule, followed by inelastic light scattering. Stokes scattering occurs when the scattered photon has lower energy than the incident photon by one or more quanta of characteristic vibrational energy (positive Raman shift relative to excitation), retaining the molecule in its first vibrational state. Conversely, anti-Stokes scattering happens when the scattered

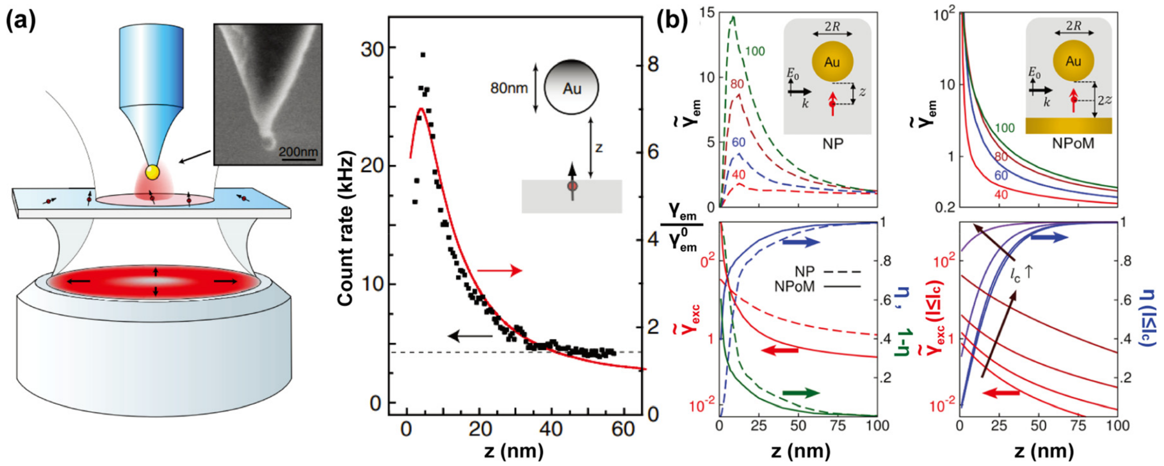

FIG. 9. (a) Sketch of the experimental arrangement, where a gold particle is attached to the end of a pointed optical fiber and fluorescence rate as a function of particle-surface distance z for a vertically oriented molecule. Reproduced with permission from Anger *et al.,* Phys. Rev. Lett. **96**, 113002 (2006). Copyright 2006 American Physical Society. (b) Fluorescence rate of an emitter with transition wavelength 650 nm placed at distance z from an isolated nanoparticle and a nanoparticle on mirror (NPoM) structure. Reproduced with permission from Kongsuwan *et al.*, ACS. Photonics. **5**, 186 (2018). Copyright 2018 Authors, licensed under a Creative Commons Attribution (CC BY) license.

photon has higher energy than the incident photon (negative Raman shift relative to excitation), resulting in the molecule returning to its ground state. In contrast to previous nanostructures that often exhibit numerous SERS blinking events, which have been utilized to demonstrate single molecule signatures but are frequently irreproducible, thus constraining their practicality,[144] more reliable and robust SERS features can be achieved by utilizing gaps precisely defined by crystalline inorganics[145] or self-assembled monolayers of short alkyl chains or aromatic thiols [Fig. 10(a)].[146] In the latter scenario, the biphenyl-4-thiol (BPT) spacers establishing a thickness of 1.1 nm gap using NPoM

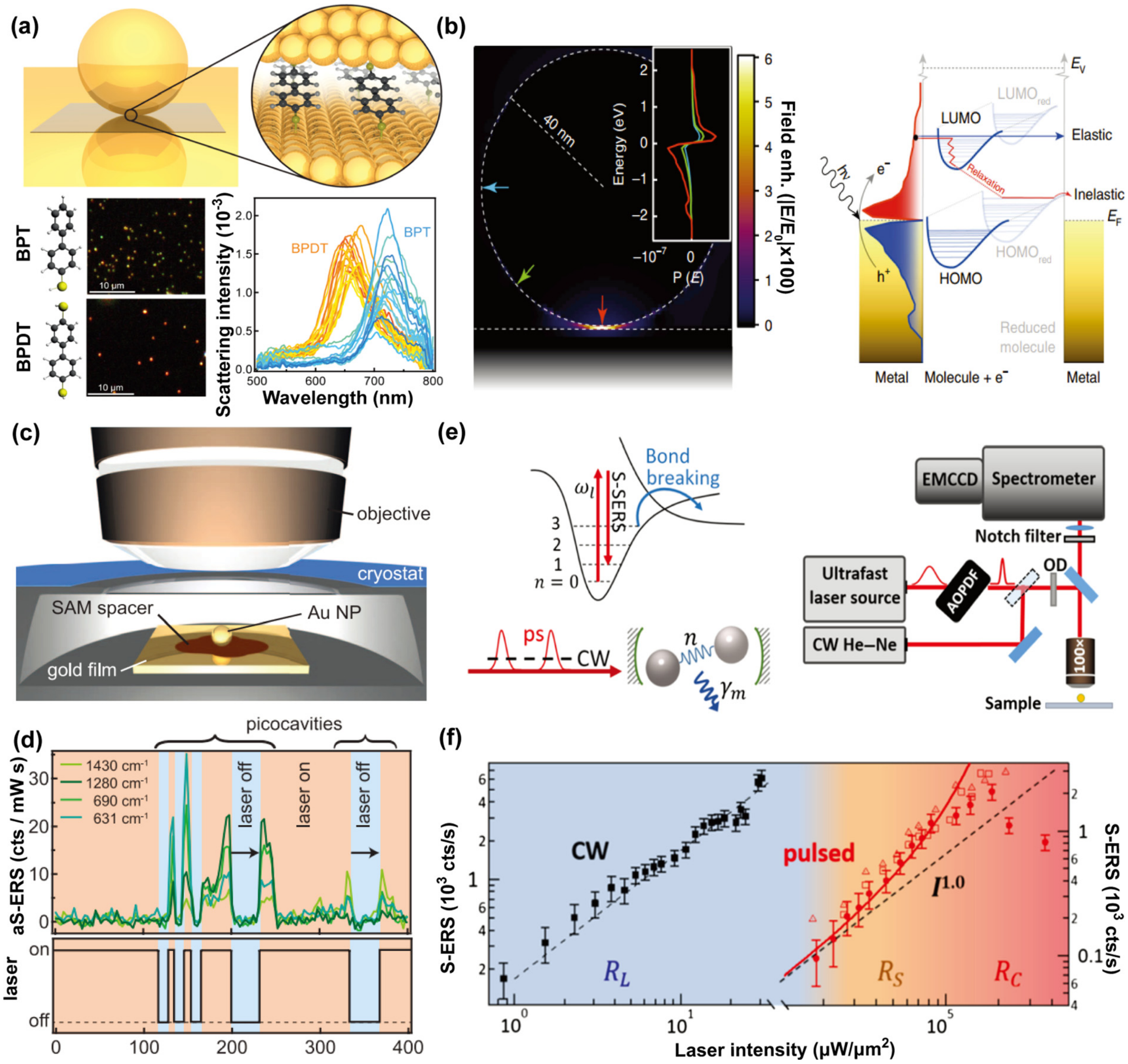

FIG. 10. (a) Schematic of nanoparticle on mirror geometry: a gold nanoparticle is placed on a gold film, separated by a thin molecular spacer layer. Below are dark field images of 60 nm gold nanoparticles and the normalized scattered intensity from individual 60 nm gold nanoparticles on BPT and BPDT are also shown. Reproduced with permission from Benz *et al.*, Nano. Lett. **15**, 669 (2015). Copyright 2015 Authors, licensed under a Creative Commons Attribution (CC BY) license. (b) FDTD-calculated electric field enhancement for NPoM structure (left) and schematic representation, which depicts the plasmon-induced hot electron transfer between Au nanoparticles and unoccupied molecular orbitals of adsorbed molecules and the consequent reduction process (right). Reproduced with permission from Nijs *et al.*, Nat. Commun. **8**, 994 (2017). Copyright 2017 Authors, licensed under a Creative Commons Attribution (CC BY) license. (c) Schematic of nanoparticle-on-mirror (NPoM) geometry for molecules in picocavities. (d) Anti-Stokes intensities as the laser (bottom) is switched on and off demonstrate the picocavity stability, which persists (arrows) without the laser. Reproduced with permission from Benz *et al.*, Science **354**, 726 (2016). Copyright 2016 American Association for the Advancement of Science. (e) Energy diagram for ground and excited molecular vibrational states and SERS setup for single nanoparticle studies, using continuous (CW) or ps pulsed excitation (right). (f) Stokes SERS intensity of 1585 cm^{-1} mode for a single NPoM vs peak laser intensity for (red circles) ps-pulsed and (black squares) CW excitation. Reproduced with permission from Lombardi *et al.*, Phys. Rev. X **8**, 011016 (2018). Copyright 2018 Authors, licensed under a Creative Commons Attribution (CC BY) license.

showed a robust Raman spectrum over time that matched well to the DFT calculations. The greatest advantage of this geometry is the high reproducibility and relative ease of assembly. On the other hand, nanocavities facilitate the observation of single-molecule SERS signatures that evolve on millisecond to second timescales. For example, the high-speed single-molecule investigations of the molecules positioned within lipid bio-membranes[147] and the information on adsorbate–adsorbate and absorbate–substrate interactions.[148] Observations of single-molecule chemistry can also be achieved. Nijs *et al.*[149] demonstrated that the hot carriers generated in the sub-nanometer cavities can facilitate the redox processes through hopping electron transport, which can be subsequently recorded using Raman spectroscopy [Fig. 10(b)].

Another remarkable property of plasmonic nanojunctions is the correlation between the coupling of molecular vibrations to light and the optomechanical Hamiltonian. In molecular optomechanics, stronger and nonlinear Raman emission can be achieved, along with the capability to vibrate molecules to the extent of breaking chemical bonds.[150,151] Hence, optomechanical effects can significantly influence Raman emission, even under ambient conditions. By localizing light to volumes well below 1 cubic nanometer (so-called "picocavities"), laser irradiation can dynamically form and disassemble the embedded molecule, yielding a factor of 10^6 enhancement of optomechanical coupling and individual molecular bonds' vibration [Figs. 10(c) and 10(d)].[102] More recently, the same group leveraged through pulsed Raman scattering, showing that stimulated vibrational pumping of molecular bonds can be achieved, revealing superlinear Stokes emission, which agreed well with pulsed optomechanical theory. They proposed that optically driven chemistry can be accessible in this scenario [Figs. 10(e) and 10(f)].[152] Furthermore, under the simultaneous electrical excitation,[153] additional vibrational heating can be triggered, with improved device stability when excited remotely.[154]

In addition, IR nanospectroscopy can also provide simultaneous spectroscopic access to both the chemical identity and morphology of molecular matter, offering molecular-level spectroscopic specificity and spatial resolution.[155] With sufficient spatial and spectral resolution, scattering scanning near-field optical microscopy (s-SNOM) can enable the exploration of heterogeneity in intra- and intermolecular coupling within a single chemically uniform nanoscale domain or crystallite. Vibrational resonances may experience frequency shifts or alterations in linewidth owing to changes in their local chemical environment. Therefore, specific marker resonances act as a sensitive tool to probe highly heterogeneous and coupled molecular systems, offering insights within individual nanoscale domains and at interfaces. In particular, through vibrational scattering–scanning near-field optical microscopy with high spectral precision, the structure–function relationship in nanophase-separated block copolymers is explored.[156] Local variations in electric fields between nano-domains can be discriminated, yielding quantitative agreement with dielectric continuum models.

4. Plasmon-induced hot carriers

The excitation of an energetic carrier within a plasmonic tunnel junction contains two parts: an electron and a hole. The term "hot" applies when their energies significantly exceed ambient temperature thermal excitations, with their energetic distribution determined by the intricate electronic structure and the excitation mechanism.[157] For example, in optical illumination, only the bright plasmon modes are excited, while tunneling currents have the capability to excite optically dark modes during electrical excitation [Figs. 11(a)–11(c)].[158–160]

One major research front in the field of plasmon-induced hot carriers is the study of the hot carrier dynamics. When photons possess sufficient energy for interband transitions, direct absorption can occur, facilitated by the momentum conservation selection rule applicable to both the initial and final electronic states. The predominant direct interband absorption for Cu and Au arises from the d-bands situated well below the Fermi level to the conduction band, resulting in the generation of high-energy holes and lower-energy electrons. The situation is reversed for Ag, and a continuous hot carrier energy distribution is expected for Al due to the different electronic structures.[161,162] Within the metallic nanojunction, electronic states become spatially localized, leading to the absence of exact eigenstates for crystal momentum, making it possible for momentum conservation prohibited transition during plasmon decay, which is known as intraband absorption. Different from interband transition, intraband absorption can be analyzed by employing the free-electron-like model and incorporating the local geometry effects within the nanostructure [Fig. 11(d)].[163] Furthermore, phonons can also participate in the transition process, facilitating phonon-assisted optical absorption, which results in the generation of hot electron and hole pairs carrying net crystal momentum [Fig. 11(e)].[164] In addition to intraband transitions, another method to preserve momentum conservation during the transition between two states with different wavevectors is through surface collision relaxation. The damping caused by surface scattering is linked to Landau damping of electrons, which also facilitates the energy transfer between electrons and photons due to field confinement.[165,166]

Hot electrons generated from plasmon decay will quickly undergo multiple relaxations by redistributing their energy into numerous lower-energy electrons via electron–electron scattering and electron–phonon scattering. Various damping mechanisms may manifest at different time stages. Following the initial excitation of hot carriers (occurring within 100 fs to 1 ps), rapid electron–electron scattering leads to prompt thermalization and the establishment of a Fermi–Dirac-like hot carrier distribution characterized by an effective electronic temperature.[167,168] Subsequently, electron–phonon scattering occurs over several picoseconds to transfer energy to the lattice, a process that can be effectively described by a two-temperature model.[169,170] Afterward, the heat gradually dissipates into the environment over a timescale of several nanoseconds. In the electrical excitation scenario, relaxation is also closely related to the photon emission process. A plasmon resonance can undergo radiative damping and emit far-field photons mediated by the hot carriers,[124,171] which will be discussed below, with its efficiency determined by two factors: whether the nanostructure supports dark (sub-radiant) plasmon modes and how high effective temperature that the hot carriers can attain.[125,172]

From a practical perspective, plasmon-induced hot carriers hold great potential to improve a wide range of applications, such as light harvesting, sensing, and catalysis. These hot carriers offer the advantage of overcoming the challenges inherent in semiconductor-based devices by surpassing the limitations imposed by the energy bandgap. Furthermore, they enable the collection of selective wavelength or polarization modes at a narrow bandwidth.

In metal semiconductor plasmonic nanodiodes, hot carrier flow and generation can be boosted through engineering the LSPR by geometrical design.[173,174] In addition to complex semiconductor

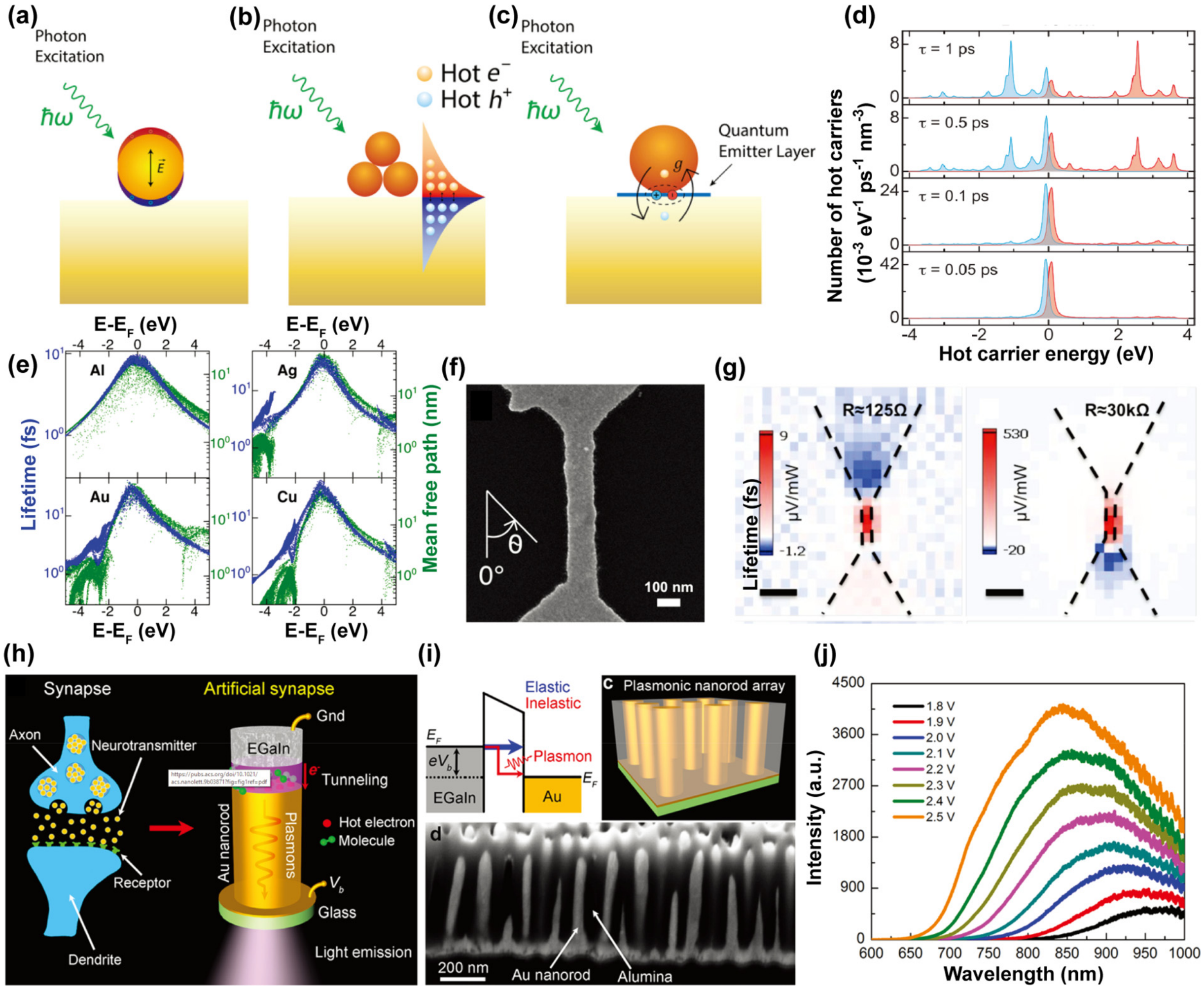

FIG. 11. (a) Photon excitation induced electrical field enhancement inside a nanoparticle (Purcell effect). (b) Photon excitation induced hot carrier generation in plasmonic nanostructures. (c) Plasmon–exciton coupling probed through optical excitation. Reproduced with permission from Zhu *et al.*, Nanophotonics **13**, 2281 (2024). Copyright 2024 Authors, licensed under a Creative Commons Attribution (CC BY) license. (d) Number of hot electrons (red lines) and hot holes (blue lines) generated per unit of time and volume as a function of their energy for a nanoparticle with diameters D = 15 nm. Reproduced with permission from Manjavacas *et al.*, ACS. Nano **8**, 7630 (2014). Copyright 2014 Authors, licensed under a Creative Commons Attribution (CC BY) license. (e) Hot carrier lifetimes as a function of energy, accounting for electron–electron and electron–phonon contributions for Al, Ag, Au, and Cu. Reproduced with permission from Brown *et al.*, ACS. Nano **10**, 957 (2016). Copyright 2016 Authors, licensed under a Creative Commons Attribution (CC BY) license. (f) SEM image of a typical bowtie device before electromigration. (g) Photothermoelectric voltage maps for the Au/Ti device recorded during the formation of the nanogap by electromigration. Reproduced with permission from Zolotavin *et al.*, J. Phys. Chem. Lett. **8**, 1739 (2017). Copyright 2017 Authors, licensed under a Creative Commons Attribution (CC BY) license. (h) Schematic diagram of the memristive light-emitting tunnel junction, which is an optoelectronic analogue to a biological synapse (EGaIn and PLH denote eutectic gallium indium and poly-L histidine, respectively). (i) Schematic diagram of the plasmonic nanorod array used to realize multiple tunnel junctions as well as cross-sectional SEM view of a nanorod array shown below. (j) Measured emission spectra of the tunneling device as a function of the applied forward bias. Reproduced with permission from Wang *et al.*, Nano Lett. **20**, 1536 (2020). Copyright 2020 Authors, licensed under a Creative Commons Attribution (CC BY) license.

plasmonic nanodevices, simple plasmonic metallic tunnel junctions have also demonstrated potential applications in hot carrier photovoltaics. Zolotavin *et al.*[175] explored the photo response of nanowires incorporating a plasmonically active nanogap created via electromigration [Figs. 11(f) and 11(g)]. The voltage generated in short, unbroken nanowires was consistent with the photothermoelectric behavior observed in single-metal thermocouples,[176] whereas they consistently detected large photovoltages ranging in the tens of millivolts and a pronounced polarization dependency under optical illumination, which can be attributed to the excited hot carriers. The rate of hot carrier generation can be further improved by eliminating the adhesion layer and adjusting the width of the nanowire.[177] Abbasi *et al.*[178] designed plasmonic tunneling junction with asymmetric plasmonic characteristics utilizing Au and Pt electrodes, showing that the directionality of optically excited hot carriers within the junction can be deliberately adjusted, resulting in the desired polarity of the photothermoelectric response. This straightforward structure for hot carrier generation also demonstrates the potential for applications such as detecting lattice distortions,[179] identifying impurities,[180] and functioning as photodetectors.[181]

In addition to hot carrier photovoltaics, hot carriers possess the ability to enhance chemical reaction rates. However, the precise role and mechanism by which hot carriers, as well as other potential mechanisms such as local heating, influence chemical reactions, remain subjects of ongoing debate.[182–184] Hot carriers with high energies have the capacity to migrate into unoccupied energy levels of acceptor molecules situated near a plasmonic nanostructure, thereby initiating diverse chemical processes. However, it is important to note that these capabilities may be constrained by the rapid hot carrier relaxation dynamics. In addition, the strong confinement of thermal processes, inherent in the large absorption cross section of plasmonic tunnel junctions, can naturally generate highly localized lattice heating, which can also contribute to enhancing chemical reactions.

Beyond plasmon-resonant noble metal nanoparticles[185,186] and antenna–reactor complexes,[187,188] nanoscale plasmonic tunnel junctions can also facilitate chemical reactions. Wang *et al.*[189] demonstrated that nanoscale tunnel junctions can achieve high reactivity under the generation of hot electrons. Utilizing high-density arrays of gold nanorods, concentrated stimulation of hot electrons, surface plasmons, and light emission across a macroscopic surface area (up to approximately 1 cm^2) can be achieved, enabling tightly confined oxidation and reduction reactions involving oxygen and hydrogen. These reactions are monitored either optically, observing changes in the intensity of light emission from the radiative decay of tunneling-generated surface plasmons, or electrically, through changes in tunneling current. Employing a similar strategy, the same research group achieved the development of a novel class of memristive devices functioning as artificial synapses, operating based on a general principle applicable to non-spiking artificial neural networks [Figs. 11(h)–11(j)].[189] Simultaneous multistate switching of resistance and inherent light emission in the junctions is achieved electronically and optically by programming them through hot-electron-mediated chemical reactions. The proposed approach enables the independent and interchangeable operation of the same device by utilizing distinct hot electron generation characteristics. The STM-based junction had also been employed for real-space and real-time observation of a plasmon-induced chemical reaction at the single-molecule level, where the dissociation of a single dimethyldisulfide molecule on silver and copper surfaces can be realized due to the optically excited plasmon within the STM junction.[190]

D. Electroluminescence in MSJs

Electroluminescence, an effect where materials emit light in response to an electric current or a strong electric field, has long been a cornerstone of optoelectronic devices, from macroscopic applications like LEDs to more refined scales such as OLEDs.[191–193] Traditionally, these devices have harnessed electroluminescence by utilizing bulk materials or thin films to convert electrical energy directly into light, enabling a wide array of technologies, including display screens[194,195] and lighting solutions.[196] In macroscopic materials, the study of electroluminescence primarily involves aggregates of particles, resulting in the observed effect being an average of numerous individual effects. This not only imposes limitations on various advanced applications but also often leads to energy quenching between molecules, reducing the efficiency and duration of the device.[197–199] Shifting the focus to the molecular scale opens avenues for addressing these by exploiting the unique quantum properties of individual molecules.[200–202] For example, different excited states of single molecules can be captured, enabling in-depth research into the dynamics of exciton transfer between molecular energy levels and the electric-light energy conversion in electroluminescence.[203,204] Therefore, single-molecule investigation is highly desired from both fundamental and practical perspectives.

1. Electroluminescence in nanocavity

In an STM setup, individual molecule on the substrate can be excited by electron tunneling or plasmon formed in the nanocavity between the STM tip and the substrate, leading to single-molecule electroluminescence.[205] However, such molecular fluorescence can be quenched due to the strong coupling between the molecules and the metal electrodes if the excited molecule is very close to or in contact with the metal electrodes. In this regard, the nanocavity of STM provides a suitable condition for molecular electroluminescence with a non-contact tip hovering above the molecule and a thin film of salt (e.g., NaCl multilayers) deposited on the metal surface as a separation layer.[206] Thus, when combined with an optical spectroscopy, STM-based methods have been widely adopted for single-molecule electroluminescence studies, as known as STML spectroscopy.

a. Intermolecular energy transfer. When multiple molecules are present on the substrate, the intermolecular energy transfer between adjacent molecules can generate electroluminescence without direct excitation from electrodes. For instance, Imada *et al.* employed STML to investigate energy transfer in individual molecular dimer consisting of a magnesium phthalocyanine (MgPc) and a free-base phthalocyanine (H_2Pc).[207] Figure 12(a) illustrates their setup, where the dimer and Ag (111) substrate are separated by three monolayers of NaCl. When the tip is positioned above the MgPc (donor), the holes are injected from the tip to the HOMO of MgPc, as shown in Fig. 12(b). While these injected holes are likely to be filled by electrons from the substrate, exciton formation can occur due to electron injection from the substrate to the LUMO of MgPc. This effect arises because the electron injection barrier to LUMO is reduced by the hole injection to HOMO and the decreasing NaCl potential. Once the Q state (exciton) of MgPc is generated, the energy transfer is inhibited due to the energy barrier between MgPc and H_2Pc. The Q state of MgPc has an energy of 1.89 eV, which is higher than the energy of the Q_x state (1.81 eV) of H_2Pc but lower than the energy of the Q_y state (1.92 eV) of H_2Pc. Therefore, the only feasible energy transfer mechanism is the resonant energy transfer (RET) from the Q state of MgPc to the Q_x state of H_2Pc. Consequently, photon emission occurs from the excited H_2Pc following RET from the MgPc exciton.

Understanding and manipulating electroluminescence in single molecules is essential for elucidating the energy transfer mechanisms within molecular systems. Additionally, electroluminescence behavior can characterize intermolecular coupling in real space, providing insight into energy transfer dynamics. Zhang *et al.* utilized the STML technique to visualize coherent intermolecular dipole–dipole coupling.[79] When two zinc phthalocyanine (ZnPc) molecules form a dimer, different dipole–dipole coupling modes produce distinct energy states. As shown in Fig. 12(c), by applying external bias to the connection region between the two molecules, the resulting luminescence spectrum displays multiple peaks corresponding to various dipole–dipole coupling configurations. Mapping the emitted photon energy allows determination of the coupling modes [Fig. 12(d)]. Thus, the electroluminescence serves as an indicator of dipole–dipole coupling,

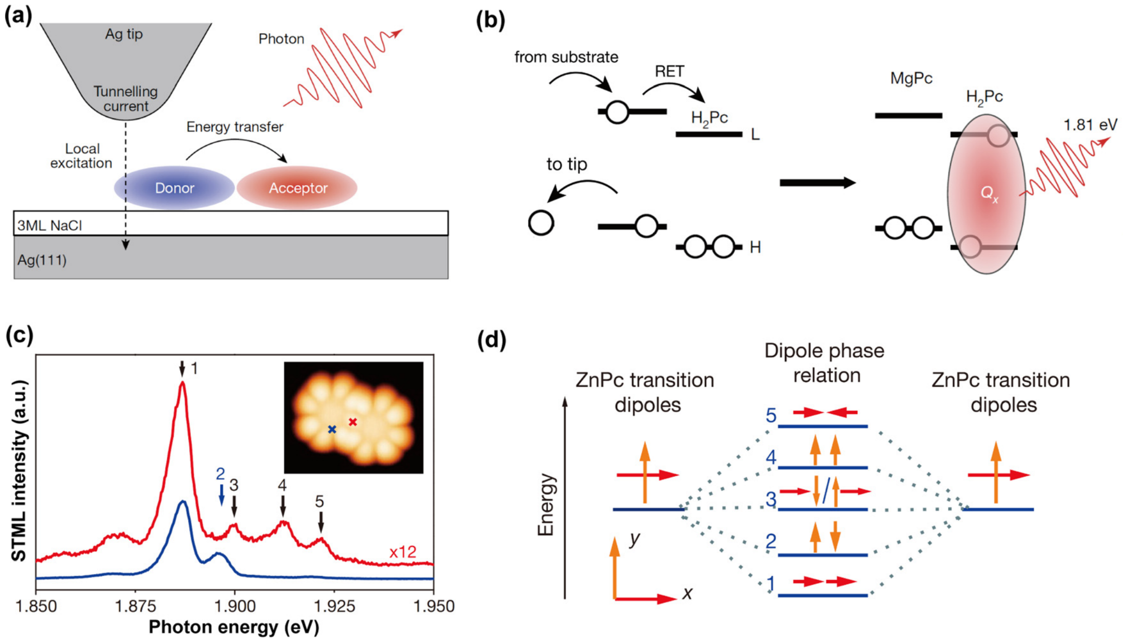

FIG. 12. (a) Schematic of electroluminescence in an STM nanocavity with donor and acceptor molecules showing the energy transfer process and photon emission. (b) Energy diagram of transferring and converting. Reproduced with permission from Imada *et al.*, Nature **538**, 364 (2016). Copyright 2016 Springer Nature. (c) STML spectra with peaks corresponding to different emission modes. (d) Exciton energy diagram of five distinct dipole–dipole coupling modes. Reproduced with permission from Zhang *et al.*, Nature **531**, 623 (2016). Copyright 2016 Springer Nature.

facilitating further investigation of energy transfer and optical processes across chromophores in both biological and artificial systems.

b. Energy transfer between molecule and nanocavity. The coherent coupling between molecules and the STM photonic nanocavity reveals photon-based quantum information,[208] which are widely used in molecular sensors and spectroscopy.[139,140,209,210] The discrete states of a molecule within the resonant plasmonic nanocavity can coherently couple with the continuous states of the cavity, resulting in distinctive spectral features known as Fano resonances.[211–213] Precise control of the localized plasmonic nanocavity position allows STML to unveil the molecule-cavity coupling with sub-nanometer spatial resolution.[79,207,214] For instance, when a ZnPc molecule is within the plasmonic nanocavity of STM, the spectrum displays a sharp molecular fluorescence peak at ~651 nm due to direct electron injection.[215] When the molecule is far from the cavity, the spectrum only shows a broad peak from the radiative decay of the excited plasmonic nanocavity. Notably, when the molecule is outside but close to the cavity, the emission spectrum exhibits a superposition of molecular and plasmonic spectra, indicating a distinct Fano resonance. The energy transfers from the excited plasmonic nanocavity to the molecule via coherent coupling, leading to photon emission from the molecular discrete excited state decay. This Fano resonance is also observed in polycyclic aromatics using the same STML technique.[216]

c. Upconversion electroluminescence. Beyond conventional electroluminescence, upconversion electroluminescence (UCEL) is a pivotal nonlinear optoelectronic phenomenon where the emitted photon energy exceeds the excitation electron energy. UCEL is particularly advantageous for a wide array of optoelectronic applications, such as excitonic electronics,[217] molecular spectroscopy,[218] and organic light-emitting diodes.[219] Despite its importance, the fundamental microscopic mechanisms driving UCEL remain complex and not fully understood. For upconversion to occur, either an intermediary energy relay state or a higher-order excitation process is necessary, facilitating the sequential absorption of two or more energy quanta from the excitation source. The primary UCEL mechanisms include intermolecular triplet–triplet annihilation (TTA), thermally assisted effects, and Auger processes. These mechanisms have been predominantly observed in bulk materials or molecular multilayers, which complicates the clear distinction and identification of the principal mechanism due to overlapping effect and intermolecular interaction. Therefore, controlled experimental studies at the single-molecule level is necessary to deepen our understanding of UCEL and eventually leverage it for energy harvesting.

To date, using STML, researchers have demonstrated UCEL at a single-molecule level at low temperatures. Very recently, Luo *et al.*[220] reported anomalously bright UCEL in a single phthalocyanine (H_2Pc) molecule isolated by electrical decoupling between electrodes [Fig. 13(a)]. Two sharp emission peaks at ~1.81 and ~1.92 eV were observed, corresponding to plasmon-enhanced fluorescence at different biases [Fig. 13(b)]. These peaks were attributed to the emission from the two lowest excited singlets states, Q_x (S_1) and Q_y (S_2), respectively. Figure 13 (c) shows the bias-independent photon intensity integrated over the Qx peak, revealing three distinct electroluminescence regions based on different UCEL mechanisms. In Region I ($V_b < 1.6$ V), UCEL involves an inefficient inelastic electron–molecule scattering (IES) process that excites the molecule to an intermediate triplet state, followed by a carrier injection (CI) process creating a singlet state. In Region II, without inefficient

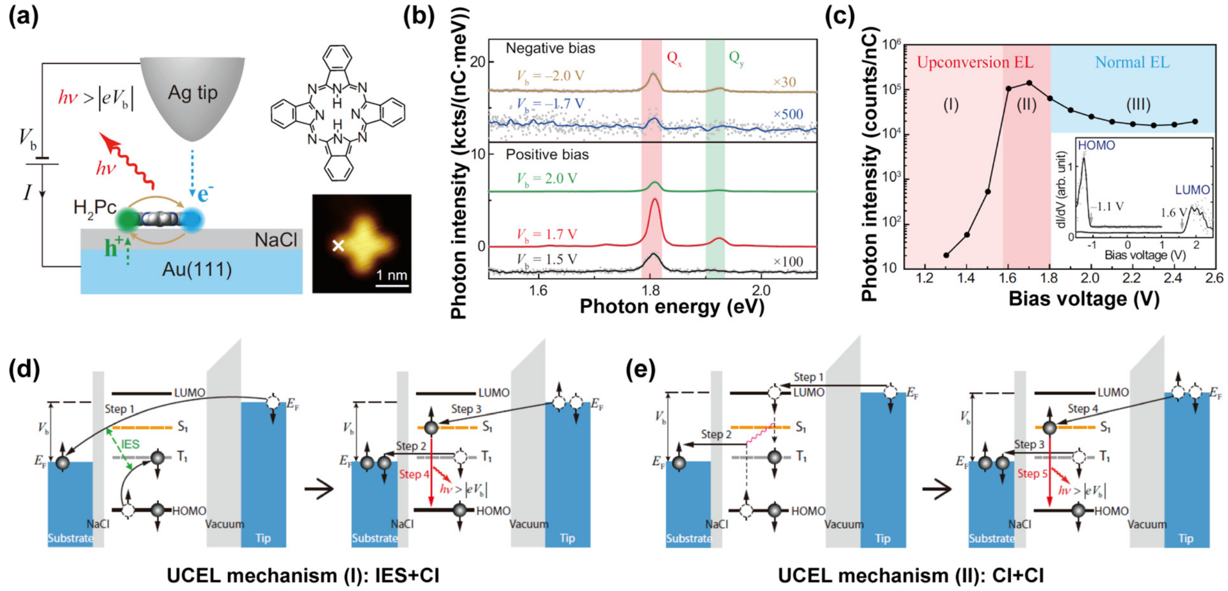

FIG. 13. (a) Schematic of STML setup. (b) Photon emission spectra under positive and negative bias. (c) Three different regions of voltage-dependent photon intensity. (d) UCEL mechanism of IES and CI processes. (e) UCEL mechanism of pure multiple CI processes. Reproduced with permission from Luo *et al.*, Nat. Commun. **15**, 1677 (2024). Copyright 2024 Authors, licensed under a Creative Commons Attribution (CC BY) license.

IES, sequential CI steps provide a new spin-triplet-mediated UCEL mechanism with anomalously enhanced photon intensity, surpassing normal electroluminescence by exciting the molecule above its optical gap in Region III. In the IES+CI upconversion mechanism [Fig. 13(d)], one tunneling electron can exchange with the HOMO electron with opposite spin and excite the molecule to the intermediate triplet state T_1 from the ground state S_0 (step 1). This transient state leads to electron tunneling to the substrate, leaving a cation (step 2). Another electron from the tip is then injected into neutral singlet state S_1 and finally decays to HOMO, emitting a photon with energy $h\nu$ higher than the driven electric energy eV_b. Due to the rather short electron–molecule collision time, IES is inefficient, resulting in low UCEL intensity in region I. In Region II, a mechanism based on sequential CI processes occurs without IES. when the Fermi level of the tip is lifted above the LUMO because of higher applied bias [Fig. 13(e)]. With higher bias, the Fermi level of the tip rises above the LUMO, enabling electron injection into the LUMO, transitioning to T_1 and creating a transient anion. Due to Coulombic interaction, the electron at HOMO gains energy and tunnel to the substrate (step 2). As T_1 is above the substrate E_F, the electron tunnels to the substrate, leaving a transient cation $D_0{}^+$, which can be neutralized by secondary CI from the tip, exciting the molecule from T_1 to S_1 state (steps 3 and 4). In this process, photon is emitted due to electron transition from S_1 to HOMO, similar to the first mechanism. This pure CI-driven mechanism results in high-photon emission intensity in the regions of 1.6 and 1.8 V. By engineering single-molecule energy alignment with interfaces, bright single-molecule UCEL can be achieved via a spin-triplet-mediated mechanism. This work provides critical insights into electro-optic conversion at the single-molecule scale and is expected to enhance single-molecule-based optoelectronic devices.

d. Single-molecule electrofluorochromism. Electrofluorochromism molecules can switch their fluorescence based on different charge states induced by external stimuli. The optical properties of these molecules can often be detected via spectroelectrochemistry in an electrochemical cell if the majority of molecules change their redox state. However, STML technique allows detection of both electron and vibronic signals at the single-molecule level. Doppagne *et al.*[221] used ZnPc molecule in an STM nanocavity to reveal two oxidation states. At +2.5 V bias, the emission spectrum shows a ZnPc luminesce character peak at 1.89 eV (X^0). However, at −2.5 V, the spectrum was dominated by another peak at 1.52 eV (X^+), corresponding to the ZnPc radical cations ($ZnPc^+$). In the energy diagram [process 1 in Fig. 14(a)], the Fermi level of the tip at high negative bias is resonant with the HOMO of ZnPc, allowing electrons to tunnel directly to the tip, forming the radical cations $ZnPc^+$. Due to decoupling from the substrate by the NaCl layer, these radical cations are stable enough to enable inelastic electron tunneling [process 2 in Fig. 14(a)]. The energy lost by the inelastic tunneling electron excites the single electron in the HOMO, resulting in photon emission with an energy fingerprint corresponding to $ZnPc^+$.

2. Electroluminescence in MSJs

Despite the quenching effect limiting contact between molecules and electrodes, electroluminescence has also been successfully observed in single-molecule junctions where the molecule bridges the electrodes. For instance, Chong *et al.*[222] explored a soft graphene nanoribbons (GNRs) with one terminal attached to an STM tip and part of the GNR lying flat on the substrate, minimizing the coupling with electrodes and reducing the quenching effect. The observed electroluminescence effect was attributed to the energy transfer between the tunneling electron and the GNR at the tip-sample junction. Using a similar setup, the wavelength of electroluminescence can be controlled precisely within the 750–1000 nm range with by employing different

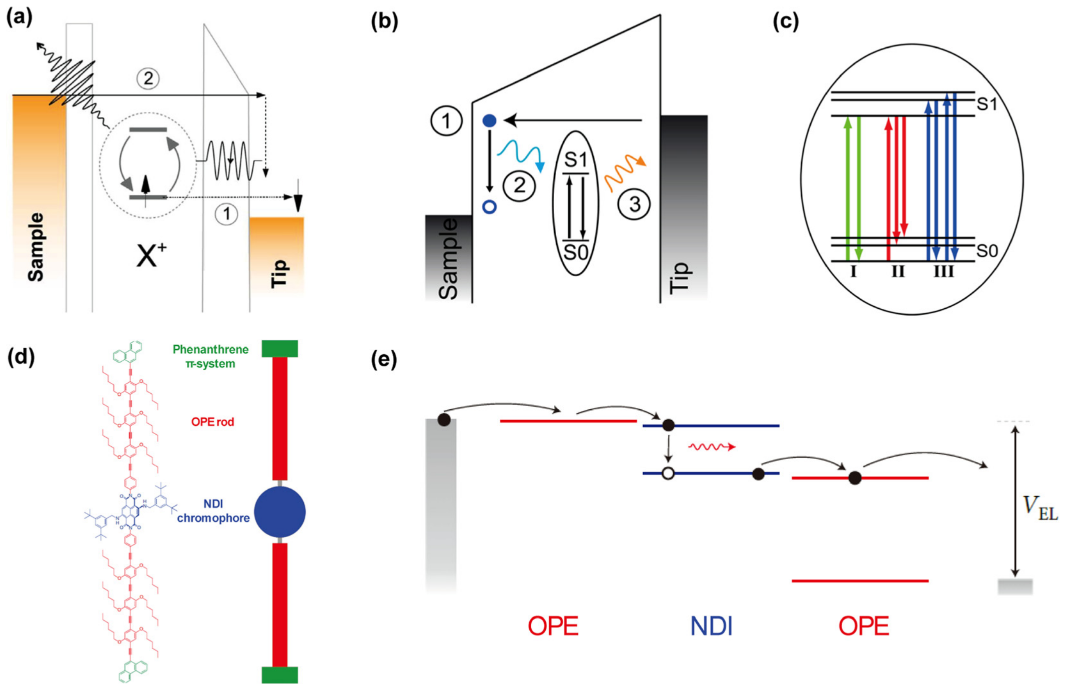

FIG. 14. (a) Energy diagram of electrofluorochromism mechanism. Reproduced with permission from Doppagne *et al.*, Science **361**, 251 (2018). Copyright 2018 American Association for the Advancement of Science. (b) and (c) Electroluminescence mechanism of different color emissions from single-molecule junction. Reproduced with permission from Chong *et al.*, Nano Lett. **16**, 6480 (2016). Copyright 2016 Authors, licensed under a Creative Commons Attribution (CC BY) license. (d) NT-M-NT structure with a rod-like molecule. (e) Charge transport and electroluminescence mechanism of NT-M-NT rod-like molecular junction. Reproduced with permission from Marquardt *et al.*, Nat. Nanotechnol. **5**, 863 (2010). Copyright 2010 Springer Nature.

emitting chromophore units (porphyrin derivatives) in the single-molecule junction.[223] As shown in Figs. 14(b) and 14(c), the electroluminescence mechanism for different emission colors can be explained by distinct paths of excitation and de-excitation processes. Green arrows indicate the normal path with high efficiency, red shows show decay to the vibrational excited levels of the S0 state, and blue arrows indicate the excitation to the vibrational excited levels of the S1 state. Furthermore, electroluminescence was also developed using a horizontal nanotube–molecule–nanotube junction (NT-M-NT).[224] In this setup, a special rod-like luminescent molecule, with oligo(phenylene ethynylene) (OPE) and naphthalenediimide (NDI) components, bridges two nanotube electrodes [Fig. 14(d)]. By aligning the molecular orbitals with E_F, an exciton is generated at the NDI part, eventually resulting in photon emission from the decay of excited electron from LUMO to HOME [Fig. 14(e)]. Although investigations into electroluminescence at the single-molecule level are still limited, recent studies have yielded exciting results and opened opportunities for future development and applications of molecular-scale photon sources.

III. HEAT-DRIVEN ENERGY CONVERSION AND TRANSPORT IN MSJs

A. Molecular thermoelectrics

Thermoelectrics concern the conversion of thermal energy into electricity via the Seebeck effect or, conversely, generating heating or cooling energy from electricity via the Peltier effect. They are solid state in nature (no moving parts) and more environmentally friendly than conventional thermal harvesting and recovery systems.[225] However, the field of thermoelectrics is currently limited by the achievable energy conversion efficiency (typically characterized by the figure of merit ZT). The research focuses on novel thermoelectric material to achieve a ZT value greater than three, which has been mostly on inorganic materials.[226] However, organic thermoelectrics possess high potential to enable high-performance thermoelectric applications due to the ample chemical space and organic synthesis methods.[227] Molecular junctions stand out as excellent experimental platforms in studying organic thermoelectrics as they can achieve distinctive and intriguing charge and heat transport characteristics.[228–231] Fundamental physical mechanisms about electron transmission, inter-molecular charge transport, and electron mobility across and within molecular junctions can be extracted by studying the relation between the Seebeck coefficient and electrical conductance. These studies are crucial for applications of MJs in nanoelectronic and thermoelectric devices.[36,38,232,233] In this section, we mainly focus on thermoelectricity and thermal conductivity, which are related to heat-electricity conversion and heat transport, respectively.

1. Strategies for enhancing thermoelectric performance at the molecular scale

A fascinating aspect of nanomaterials and nanostructures in leveraging them to enhance thermoelectric performance is that the electrical and thermal properties, $\kappa, \sigma,$ and S in ZT can be addressed independently to a larger extent compared to macroscopic materials.[234] Datta theoretically suggested that the thermopower of a single-molecule junction is measurable and can offer valuable insights into the relative alignment of HOMO and LUMO levels with the Fermi level.[39] Afterward, other research groups conducted theoretical studies on the thermoelectric properties of molecular junctions (MJs) to investigate different methods and their potential for achieving high ZT.[38,39,232,235–244] A promising method includes introducing Fano resonances near the Fermi level(*133*). For instance, Finch *et al.*[38] demonstrated that by adjusting the orientation of a side group of CSW-479-bipyridine, the thermopower could be significantly increased. This was attributed to the Fano resonances caused by the degenerate energy level in the molecular backbone and side groups. For this approach, it is essential to have control over the energy spectrum of the molecule to optimize the Seebeck coefficients.

Another thermopower-enhancing method includes modifying the electron transmission function to increase the slope at the Fermi level, which could be achieved by electron quantum interference (EQI).[242,245–247] Several computational studies showed that EQI can dramatically improve the Seebeck coefficient.[232,248,249] Bergfield *et al.*[232] investigated polyphenyl ether (PPE) molecules bridged between gold electrodes and demonstrated that a sharp peak in the transmission function near the Fermi energy, attributed to EQI effects, could result in very high value of ZT (>4). Similarly, Karlström *et al.*[250] showed that achieving the irreversible energy conversion limit was possible by modifying the transmission function using EQI.

Furthermore, it has also been found that utilizing spin-crossover[251,252] or applying mechanical stretching or compression[233] could also modify electron transport. The spin-dependent transport and thermoelectric spin-crossover molecule (iron complex of 2-(1H-pyrazol-1-yl)-6-(1H-tetrazole5-yl)pyridine)-based junction was explored by Ghosh *et al.*,[252] showing extremely efficient spin-crossover magneto thermopower generation with four orders of magnitude change of the thermocurrent from a low-spin state to a high-spin state.

Additional methods to modify the electronic transmission function also include redox control in phase coherent molecular wires[253] and generation of efficient π-π overlap between anchor group and electrodes,[254] and modification of the transition metal center of metalloporphyrin connected by thiol anchor groups to gold electrodes.[255] Rivera Mateus *et al.*[256] performed tight-binding Hamiltonian modeling and proposed a semiconductor-like molecular device with improved ZT. Increasing the Seebeck coefficient or electrical conductance is necessary; however, the thermal conductance of the MJs needs to be considered to get an estimate of ZT. One potential approach could involve substituents that, theoretically, induce destructive interference, thereby suppressing thermal conductance in benzene and oligo (phenylene ethynylene) derivatives.[257] Although destructive interference in molecules has been observed before,[258] substituting single atoms within a molecule presents significant challenges.

2. Experimental techniques for molecular thermoelectric characterization

The research on molecular thermoelectrics has benefited from progress in nanotechnologies, particularly the advances in nanofabrication techniques. Fabricating electrode–molecule–electrode junction had long posed a significant challenge in molecular electronics. However, this challenge has been partially addressed by several pioneering studies conducted in the 1990s, which paved the way for molecular thermoelectrics. Variances in electrode materials, organic–electrode interfaces, and the number of active molecules within a junction create diverse junction configurations, each with distinct thermoelectric performance. Compared to junctions for electrical conductance studies, the connections between various junction structures (as well as measurement methods) and the functioning of thermoelectric junctions remain relatively unexplored. The early experimental platforms are based on MCBJ,[259–261] STMBJ,[262,263] EMBJ,[264,265] and conductive atomic force microscopy (CAFM). MCBJ and STMBJ are used to study single molecules,[266–269] whereas EMBJ and CAFM methods are used for few molecules or ensembles of monolayers.

a. Mechanically controlled break junction. This technique forms junctions through mechanical rupture using piezo actuators. The key concept behind achieving stable sub-picometer gap size control relies on the small fraction of electrode movement compared to the displacement of the piezo actuator, which operates like a leverage principle. Since the MCBJ technique exhibited superior mechanical stability compared to other break-junction techniques, it has been widely used in studying the transport properties of MJs and atomic junctions.[270] However, obtaining sufficient statistical data was challenging due to difficulties in junction fabrication.

b. Scanning tunneling microscopy break junction. In STM-BJs, repetitively, a metallic tip moves toward and away from the substrate surface with a molecular monolayer. This allows the molecules to bridge the nanoscale gap between the substrate and the STM tip[271–273] with a high junction formation probability (∼70%–95%).[274] An electrical bias is applied between the sharp tip (usually made of gold) and a substrate with a monolayer of molecules chemically bound via end groups like thiols. The electrical current between the tip and the sample is monitored simultaneously until an electrical contact with low resistance is reached. Subsequently, the tip is retracted, leaving a few molecules bridging the tip and the substrate due to a stochastic process, resulting in only one molecule bridging before the junction ruptures [Fig. 15(a)]. To study the thermoelectric effects of MJs, a temperature difference across the junctions is applied either with a hot tip and cold sample or a hot sample and cold tip.[87,88,275,276]

Thermopower can be measured by circuit switching,[87,263,273,276] thermocurrent,[88,262] and current–voltage curve methods.[272,277] Circuit switching relies on changing the circuit from measuring the electrical current (current amplifier) to measuring open circuit thermoelectric voltage (voltage amplifier). This method is less robust as it cannot simultaneously measure thermopower and electrical conductance [Fig. 15(b)]. Conversely, the thermocurrent measurement technique can simultaneously measure conductance and thermopower in the same junction.[88] Finally, the current–voltage (I–V) curve methods apply a bias voltage sweep to the junction, while the distance between the STM tip and substrate is fixed. The temperature-dependent voltage offset in the I-V sweep curve can be used to obtain the Seebeck coefficient.[277]

c. Conductive atomic force microscopy break junction. The formation of single-molecule junctions does not result in junctions with the desired atomic configuration upon contact.[278] Here, the molecule junction consists of several molecules (∼100) by having an electrically conductive AFM probe in soft mechanical contact (∼1nN) with a molecular monolayer [Fig. 15(c)].[279] Like investigations with single-molecule junctions, determining whether the Fermi level of the electrode is close to the HOMO or the LUMO can be achieved by experimentally evaluating the sign of the thermopower.[280,281]

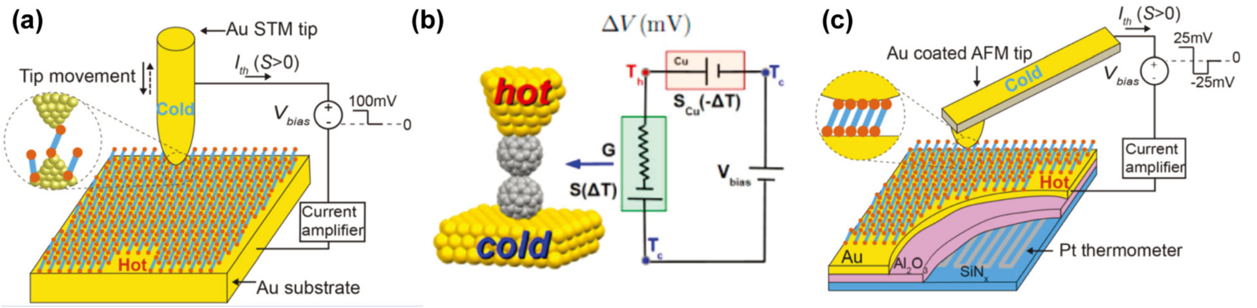

FIG. 15. (a) Schematics describing transport in molecular junctions and experimental approaches showing geometry of Au—(para-OPE3)—Au junctions with STMBJ. Reproduced with permission from Miao *et al.*, Nano Lett. **18**, 5666 (2018). Copyright 2018 Authors, licensed under a Creative Commons Attribution (CC BY) license. (b) Schematic representation of the setup. The tip is heated to a temperature above ambient temperature, while the substrate is maintained at ambient temperature. Reproduced with permission from Evangeli *et al.*, Nano Lett. **13**, 2141 (2013). Copyright 2013 Authors, licensed under a Creative Commons Attribution (CC BY) license. (c) Schematics showing geometry of Au—(meta-OPE3)—Au junctions with CAFM. Reproduced with permission from Miao *et al.*, Nano Lett. **18**, 5666 (2018). Copyright 2018 Authors, licensed under a Creative Commons Attribution (CC BY) license.

3. Effects of molecular length

Electrically increasing the length of the molecule indicates a decrease in electrical conductance and a transition from electron hopping to tunneling regimes [Fig. 16(a)].[282] When molecules are short (<3 nm), the electrons move by tunneling, and as the length increases, the charge is transferred from electrode to molecule, interacts with the molecular vibration and the environment, gets relaxed and trapped temporarily on the molecule, and then hops to the next site initiated by the thermal excitation until finally to the other electrode. In the tunneling regime, the resistance and thermopower of the molecule change logarithmically with length, whereas in the hopping regime, they change linearly with length. The thermopower tunneling to hopping transition is observed experimentally for two ONI/OPI molecular systems and for the DNA oligomer systems. For length-dependent studies, several molecular backbones have been investigated, including phenylene [Figs. 16(b) and 16(c)],[88,273,281] thiophene 1,1′-dioxide,[283] n-alkane,[87,284] DNA [Fig. 16(b)],[285,286] C_{60} [Fig. 16(d)],[277] and 3,3′-biphenyl and polyphenyl ether [Figs. 16(e) and 16(f)].[232] For alkane chains, a decrease or near-constant Seebeck coefficient is observed with increasing length [Fig. 6(g)],[87,287] while an increasing trend is observed for phenylenediamine and phenylenedithiols.[87,273] Such an opposite trend in alkane chains can be largely attributed to gold–sulfur metal-induced gap states residing between the HOMO and the LUMO. For phenylene backboned molecules, the HOMO shifts closer to the Fermi energy but becomes more decoupled from the contacts as the molecular length increases, leading to the observed conductance reduction and thermopower increase. Similar results are found for other molecular backbones (alkanes and oligophenyls) terminated with trimethyltin end groups.[88] Evangeli *et al.*[277] reported an experimental study in which the Seebeck coefficient for a C-60 dimer was twice when compared to a monomer. They computationally showed that it could be doubled with a C_{60} trimer. This was the first demonstration of the Seebeck coefficient for a non-covalent bonded dimer. In addition, transport fluctuations and variations were quantified for thiol-bound aromatic molecules of various lengths and degrees of freedom [Fig. 16(h)].[278]

The length dependence of thermopower was also investigated in junctions constructed from DNA molecules of varying sequences. Li *et al.* theoretically studied the thermoelectric performance of PolyG-PolyC and PolyA-PolyT double-stranded chains connected between organic contacts at different temperatures based on an effective model Hamiltonian, showing that significant enhancement of the Seebeck coefficient can be achieved if resonance effects occur at the Fermi level.[288] Li *et al.*[285] [Fig. 16(i)] reported on charge transport and thermoelectric effects in single dsDNA molecules with different sequences and lengths. The dominant hole-hopping transport mechanism in CG sequences results in a weakly length-dependent Seebeck coefficient, which can be tuned substantially by inserting a block of AT base pairs in the middle of the CG sequence. More recently, Guo *et al.*[289] performed first-principle calculation for thermoelectric properties of four kinds of DNA bases sandwiched between two zigzag-edge graphene nanoribbon electrodes, revealing that the thermopower and efficiency can be significantly enhanced in the guanine and electrode coupling configuration showing EQI.

4. Effects of mechanically induced changes in molecular conformation

Researchers have also investigated the impact of mechanical deformations on the thermoelectric properties of molecular junctions.[260,290] Rincón-García *et al.*[291] found that the sign and magnitude of the Seebeck coefficient of $Sc_3N@C_{80}$ bridged between gold electrodes depended strongly on the molecule orientation and applied pressure. This observation is consistent with calculations indicating that applied pressure can adjust the energy position of the sharp resonance near the Fermi level induced by Sc3N, thereby modifying the thermopower. Lee *et al.*[292] studied the thermoelectric properties of MJs created from fullerene-based molecules, finding an enhanced thermopower for fullerene derivatives [Figs. 17(a) and 17(b)]. Malen *et al.*[278] performed statistical analysis on the thermopower measurements, showing that thermopower variations arose during junction formation, increase with molecular length, and are primarily influenced by variations in contact geometry, orbital hybridization, and intermolecular interactions. Several research groups have also studied the impact of molecular conformation on electrical conductance.[293,294] Using a combination of DFT and tight-binding calculations, Vacek *et al.*[233] demonstrated that by mechanically stretching or compressing to modify the length of the MJ, electronic properties could be significantly changed, leading to a switching behavior of the thermopower with several orders of magnitude on/off ratio [Figs. 17(c) and 17(d)].

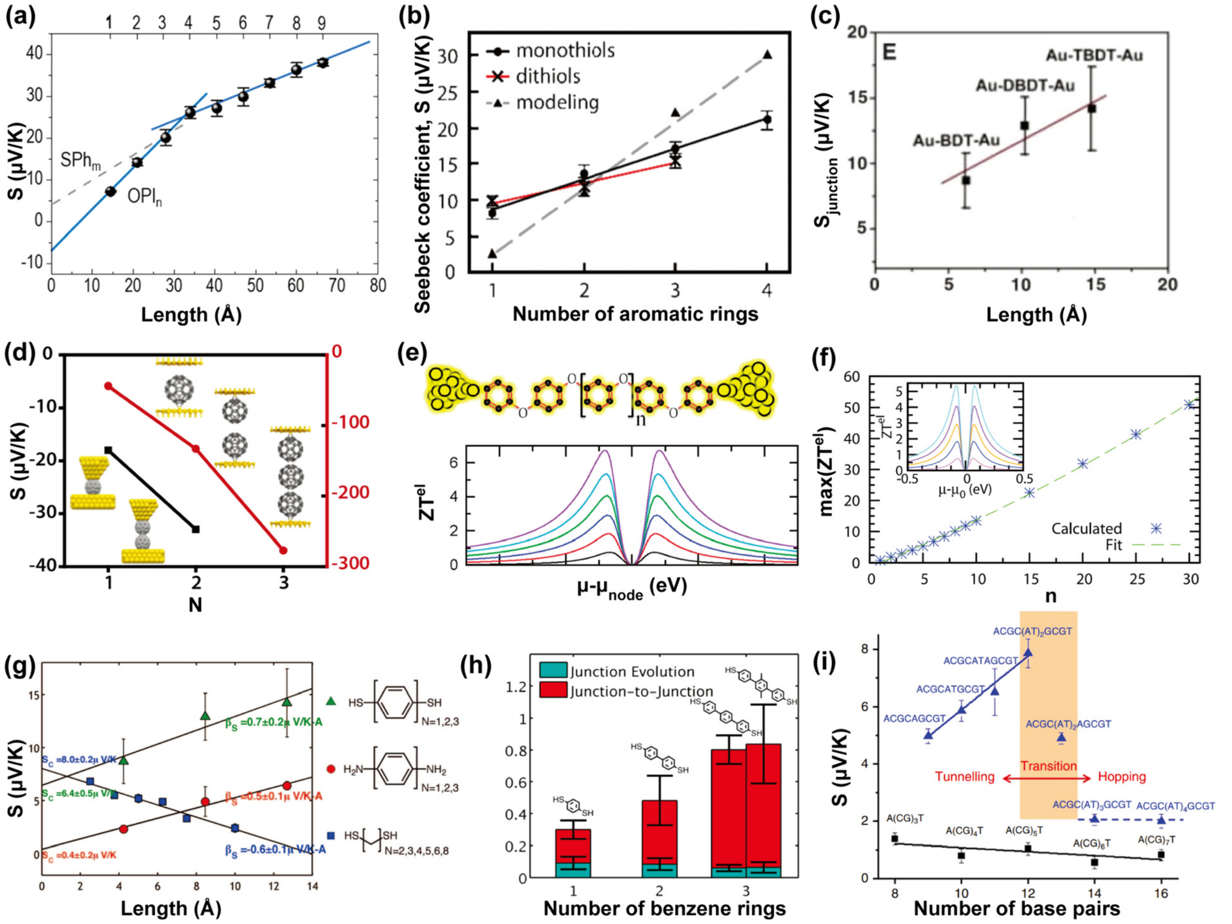

FIG. 16. (a) Length dependence of the Seebeck coefficient (S, μV/K) for the junctions. The gray dotted line indicates the S values of oligophenylenethiolates (SPhm, m = 1, 2, 3) as standards for comparison. Reproduced with permission from Park *et al.*, Nano Lett. **22**, 7682 (2022). Copyright 2022 Authors, licensed under a Creative Commons Attribution (CC BY) license. (b) Plots of the Seebeck coefficients of the dithiol and monothiol junctions along with the computed values for the Seebeck coefficient of the dithiol junctions. Reproduced with permission from Tan *et al.*, J. Am. Chem. Soc. **133**, 8838 (2011). Copyright 2011 Authors, licensed under a Creative Commons Attribution (CC BY) license. (c) Plot of measured junction Seebeck coefficient as a function of molecular length for BDT, DBDT, and TBDT. Reproduced with permission from Reddy *et al.*, Science **315**, 1568 (2007). Copyright 2007 American Association for the Advancement of Science. (d) Experimental (square, left axis) and computational (circle, right axis) results of C_{60} monomer, dimer, and trimer (only computational data shown for trimers). Reproduced with permission from Evangeli *et al.*, Nano Lett. **13**, 2141 (2013). Copyright 2013 Authors, licensed under a Creative Commons Attribution (CC BY) license. Reproduced with permission from Cui *et al.*, J. Chem. Phys. **146**, 092201 (2017). Copyright 2017 AIP Publishing. (e) Supernode enhancement of ZT, thermopower S, and Lorenz number L for polyphenyl ether (PPE) SMJs with n repeated phenyl groups, with schematic shown above. (f) Near a second-order supernode in a device's transmission spectrum, where an order-dependent enhancement of the electronic thermoelectric response, which is limited only by the electronic coherence length, can be found. Reproduced with permission from Bergfield *et al.*, ACS. Nano **4**, 5314 (2010). Copyright 2010 Authors, licensed under a Creative Commons Attribution (CC BY) license. (g) Seebeck coefficient vs molecular length. The Seebeck coefficient is plotted as a function of molecular length for N-unit phenylenedithiols (N) 1, 2, 3), phenylenediamines (N) 1, 2, 3), and alkanedithiols (N) 2, 3, 4, 5, 6, 8). Reproduced with permission from Malen *et al.*, Nano Lett. **9**, 1164 (2009). Copyright 2009 Authors, licensed under a Creative Commons Attribution (CC BY) license. (h) ΔS/S plotted as a function of molecular length and separated into fluctuations during a given junction's evolution and fluctuations from junction-to-junction. Reproduced with permission from Malen *et al.*, Nano Lett. **9**, 3406 (2009). Copyright 2009 Authors, licensed under a Creative Commons Attribution (CC BY) license. (i) Seebeck coefficients of DNA with different molecular lengths and sequences. Reproduced with permission from Li *et al.*, Nat. Commun. **7**, 11294 (2016). Copyright 2016 Authors, licensed under a Creative Commons Attribution (CC BY) license.

They proposed that mechanically manipulating electric conductance and thermopower could be extended to other non-planar molecules such as cycloparaphenylenes, cyclacenes, spherical molecules, and short DNA molecules. Recently, by mechanically controlling the tip–electrode separation distance in an STMBJ, Fuji *et al.*[295] shifted the conduction orbital energies and tuned the thermopower for single-molecule junctions of C_{60}, 4,4′-bipyridine (BPY) and p-phenylenediamine (PPD) [Figs. 17(e)–17(g)].

5. Effects of anchor and side groups

Anchoring groups are essential in reorganizing frontier molecular orbitals (FMOs) during the forming of molecular junctions, significantly impacting both charge transport and thermoelectric properties.[296–299] Thiol-terminated and trimethyl tin-terminated MJs exhibit a positive thermal power, with the latter having higher values,[87,88] whereas a negative thermopower is observed for isocyanide-terminated junctions[281] In particular, Balachandran *et al.*[300] showed

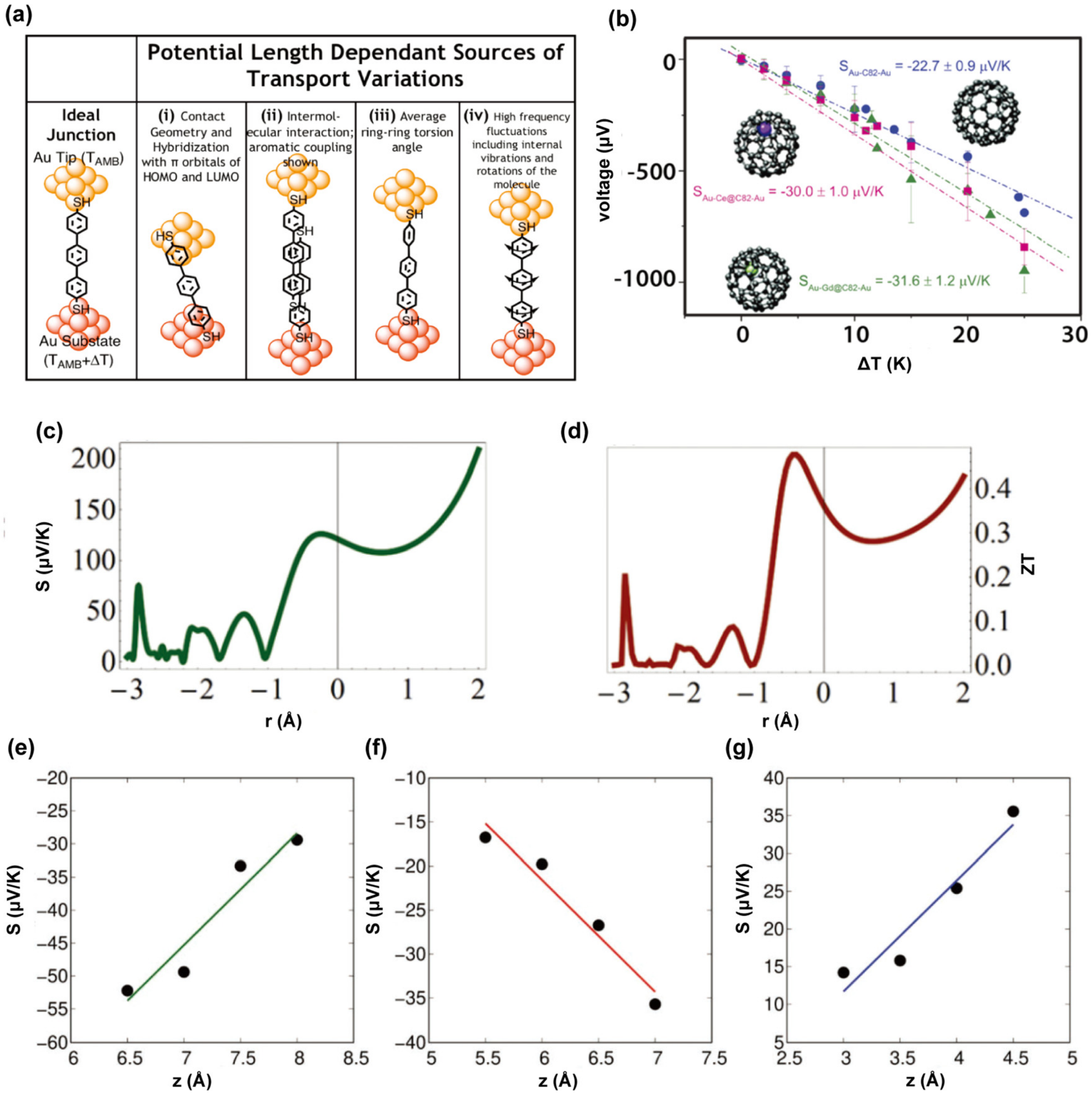

FIG. 17. (a) Potential sources of transport fluctuations are illustrated as deviations from an ideal junction. Each of these sources has increased variability with molecular length. Reproduced with permission from Rincón-García *et al.*, Chem. Soc. Rev. **45**, 4285 (2016). Copyright 2016 Royal Society of Chemistry. Reproduced with permission Malen *et al.*, Nano Lett. **9**, 3406 (2009). Copyright 2009 Authors, licensed under a Creative Commons Attribution (CC BY) license. (b) Seebeck coefficient of C_{82} derivative based junctions: C_{82} (blue circle), Gd@C82 (green triangle), and Gd@C_{82} (magenta square). Reproduced with permission from Lee *et al.*, Nanoscale **7**, 20497 (2015). Copyright 2015 Royal Society of Chemistry. Reproduced with permission from Cui *et al.*, J. Chem. Phys. **146**, 092201 (2017). Copyright 2017 AIP Publishing. (c) Thermopower (absolute value) $|S|$ as a function of inter-electrode distance. (d) The Lorentz number $\kappa/\sigma T$ as a function of inter-electrode distance. Reproduced with permission from Vacek *et al.*, Nanoscale **7**, 8793 (2015). Copyright 2015 Authors, licensed under a Creative Commons Attribution (CC BY) license. (e)–(g) Calculated thermopower as a function of the electrode separation for (e) C_{60}, (f) BPY, and (g) PPD junctions. Reproduced with permission from Fujii *et al.*, Adv. Electron. Mater. **8**, 2200700 (2022). Copyright 2022 Authors, licensed under a Creative Commons Attribution (CC BY) license.

that MJs with isocyanide, nitrile, and amine end groups demonstrate a notable overall downward shift in the energies of FMOS and place the HOMO peak closer to the Fermi level. On the other hand, thiol and hydroxyl end-group molecular junctions, with charge transfer into the molecule, exhibit a smaller overall downward shift, placing the LUMO peak closer to the Fermi energy. Furthermore, Baheti *et al.*[301] found that cyanide end groups can change transport relative to BDT in a way that transport was dominated by the LUMO in 1,4-benzenedicyanide, whereas substituents on BDT created small and predictable changes in transmission [Figs. 18(a)–18(c)].

Thermal power for molecules with N-heterocyclic carbene (NHC) had also been studied [Fig. 18(d)],[302,303] where the replacement of thiol with NHC addresses the instability issue observed in thiol-based MJs, leading to a linearly increased Seebeck coefficient with molecule length. More recently, Park *et al.*[304] showed that the robust NHC-based MJs could withstand temperatures up to 573 K, maintaining

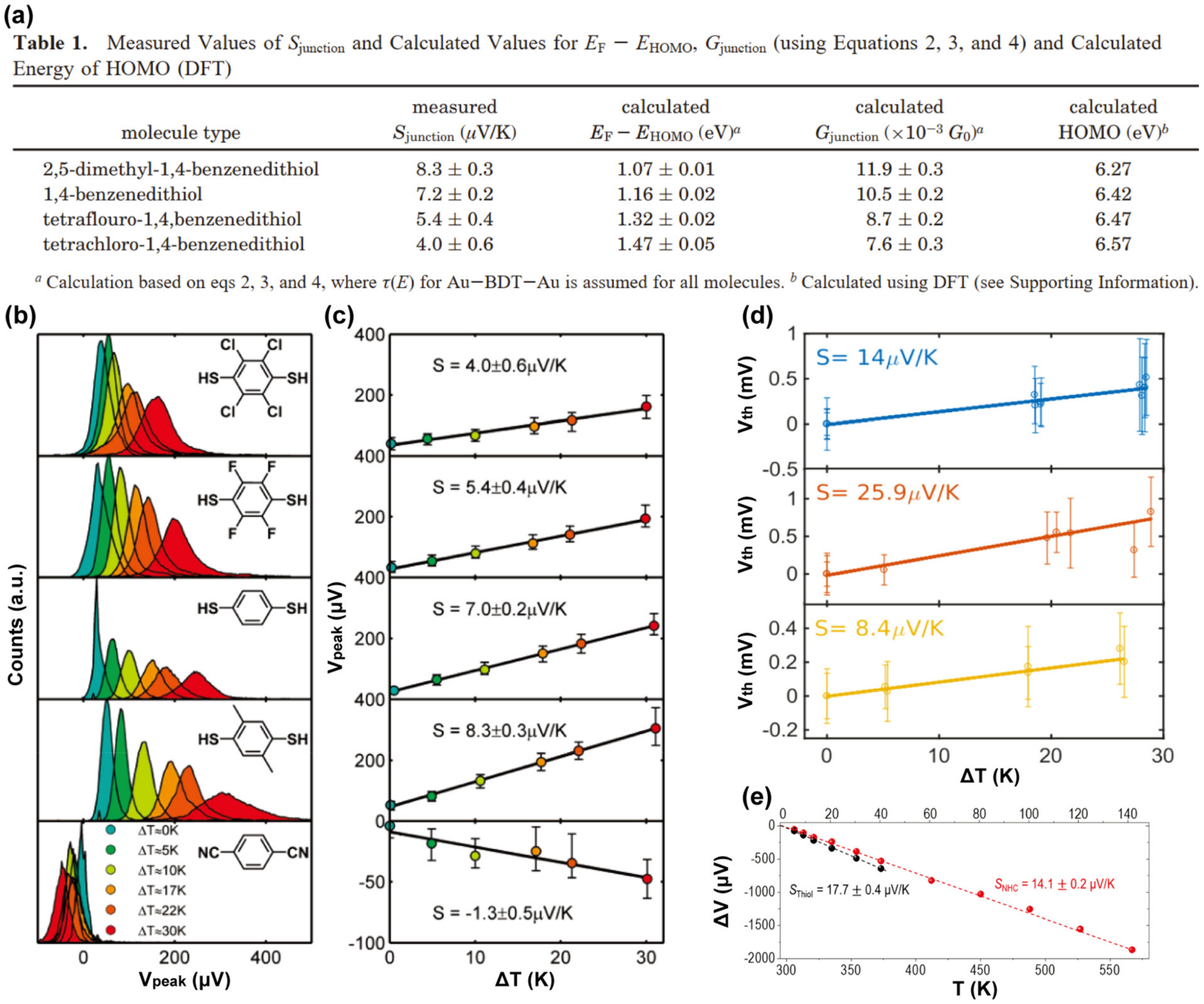

Table 1. Measured Values of S_{junction} and Calculated Values for $E_F - E_{\text{HOMO}}$, G_{junction} (using Equations 2, 3, and 4) and Calculated Energy of HOMO (DFT)

molecule type	measured S_{junction} (μV/K)	calculated $E_F - E_{\text{HOMO}}$ (eV)^a	calculated G_{junction} ($\times 10^{-3}$ G_0)^a	calculated HOMO (eV)^b
2,5-dimethyl-1,4-benzenedithiol	8.3 ± 0.3	1.07 ± 0.01	11.9 ± 0.3	6.27
1,4-benzenedithiol	7.2 ± 0.2	1.16 ± 0.02	10.5 ± 0.2	6.42
tetraflouro-1,4,benzenedithiol	5.4 ± 0.4	1.32 ± 0.02	8.7 ± 0.2	6.47
tetrachloro-1,4-benzenedithiol	4.0 ± 0.6	1.47 ± 0.05	7.6 ± 0.3	6.57

^{a} Calculation based on eqs 2, 3, and 4, where $\tau(E)$ for Au−BDT−Au is assumed for all molecules. ^{b} Calculated using DFT (see Supporting Information).

FIG. 18. (a) Table for measured S_{junction} for BDT4Cl, BDT4F, BDT, BDT2Me, and BDCN between gold contacts. (b) Normalized histograms for each ΔT plotted on a common axis and obtained by analyzing approximately 1000 consecutive thermoelectric voltage curves for BDT4Cl, BDT4F, BDT, BDT2Me, and BDCN. (c) Histogram peaks as a function of the temperature differential for BDT4Cl, BDT4F, BDT, BDT2Me, and BDCN. Reproduced with permission from Baheti *et al.*, Nano. Lett. **8**, 715 (2008). Copyright 2008 Authors, licensed under a Creative Commons Attribution (CC BY) license. (d). Mean thermovoltage V_{th} and standard deviation values from Gaussian fits applied to each experimental run performed. Reproduced with permission from Hurtado-Gallego *et al.*, Nano. Lett. **22**, 948 (2022). Copyright 2022 Authors, licensed under a Creative Commons Attribution (CC BY) license. (e) Plots of ΔV as a function of heating temperature and temperature differential. Black and red dots correspond to the thiol and NHC SAMs, respectively. Reproduced with permission from ark *et al.*, Nano. Lett. **22**, 3953 (2022). Copyright 2022 Authors, licensed under a Creative Commons Attribution (CC BY) license.

a consistent and reliable thermoelectric performance. In contrast, the thiol-based molecular junctions quickly undergo thermal degradation, typically around 323 K [Fig. 18(e)]. More recently, Ismael *et al.*[305] tuned the thermoelectrical properties of anthracene-based self-assembled monolayers by employing synthetic methodologies to alter the terminal anchor groups around aromatic anthracene cores. This approach led to a remarkable enhancement in thermopower by more than an order of magnitude.

Side group modification can shift the transmission function peak relative to the Fermi energy, affecting the thermopower of the molecule. For example, leveraging DFT and non-equilibrium Green's function (NEGF) formalism, it is shown that the thermopower can be either suppressed or enhanced by varying combinations of side groups at different positions, depending on how the charge-donating or charge-accepting nature of the side group functions interact.[306] In addition to shifting the transmission peak, electron mobility can also be affected, as investigated experimentally for 2,7-dipyridylfluorene[307] and oligo(phenylene–ethylene) derivatives.[308,309]

6. Effects of electrode–molecule coupling

Different electrode materials can show unique thermoelectric properties in MJs[240,310,311] as the Fermi energy of the electrodes closer to the dominant molecular orbital is responsible for the charge transport. Kim *et al.*[312] investigated the impact of various electrodes on the thermopower of single-molecule junctions, where the MJs were created using silver (Ag) or Au electrodes, with Au electrodes showing a larger thermopower (∼1.4×) compared to the Ag electrodes. The lower work function of Ag can explain this change due to the alignment of HOMO relative to the Fermi energy. When Pt replaces the Au, the Seebeck coefficient is also found to be suppressed for fullerene-based molecules.[263]

In contrast, for carbon nanotubes,[313] graphene nanoribbons,[314] a high thermopower can be obtained due to the reduction of electron-like contributions to the thermopower and the blocking of the HOMO transmission tails within the semiconductor bandgap. BDT MJs with Au and Ni electrodes using the STMBJ technique have been studied, where the Ni-BDT-Ni junctions exhibit a negative thermopower, contrasting with the positive thermopower observed in the Au–BDT–Au junction.[276] Despite the work function of Ni being similar to that of Au, first-principles calculations reveal that the HOMO of BDT can interact with both s- and d-states of the Ni electrode. This interaction leads to spin-split hybridized states, resulting in two peaks in the transmission function for up and down spins and, thus, a negative thermopower value. The impact of electrode, doping, electrochemical gating, and electrostatic control on the thermoelectric performance of the weakly coupled system was also examined, indicating that achieving outstanding thermopower is possible in proximity to the Fermi level (Fig. 19).[315–320]

Other than the electrode material, the effects on the variation of the electrode size have been investigated.[225] Three variations of electrode size, STMBJ (<5 nm), SAM (<100 nm), and bulk (>1 nm), using MCBJ have been explored.[260,321] The study revealed that the thermopower of diketopyrrolopyrrole (DPP) molecules could increase by up to one order of magnitude with rising packing density, indicating that thermopower rises with greater neighboring intermolecular

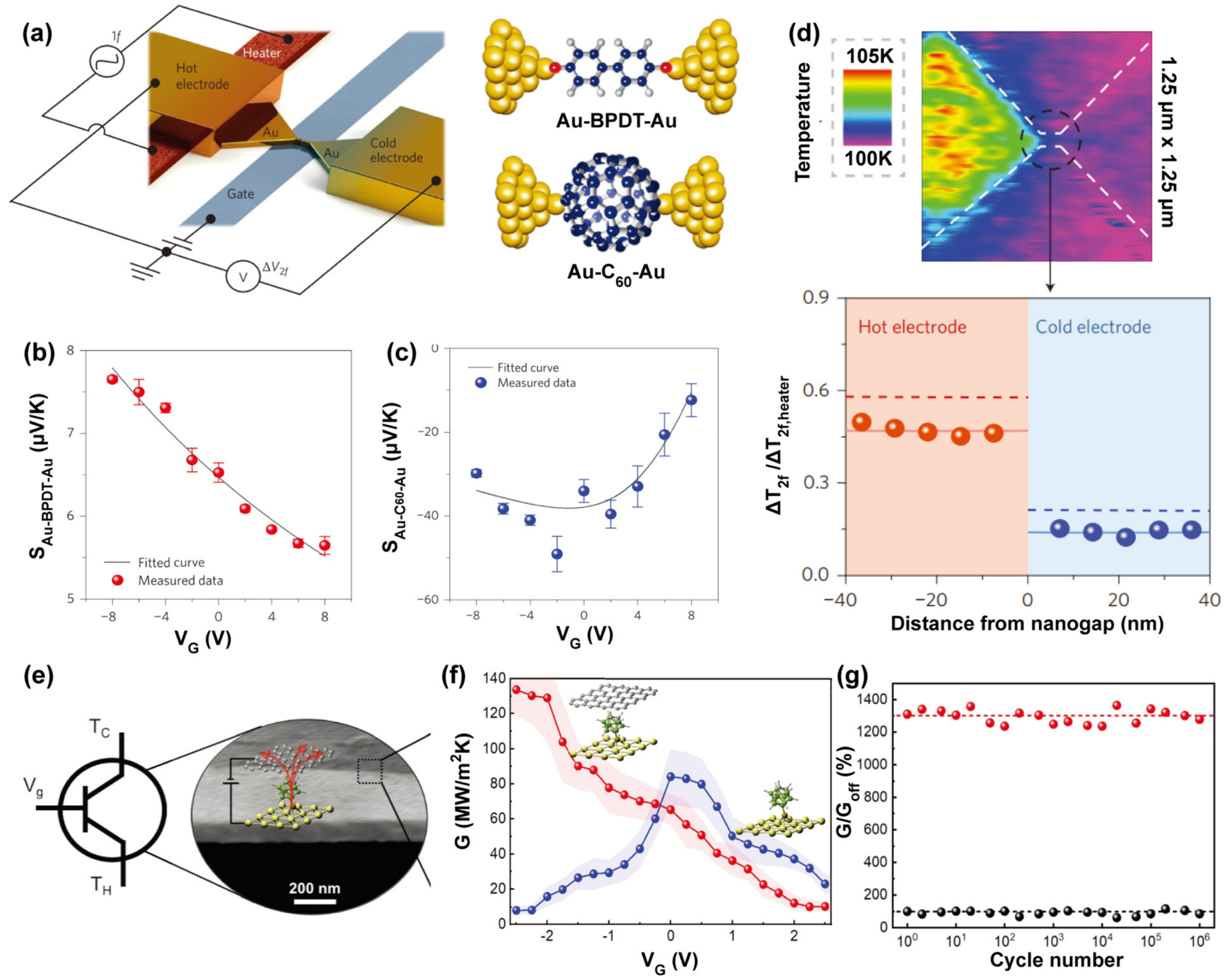

FIG. 19. (a) Schematic of the electromigrated break junctions with integrated heater (left) and the molecular junctions studied in this work (right). (b) and (c) Seebeck coefficient of the molecular junction as a function of gate voltage with (b) Au–BPDT–Au junction. (c) Au–C_{60}–Au junction. (d) Top: thermal map of a nanogap junction obtained using SThM at 100 K. Dashed lines: outline of the sample. Bottom: normalized temperature profile in the vicinity of the nanogap junction measured using SThM (circles) and calculated by thermal modeling (dotted line). Reproduced with permission from Kim *et al.*, Nat. Nanotechnol. **9**, 881 (2014). Copyright 2014 Springer Nature. (e) Conceptual illustration of the three terminal thermal devices. (f) The measured thermal conductance as a function of gate voltage. Red and blue curves represent device structures with and without graphene, respectively. (g) Reversibility test of electrical gating between ± 2.5 V on cycling measurements of the thermal device with graphene up to 1 million times. Reproduced with permission from Li *et al.*, Science **382**, 585 (2023). Copyright 2023 American Association for the Advancement of Science.

interactions and reduced HOMO–LUMO gap, which agrees with the combined DFT calculations.

Contact geometry can also be significant, and the molecule can be changed from an n-type to a p-type and vice versa.[314] Computationally, it has been shown that the thermoelectric performance of benzothiophene derivatives (Cn-BTBT) bridged between graphene nanoribbon electrodes can be significantly changed by alternating the connection position between the molecule and electrodes. When the electrode is connected to the lumbar region of the central molecule, both the electrical conductance and thermopower can be greatly enhanced.

7. Effect of electron quantum interference on molecular thermoelectricity

The effect of electron quantum interference (EQI) originates from the interference of quantum wave functions of electrons that coherently propagate through different discrete molecular orbitals (MOs) in single-molecule junctions. Following computational investigations [Fig. 20(a)],[242,245–248,250,322] experimental studies have also demonstrated that EQI affects the thermoelectric power in thiophene[323] biphenyl[324] and benzenedithiol.[325] Miao *et al.*[279] examined the thermoelectric properties of oligo (phenylene ethynylene) derivatives featuring

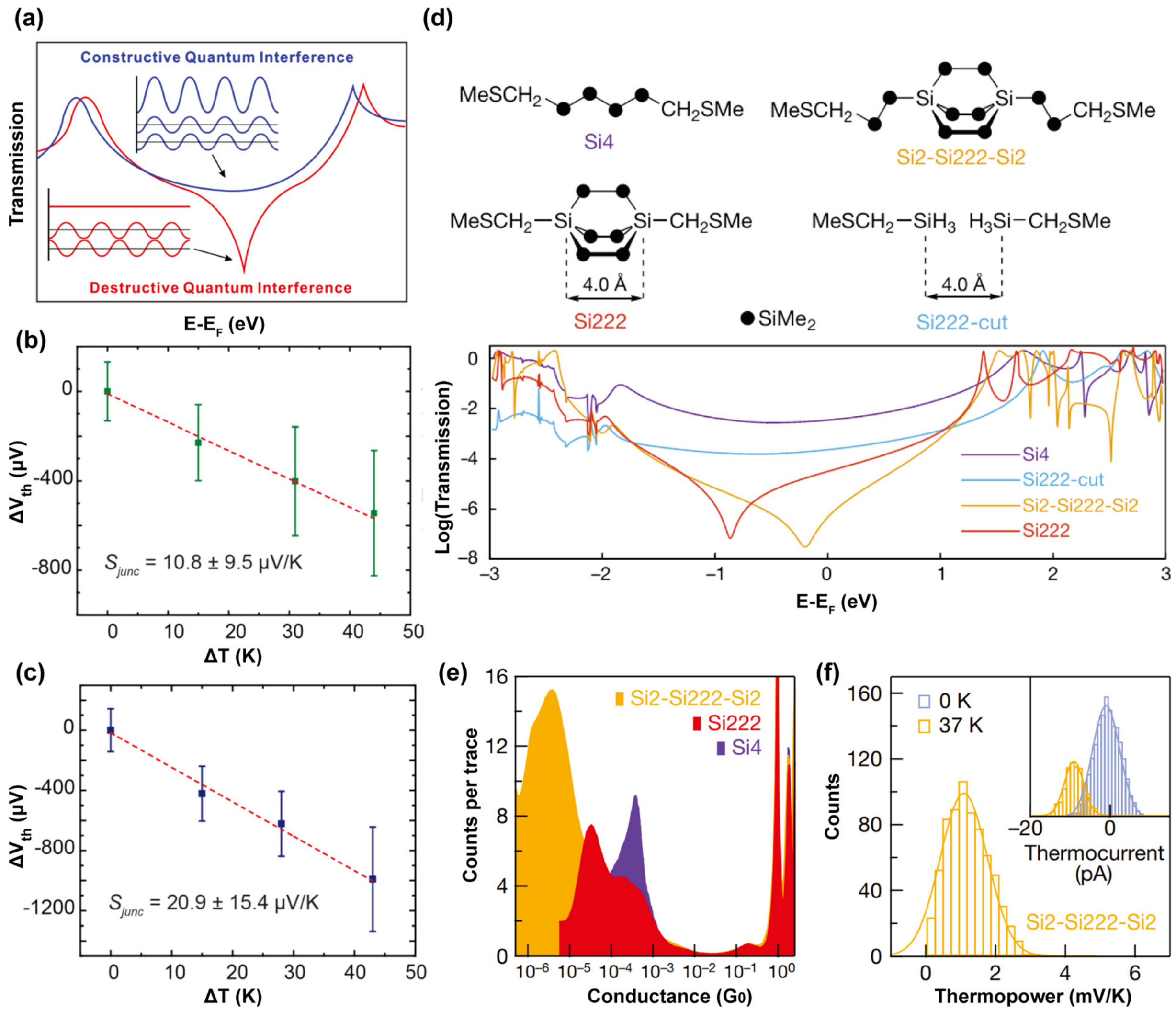

FIG. 20. (a) Schematic illustration of constructive and destructive EQI. Reproduced with permission from Liu *et al.*, Acc. Chem. Res. **52**, 151 (2019). Copyright 2019 Authors, licensed under a Creative Commons Attribution (CC BY) license. (b) and (c) Thermoelectric voltage as a function of Δ*T* for single-molecule junction experiments with Au—(para-OPE3)—Au (left column) and Au—(meta-OPE3)—Au (right column). Red dashed lines are linear fits. Reproduced with permission from Miao *et al.*, Nano. Lett. **18**, 5666 (2018). Copyright 2018 Authors, licensed under a Creative Commons Attribution (CC BY) license. (d) Landauer transmission plotted semi-logarithmically against energy relative to Fermi energy, with the structure of the molecules plotted above. (e) Logarithmically binned 1D conductance histograms for Si222, Si4, and Si2-Si222-Si2 (100 bins per decade). (f) Histogram of thermopower determined from the zero-bias thermoelectric current and junction conductance for each Si2-Si222-Si2 junction measured at a temperature difference of 37 K (approximately 700 junctions). Reproduced with permission from Garner *et al.*, Nature **558**, 415 (2018). Copyright 2018 Springer Nature.

a meta- or para-substituted central phenyl ring and dithiolate end groups, demonstrating experimental evidence of the quantum interference effect in STMBJ [Figs. 20(b) and 20(c)]. Such interference arises from the distinct phase difference between the HOMO and LUMO channels, resulting in a distinct peak in the electron transmission curve. Zhang *et al.*[229] showed that destructive interference can suppress the conductance of small saturated heterocyclic alkanes, which could be explained by computed ballistic current density analysis. However, the destructive interference in π-conjugated molecular building blocks cannot achieve ultralow conductance levels due to the presence of covalently bonded σ-transport channels. Therefore, suppressing the σ-contribution through σ-destructive interference is essential to obtain ultralow conductance and an increase in their Seebeck coefficients due to the existence of the gauche configuration [Figs. 20(d)–20(f)].[230] By selectively suppressing the constructive interference and enhancing the destructive interference between the HOMO and strongly coupled occupied orbitals of the opposite phase, Greenwald *et al.*[326] created highly nonlinear single-molecule circuits based on a series of fluorene oligomers. More recently, in stable Blatter radical molecules, a counter-intuitive quantum interference effect was observed, where constructive interference took place for a meta-connected radical, resulting in additional enhancement of thermoelectric properties.[303] Constructive interference-boosted thermoelectricity has also been found for anthracene-based molecular films.[327–329]

B. Thermal transport in MSJs

In MJs, thermal energy is primarily carried by phonons due to the high electrical resistance of most organic molecules. Single MJs, the smallest test bed possible, can reveal fundamental thermal phonon characteristics, such as interference, bond stiffness dependence, and electron–phonon interactions. Beyond fundamental insight, understanding thermal transport in MJs is crucial for designing the ZT of molecular thermoelectrics through phonon filtering and confinement,[330] improving heat dissipation in molecular electronics by enhancing phonon transport,[331] and developing thermally conductive polymers by reducing phonon scattering.[329] In macroscopic systems, the thermal energy conduction transport is well described by Fourier's law, $J = -\kappa \Delta T$, where J is the heat flux density. However, Fourier law fails as the characteristic length of a system becomes closer to the mean free path of an energy carrier.

Under the linear response regime, the heat current transport through MJs by electrons can be described with Landauer formalism, which is given by[332]

$$J_e = \frac{2}{h}\int_{-\infty}^{\infty} (f_L(\varepsilon) - f_R(\varepsilon))(\varepsilon - \mu)\tau(\varepsilon)d\varepsilon. \tag{3.1}$$

f_L and f_R are the Fermi functions of left and right electrodes $(f_{L/R}(\varepsilon) = 1/\{\exp[(\varepsilon - \mu_{L/R})/k_B T_{L/R}] + 1\}$. Here, the chemical potential (μ) can be approximated as the Fermi energy of ε_F electrodes. $T_{L/R}$ are the temperatures of electrodes. $\tau(\varepsilon)$ is the energy dependent electron transmission that can be split into elastic and inelastic contributions, $\tau(\varepsilon) = \tau_{el}(\varepsilon) + \sum_\nu \tau_{in}^{\nu}(\varepsilon)$. This transmission function can include the effects of electron–phonon interactions, electron–electron interactions, and inelastic scattering processes.[333,334]

For a full harmonic approximation of atomic displacements,[335] the Landauer type expression that gives elastic steady-state heat current through MJs by phonons is

$$J_p = \int_0^{\infty} (n_L(\nu) - n_R(\nu))\tau_p(\nu)h\nu d\upsilon, \tag{3.2}$$

where ν is the phonon frequency, and n_L and n_R represent the Bose–Einstein distributions of left and right electrodes $(n_{L/R} = 1/[\exp(h\nu/k_B T_{L/R}) - 1])$. $\tau_p(\nu)$ is the phonon transmission function, that is given as $\tau_p(\nu) = \frac{\pi^2}{(\hbar\nu)^2} k_{\mathrm{l}}^2 k_{\mathrm{r}}^2 \rho_{\mathrm{L}}^2(\nu)\rho_{\mathrm{R}}^2(\nu)\left|D_{\mathrm{lr}}(\nu)\right|^2$.[257] $\rho_{L/R}$ corresponds to the phonon density of states for left and right electrodes. $k_{l/r}$ are the coupling constants to the electrodes, where *l,r* indexes denote the corresponding atom of the molecule coupled to left and right electrodes, respectively. $D_{\mathrm{lr}}(\nu)$ is the eigenvalue matrix element of Green's function for frequency of ν.

To evaluate the non-linear forces, anharmonicities and accounting many-body effects in energy transport non-equilibrium Green function (NEGF) formulation can be used,[336] which describes the response of a system to external perturbations. It is also shown that the NEGF method can incorporate electron–phonon coupling corresponding to inelastic scattering into a unified framework in contrast to Landauer formulation.[337] However, a more promising method to evaluate large systems and high temperatures is molecular dynamics.[338]

Based on the Landauer formalism, when a voltage V is applied across the junction, both tunneling current and heat dissipation are presented. If the heat dissipation within the molecule is negligible (considering only the heat dissipation from the electrodes due to the chemical potential difference), the heat dissipated by left and right electrodes is expressed by[339]

$$Q_L = \frac{2}{h}\int_{-\infty}^{\infty} (f_L - f_R)(\mu_L - \varepsilon)\tau(\varepsilon)d\varepsilon, \tag{3.3}$$

$$Q_R = \frac{2}{h}\int_{-\infty}^{\infty} (f_L - f_R)(\varepsilon - \mu_R)\tau(\varepsilon)d\varepsilon, \tag{3.4}$$

where Q_L and Q_R are the heat dissipation flux from the left and right electrodes, respectively, and $\mu_{L/R}$ represents the chemical potential for left and right electrodes.

The Landauer approach can be effectively used to simulate phononic conduction in extended systems, provided that the molecular normal modes and their hybridization with the contacts are known. However, the Landauer-elastic scattering model becomes inadequate when interactions, such as anharmonicities, are introduced. Various techniques have been developed to account for these anharmonic effects, such as the self-consistent reservoir (SCR) model simulating the inelastic scattering of phonons by incorporating temperature probes,[340] nonequilibrium density-matrix description,[341] and the NEFG technique mentioned above for capturing many-body effects.

In Sec. III B, we present the theoretical and experimental development over the past decade on the understanding of thermal effects in molecular junctions.

1. Experimental methods

Experimentally measuring thermal conductance and temperature distributions across molecular junctions is very challenging, given the difficulty in precisely measuring and manipulating small temperature gradients across molecular-scale objects[342] The signal-to-noise ratio is another concern, given the typical low thermal conductance value in these molecular junctions compared to the background thermal noise. Sections III B 1 will discuss experimental techniques of thermal measurements for ensembled systems and single molecules.

a. Thermal measurement techniques for ensembled systems. Three techniques based on laser spectroscopy have been widely used for thermophysical characterization: time-domain, frequency-domain thermoreflectometry (TDTR and FDTR), and sum frequency generation vibrational spectroscopy (SFG-VS). Both TDTR and FDTR operate based on a similar mechanism[343,344] [Figs. 21(a)–21(c)]: a pump laser pulse excites electrons within the transducer film in a matter of picoseconds, causing a temperature rise and afterward leading to heat conduction into the SAM. For TDTR, following the heating from the pump laser pulse, the probe laser pulse records the thermoreflectance decay over time. For FDTR, a range of pulsed or continuous wave laser pulses are employed to gauge the phase shift in the thermoreflectance signals based on frequency. The thermal conductance can then be obtained by fitting the experimental data to the theoretical Fourier's diffusion model. The SFG-VS technique can be employed to investigate the thermal disordering of self-assembled monolayers of molecules after flash heating by a femtosecond laser pulse directed toward the metal film beneath the molecular layer [Fig. 21(d)].[243] The laser spectroscopy methods have a significant disadvantage as the theoretical model to obtain thermal conductivity is based on classical physics and any sort of quantum size effects are overlooked. In addition to them, a vacuum-operated scanning thermal microscope has also been employed to study the thermal conductance of monolayers of nine different alkane thiols self-assembled on Au(111) surfaces with a tunable contact area [Fig. 21(e)].[345]

The $3\,\omega$ method is another experimental tool to characterize the thermal transport of nanomaterials. Briefly, it employs a thin metallic strip, typically made of platinum or another metal, serving both as a heater and a resistive temperature sensor.[346] This metallic strip is usually mounted on the surface of the material to measure its thermal conductivity. In brief, an alternating current with frequency ω is passed through the metallic strip, causing Joule heating and generating a temperature oscillation in the material at $2\,\omega$ ($\Delta T_{2\omega}$). This temperature oscillation alters the resistance (R) of the metallic strip depending on its temperature coefficient (α) of resistance also at $2\,\omega$ frequency. Because of the nonlinearity inherent in the temperature-dependent resistance, a third harmonic voltage signal at $3\,\omega$ arises in the strip ($V_{3\omega} = \Delta T_{2\omega} \alpha I_{\omega} R/2$), which can be detected to determine the temperature. The heat conductance of the material is then obtained through $\Delta T_{2\omega}$ and the electrical power that is dumped into the strip. Operating in an AC regime substantially diminishes shot noise and other instrumental noises compared to DC methods, facilitating the reliable measurement of materials with exceptionally low thermal conductivity [Fig. 21(f) and 21(g)].[347]

b. Scanning thermal microscopy for thermal transport and dissipation characterization at the single-molecule level. Studying heat transport in single-molecule junctions presents unique opportunities to unveil the fundamental mechanisms of vibrational (phonon) energy transport. Even at room temperature, thermal phonons exhibit coherent transport in short molecule junctions, resulting in particular phenomena such as the quantum interference of thermal transport.[227] However, performing thermal transport measurements at the atomic scale presents several challenges. First, atomic-scale structures, given their nanoscale nature, cannot be visually accessed using optical microscopy tools, thus hindering efforts to conduct *in situ* observations and manipulations of the studied objects while simultaneously performing transport measurements. Second, the magnitude of heat flow in such structures is extremely small, necessitating high-resolution thermal sensing techniques to reliably capture the desired signals. To surmount these challenges, researchers have devised approaches based on scanning thermal microscopy (SThM),[348–350] which typically involves integrating custom-fabricated high-resolution thermal sensors into the scanning probes to achieve nanowatt or even picowatt heat flux resolution.

A calorimetric scanning thermal microscopy (C-SThM) was developed by Cui *et al.* to simultaneously enable the creation of atomic junctions and resolve heat flow among them [Figs. 22(a) and 22(b)].[351] The micro-fabricated probes incorporate a suspended island isolated by two long "T"-shaped supporting beams with a significant thermal resistance ($\sim 1.3 \times 10^6$ K/W). A high-resolution Pt thermometer with a temperature resolution of <1 mK and a bandwidth of 10 Hz is embedded in the island, enabling the measurement of a thermal conductance variation of approximately 25 pW/K when applying a temperature difference of around 20 K across the molecular junction. The purpose of the supporting beam here is to supply a high stiffness value ($>10^4$ N/m) to reduce thermal fluctuation as well as strengthen the stability of the junction. A voltage bias and temperature differential are applied across the tip and the substrate to concurrently quantify both electrical conductance and thermal conductance. In brief, the heat current flowing into or out of the C-SThM probe is assessed by measuring the slight temperature shift (typically ~ 1 mK or smaller) of the suspended island using the integrated Pt thermometer. The thermal conductance of the atomic junctions can then be correlated with the temperature variation. It can be seen that, as the separation between the tip and substrate is increased, the electrical and thermal conductance of the junction decreases in steps. It can be seen that the electrical and thermal conductance of the junction decrease in steps, aligning with values corresponding to multiples of the quantized conductance for electrical and thermal, respectively. This serves as compelling evidence of thermal transport quantization in single-atom junctions. Mosso *et al.* also investigated heat transport across Au atomic-scale junctions using a different experimental setup [Figs. 22(c) and 22(d)].[352] In summary, they utilized a similar suspended device embedded with an integrated thermal sensor to quantify the temperature alteration upon the rupture of an atomic junction between an Au STM tip and an Au-coated region of the suspended device. A robust correlation between the measured thermal and electrical conductance traces is evident, although some disparities are noted, possibly due to the presence of absorbed contaminant molecules (such as CO or H_2O) on the Au membranes. More recently, the same technique has been pushed forward by Cui *et al.* to measure the thermal conductance of a series of single alkanedithiol molecule junctions revealing the dependence of thermal transport on the molecular length [Figs. 22(e)–22(g)].[353] To enhance the signal-to-noise ratio of thermal measurements, they employed a time-averaging approach involving conducting numerous electrical and thermal measurements as a function of time and subsequently utilizing the electrical conductance vs time

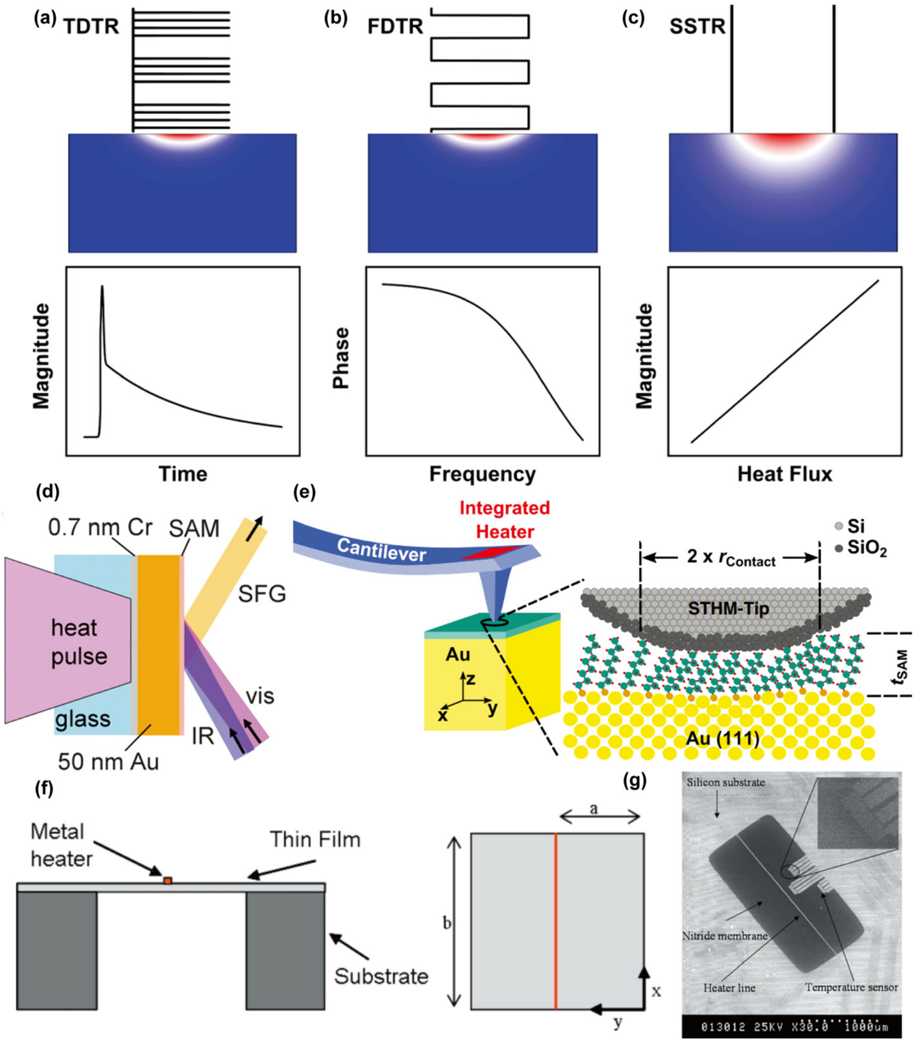

FIG. 21. Characteristic excitations and corresponding responses for (a) TDTR, (b) FDTR, and (c) SSTR techniques. Reproduced with permission from Olson *et al.*, J. Appl. Phys. **126**, 150901 (2019). Copyright 2019 AIP Publishing. (d) Concept of ultrafast flash thermal conductance measurements. IR and visible pulses combine to generate SFG in a ∼200-mm-diameter region containing $\sim 10^{11}$ alkane chains. Reproduced with permission from Wang *et al.*, Science **317**, 787 (2007). Copyright 2007 American Association for the Advancement of Science. (e) Schematic of the contact geometry. The contact radius is a function of the applied load and the thickness of the SAM. Reproduced with permission from Meier *et al.*, Phys. Rev. Lett. **113**, 060801 (2014). Copyright 2014 American Physical Society. (f) Spatially resolved thermoreflectance techniques for thermal conductivity measurements using 3ω technique. (g) SEM showing the silicon nitride freestanding thin film microdevice. Reproduced with permission from Jain and Goodson, J. Heat Transfer **130**, 102402 (2008). Copyright 2008 The American Society of Mechanical Engineers.

traces to pinpoint the moment of junction rupture. The results of thermal conductance averaged over 20, 50, 100, and 300 traces are depicted, revealing a distinct thermal conductance drop corresponding to the rupture of the single-molecule junction, which is completely merged into the thermal noise for a single trace.

To investigate the dissipation of heat (the Joule effect) in atomic-sized junctions, Lee *et al.* devised an experimental method employing nanoscale thermocouple-integrated scanning thermal microscope probes[354] Unlike the C-SThM probes, these probes incorporate a highly sensitive nanoscale thermal sensor comprising an Au–Cr junction, situated in close proximity to the tip apex. To investigate heat dissipation, a voltage bias is applied across the formed atomic or single-molecule junction, with the energy dissipation-induced temperature increase (ΔT) readout by the nanoscale thermocouple. Subsequently, the heat dissipation (Q) in the Au electrode of the SThM probe can be quantified using $Q = \Delta T / R_p$, where R_p denotes the thermal resistance of the SThM probe. For single-molecule junctions exhibiting strongly energy-dependent transmission characteristics, asymmetric heat dissipation was observed in the two electrodes where the junction forms. Furthermore, the dominant carriers (electron or hole) as well as the bias polarity, will also strongly influence the heat dissipation. For Au atomic junctions, the measured heat dissipation exhibits no significant asymmetry due to the weak energy-dependent electronic transmission spectra. This work is the first experimental evidence validating the use of the Landauer formalism to comprehend heat dissipation in elastic electron transport-dominated systems.

The current passing through molecular junctions leads to both heat dissipation through the Joule effect and cooling through the Peltier effect. The observation of Peltier cooling in molecular junctions, a crucial milestone for the development of molecular-based refrigeration, has remained elusive. Net refrigeration becomes apparent only when the magnitude of Peltier cooling power exceeds that of Joule heating. Cui *et al.*[355] developed an experimental platform where custom-fabricated calorimetric microdevices with embedded high-resolution Pt thermometers enabled a temperature resolution as small as 0.1 mK [Figs. 23(a) and 23(b)]. Excellent thermal isolation is achieved through four lengthy and doubly clamped SiN_x beams, facilitating precise measurements of heating and cooling with a resolution

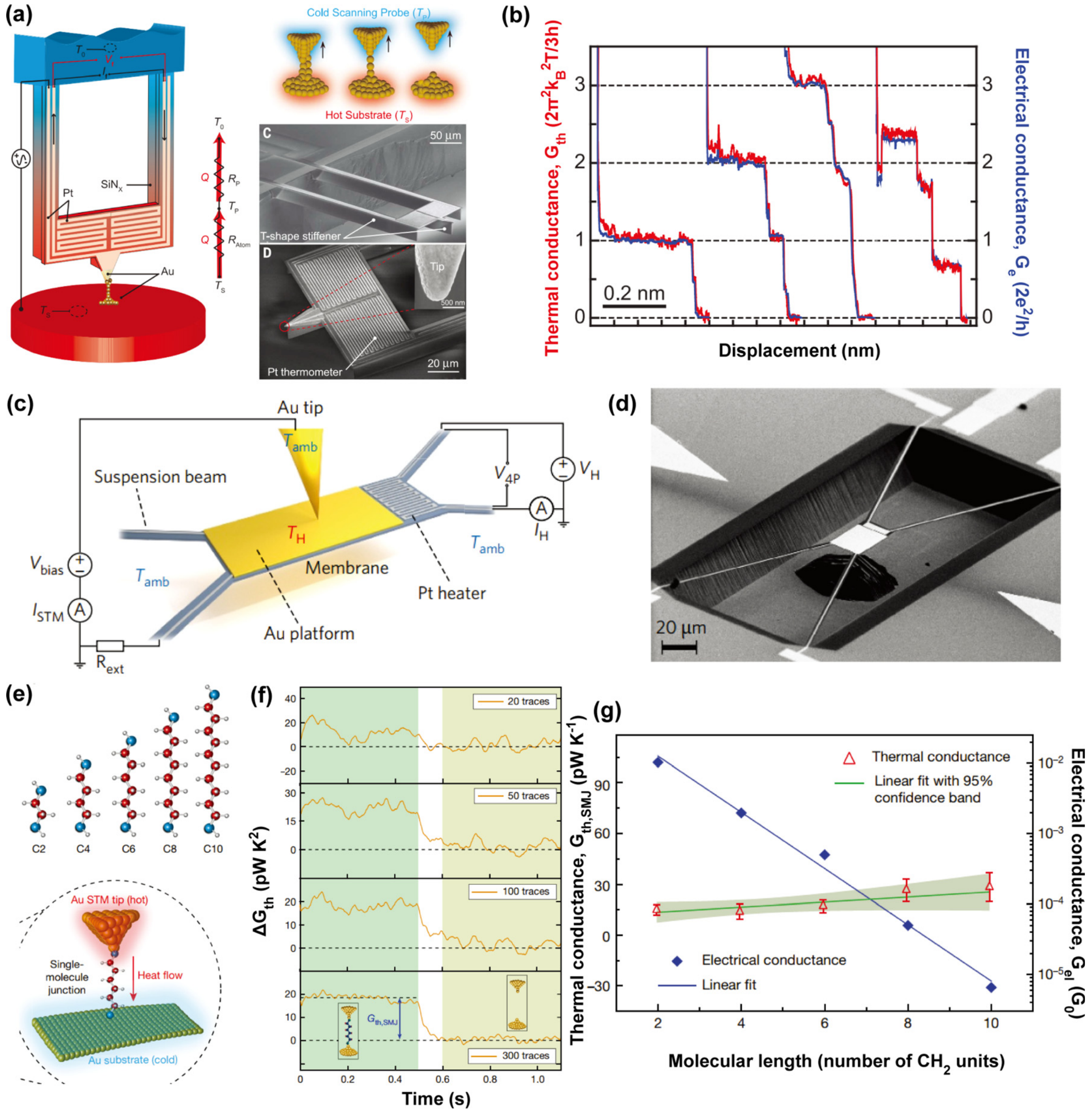

FIG. 22. (a) Schematic of a calorimetric scanning thermal microscopy (C-SThM) probe, which is used to make atomic junctions with a heated metallic substrate. The tip and substrate coatings can be either Au or Pt. The electrical conductance of the tip–substrate junction is monitored by applying a small sinusoidal voltage bias and measuring the resultant current. The resistance of the Pt resistance thermometer is monitored by applying a sinusoidal current and recording the voltage output. (b) Representative traces of thermal and electrical conductances measured while reducing the transverse constriction of Au atomic junctions by displacing the Au tip of the C-SThM probe away from the Au substrate. Reproduced with permission from Cui *et al.*, Science **355**, 1192 (2017). Copyright 2017 American Association for the Advancement of Science. (c) and (d) Schematic diagram and SEM image of the MEMS structure. Reproduced with permission from Mosso *et al.*, Nat. Nanotechnol. **12**, 430 (2017). Copyright 2017 Springer Nature. (e) Schematics of the alkanedithiol molecules (C_n) studied; n = 2, 4, 6, 8, and 10 denotes the number of carbon atoms in the molecules (red, carbon atom; gray, hydrogen atom; blue, sulfur atom). (f) An improved signal to-noise ratio is obtained upon aligning via electrical conductance jump and averaging multiple thermal conductance traces. (g) Measured electrical (blue diamonds, right axis) and thermal conductance (red triangles, left axis) as a function of the molecular length. Reproduced with permission from Cui *et al.*, Nature **572**, 628 (2019). Copyright 2019 Springer Nature.

as fine as 30 pW. A soft contact is established with a monolayer of self-assembled organic molecules on top of the Au layer of the microdevice using a sharp Au-coated contact-mode AFM tip, embedding approximately 100 molecules within the nanoscopic volume between the AFM tip and the substrate. An embedded Pt thermometer was used to record the heating and cooling applied by a small voltage bias of less than 20 mV, with the electrical conductance simultaneously measured by monitoring the electrical current. Peltier cooling in molecular junctions embedding biphenyl-4,4′-dithiol (BPDT), terphenyl-4,4″ (TPDT)-dithiol, and 4,4′-bipyridine (BP) can be observed in a narrow voltage interval at small biases, with a maximum cooling power around 300 pW for nearly 100 individual molecules. The parabolic form of the heating or cooling power as a function of the applied voltage can be understood as the total cooling and heating power resulting from the summation of the Peltier effect and Joule effect under the condition of a small bias limit. This developed platform opens new avenues for characterizing multiple transport parameters including electrical conductance and the Seebeck coefficient at the single molecular level.

2. Thermal transport in single-molecule junction: Computational results

a. Phonon interference effect. Akin to EQI discussed in Sec. III, phonons can also interfere depending on the molecular configuration. Markussen.[227] first calculated phonon interference (PI) using DFT that the phonon transmission function will have nodes like EQI for meta and para structures of the molecule, resulting in a thermal conductance difference between two and five times. This observed suppression of phonon transport could play a key role in designing a High ZT thermoelectric molecule. Klöckner *et al.*[257] conducted *ab initio* studies for the influence of interference effects on the thermal conductance of single-molecule junctions composed of various benzene and oligo (phenylene ethynylene) derivatives [Figs. 24(a) and 24(b)]. Their study revealed that interference effects exhibit as antiresonances in the phonon transmission, with the energy positions of these antiresonances being adjustable by altering the mass of the substituents. Zeng *et al.*[330] theoretically analyzed the phonon transport properties in intermediately coupled molecular junctions, demonstrating that the twist angle can function as an independent degree of freedom to control phonon interference and, thus, more precisely regulate the thermal conductance of molecular junctions. In this regard, the conduction of in-plane phonon modes can be effectively suppressed, permitting only out-of-plane transport through the molecular junction, thereby enabling further suppression of thermal conductance. Markussen.[227] theoretically studied the coherent phonon transport through organic, π-conjugated molecules, showing that the destructive interference features observed in four distinct cross-conjugated molecules led to a substantial reduction in thermal conductance compared to their linearly conjugated counterparts. Similarly, Li *et al.*[356] found that the thermal conductance of π-stacked systems could be decreased by approximately 95% when compared with that of a covalently bonded molecular junction. Further theoretical works have also demonstrated that phonon interference is crucial in suppressing phonon transport.[357,358] In particular, Sadeghi demonstrated a systematic enhancement of the room-temperature ZT in molecular junctions accomplished through suppressed thermal conductance due to phonon interference and enhanced electrical conductance as well as Seebeck coefficient resulting from quantum interference [Figs. 24(c)–24(f)].[357]

To sum up, phonon confinement and suppression in single MJs is currently limited as a theoretical field, even though it is of great fundamental interest, due to the experimental difficulty in distinguishing the small difference in the absolute thermal conductance values of individual molecules.

b. Anchor group and side group. An anchor group of a molecule interacts directly with the electrode, and the bond strength/bonding force determines the interfacial thermal resistance. Stronger bonds like covalent have lower thermal resistance than weaker bonds like hydrogen and van der Waals.[359]

Zhang *et al.* summarized the interfacial thermal conductance between Au and multiple materials as a function of bonding force.[360] Famili *et al.*[361] showed that side groups forming Christmas tree-like structures exhibited Fano resonances and suppressed phonon transport along the trunk of Christmas tree-like molecules constructed from alkane or acene trunks with various pendant branches [Figs. 25(a) and 25(b)]. Noori *et al.*[362] found that the thermal conductance of OPE3 with a thiol anchor was higher than those with methyl sulfide but lower than the OPE3 with a pyridyl anchor group [Fig. 25(c)]. Klöckner *et al.*[257] calculated through *ab initio* method for phonon transmission as a function of energy for Au–benzenediamine–Au junctions with different halogen atom substitution, revealing that introduction of substituents effectively alters phonon transport across

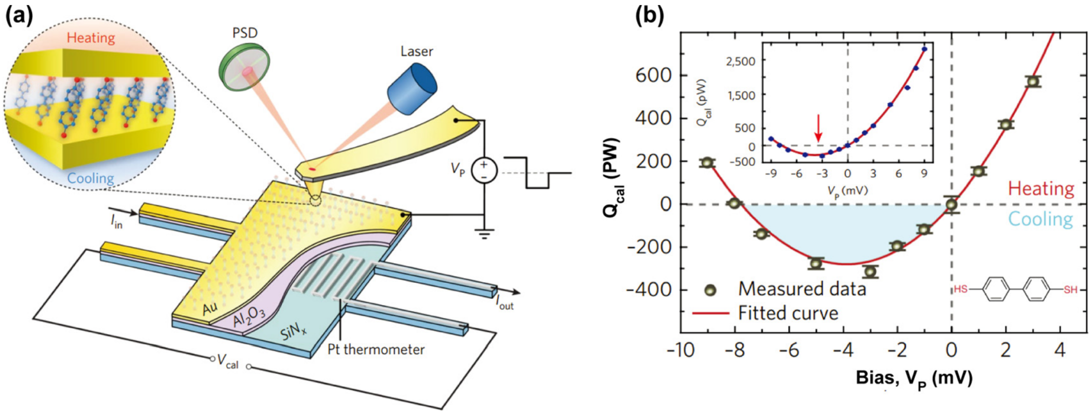

FIG. 23. (a) Schematic of the experimental platform. Molecular junctions are formed by placing an Au-coated AFM tip in gentle contact with a self-assembled monolayer created on a Au-coated calorimetric microdevice. (b) Measured voltage-dependent thermal power for BPDT junctions. The solid red line indicates the fitted curve, the measured Seebeck coefficient, and the electrical conductance. The shaded blue region indicates the voltage region where net cooling (refrigeration) is observed. Reproduced with permission from Cui *et al.*, Nat. Nanotechnol. **13**, 122 (2018). Copyright 2017 Springer Nature.

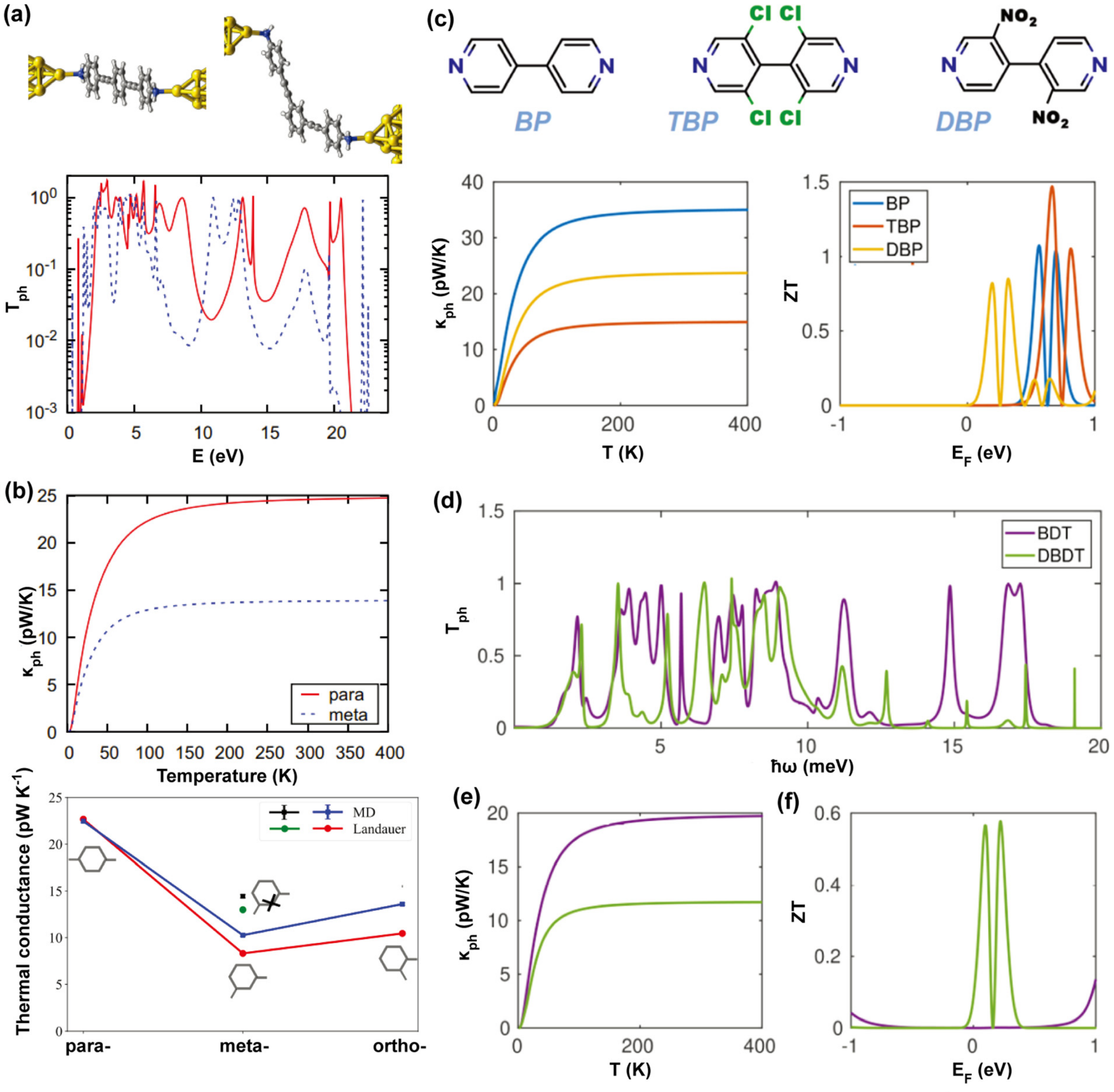

FIG. 24. (a) Phonon transmission as a function of energy for the Au–OPE3–Au junctions shown above for both para (left) and meta (right) binding configurations at the central benzene ring. (b) The corresponding phononic thermal conductance as a function of temperature. Reproduced with permission from Klöckner *et al.*, Phys. Rev. B **96**, 245419 (2017). Copyright 2017 American physical Society. (c) Phonon thermal conductance and room temperature *ZT* vs Fermi energy of BP, TBP, and DBP junctions. (d) Phonon transmission coefficient vs energy and LUMO states of BDT and DBDT. (e) Phononic thermal conductance vs temperature and (f) Room temperature ZT vs Fermi energy of BDT and DBDT. Reproduced with permission from Sadeghi *et al.*, J. Phys. Chem. C **123**, 12556 (2019). Copyright 2019 Authors, licensed under a Creative Commons Attribution (CC BY) license.

all energy levels, but the alteration is notably significant at the energies corresponding to the antiresonances [Figs. 25(d) and 25(e)].

c. Length dependence. Many computational studies have proposed that Fourier's law is inadequate for modeling thermal transport in single-molecule chains and junctions. This fundamental characteristic was historically recognized in the pioneering work of Fermi, Pasta, and Ulam (the FPU problem).[363] In 1955, Fermi developed a diffusive model when investigating the dynamics of a 1D lattice chain with N monatomic particles. They observed a divergence in thermal conductivity when a small nonlinearity is presented in the 1D chain of particles. This model has been further employed to explore the thermal transport in 1D chain-based systems,[364,365] including MJs. For alkane chains, Segal *et al.*[366] presented a comprehensive theory based on molecular dynamics for heat conduction through three-dimensional harmonic chains, resulting in a generalized quantum Langevin equation for a system coupled to a harmonic heat bath. Sadeghi *et al.*[367] employed *ab initio* methods for alkanes and oligoynes, showing different length-dependent thermal conductance behavior, which can be attributed to phonon filtering by the gold electrodes that diminishes when higher-Debye-frequency electrodes are used. Furthermore, first-principles calculations and molecular dynamics simulations have also been performed for PTFE [Fig. 25(f)],[368] both linear-/cross-conjugated molecules[227] as well as self-assembled monolayers of molecules.[369–371] Observing unusual phonon transport phenomena in MJs has stimulated several proposals for controlling and tuning interesting thermal properties on the molecular scale. For instance, there have been theoretical proposals suggesting that MJs could be utilized to create thermal rectifiers,[372–375] field-effect phononic thermal transistors,[376] tunable thermal modulators,[377] and quantum heat pumps.[378]

d. Local heating and cooling. Current flowing through the electrically biased MJ typically results in heat dissipation, with the total dissipated power given by $Q = IV$. During the inelastic process, power can be dissipated directly into the MJ through electron–phonon interactions. Even a minor heat input can drive the molecule out of thermal

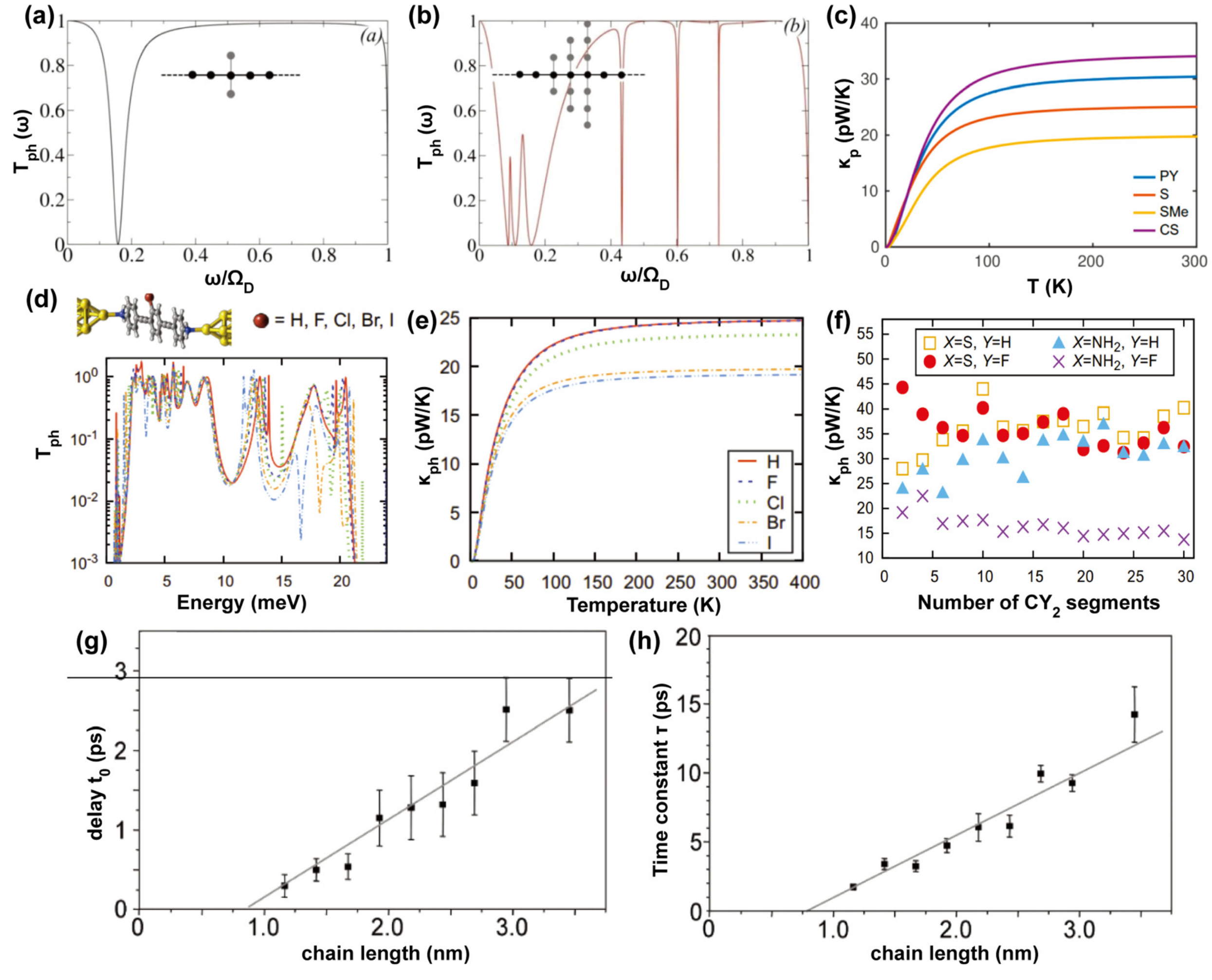

FIG. 25. (a) and (b) Transmission coefficient for N = 1, 3 side branches, respectively. Reproduced with permission from Famili *et al.*, ChemPhysChem **18**, 1234 (2017). Copyright 2017 European Chemical Societies Publishing. (c) Phonon thermal conductance vs temperature *T* for OPE3 with different anchor groups. Reproduced with permission from Noori *et al.*, Appl. Sci. **11**, 1066 (2021). Copyright 2021 Authors, licensed under a Creative Commons Attribution (CC BY) license. (d) Phonon transmission as a function of energy for Aupara-OPE3-Au junctions, where a H atom of the central benzene ring has been substituted by a halogen atom (X = F, Cl, Br, I). (e) The corresponding phononic thermal conductance as a function of temperature for the different para-OPE3 derivatives. Reproduced with permission from Klöckner *et al.*, Phys. Rev. B **96**, 245419 (2017). Copyright 2017 American Physical Society. (f) Room-temperature (*T* = 300 K) phonon thermal conductance as a function of the number of CY2 units (Y = H, F) in the molecule for both anchoring groups, thiol and amine. Reproduced with permission from Klöckner *et al.*, Phys. Rev. B **94**, 205425 (2016). Copyright 2016 American Physical Society. (g) Dependence on chain length of the delay time between the flash-heating pulse and the arrival of the initial burst of heat at the methyl head groups. (h) Dependence on the chain length of the time constant t for thermal equilibration between flash-heated Au and alkane chains. Reproduced with permission from Wang *et al.*, Science 317, 787 (2007). Copyright 2007 American Association for the Advancement of Science.

equilibrium because of its limited heat capacity, necessitating the introduction of the concept of "effective temperature."[354] Several computational studies have explored heat dissipation and local heating effects in MJs, either based on the Landauer picture[239] or the non-Landauer picture.[379,380] Pecchia *et al.* conducted first-principle calculations to determine the power emitted in a molecule as a result of scattering with localized vibrations, demonstrating that how electron–phonon coupling, incoherent transmission, and phonon dissipation rate significantly influence the local temperature[331] Apart from investigating the contribution of electron–phonon scatterings to local heating, D'Agosta *et al.* have also examined the effect of electron–electron scatterings.[381] In addition to exploring local heating effects, local cooling phenomena have also been investigated in the MJ,[382,383] showing that under voltage biases across the MJs, the local temperature can reach values below the ambient temperature.

3. Thermal transport in single-molecule junction: Experimental results

Experimentally, Cui *et al.*,[353] for the first time, measured the thermal conductance of a single molecule junction using the SThM-BJ technique in conjunction with a time-averaging scheme. This approach allowed them to achieve an ultrahigh resolution of 80 picoWatt (pW) at room temperature, facilitating the quantitation of thermal conductance for single molecules. They used a custom scanning thermal probe, as discussed in the experimental technique section above. For Au–alkanedithiol–Au junctions with two to ten carbon units. They measured that thermal conductance is independent of molecular length to a first approximation, which agreed with detailed *ab initio* simulations.[353] However, due to the short length of carbon units, FPU cannot be deterministically evaluated. Nevertheless, the possibility of an experiment evaluating the thermal conductance of a single-molecule junction opens a prospect for future work to study different effects like phonon interference and Fano resonance, as well as topics discussed in the above sections. In addition, Mosso *et al.* measured the thermal conductance of octane-di-thiol and Para OPE3 using a sample as a sensor and an averaging scheme.[352] Nevertheless, a deterministic measurement of a single molecule without an averaging scheme is yet to be realized.

In addition, some experimental studies have been conducted to quantify heat dissipation in MJs and gain insights into the inelastic processes occurring within the molecular region and the electrodes. By analyzing the conductance fluctuation, effective temperature was found to scale with the square root of electrical bias in Au atom-sized contacts.[384] Tsutsui *et al.*[385] also evaluated current-induced local heating in Au/BDT/Au MJs through a self-breaking technique, yielding an effective temperature of 463 K at 1 V bias. Huang *et al.*[386] found that in an STMBJ, the effective local temperature of the MJ (6-, 8-, and 10-alkanedithiol) initially rose with applied bias, reaching a maximum before subsequently decreasing, with a decreasing trend when increasing the molecular length at a fixed bias. In addition, inelastic electron tunneling spectroscopy (IETS)[387] and surface-enhanced Raman spectroscopy (SERS) have been used to evaluate the local effective temperature.[388,389]

4. Thermal transport in ensemble systems: Theory and experiment

Unlike single-molecule length dependence studies, there has been numerous experimental progress in ensemble systems, including large contact area junctions and nanoscale oligomer/polymer fibers. In this section, both computational and experimental results will be reviewed, with emphasis on different topics.

a. Length dependence. A recent study by Yang *et al.*[390] measured length-dependent thermal conductance at room temperature for van der Waals crystal $NbSe_3$ nanowires. These nanowires exhibit superdiffusive phonon transport, which is contrary to the classical size effect based on phonon-boundary scattering. They also observe thermal transport transitions from 1D to 3D model-like at a specified characteristic length indicating a glimpse into the FPU divergence phenomenon. Wang *et al.*[243] investigated heat transport through self-assembled monolayers of long-chain hydrocarbon molecules anchored to a gold substrate by rapidly heating the gold with a femtosecond laser pulse [Figs. 25(g) and 25(h)]. They performed measurements using TDTR for carbon chains up to 24 and observed no thermal conductance difference with increasing length.

In polymer nanofiber systems, it was experimentally observed that for polyethylene with an extrusion ratio of 25, the thermal conductivity along the extrusion direction can achieve an extremely high value that is close to that of stainless steel.[391] Such high value inspired various computational and experimental works on single polymer chains of various lengths [Figs. 26(a)–26(c)].[328,329,392–394] Shrestha *et al.*[395] developed crystalline polymer nanofibers with ultrahigh strength and thermal conductivity, surpassing any existing soft materials [Fig. 26(d)]. Yang *et al.*[396] observed that the competition between ballistic and diffusive phonons was identified as the underlying cause for aromatic monomers to possess a thermal conductivity approximately five times greater than that of a polyethylene (PE) chain. Furthermore, the divergent thermal conductivity in individual polyethylene chains was attributed to the cross-correlations for midfrequency longitudinal-acoustic phonons.[392] Additionally, the simulations suggest an additive relationship in total thermal conductance as the number of linking polymers in the dimer increases from 1 to 3.

b. Interfacial thermal resistance. Interfacial thermal resistance (ITR) is a principal barrier to heat transfer between different materials and is a significant concern for ensemble thermal measurements. For example, the thermal conductance between hydrophilic surfaces and water was observed to be several times greater than that between hydrophobic surfaces and water for solid–SAM–water junctions, highlighting the significant role of the self-assembled monolayer in modulating interface thermal transport. This was confirmed later by introducing thiolated alkane molecules between the water–solid interface, which can enhance thermal conductance several times.[397] On the other hand, Wang *et al.*[398] performed thermal conductance measurements on an MJ in a solid–SAM–liquid configuration (Au–ADT–GaAs), which is fabricated by transferring a thin gold film deposited on a silicon stamp to SAM-coated GaAs substrate, showing robust thermal conductance with insensitive length dependence [Fig. 26(e)]. In another study, it was shown that phonon transport in the alkane chains is ballistic and can be restricted by the Au–SAM interface for long-chain alkanethiols.[243] Furthermore, Ota *et al.*[399] discovered that the ITR was directly proportional to the surface coverage of covalently bonded triazine linkers [Fig. 26(f)]. They observed that the proportionality constant for the increment rates was approximately unity.

The interfacial thermal conductance can be elucidated through two theoretical models that have proven effective in predicting the behavior of phonons: the acoustic mismatch model (AMM) and the diffuse mismatch model (DMM). In AMM, a straightforward simplification involves treating both materials as continuous media separated by an ideal plane, neglecting the details of lattice structures, and allowing phonons to be treated as elastic waves. The AMM effectively describes the observed temperature dependence of ITR at low temperatures, whereas the model typically yields predictions that are higher than the measured values.[400] Unlike AMM, the DMM assumes complete diffusive scattering of incident phonons, whereas outgoing phonons in the DMM have no recollection of their previous trajectory.[401] The most common and straightforward approach to model diffusive phonon scattering across solid interfaces and the consequent thermal boundary conductance is by implementing the DMM, where electrons and phonons scatter diffusively across the interface.[402] It was found that an increase in roughness typically results in a decrease in ITR at solid–solid interfaces.[403] Similar findings were also reported for solid–SAM–solid interfaces.[404,405]

The structural disorder of molecules within the SAM can induce phonon transport scattering or result in poorer effective contact between the SAM surface and substrates. In large-area junctions, when

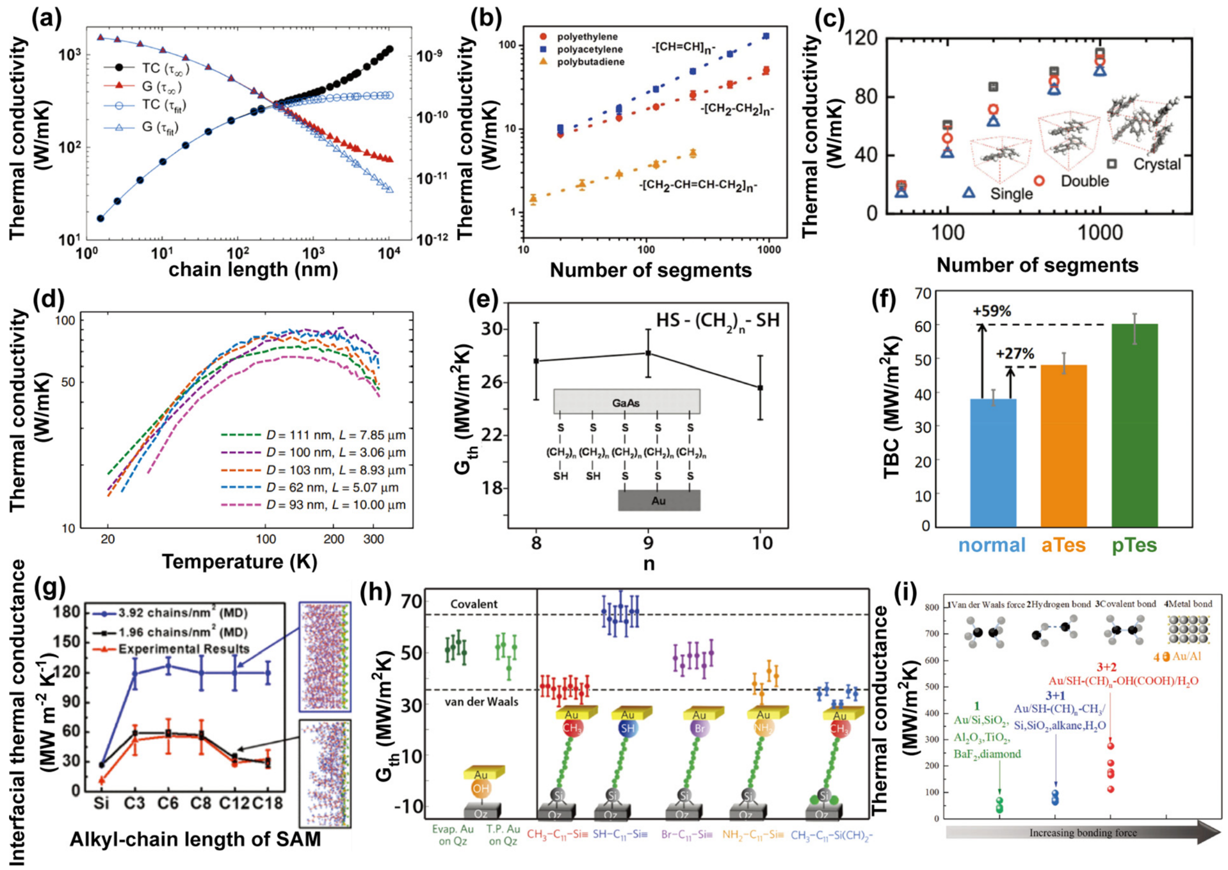

FIG. 26. (a) Thermal conductivity (circles) and corresponding thermal conductance (triangles) predictions for a single PE chain. Reproduced with permission from Henry and Chen, Phys. Rev. Lett. **101**, 235502 (2008). Copyright 2008 American Physical Society. (b) Effect of double bonds and bond-strength disorder compared to polyethylene. Reproduced with permission from Liu and Yang, Phys. Rev. B **86**, 104307 (2012). Copyright 2012 American Physical Society. (c) Axial thermal conductivity as a function of the number of segments in single-chain (triangle), double-chain (circle), and crystal (square) PPPs. The colored band represents the uncertainty of the simulation results. Reproduced with permission from Yang *et al.*, J. Phys. Chem. B **127**, 6804 (2023). Copyright 2023 Authors, licensed under a Creative Commons Attribution (CC BY) license. (d) Thermal characterization of PENF, with $k(T)$ of all reported samples after adjusted for $2R_c$. Reproduced with permission from Shrestha *et al.*, Nat. Commun. **9**, 1664 (2018). Copyright 2023 Authors, licensed under a Creative Commons Attribution (CC BY) license. (e) Thermal conductance of Au–alkanedithol ($n = 8, 9, 10$)–GaAs junctions at room temperature. Inset: schematic of the sample. Reproduced with permission from Cui *et al.*, J. Chem. Phys. **146**, 092201 (2017). Copyright 2017 American Institute of Physics. Reproduced with permission from Wang *et al.*, Appl. Phys. Lett. **89**, 173113 (2006). Copyright 2006 American Institute of Physics. (f) Time-domain thermoreflectance (TDTR) measurement results of obtained TBC of graphite/Al interfaces. Reproduced with permission from Ota *et al.*, Appl. Mater. Interfaces **11**, 37295 (2019). Copyright 2019 Authors, licensed under a Creative Commons Attribution (CC BY) license. (g) ITCs of PS/SAM/Si with different packing densities and chain lengths, and the right graphs are the relaxed configuration of C12-SAMs with different densities. Reproduced with permission from Lu *et al.*, ACS. Appl. Mater. Interfaces **11**, 42708 (2019). Copyright 2019 Authors, licensed under a Creative Commons Attribution (CC BY) license. (h) Measured thermal conductance of SAM junctions for various end groups. Reproduced with permission from Losego *et al.*, Nat. Mater. 11, 502 (2012). Copyright 2012 Springer Nature. (i) The interfacial thermal conductance between Au and multiple materials. Reproduced with permission from Zhang *et al.*, Adv. Mater. Interfaces **9**, 2200078 (2022). Copyright 2022 Wiley.

the packing density of a SAM is insufficient to maintain a well-defined lateral structure, the supramolecular assembly can experience back folding, thereby inducing conformational disorder. It was experimentally reported that such structural disorder could result in a decrease in the ITR for amorphous polyethylene with various alkyl chains [Fig. 26(g)].[406,407]

c. Electron–phonon interactions at molecule/electrode interface. Heat transfer across a metal–molecule interface is governed by the interplay among various heat carriers. Within metal, both electrons and phonons play a role in heat conduction, whereas in molecules, phonons are the primary heat carriers. These interactions among the carriers can be categorized into three channels, each corresponding to a distinct heat transfer mechanism: phonon(metal)–phonon(molecule), electron(metal)–phonon(molecule), and electron (metal)–phonon (molecule) direct interactions. Distinguishing the contributions from these channels is challenging both experimentally and theoretically due to limitations in the resolution and sensitivity of experimental systems as well as the difficulty in accurately determining the interfacial states at the nanoscopic level and the local temperature.

For the first channel on the phonon(metal)–phonon(molecule) channel, Khalatnikov's AMM theory serves as a foundational point for subsequent theories concerning ITR, as it relies solely on the mass densities and phonon velocities in both materials without any fitting parameter.[408] However, it was found that the observed ITR was always underestimated[409,410] even when additional channels from multiphonon scattering caused by anharmonicity are considered,[411–413] suggesting that contributions from other channels cannot be neglected. Singh *et al.*[414] showed that the thermal resistance due to electron–phonon coupling could be calculated using the Fermi golden rule under a deformed potential. Furthermore, investigations revealed that the electron–phonon coupling constant can be altered by the chemistry of the interface.[415] Li *et al.*[416] introduced a third channel of electron–phonon direct interaction through a modification to the two-temperature (TT) model. They showed that the above-mentioned three channels could be represented by an equivalent series-parallel thermal resistor network, where an analytical expression for the thermal boundary conductance can be derived. Medrano Sandonas *et al.*[417] computationally discovered that heterogeneous molecular junctions, comprising molecular wires connecting two distinct nanocontacts, could function as a selective phonon filter, generating a gap in the transmittance spectrum.

d. Molecule–electrode bonding. Bonding forces between the molecule and the electrode can be categorized into van der Waals force, hydrogen bond, and covalent bond, with their bonding strength varying from weak to strong. It was shown that the ITR increases with the bonding strength [Fig. 26(h)].[362,418–422] The bonding strength is crucial in determining whether a Debye temperature mismatch or the overlap between the vibrational density of states (VDOS) contributes to the MJ's thermal conductance. For stronger bond strength between SAM and the electrode, a large Debye temperature mismatch can result in lower thermal conductance, whereas for van der Waals bonded contacts, the Debye temperature mismatch effect is comparatively weak.[423] When two materials are in contact, van der Waals force usually occurs, and a modified AMM that captures the effects of interface bonding parameters can include it in the phonon transport.[424]

Hydrogen bonds are typically stronger than van der Waals interactions and are predominantly found in water and organic materials. The range of ITR can be widely adjusted by varying the degree of functionalization. Molecular dynamics simulations demonstrated that stronger hydrogen bonds induce closer proximity of organic molecules to the interface. This proximity enhances interatomic forces across the interfaces, consequently yielding greater interfacial heat flux and higher thermal conductance.[425] Ge *et al.*[426] utilized TDTR to measure thermal conductance values across interfaces between water and self-assembled monolayers with hydrophobic (CH3-terminated) and hydrophilic (OCH3- and OH-terminated) properties, revealing a 2–3 times Kapitza length at hydrophobic interfaces. More recently, Zhang *et al.*[427] showed that a remarkable 273% enhancement of ITR can be achieved across the interfaces between graphene and poly(methyl methacrylate) (PMMA) through the introduction of hydrogen-bond-capable hydroxyl groups to the interfaces.

A covalent bond denotes a relatively stable chemical structure where two or more atoms share electrons to achieve electron saturation. Losego *et al.*[418] employed TDTR and laser spallation measurements to experimentally correlate bonding strength with heat flow at the gold–SAM interface. Their findings revealed an 80% increase in the ITR when transitioning from van der Waals to covalent bonding, which can be further tuned by adjusting the density of covalent bonds.

e. Intermolecular interactions in large-area junctions. For large-area junctions, unlike single-molecule junctions, it is essential to consider intermolecular interactions within monolayers [Fig. 26(i)].[360] Monolayers exhibit a certain degree of structural disorder and noncovalent lateral interactions between adjacent molecules, resulting in vibrational energy states with low frequencies. Lu *et al.*[428] conducted FDTR cross-plane heat conductance measurements on a range of polarized phosphonate-functionalized azastibazolium π-electron (PAE) films and high-k dielectric metal oxide (ZrO_2 or HfO_x) films with varying thicknesses. Their findings revealed a linear correlation with the mole fraction of the chromophores, suggesting that chromophores operated as independent channels with minimal interfacial interaction. On the contrary, a combination of strong cross-interface intermolecular interactions and good thermal coupling via soft vibration modes at liquid—liquid interfaces can be used to explain high Kapitza resistance across water—organic liquid, water—surfactant, and surfactant—organic liquid surfaces.[429,430]

IV. CHEMICAL REACTION IN MSJs

The induction effects of external stimuli on chemical reactions play a critical role in energy storage and conversion processes. They enhance efficiency by lowering the activation energy of reactions, optimize energy utilization by reducing by-product formation, improve system stability, extend equipment lifespan, and support the efficient conversion of renewable energy. For instance, stress-induced effects convert mechanical energy to chemical energy, while electric and light-induced effects transform electrical and light energy into stored chemical energy. Thermocatalysis effects maximize energy conversion efficiency by controlling reaction conditions, facilitating efficient and sustainable energy management. In single-molecule junctions, the study of induction effects encompasses stress-induced, electric-induced, and thermocatalysis effects to optimize chemical reactions and energy conversion processes. Stress-induced effects regulate molecular and electronic structures through mechanical stress, electric-induced effects promote redox reactions and charge injection via applied electrical energy, and thermocatalysis effects optimize reaction conditions through thermal energy. Collectively, these effects significantly enhance reaction rates, selectivity, and energy conversion efficiency.

A. Stress-induced effects

The stress-induced effect refers to the phenomenon where the application of stress to a system causes a change in the molecular structure, thereby altering the reaction rate of molecules. This phenomenon typically occurs in solid materials, especially in metals and alloys.[50,431] In the case of solid materials, external stress can lead to deformation of the atomic structure, potentially increasing lattice defects and dislocation density, affecting the interactions between atoms within the material, and thereby influencing the reaction rate. At the molecular level, stress can induce changes in molecular structure, thereby affecting chemical properties and reactivity. A typical example of this is the alteration of redox potential before and after stress induction.

Li *et al.*[432] used STMBJ technology to apply external stress to molecules, adjust the distance between the source and drain electrodes, and alter the molecular structure, thereby successfully achieving precise control of the redox potential. To accurately capture the differences in redox potential, Li *et al.* chose molecules with a ferrocene core, as shown in the Fig. 27(a). Ferrocene is not only an ideal system for testing redox potentials but also undergoes structural changes under stress. As shown in Figs. 27(b)–27(f), the cyclic voltammetry plot demonstrates a clear and reversible redox peak at 0.4 V, serving as a baseline for subsequent stress application experiments. At lower potentials, when Fe ions are in the +2 oxidation state (reduced state), the molecular conductance was measured at $0.011 \pm 0.002\ G_0$. At higher potentials, when Fe ions are oxidized to the +3 oxidation state, the conductance increases fivefold, reaching $0.053 \pm 0.007\ G_0$. At a stretching force of 1.5 nN, the molecule is stretched by 0.01 nm, corresponding to an approximate 65 mV shift in the adiabatic ionization potential. Assuming that the thermodynamic and entropy contributions remain unchanged during the stretching process, this corresponds to a reduction in the redox potential by approximately 65 mV, which is in excellent agreement with the experimental results. The DFT calculations demonstrate the correlation between stretching and the redox potential. During the stretching process, the molecule undergoes various conformational changes. Initially, the length of the molecular junction increases, which can be accommodated by slight deformations in the alkyl side chains. With further stretching, the ferrocene ring begins to twist until the dihedral angle reaches 180°. As shown in Figs. 27(g)–27(i), the energy changes for the reduction and oxidation states as a function of stretching length can be fitted to a quadratic function. The calculations indicate that stretching occurs across multiple bonds but predominantly within the ferrocene ring. This research demonstrates that the stretching of molecular junctions induces an effect on molecular redox reactions. Stretching can alter the bond lengths within the molecule and drive the reaction toward a final state that favors bond length changes, thereby achieving an induced effect of mechanical stress on chemical reactions at the molecular level.

In MSJs, the conversion between mechanical energy and chemical energy can occur not only through the redox reaction of ferrocene, but also in the spiropyran system. In 2019, Walkey *et al.*[433] achieved a delicate conversion from mechanical energy to chemical energy in the spiropyran molecular system using the STMBJ technology. This energy conversion is prominently characterized in the conductance platform curve by a sudden and dramatic current jump occurring just as the current plateau ends. Due to the short lifespan of this conductance jump, and its occurrence only at the end of the current curve, they attributed this phenomenon to the energy conversion effect resulting from the *in situ* rupture of the C-O bond in the spiral structure. Overall, the conversion between chemical and mechanical energy in MSJ involves microscopic processes such as conformational changes within the molecule, and the breaking and forming of chemical bonds. Studying these processes not only deepens the understanding of microscopic phenomena like molecular dynamics and chemical reaction mechanisms, but also helps to discover new pathways for energy conversion, thereby improving energy conversion efficiency.

B. Electrostatic field effects

Chemical reactions fundamentally involve electron transfer, and any form of electron transfer can potentially be influenced by an electrostatic field.[434] Therefore, theoretically, electrostatic induction can be considered as a potential method to promote any chemical reaction.[435,436] Depending on the mechanism of action in reactions, electrostatic induction can be divided into electrostatic field induction and charge injection induction.

The electrostatic field induction is a method that utilizes an externally applied static electric field to enhance chemical reactions. This approach can increase reaction rates, improve reaction selectivity, and reduce the required energy input. In terms of energy storage, electrostatic field induction can optimize chemical reactions in batteries, thereby increasing their energy density and efficiency. Additionally, it can effectively convert and store energy in fuel cells and other energy storage devices. The principle behind electrostatic field induction is that an external electric field can alter the electron distribution of reactants and the energy barriers of reaction transition states, thus facilitating the progress of chemical reactions. When an external electric field interacts with reactant molecules, it triggers a rearrangement of electrons within the molecules, leading to changes in the electron distribution of the reactants. This electron rearrangement can lower the energy barrier for the reactants, make the reaction more favorable, and enable more efficient energy conversion.

Therefore, electrostatic field induction offers a promising approach to accelerate and control chemical reactions, providing new avenues for green and efficient chemical synthesis. Research in the electrostatic field induction will contribute to the development of more sustainable chemical processes. Aragonès *et al.*[437] proposed a novel concept: using an electric field to control reactant orientation can manipulate non-redox reaction kinetics and thermodynamics. To prove this, they combined surface reactions with STMBJ technology, studying the Diels–Alder reaction at a single-molecule level in Fig. 28(a).

To investigate the promoting effect of the electric field on the D-A reaction, they first conducted a detailed theoretical analysis. Figure 28(b) clearly shows the potential resonance structure in the reaction transition state, while Fig. 28(c) elaborates on the two enantiomers of furan, with its substituents located on either side of the molecule. Subsequently, the calculations in Fig. 28(d) clearly reveal the impact of the external electric field strength and direction on the reaction barrier

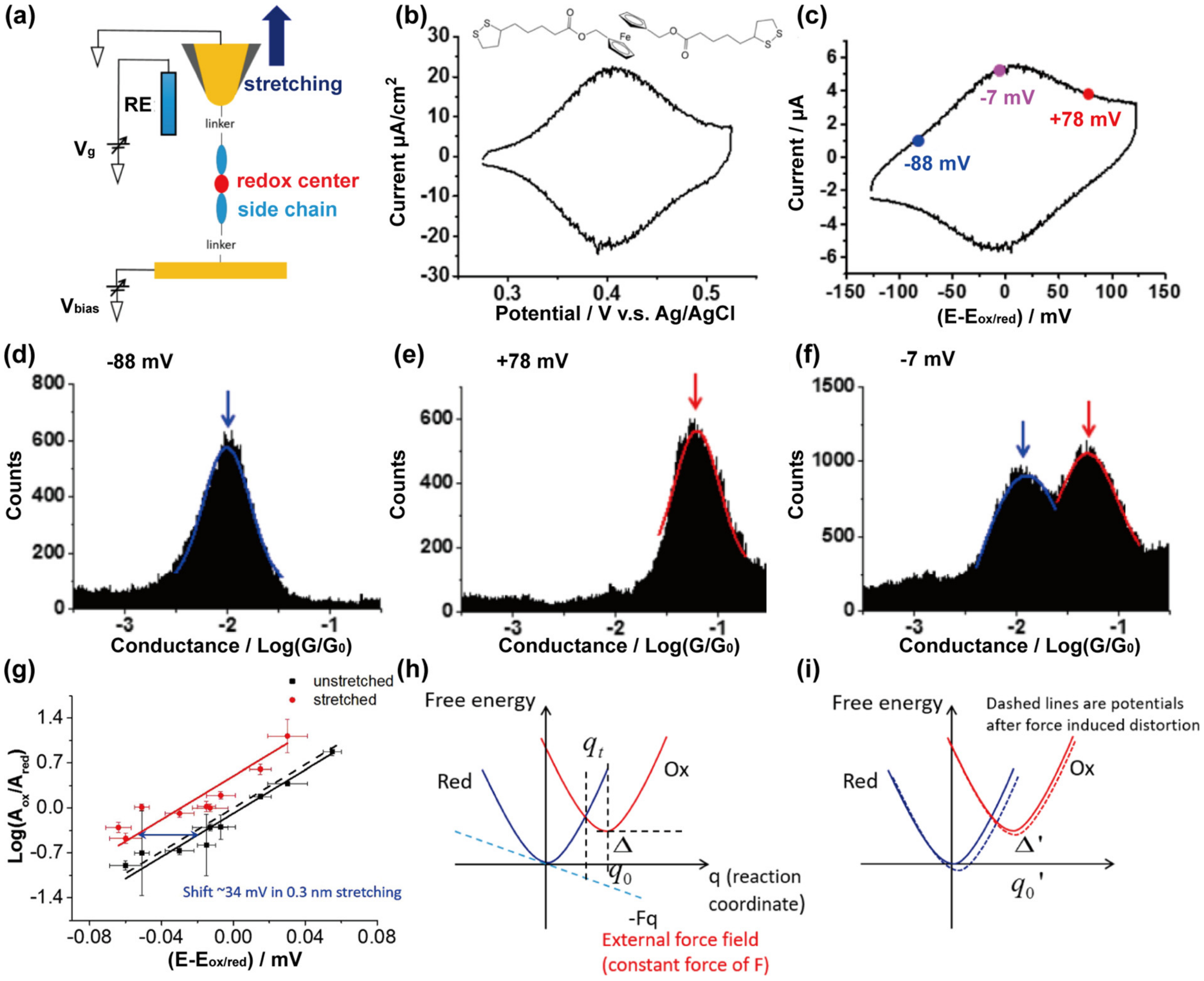

FIG. 27. (a) Experimental setup showing a redox molecule bridged between a gold STM tip and gold substrate. (b) Structures of Fc-Lip and cyclic voltammogram of Fc-Lip on a gold surface showing well-defined oxidation and reduction peaks at ∼0.4 V vs Ag/AgCl. (c) Cyclic voltammogram of Fc-Lip, where the colored dots mark the potentials at which the mechanical stretching and conductance measurements in (d)–(f) are carried out. (g) The logarithmic ratio of the conductance histogram peak area for the oxidized state to that of the reduced state of unstretched (black dots) and stretched (red dots) Fc-Lip vs potential. Schematic free energy surfaces of the reduced (blue) and oxidized (red) species (h) without mechanical stretching and (i) with mechanical stretching. Reproduced with permission from Li *et al.*, J. Am. Chem. Soc. **139**, 14699 (2017). Copyright 2017 Authors, licensed under a Creative Commons Attribution (CC BY) license.

height, highlighting the significant promoting effect of the electric field on the D–A reaction. Notably, the blue structure shows almost no response within the experimental range of the electric field, whereas the red structure exhibits high sensitivity to the electric field.

Theoretical findings ultimately require experimental validation. Under the condition of maintaining a constant preset current, Aragonès *et al.* carefully adjusted the bias voltage, allowing it to fluctuate between +0.75 and −0.75 V, thereby ensuring a constant distance between the surface and the tip. They meticulously recorded the current response data during this process, as shown in Fig. 28(e). Furthermore, the data in Fig. 28(f) show that when the bias voltage was gradually increased from −0.05 to −0.75 V, the frequency of product formation increased by 4.4 times. This finding not only aligns with the theoretical predictions in Fig. 28(d) but also directly demonstrates that the red structure dominated the reaction. It also fully validates that the catalytic effect of the electric field occurs only in a specific direction, effectively accelerating the reaction.

Research into the effects of directed external electric fields on chemical reactions has made initial progress, but the extent of acceleration of chemical reactions by electric fields and the effects of electric fields in more complex study systems still require further exploration when compared to non-electric field environments.

Huang *et al.*[438] collaborated to control both the electric field and the direction of reactants using MCBJ technology [shown in Fig. 29(a)]. They successfully investigated the selective induced effects of OEEFs (orientation-enhanced electric fields) on a two-step cascade Diels–Alder addition reaction and an aromaticity reaction. Under the same reaction conditions as macroscopic *in situ* NMR and conductance testing, *in situ* electrical property measurements were conducted for better comparison. For conductance testing, a bias voltage of 100 mV was applied in the experiments, and the electrical signals were then recorded at 5-min intervals [shown in Fig. 29(b)]. By fitting the peak positions, the conductance values at different time points were obtained. As the reaction progresses, a gradual decrease appears in the conductance peak area for "a" and the appearance of a conductance peak at $10^{-3.91}$ G_0, indicating the gradual formation of product "b." When the reaction reaches 110 min, the conductance peak of "a" disappears, indicating the complete conversion to product "b." Over time, a new peak appears at $10^{-4.72}$ G_0, while the peak for "b" gradually decreases. Separate tests confirmed that this was the conductance peak of product "c." In Fig. 29(c), for NMR tests in macroscopic reactions, the conversion of product "b" to product "c" takes more than 26 h, while under single-molecule electrical testing conditions, it only takes 280 min. This suggests that the second step, the aromatization reaction, is selectively accelerated under single-molecule electrical measurement conditions [shown in Figs. 29(d) and 29(e)].

Through DFT calculations, the spatial distance for direct proton transfer to the next site decreases under the influence of the electric field, resulting in a reduction in the energy of the transition state and a lower reaction barrier. As the reaction axis for this process is

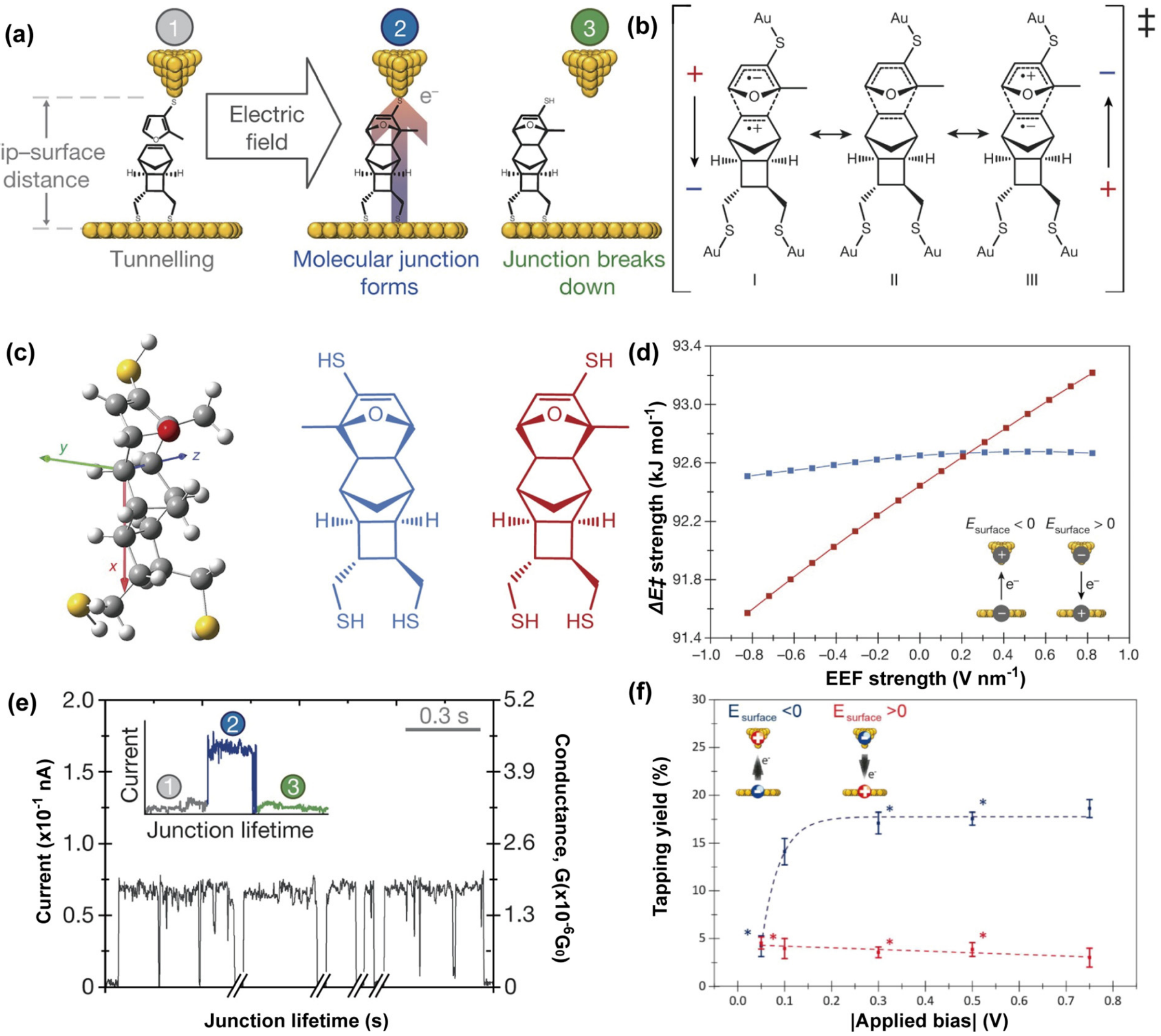

FIG. 28. (a) The stages encountered during a blinking event. (b) Possible resonance structures of the transition state. (c) The two diastereoisomers of the exo–syn product of this reaction. In the blue diastereomer, the substituents of the furan are located on the left of the molecule; in the red diastereomer, these substituents are located on the right. (d) The predicted effects of the strength and direction of the external electric field (EEF) on the reaction-barrier height (ΔE‡) for the formation of the two exo–syn diastereoisomers. (e) A real-time data capture of blinking events. The time breaks in the x-axis are about 2 min. The inset shows the STM current response before (1), during (2), and after (3) the formation of a single blink (junction). (f) Tapping yield (number of molecular junctions formed/total number attempts) at different negative and positive bias. Reproduced with permission from Aragonès *et al.*, Nature **531**, 88 (2016). Copyright 2016 Springer Nature.

non-orthogonal to the electric field, the component of the external electric field in the reaction axis direction promotes the reaction, while the Diels–Alder reaction axis is nearly perpendicular to the electric field direction, explaining the minimal effect of the electric field on the Diels–Alder reaction.

The above-mentioned literature has demonstrated that although there has been preliminary progress in studying the effects of directed external electric fields on chemical reactions, the investigation of the extent to which each step of the D–A reaction process responds to electric fields remains a challenging task. D–A reactions typically involve a concerted pericyclic mechanism with a six-membered ring transition state, leading to the formation of two new bonds simultaneously. Some theoretical work has predicted that external electric fields can promote D–A reactions and induce the crossing of potential energy surfaces between concerted pathways and pathways involving zwitterionic intermediates. However, experimentally detecting the minuscule, short-lived reaction trajectories and proving the existence of different pathways under such stringent conditions remains a significant challenge.

For this purpose, Yang *et al.*[439] made a significant breakthrough by directly observing the precise time trajectory and detailed reaction pathway of the D–A reaction through precise single-molecule detection on an *in situ* unlabeled single-molecule electrical detection platform [in Figs. 30(a) and 30(b)], confirming the concerted mechanism and elucidating the role of charge transfer complexes in the reaction. They employed electron beam-exposed polymethyl methacrylate (PMMA) templates and oxygen plasma technology to prepare graphene dot electrodes with carboxylic acid terminals and realized the connection between the molecule and the electrodes. According to the theory of molecular electronics, the conductance of a molecule is closely related to its structure, so changes in the conductive states can reflect the chemical reaction process. The experiment recorded nanoampere-level currents under biases ranging from 100 to 600 mV at 393 K, which are shown in Fig. 30(c). At the low bias of 100 mV, five conductive states appear, and with the increase in bias to 200 mV, the sixth conductive state also emerges. Moreover, as the bias continues to increase, the appearance frequency of the sixth conductive state

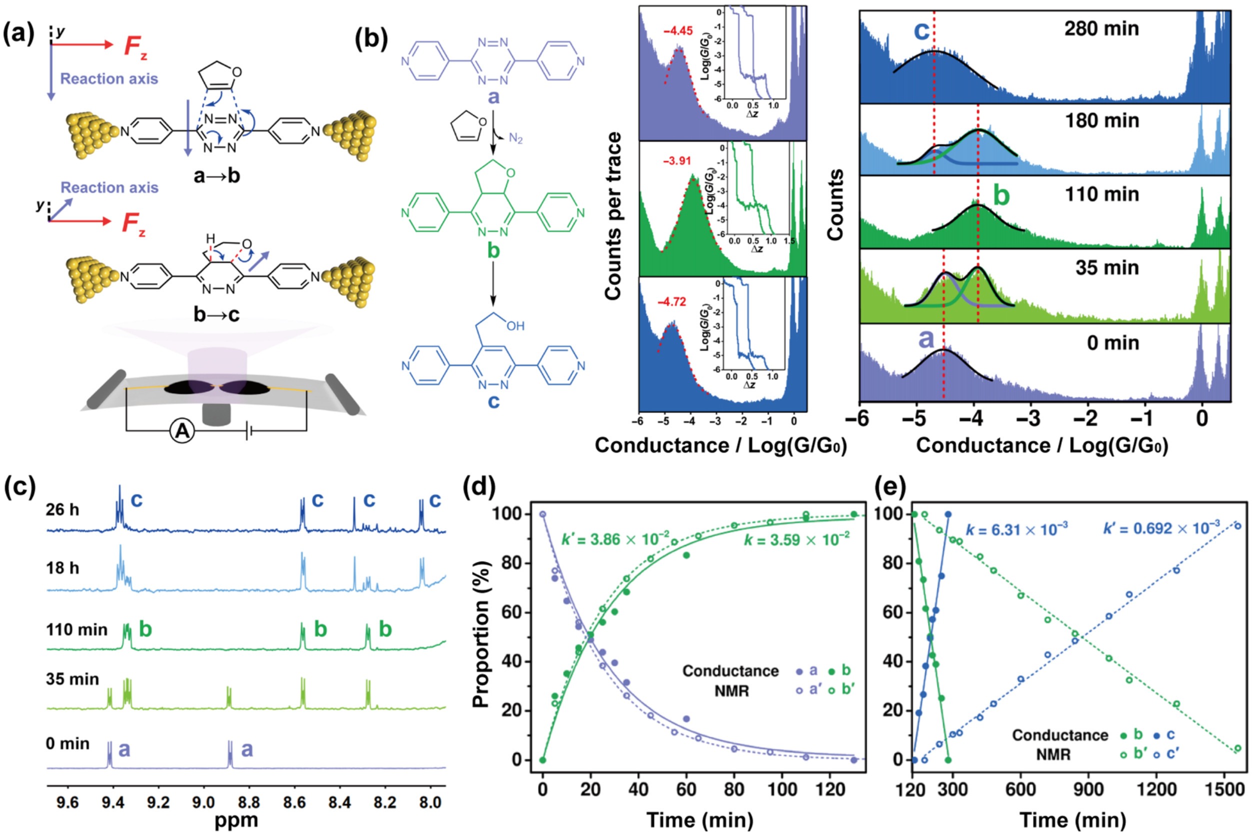

FIG. 29. (a) Schematic of the MCBJ technique for *in situ* single-molecule conductance measurement. (b) The Diels–Alder reaction between 3,6-di(4-pyridyl)-1,2,4,5-tetrazine and 2,3-dihydrofuran to form compound b, which goes through an aromatization process to form compound c. The single-molecule conductance of each compound was characterized in the right column Monitoring the complete transformation from a to c through conductance for 4.7 h. Monitoring the complete transformation from a to c through ^{1}H NMR (C) for 26 h. The dashed lines represent the conductance value of each compound. The relative proportion between different components was analyzed using *in situ* single-molecule conductance measurement and NMR analysis for (d) the Diels–Alder addition process and (e) the aromatization process in this cascade reaction. The hollow circles and solid circles represent the results analyzed from NMR and conductance histograms, respectively. The data points were fitted with dashed and solid lines, respectively. Reproduced with permission from Huang *et al.*, Sci. Adv. **5**, eaaw3072 (2019). Copyright 2019 Authors, licensed under a Creative Commons Attribution (CC BY) license.

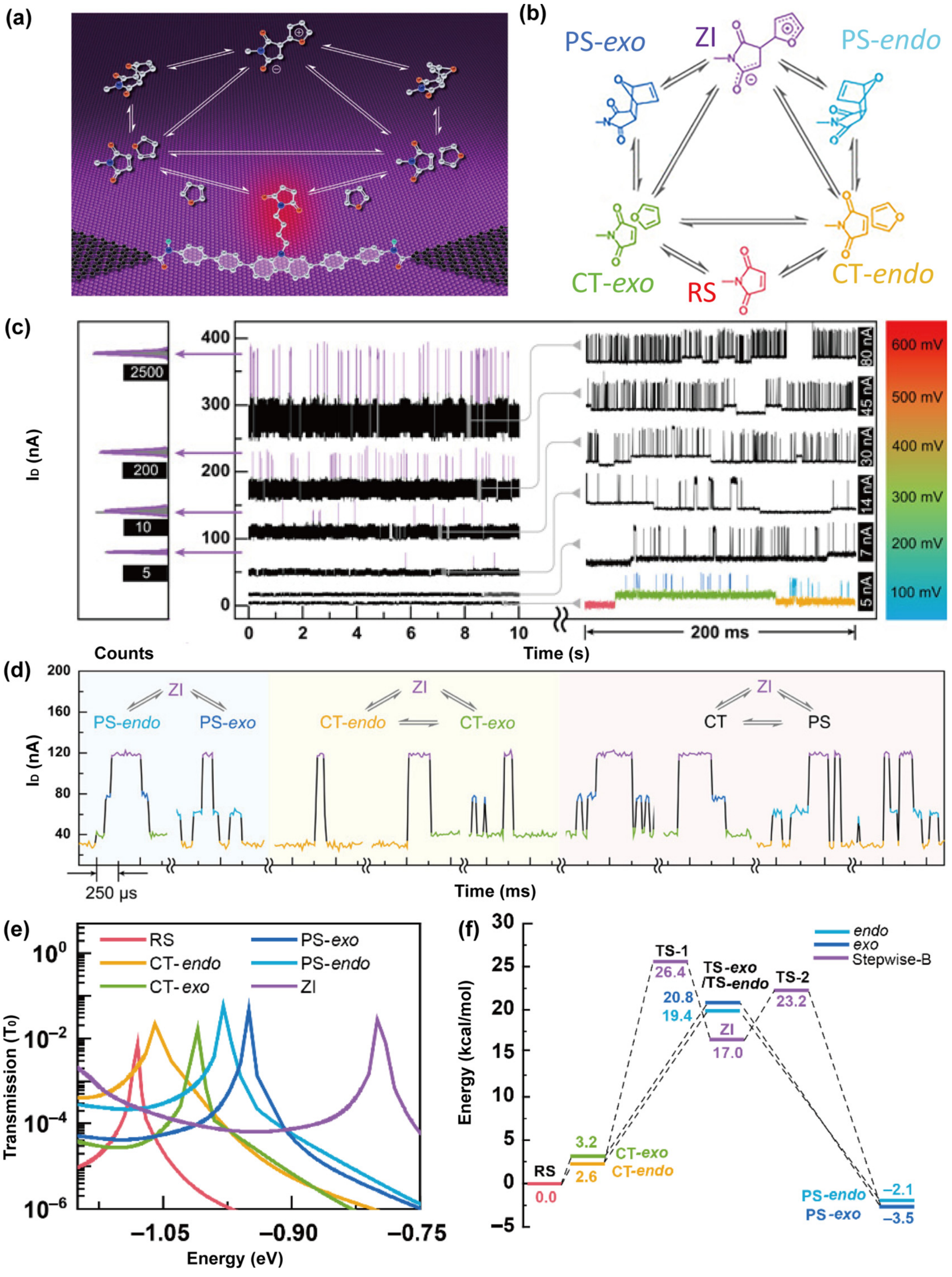

FIG. 30. (a) Schematic diagram of the single-molecule electrical monitoring platform. (b) Reaction mechanism under 100 mV and the corresponding attribution of the six conductance states obtained from Gaussian fittings of I–t measurements. (c) Bias voltage-dependent experiments under 100–600 mV at 393 K. The right side is the zoom-in picture of the concerted reaction process. The left side is the statistical histogram of the highest conductivity state [zwitterionic intermediate (ZI)] under 300–600 mV. (d) Time sequence of the transitions among different species during the Diels–Alder reaction. (e) Transmission spectra of six species, where the dominated transmission orbitals (p-HOMOs) are displayed. (f) Gibbs free energies for the concerted and stepwise pathways at −2.57 V/nm. Reproduced with permission from Yang *et al.*, Sci. Adv. **7**, eabf0689 (2021). Copyright 2021 Authors, licensed under a Creative Commons Attribution (CC BY) license.

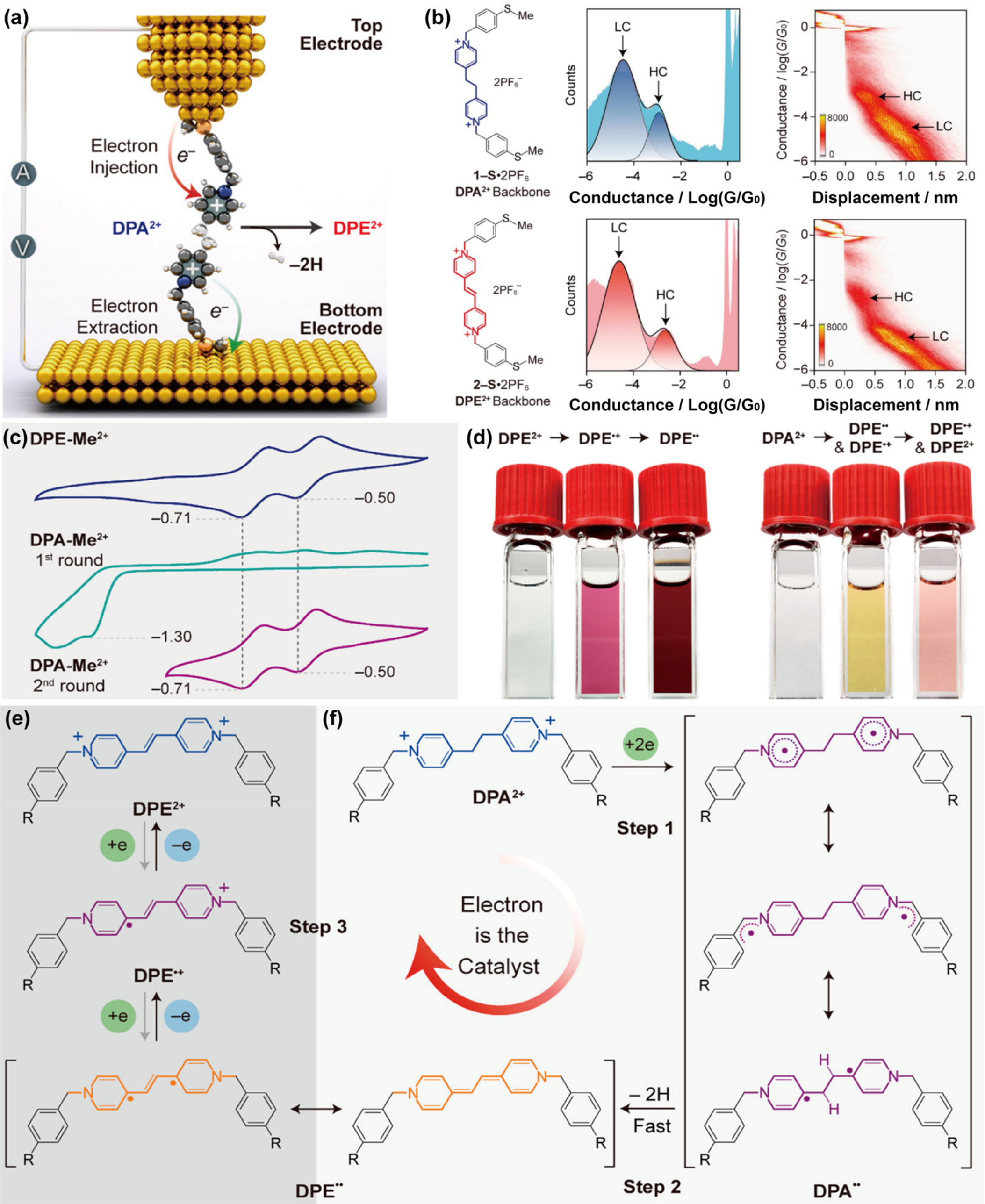

FIG. 31. (a) Schematic illustration showing the electron-catalyzed DPA^{2+} to DPE^{2+} dehydrogenation at an STM junction. (b) The structural formula for 1—S·2PF$_6$ and 2—S·2PF$_6$ employing a non-conjugated DPA^{2+} backbone. 1D and 2D conductance—displacement histograms for 1—S·2PF$_6$ and 2—S·2PF$_6$. (c) Cyclic voltammograms (CVs) show evidence for DPA^{2+} to DPE^{2+} transformation. (top) is a reductive CV of dimethyl dipyridinium ethene (DPE-Me^{2+}). (middle) illustrates a first-cycle wide-range CV scan of dimethyl dipyridinium ethane (DPA-Me^{2+}) (bottom) shows the second-cycle CV scan at a narrow range (0 to −1 V). (d) Change of the color of 2—S·2PF$_6$ (left) and 1—S· 2PF$_6$ (right) solutions under different reduction potentials. (e) and (f) A proposed reaction cycle of the electron-catalyzed dehydrogenation in solution. Reproduced with permission from Chen *et al.*, J. Am. Chem. Soc. **143**, 8476 (2021). Copyright 2021 Authors, licensed under a Creative Commons Attribution (CC BY) license.

also increases. A series of tests related to liquid-phase concentrations and temperature were conducted to determine the nature of these six conductive states. According to theoretically calculated and the experimental results in Figs. 30(d) and 30(e), the transitions between the five lower conductive states with a fixed time sequence display a typical Diels–Alder reaction mechanism: the substrate RS (red) and furan first form charge-transfer complexes of the endo- (CT-endo, orange) or exo- (CT-exo, green) configurations, followed by the formation of the respective products PS (light blue, PS-endo, and dark blue, PS-exo) through a six-membered ring addition reaction.

To further investigate the effect of the electric field on the D–A reaction, they considered the electric field for two specific orientations of the reactants. Specifically, the external electric field (EEF) in pathway A (indicated by the gray line) is oriented along the bonding axis, whereas the EEF in pathway B (indicated by the purple line) is oriented along the dipole moment vector connecting the negative and positive charges. According to the theoretical calculation data shown in Fig. 30(f), the $\Delta G^{\ddagger}$ value for pathway B is significantly lower than that for pathway A. This result reveals that the electric field orientation along the bonding axis provides more stability to the transition state structure compared to the reaction axis orientation. Additionally, both theoretical and experimental data consistently indicate that a strong external electric field can significantly reduce the energy barriers for both concerted and stepwise reactions. However, it is noteworthy that the extent of its effect varies depending on the direction of the electric field.

This study has utilized a single-molecule detection approach to comprehensively analyze the Diels–Alder reaction process. Through an ultrahigh-resolution integrated monitoring method, it has clarified the process that substrates like maleimides and furans must undergo to form charge transfer complexes during the cycloaddition, and it has explored the extent to which these processes respond to the electric field. Among them, at the same temperature, with the application of an electric field, the concerted kinetic pathway, concerted thermodynamic pathway, and stepwise reaction pathway can gradually be opened. This research lays the foundation for future universal catalysis, lowering reaction barriers, saving reaction costs, and regulating chemical reactions and processes in life sciences.

C. Charge injection-induced effect

Unlike the electrostatic field induction effect, the charge injection-induced effect refers to the phenomenon or method of altering the electron structure or energy state of reactants in a chemical reaction system by injecting external charges. This method can utilize an external electric field or electrodes to introduce additional charges during the reaction process, thereby influencing the electron distribution of reactants, lowering the activation energy of reactions, or improving reaction rates and selectivity. In the STMBJ process, the electron transfer process is generally divided into the following steps: 1. electrons are injected into molecules from one end of the electrode; 2. electrons participate in the intramolecular redox catalytic cycle; and 3. the electron is captured by the other electrode, and the cycle ends.

Chen *et al.*[440] used STMBJ technology to test the single-molecule conductance of a series of molecules, as shown in Fig. 31(a). The main chains of these molecules contain nonconjugated 1,2-bis (4-pyridine) ethane (DPA^{2+}) and conjugated 1,2-bis (4-pyridine) ethylene (DPE^{2+}) units, respectively. In the conductance test [Fig. 31(b)], although there are significant differences in the conjugation degree of the two main chains, and the torsion angle of the two pyridine rings also changes greatly, the test results show that their conductance values are almost the same. Therefore, researchers have proposed a hypothesis that, in the nanogap of STMBJ, the main chain of DPA^{2+} undergoes *in situ* dehydrogenation reaction, converting ethane to ethylene so that it has a completely conjugated skeleton similar to DPE. To test this hypothesis, as shown in Fig. 31(c), the researchers conducted cyclic voltammetry (CV) tests on DPE-Me·$2PF_6$ and DPA-Me·$2PF_6$, using CH_3CN solution containing 0.5 mm target compound and 0.1 M $TBAPF_6$ as supporting electrolyte. It should be noted that all potentials in CV measurement are based on Ag/AgCl and cannot be simply balanced with the bias voltage of STM. DPE-Me·$2PF_6$ shows two reversible redox peaks, corresponding to two continuous redox processes related to DPE: $DPE^{2+}/DPE^{\bullet+}$(-0.50 V) and $DPE^{\bullet+}/DPE^{\bullet+}$($-0.71$ V). However, the situation of DPA-Me·$2PF_6$ is different. First, the extensive scan in the first cycle is irreversible, and there is no reduction peak between 0 and -1.0 V. Second, the scanning in the second cycle became reversible again, showing two reversible redox peaks, and their potentials are exactly the same as DPE-Me·$2PF_6$. The color of the solution also changes significantly during CV scanning [Fig. 31(d)]. The formation of pyridine radical is the key step to trigger the dehydrogenation of DPA-Me·$2PF_6$ [Fig. 31(e)]. In order to clarify the mechanism between electric field and dehydrogenation, the reaction pathway was theoretically studied based on DFT. Charge injection induction is carried out in three steps: (I) reduction ($DPA^{2+}+2e^- \rightarrow DPA^{\bullet\bullet}$) (II) dehydrogenation ($DPA^{\bullet\bullet}\rightarrow DPE^{\bullet\bullet}+H_2$), and (III) oxidation ($DPE^{\bullet\bullet} - 2e^- \rightarrow DPE^{2+}$). The oriented externally electric field (OEEFs) is s*et al*ong the direction of the main chain (z direction), and the energy of all molecules under the electric field is reduced by 2.06 V/nm. It is worth noting that in the dehydrogenation step, the dehydrogenation energy decreases from -7.11 to -8.86 kcal/mol, indicating that OEEFs can promote the thermodynamic process of dehydrogenation. In addition to the thermodynamic promotion of dehydrogenation energy, a stronger electric field will lead to a smaller dehydrogenation activation energy barrier, revealing the role of OEEFs in promoting the kinetic process.

This study clearly shows that electron-catalyzed dehydrogenation can be achieved in solution and fracture junctions based on a scanning tunneling microscope. Researchers explained the conductance similarity between molecules with different bipyridyl ethane or bipyridyl ethylene skeletons through the conversion of ethane to ethylene. Using DFT calculation, it was found that electron-triggered redox catalysis and electric field promoted dehydrogenation. The findings reported in this paper prove the importance of electronic catalysis in explaining the results of single-molecule conductance and provide some basic understanding of electrocatalytic hydrogen production at the single-molecule level, realizing the conversion of electrical energy to chemical energy at the molecular level.

In the field of molecular electronics, the electrostatic field can be applied not only at both ends of the source and drain electrodes but also at the gate to form a field effect transistor at the molecular level. Different from the traditional field effect transistor, the applied gate voltage in the single molecule heterojunction can regulate the electrostatic potential of the molecule, thus changing the energy level of the molecule. This regulation can not only affect the conductance properties of molecules but also provide the vibrational modes, excited states, and vibration-related information of molecules. In addition, for molecular systems with redox activity, the conductance characteristics of molecules in different oxidation states can be studied by applying gate voltage.

D. Thermal activation effect

The core purpose of applying mechanical stress and electric fields is to inject additional energy into the system, thereby promoting the

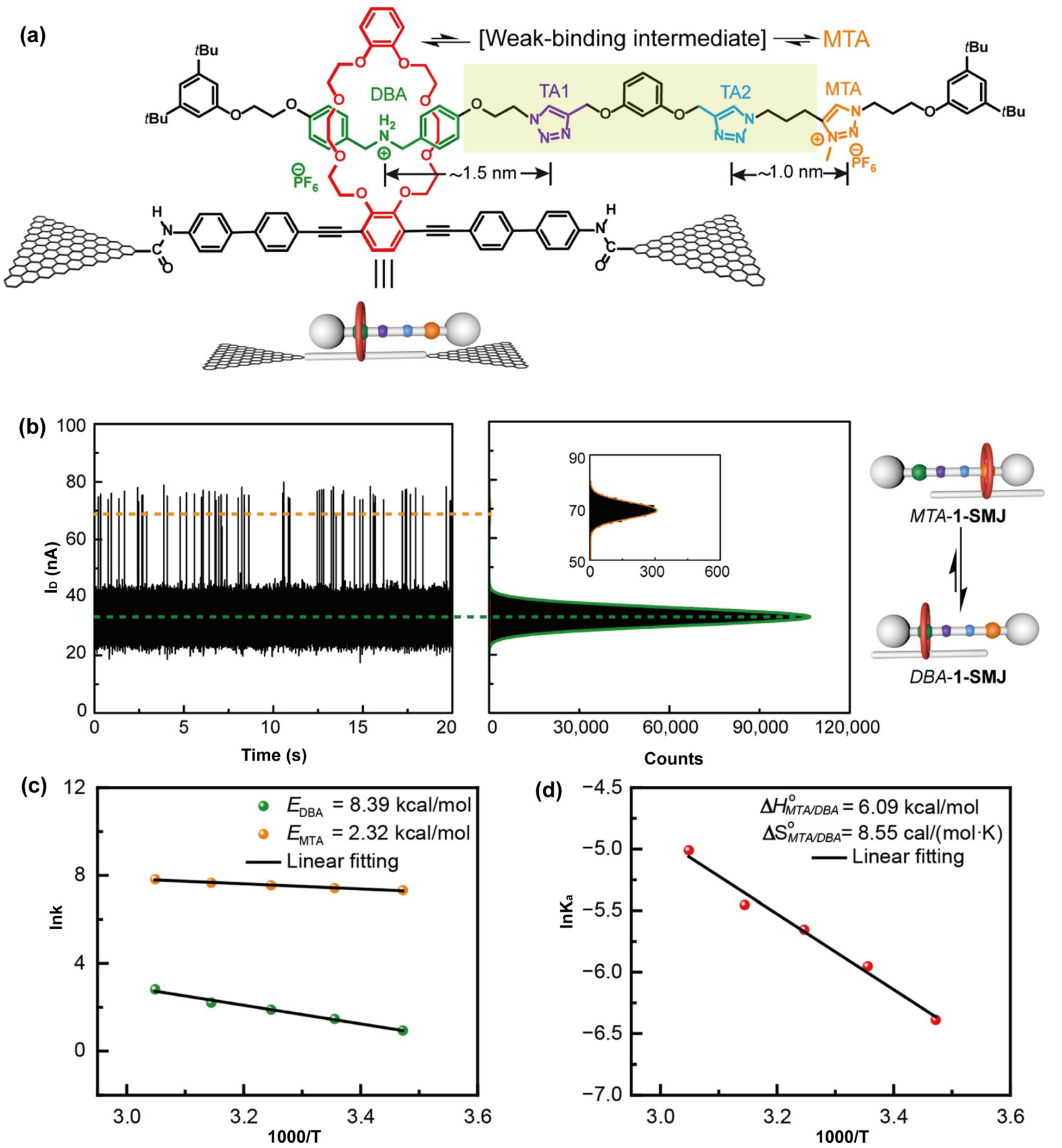

FIG. 32. (a) Chemical structure of 1-SMJ. Molecular shuttle 1 contains DBA and MTA units as the principal binding sites, bridged by a spacer containing two triazole rings (TA1 and TA2) and a 1,3-phenyl diether group. (b) *I*–*t* curve of **1-SMJ** immersed in CH_3CN at 298 K for 20 s with a sampling rate of 57.6 kSa/s. (c) Arrhenius plots of activation energy of both sites (EDBA = 8.39 kcal/mol, EMTA = 2.32 kcal/mol). (d) Plots of the thermodynamics parameters (ln Ka vs 1000/T). Reproduced with permission from Chen *et al.*, Chem **8**, 243 (2022). Copyright 2021 Elsevier.

progression of chemical reactions. Heat, as a form of energy, can also catalyze chemical reactions.[441–446] Among them, the most direct thermal activation method is to adjust the temperature. Excluding the interference of catalysts, the thermal catalytic effect mainly regulates reaction rates by changing the activation energy. The advancement of chemical reactions often requires passing through one or more energetically higher intermediate states, which are called activated states. Increasing the temperature can provide more energy to the reaction system and lower the activation energy of reactants, making it easier for molecules to reach the required energy threshold for the reaction, thereby accelerating the reaction rate.

To the conformational changes in aggregation-induced emission systems, the thermal catalytic effect also plays an important role in promoting the movement of rotaxane molecular motors. Chen *et al.*[447] utilized graphene–molecule–graphene single-molecule junction technology to extensively study the shuttle dynamics of individual rotaxane molecules and explore the kinetics and thermodynamic parameters at different temperatures [as shown in Fig. 32(a)]. They selected the crown ether–dibenzylammonium–triazole system as the research object, which has two crown ether binding sites, namely, the dibenzylammonium moiety (DBA) and the methyl triazole group (MTA). Due to the higher binding affinity of the DBA unit to dibenzo-24-crown-8 (DB24C8) crown ether than the MTA group, the probabilities of the existence of the two conformations DBA-1-SMJ and MTA-1-SMJ may differ. In acetonitrile solvent at 298 K, after performing 20 s of electrical testing on the 1-SMJ device, they found, based on the I–t curve and current distribution histogram, a clear bimodal distribution of current values at 32 and 69 nA in Fig. 32(b). Among these, the Gaussian peak area corresponding to the low-conductance state is much larger than that of the high-conductance state, indicating that the low-conductance state corresponds to the main conformation during molecular shuttling, while the high-conductance state corresponds to a minor conformation. Each transition between high- and low-conductance states represents the shuttle process of the molecular axis within the crown ether ring. Through combined potential energy surface calculations and transmission spectrum calculations in Figs. 32(c) and 32(d), they confirmed that the low-conductance state corresponds to MTA-1-SMJ, and the high-conductance state corresponds to DBA-1-SMJ, which is fully consistent with previous speculations.

They recorded the current–time curves of the 1-SJM device at five different temperatures ranging from 288 to 328 K to explore the influence of temperature on the shuttle process. Experimental results indicate that, at each temperature, the current signals exhibit a bimodal distribution, with the low-conductance state consistently dominating. As the temperature increases, the transition speed between high- and low-conductance states accelerates, and the proportion of the high-conductance state gradually increases. Based on the previous assignment of conductance states, they found that the elevated temperature not only enhances the shuttle rate of the molecule but also increases the proportion of MTA-1-SMJ while the proportion of DBA-1-SMJ slowly decreases. At higher temperatures, the transition between the two states occurs more rapidly, indicating an increased shuttle rate of the DB24C8 macrocycle between the DBA and MTA binding sites. In terms of thermodynamics, the equilibrium constant Ka of the reaction can be represented by the ratio of the concentrations of the high- and low-conductance states.

Temperature not only significantly promotes the motion of molecular motors, but also exhibits a notable activation effect in many classical chemical reactions, such as the Claisen rearrangement and the isomerization of azobenzene. In 2021, Guo *et al.*[448] successfully captured the intermediate state of the Claisen rearrangement reaction at the experimental level and convincingly confirmed the positive effect of temperature on the Claisen rearrangement within the temperature range of 353–373 K. Furthermore, in 2022, Meng *et al.*[64] focused on the isomerization process of azobenzene in MSJs. They thoroughly investigated the close relationship between temperature and the isomerization rate within the temperature range of 115–250 K, revealing that the isomerization rate of the azobenzene components significantly increases with rising temperature. Notably, temperature also plays a critical role in promoting the transition from a closed-shell singlet state to an open-shell triplet state structure. In 2024, Yang *et al.* used a combination of advanced techniques such as variable-temperature proton nuclear magnetic resonance, electron spin resonance (ESR) spectroscopy, multi-temperature real-time current monitoring, and theoretical simulations, systematically demonstrated that as the temperature gradually increases, the transition from singlet to triplet state not only becomes more probable, but also occurs at a significantly faster rate.[446]

V. SPIN-MEDIATED EFFECT IN MSJs

Spin, as an inherent property of electrons, exhibits two states: spin-up and spin-down. In the absence of a magnetic field, these two spin states are degenerate, meaning they possess the same energy. However, when placed in a magnetic field, the degeneracy is broken, resulting in a splitting of the spin states and a difference in the energies of different spin states. Given the crucial role of spin in determining the symmetry of molecular/atomic wave functions, it profoundly influences the structure and functionality of matter. Utilizing single-molecule devices, we can more easily manipulate the spin states of individual molecules, thereby revealing inherent molecular properties, including molecular vibrations and electronic transitions. Moreover, such devices enable us to investigate a range of molecular-scale physical effects such as the spin Seebeck effect,[449–454] the Kondo effect,[455–459] the CISS,[460–463] and the spin MR effect,[464,465] thereby facilitating the conversion and control of electrical, magnetic field, and thermal energy at the single-molecule scale. In addition to the aforementioned, given the inherent energy difference between spin degenerate states and their mutual convertibility, future technological explorations may well concentrate on harnessing the transition between these two states to realize the conversion of spin energy into optical energy, thereby broadening the application prospects of light waves across a wider range of wavelengths.

A. Spin Seebeck effect

The spin thermoelectric effect is a phenomenon that utilizes temperature differences to regulate heat flow, charge flow, and spin flow. Among its key parameters is the spin Seebeck effect.[449,466] Specifically, the spin Seebeck effect describes the unique process of generating spin voltage in a material under the action of a temperature gradient, which can further be converted into an observable electric potential under the influence of the inverse spin Hall effect.[467,468] Compared to traditional thermoelectric effects, the spin Seebeck effect excels in material simplicity and exhibits significant advantages in thermally induced spin voltage generation.[469,470] Therefore, it has shown broad application prospects in various fields such as energy conversion and storage, sensing technology, and information processing.

At the single-molecule scale, in-depth research on the spin Seebeck effect can help us further understand the thermoelectric conversion mechanism and reveal unique phenomena exhibited by individual molecules during the process of thermoelectric conversion, which provides a solid theoretical foundation and technical guidance for the development of more efficient and environmentally friendly thermoelectric materials and technologies.[471] Single-molecule magnets (SMMs), with their remarkable local spin and intrinsic anisotropy characteristics, serve as an ideal platform for studying spin Seebeck effects at the molecular scale under low-temperature conditions.

As early as 2010, Wang *et al.*[472] conducted a thorough study on the thermoelectric effect of SMM junctions in the sequential tunneling region through theoretical methods of formula derivation and parameter. They successfully applied the SMM model to investigate the linear response thermoelectric effect of magnetic molecules in the sequential tunneling region. The research found that, under low-temperature conditions, the intrinsic magnetic anisotropy of SMMs leads to

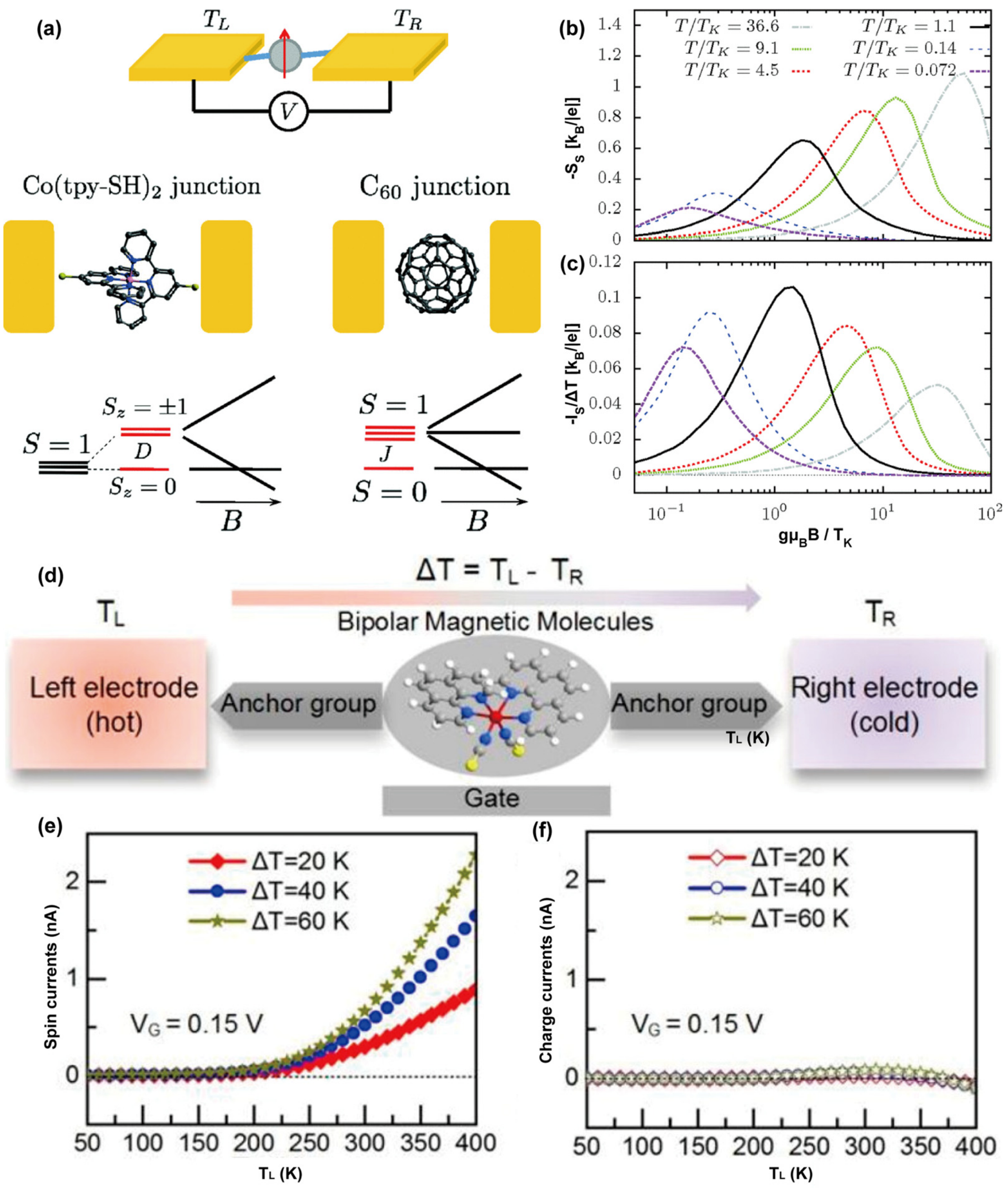

FIG. 33. (a) Schematic representations of the Co(tpySH)$_2$ and C$_{60}$ molecular junctions. (b) Spin Seebeck coefficient S_s and spin current I_s for an isotropic molecule (D = 0); $Ss = S_\uparrow - S_\downarrow$ as a function of the magnetic field for different temperatures. (c) Spin current as a function of $g\mu_B B$ in the zero-charge current condition ($I_c = 0$). Reproduced with permission from Cornaglia *et al.*, Phys. Rev. B **86**, 041107 (2012). Copyright 2012 American Physical Society. (d) a schematic representation of a BMM-based spin thermoelectric device under a gate voltage. The corresponding spin current (e) and charge current (f) vs T_L for different ΔT under gate voltages $V_G = 0.15$ V. Reproduced with permission from Hu *et al.*, Nano. Lett. **23**, 7890 (2023). Copyright 2023 Authors, licensed under a Creative Commons Attribution (CC BY) license.

changes in charge thermopower with the oscillation of gate voltage, which significantly violates the Wiedemann–Franz law (WF law) and exhibits characteristics similar to the Coulomb blockade effect. Even more remarkable is the fact that the spin Seebeck coefficient in SMMs can even exceed its charge Seebeck coefficient, and pure spin thermopower can still be obtained even when the charge thermoelectric effect disappears. This unique spin Seebeck effect is mainly attributed to spin-dependent transitions controlled by spin selection rules closely related to the intrinsic magnetic state. Amazingly, even without an external magnetic field and ferromagnetic electrodes, pure spin thermopower and pure spin current can still be thermally generated by adjusting the gate voltage, opening up new possibilities for spin-thermoelectric conversion technology. In 2012, Cornaglia *et al.*[473] conducted a thorough investigation using gold as the electrode material, exploring the relationships between charge/spin Seebeck effects and temperature, applied magnetic fields, and magnetic anisotropies [as shown in Figs. 33(a)–33(c)]. Utilizing Wilson's numerical renormalization group method, the researchers systematically studied charge and spin Seebeck effects in spin-1 molecular junctions, paying special attention to the interactions of these effects with temperature, applied magnetic fields, and magnetic anisotropies (D). The results shows that the hard-axis magnetic anisotropy significantly enhances the charge Seebeck coefficient Sc (∼kB/lel), whose value is mainly determined by the residual interactions between quasiparticles in the low-temperature Fermi-liquid state. In the unprotected spin-1 Kondo system, the high sensitivity of the system to magnetic fields allows for the observation of significant spin Seebeck coefficient values even when the magnetic field is much smaller than the Kondo temperature. Similar effects have also been observed in C_{60} junctions, where the controlling parameter is no longer magnetic anisotropy (D) but the energy level difference between the singlet and triplet molecular states. By 2023, Hu *et al.*[474] innovatively proposed a design for single-molecule devices based on bipolar magnetic molecules (BMMs), combining density functional theory calculations with non-equilibrium Green's function techniques [as shown in Figs. 33(d)–33(f)]. Due to the unique energy level structure of BMMs, where HOMO and LUMO originate from two different spin channels, thermally induced spin-up and spin-down currents flow in opposite directions. By finely adjusting the gate voltage, the researchers achieved nearly balanced spin-up and spin-down current magnitudes.

Currently, research on single-molecule Seebeck effects is still in its infancy, and there are many technical challenges that need to be overcome. For example, how to stably fabricate single-molecule devices with excellent thermoelectric performance and how to achieve efficient conversion of thermal energy into electrical energy are currently hot and difficult topics in research. Therefore, substantial research efforts are still needed to promote further development and breakthroughs in the practical applications of single-molecule Seebeck effects.

B. Kondo effect

The Kondo effect manifests macroscopically as the emergence of extremely low resistance at low temperatures when a small amount of magnetic impurities exist in crystalline metals.[475,476] In microscale devices, the Kondo effect serves not only as a crucial criterion for determining the presence of spin in devices, such as identifying unpaired electrons in radicals and metal complexes, but also as a primary means to optimize the performance of spin devices. In single-molecule devices exhibiting the Kondo effect, the spin electrons within the molecule strongly couple with the conduction electrons in the device, resulting in a significant increase in electrical conductivity. This anomalous increase is more pronounced in molecules with stronger Kondo effects, where the energy difference between high and low spin states is greater, providing an important basis for screening the performance of subsequent spin devices. The prominence of the Kondo effect can, to a certain extent, reflect the energy differences between spin states, thereby providing a clear direction for material optimization in the processes of energy conversion and storage resulting from spin state transitions. Furthermore, this can be controlled by adjusting external magnetic fields and ambient temperatures to find the optimal operating conditions for spin devices, thereby exploring their potential applications in nanoelectronics and quantum information processing.

The idealized version of the Kondo effect model is the Anderson single-level impurity model. In this model, electrons with a nonzero net spin are placed on a specific energy level, labeled as ε0.[477] The model assumes that orbitals below this energy level are completely filled with electrons, while orbitals above it remain empty. When ε0 is below the Fermi level of the electrodes, an unpaired electron is captured and hops from the molecule to the electrode, while an electron from the other electrode fills the vacancy left on the molecule. This newly hopped electron can have either spin-up or spin-down. The superposition of multiple such tunneling events leads to the screening of the local spin, resulting in the Kondo effect. In single-molecule devices, the tunneling phenomenon of a single magnetic site dominates the transport properties of the device. At this point, the enhanced scattering is primarily manifested as forward scattering, which effectively connects the state densities of the source and drain electrodes, thereby increasing the conductance accordingly.

There are two main methods to introduce electrons with a nonzero net spin: one is through the inherent net spin characteristics of the molecule itself, and the other is to introduce additional electrons using electrochemical means. The properties of the molecule itself, especially the carried radicals and spin electrons, play a crucial role in this process. In 2015, as shown in Fig. 34(a), Frisenda *et al.*[478] studied the perchlorotriphenylmethyl radical molecule under low-temperature conditions confirmed the insensitivity of the Kondo anomaly effect in solid-state devices to mechanical stress and static conditions. Both experimental data and theoretical calculations indicate that the Kondo effect originates from the local orbitals in the radicals. Building on this foundation, in Fig. 34(b), Mitra *et al.*[479] further studied the interaction between the charge transport properties and magnetic field of the perchlorotriphenylmethyl radical structure with the Kondo effect through magnetic field control, namely, the magnetoresistance effect. The current-bias characteristics of the molecular junction exhibited a distinct zero-bias anomaly. Notably, molecular structures without the Kondo effect exhibited stronger magnetoresistance (MR), suggesting an inverse correlation between magnetoresistance and the Kondo effect. The cause of high magnetoresistance involves interference effects from spin-dependent scattering at the metal–molecule interface, while the Kondo effect is caused by unpaired spins at the center of asymmetric molecular configurations. Electrochemical methods provide another approach to introduce multiple extra electrons. In 2016, Manso *et al.*[480] utilized the MCBJ technique to study the redox-active indolyl-extended tetrathiafulvalene (IF-TTF) molecule [as shown in Fig. 34(c)]. Through the gating device, the molecule is charged to generate a radical cation with a nonzero net spin. This study discovered a repeatable Kondo effect (zero-bias conductance), which was directly attributed to the existence of the net spin. These studies not only deepen our understanding of the Kondo effect but also provide new ideas for the design and application of future single-molecule devices.

Through in-depth research on the Kondo effect in single molecules, we can gain a deeper understanding of the complex interaction mechanisms among spin electrons, magnetic moments, transport orbitals, and excited state transition orbitals. This not only contributes to advancing the collection and utilization of spin state transition energy but also provides experimental and theoretical support for controlling spin qubits. By precisely manipulating these interactions, future research on energy conversion is poised to make new breakthroughs, expanding its potential applications in photovoltaics, quantum information processing, and other advanced technologies.

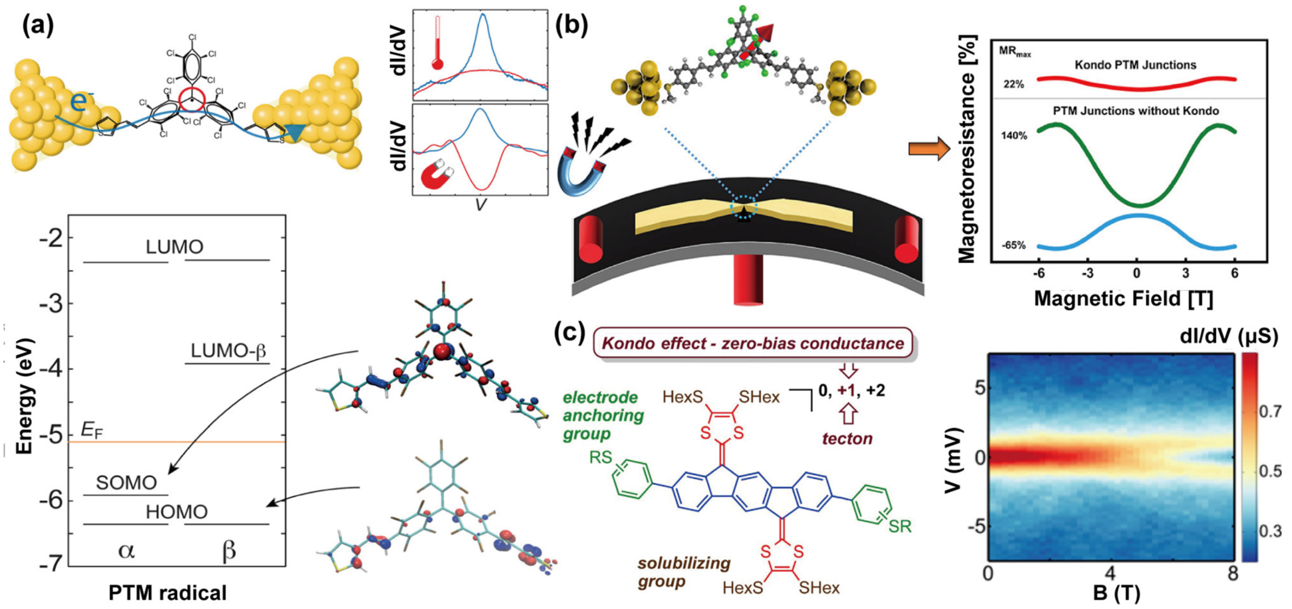

FIG. 34. (a) Top panel: the ideal arrangement of the molecular junction and the dI/dV traces for temperature and the magnetic field; Bottom panel: energy level diagram for the two spin channels α and β of the PTM-radical molecule. Reproduced with permission from Frisenda *et al.*, Nano Lett. **15**, 3109 (2015). Copyright 2015 Authors, licensed under a Creative Commons Attribution (CC BY) license. (b) Left panel: Schematic of the MCBJ setup and the structure of PTM radical molecule; Right panel: MR measurements on different SMJs of PTM measured at 4.2 K with an applied bias of 30 mV, and categorized with respect to the presence or absence of a Kondo peak. Reproduced with permission from Hayakawa *et al.*, Nano Lett. **22**, 5773 (2022). Copyright 2022 Authors, licensed under a Creative Commons Attribution (CC BY) license. (c) Schematic representations of IF-TTFs and d*I*/d*V* map (taken at Vg = 6 V and T = 2.2 K) as a function of the magnetic field of the zero-bias peak. Reproduced with permission from Manso *et al.*, J. Org. Chem. **81**, 8406 (2016). Copyright 2016 Authors, licensed under a Creative Commons Attribution (CC BY) license.

C. Chirality-induced spin selectivity effect

Spin polarization, referring to the ordered arrangement or bias of electron spins in a specific direction, hinges on the inherent "internal rotation" property of electrons, namely, their up-spin and down-spin states. This polarized current can be precisely induced in specific materials through external conditions such as magnetic or electric fields, exhibiting significant potential for applications in magnetic memory, spintronics, and magnetic sensors due to its unique directionality. Moreover, spin polarization is closely intertwined with emerging technologies like quantum computing, underscoring the pivotal role and profound impact of the discontinuous and splitting characteristics of electron spins in scientific research and technological innovation. CISS serves as an effective means to achieve spin polarization at the microscopic level, holding significant applications and research value in magnetic materials, spintronics devices, and quantum information processing. The CISS refers to the ability to achieve spin polarization through the interaction between chiral molecules and spins without the need for external magnetic fields or doping with heavy metals.[460,461] Since the discovery of the CISS effect, chiral molecules and chiral nanostructures have gradually emerged in the fields of organic electronics and organic spintronics devices.[462,463] Due to the inherent electron–phonon (e–ph) coupling within organic molecules, trapped charge carriers and excited states exhibit unique charge-spin relationships. Therefore, chirality plays a crucial role in physical properties such as magnetism[461,481] or conductivity.[482–484]

The introduction of chirality will undoubtedly have a profound impact on the performance regulation of organic photoelectric devices. As early as 2011, Xie *et al.*[485] studied double-stranded DNA molecules using CPAFM technology to inject polarized electrons into molecular junctions and conducted a thorough analysis of their I–V characteristic curves [Fig. 35(a)]. Experimental results show that the polarization of electrons has a significant influence on molecular conductivity. When polarized electrons are transported through chiral structures, their direction is regulated by an external electric field, demonstrating the potential application of chiral spin selectivity in organic spin filters. Notably, when polarized electrons are transported in chiral structures, they exhibit different spin-filtering effects depending on their polarization direction, resulting in distinct spin current selection characteristics. In addition to chiral DNA structures, chiral amino acids and chiral peptides also exhibit similar current selection properties [Figs. 35(b) and 35(c)].[486] Although strong spin polarization has been observed in numerous chiral organic compounds and biomolecules, the physical origin of CISS that produces high spin polarization, namely, the complex relationship between chiral structures and electron spins, remains an unresolved puzzle.

The CISS effect grants the ability to manipulate and control spintronic interfaces, eliminating the need for permanent ferromagnetic layers and thereby advancing the development of streamlined nanostructures and high-power-efficiency spintronic devices. Notably, through the spin-selective electron transport mechanism of chiral molecules, efficient local spin currents can be generated even at room temperature, making these molecules exceptional spin filters. In the frontier exploration of MSJs, logic memory devices based on the CISS effect are particularly noteworthy, showing revolutionary potential.

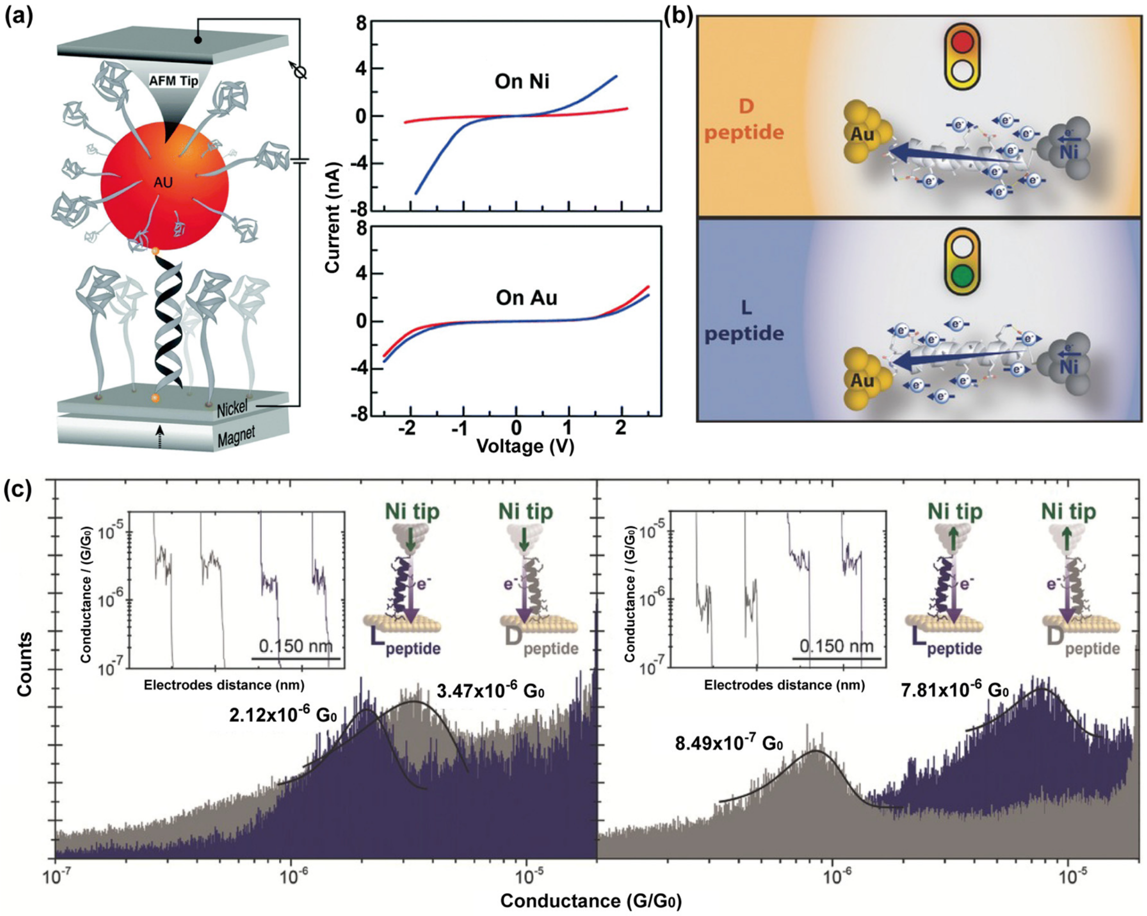

FIG. 35. (a) Left panel: the experimental setup; Right panel: Current vs voltage curves for long DNA oligomers adsorbed on Ni and gold. Reproduced with permission from Xie *et al.*, Nano Lett. **11**, 4652 (2011). Copyright 2011 Authors, licensed under a Creative Commons Attribution (CC BY) license. (b) Sample bias voltage (defined as sample minus tip voltages) is positive for the L-peptide, meaning the electrons flow from the Ni to the Au electrodes, while negative for the D-peptide. (c) Semilog conductance histograms for the dextrorotatory and levorotatory α-22AA-peptides under spin down (left) and up (right) Ni magnetic polarizations. Reproduced with permission from Aragonès *et al.*, Small **13**, 1602519 (2016). Copyright 2016 Wiley.

In the field of logic storage, the CISS effect presents two highly promising application branches: electric memory[487] and optical memory.[488] In these advanced devices, the switching of magnetization states cleverly relies on the injection of spins and the extraction of opposite spins. This mechanism triggers the generation of total spin transfer torque in logic devices, allowing precise control of electron spin direction through an external magnetic field, thereby effectively regulating the total resistance. The CISS effect not only opens up a new pathway for efficient energy storage and conversion, but also profoundly reveals the fundamental physical laws underlying the intrinsic relationship between electron spin and molecular chirality.

D. Magnetoresistance effect

The MR effect refers to the physical phenomenon where the resistivity of a system containing spin electrons changes correspondingly under the influence of a magnetic field.[464,465] The MR effect is not only an important tool for studying the behavior of spin electrons but also a key technology for developing new magnetic materials and devices. Its application potential covers a wide range of fields from magnetic storage to magnetic sensors. The magnitude of the magnetoresistance effect allows us to measure the sensitivity of spin electrons in the spin system to external magnetic fields, thereby exploring and optimizing materials suitable for magnetic storage devices. In addition, the magnetoresistance effect can be used to achieve electrical conductivity control under magnetic field conditions. By adjusting the strength and direction of the external magnetic field, the resistance of devices can be effectively controlled, thereby influencing the voltage across the device terminals and the current within the device. This provides new insights and methods for the design of magnetic sensors and other energy conversion and storage devices. Typically, magnetoresistance is expressed as the percentage difference between resistance without a magnetic field and resistance with an applied magnetic field.

As shown in Figs. 36(a) and 36(b), Aragonès *et al.*[489] conducted spin-dependent single-molecule charge transport studies using [M(tzpy)$_2$(NCSe)$_2$] (where M is Mn, Co, or Ni) as the core structure, with

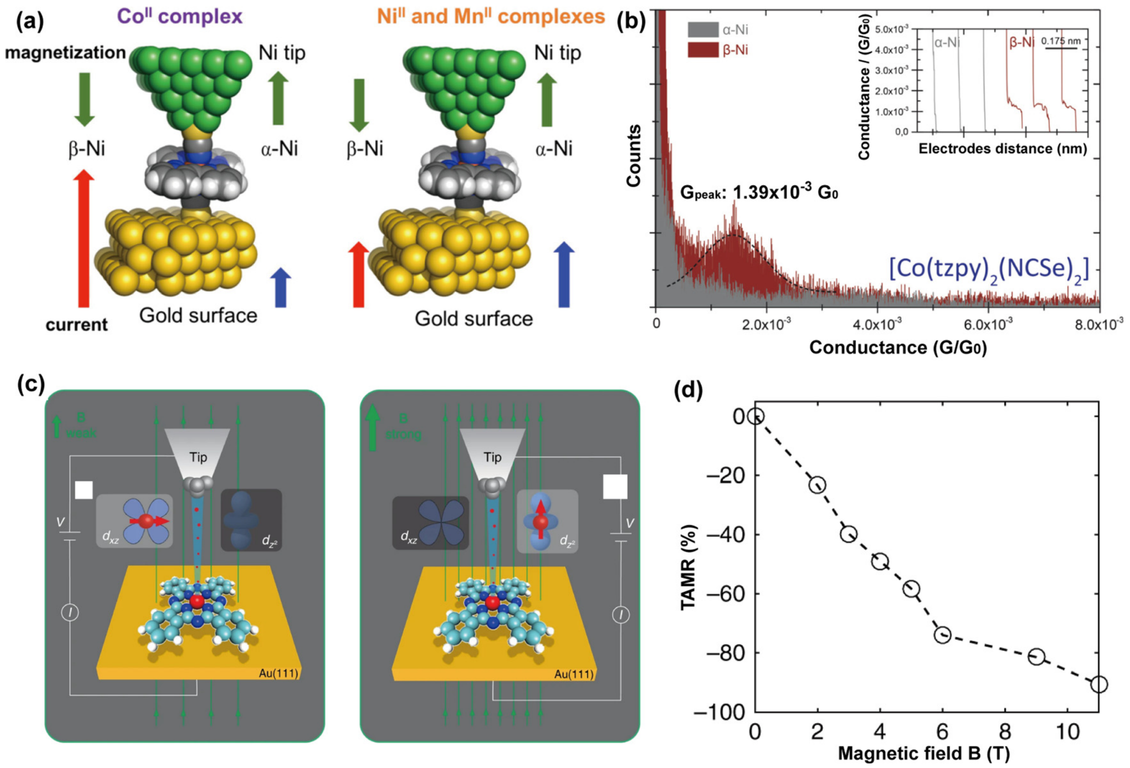

FIG. 36. (a) Schematic representation of the single-molecule devices studied under two opposite Ni tip magnetic polarizations (green arrows, labeled α and β). (b) Single-molecule conductance histogram for the metal complexes: S = 3/2 [Co(tzpy)$_2$(NCSe)$_2$]. Reproduced with permission from Aragonès *et al.*, J. Am. Chem. Soc. **139**, 5768 (2017). Copyright 2017 Authors, licensed under a Creative Commons Attribution (CC BY) license. (c) Schematics of the electron transport process through an FePc molecule adsorbed on an Au(111) surface at different magnetic fields. (d) TAMR values at different magnetic fields calculated from the d*I*/d*V* spectra taken on the Fe center at the bias voltage of −1.06 mV. Reproduced with permission from Yang *et al.*, Nat. Commun. **10**, 3599 (2019). Copyright 2019 Authors, licensed under a Creative Commons Attribution (CC BY) license.

a gold electrode as the source electrode and a magnetically polarized Ni electrode as the spin-polarized drain electrode. They found that when Co was chosen as the metal core of the molecular structure, conductivity was only measured under a β-polarized Ni electrode, while the conductivity value under an α-polarized Ni electrode was below the detection limit of the testing technology. Given that Co, Ni, and Mn all have unpaired electrons, this difference in conductivity may be attributed to the electronic structural characteristics of different metal ions. Theoretical simulations reveal that for the Co complex, its $t_{2g}^{5}e_{g}2$ electronic configuration provides efficient spin-selective channels. Compared to the highest occupied αeg orbital, the lowest unoccupied βt_{2g} orbital is closer to the Fermi level. Additionally, the broadening of the energy levels between the two orbitals also demonstrates hybridization effects with other metal electrode orbitals. Therefore, this molecular system exhibits higher measured conductivity through the β-orbital channel of the single-molecule junction. Building on this foundation, in Figs. 36(c) and 36(d), Yang *et al.*[490] further studied iron phthalocyanine. By analyzing the linearity and spatial distribution characteristics of the Kondo resonance in FePc, they demonstrated that in single-molecule devices, electronic pathways can be selected between the dπ and dz2 molecular orbitals by adjusting the magnetic field, achieving a tunable anisotropic magnetoresistance of up to 93%. The TAMR effect shown in the figure clearly illustrates the dependence of magnetoresistance on magnetization orientation and reveals a monotonic increase in magnetoresistance as the magnetic field approaches zero bias.

In addition to the significant magnetoresistance response exhibited by magnetic molecules in a magnetic field, the combination of magnetic electrodes with non-magnetic molecules can also induce substantial magnetoresistance effects. In 2015, Li *et al.*[491] ingeniously employed a jump-to-contact STMBJ technology, applying an externally controlled magnetic field (either parallel or perpendicular to the electron transport path) to precisely measure the charge transport performance of Fe–terephthalic acid (TPA)–Fe molecular junctions. Remarkably, the team observed a significant magnetoresistance effect exceeding 53% at room temperature, which was attributed to the unique electronic coupling mechanism at the Fe–TPA–Fe interface. Building on this groundbreaking research, Li *et al.*[492] continued to use this technique in 2021 to further explore the differences in magnetoresistance effects between aliphatic and conjugated dicarboxylic acids. For the aliphatic dicarboxylic acid system, it demonstrated insensitivity to changes in molecular length and achieved a magnetoresistance effect of up to 44%, highlighting the potential of such molecules in magnetoresistance applications. In contrast, the conjugated dicarboxylic acid system, while exhibiting only half the magnetoresistance effect of the aliphatic system, showed an intriguing trend: the magnetoresistance effect slightly increased with the length of the molecule, offering new insights and directions for tuning magnetoresistance performance through molecular design.

VI. VIBRATION EFFECT IN MSJs

The law of energy conversion and conservation is a fundamental physical principle. It exists not only in various physical phenomena in the macroscopic world, but also extends into the interactions between minute particles in the microscopic world, such as the vibration of atoms and the transition of electrons. Among these forms, vibration stands as a crucial and fundamental element, understood as the periodic oscillation of particles within matter at precise frequencies. When these particles are influenced by external forces, they transition from their ground state to higher energy vibration states, a process known as vibration excitation. This excitation not only injects additional energy into matter but also can induce significant changes in its properties and behavior. For the chemistry, the excitation of molecular vibrations is closely linked to the rate and pathway of chemical reactions. Specifically, the coupling of vibrations between molecules and electrodes, as well as the vibration states of molecules themselves, significantly influences the fluctuations in conductivity. On the one hand, this vibration coupling optimizes paths for charge transfer, reducing energy losses and enhancing energy conversion efficiency. On the other hand, changes in molecular vibration states affect the electronic structure of molecules, further modulating reaction kinetics and optimizing the energy conversion process. A deep understanding and precise control of molecular conductivity fluctuations and vibration effects are crucial for developing more efficient and stable energy conversion systems. This not only advances the rapid development of clean energy technologies but also provides a solid scientific foundation for innovating future energy utilization methods. The study of the vibration effect is of great significance for revealing the comprehensive physical information of a single molecule and realizing the functionalization of single-molecule optoelectronic devices.[493] The relationship between vibrational modes and charge transport properties is actually the conversion between vibrational energy and electrical energy. The vibrational effect typically refers to how the vibration of molecules or atoms at the microscopic level affects their physical and chemical properties. Research in this field spans across multiple disciplines, including spectroscopy,[494–496] thermodynamics,[497,498] and chemical reactions,[499] playing a pivotal role in deepening our understanding and predicting the properties and behaviors of substances. In single-molecule structures, the vibrational effect specifically manifests when molecules within the structure vibrate in response to energy inputs such as electrical, optical, or thermal energy. This vibration leads to subtle changes in the structure of the molecule, ultimately affecting the properties of charge transfer within the molecule structure.

A. Electro-induced vibrational effect

Under the external electric field, when energetic electrons are injected into a molecular structure, the resulting vibrational effect is commonly referred to as the electro-induced vibrational effect. The inelastic electron tunneling refers to the process where electrons with sufficient energy transfer part of their energy to the molecule during tunneling, thereby exciting molecular vibrations or inducing processes such as electron spin flipping.[500,501]

Kumagai *et al.*[502] utilized STM to focused particularly on the pivotal role of vibrational effects in the mutual isomerization reactions of individual hydrogen atoms within porphyrin molecules on the Cu (110) surface as shown in Fig. 37. They not only induced and verified it through inelastic electron tunneling spectroscopy at a temperature of 5 K but also delved into how specific molecular vibrational excitations influence this reaction process. By precisely positioning the STM probe on hydrogen atoms within the porphyrin molecule cavity and monitoring real-time changes in molecular tunneling currents, they successfully achieved real-time observation of vibration-induced mutual isomerization reactions. Experimental results show that the transfer of hydrogen atoms correlate closely with molecular vibrations, leading to random telegraph noise between two conductive states. Each current jump corresponds to an independent isomerization process driven by molecular vibrational excitations.

Furthermore, the study reveals that under different biases, the mutual isomerization rates exhibit a power-law relationship $R \sim IN$ between current and voltage, where N is closely related to the number of electrons involved in tunneling. When the bias exceeds 275 mV, N approached 1, indicating that the reaction is predominantly governed by single-electron processes. As biases decrease to 250 and 200 mV, N values increase to 1.35 and 1.67, respectively, reflecting the intersection of single-electron and double-electron processes. This crossover phenomenon reveals that under low bias conditions, insufficient energy transfer might hinder vibration-induced mutual isomerization reactions, necessitating the involvement of multi-electron processes. Therefore, vibrational effects play a crucial role in these reactions, influencing both reaction rates and specific mechanisms.

The results of deuterium-substituted isotopes provide a more detailed understanding of the isomerization mechanism. It has been confirmed that such mutual isomerization processes occur through the excitation of the N–D stretching mode within the molecular cavity. Additionally, based on the analysis of dI/dV conductance spectra of individual H-porphyrin and D-porphyrin molecules, they found characteristic peaks and valleys at 175 and 380 mV for H-porphyrin molecules and a characteristic valley at 284 mV for D-porphyrin molecules under two positive biases. The voltage ratio of these two valleys (1.34) matches the simple ratio of N-H and N–D reduced mass, further supporting the origin of such mutual isomerization. It is noteworthy that the peak at 175 mV aligns with the initial value of STM-induced mutual isomerization, and this process does not exhibit a pronounced isotope effect. Therefore, this peak cannot be simply attributed to a single vibrational mode but should consider multiple influencing factors, including in-plane vibrations of N and H atoms. This discovery provides a new perspective for understanding the isomerization process in porphyrin molecules.

B. Thermally induced vibrational effect

Temperature is one of the key parameters affecting the structure of molecules. With temperature variations, specific molecular vibrations are excited, thereby fine-tuning their structures and significantly influencing the charge transport capabilities and mechanisms of molecular junctions. These thermally induced vibrations not only lead to subtle adjustments in molecular structure but also alter the effective pathways and rates of charge transport. Within molecular structures, changes in vibrations can induce electron localization or dissociation, thereby affecting the conductivity and transport mechanisms of the

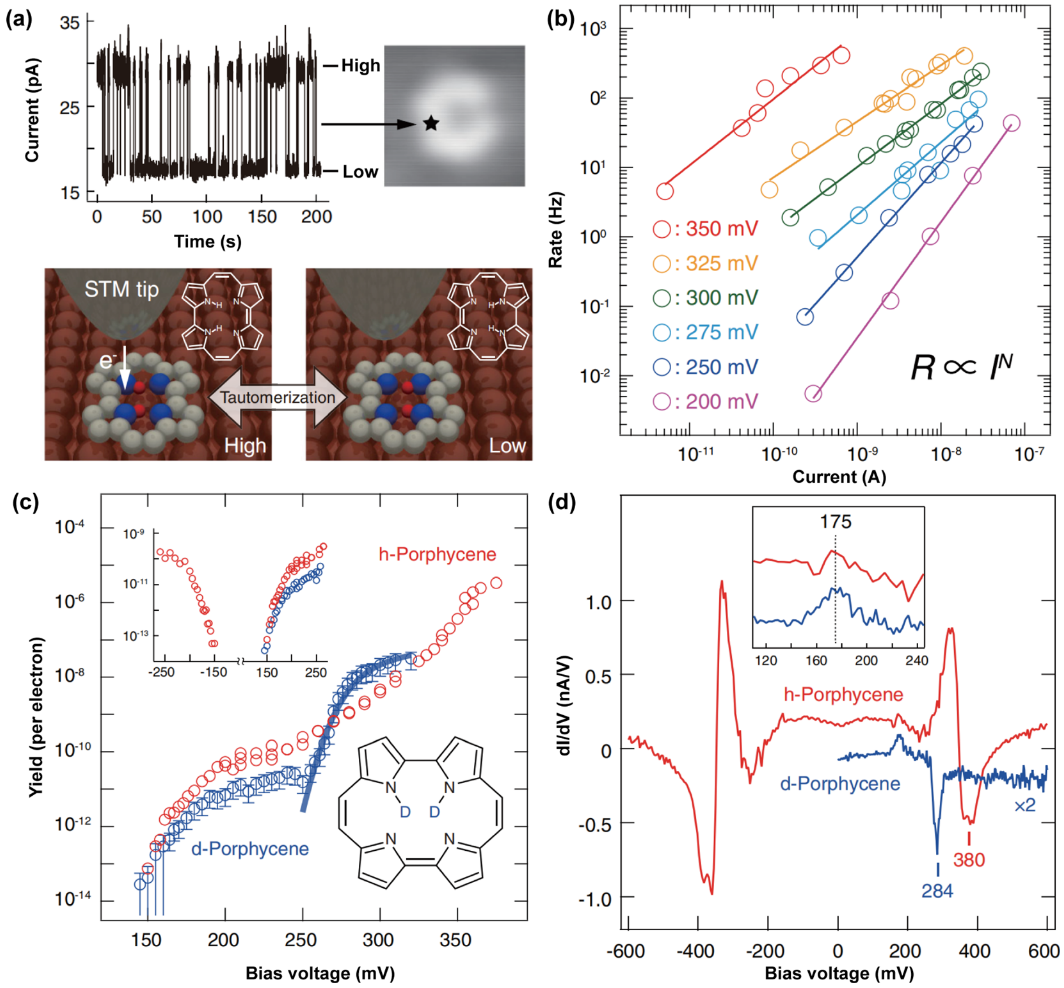

FIG. 37. (a) A typical current trace during a voltage pulse of 300 mV while the STM tip is fixed over a molecule (indicated by the black star in the image) with gap conditions of 100 mV and 10 pA; and the schematics of the tautomerization process. (b) Current dependence of the tautomerization rate at various bias voltages. (c) Voltage dependence of the tautomerization yield for h- (red circles) and d-porphycene (blue circles) at 5 K (the latter is sketched in the inset). (d) dI/dV conductance spectra of single h- and d-porphycene molecules. Reproduced with permission from Kumagai *et al.*, Phys. Rev. Lett. **111**, 246101 (2013). Copyright 2013 American Physical Society.

molecules. Therefore, understanding and controlling the temperature effects in molecular structures are crucial for designing efficient molecular electronic devices.

The rotation of the benzene ring and substituent along a fixed axis within a molecule is a relatively typical example of thermodynamic vibration. Yang *et al.*[503] utilized graphene–molecule–graphene single-molecule junctions as a platform to investigate the stereochemical dynamic effects induced by thermodynamic vibration at the single-molecule level as shown in Fig. 38. Through molecular engineering design, they synthesized derivatives based on tetraphenylethene (TPE) and embedded them into the nanogaps of graphene electrodes via covalent amide bonds, successfully constructing graphene single-molecule junctions. To more accurately study the influence of temperature on intramolecular double bond twisting and benzene ring rotation, they chose the TPE-2A molecule as the research object and obtained its current state at different temperatures ranging from 10 to 80 K in Fig. 38(a). In Fig. 38(b), experimental results show the existence of two conductive states (state 1 and state 2) in the I–t curve, attributes to the transition between quasi-planar and perpendicular conformations induced by double bond rotation. This rotation is attributed to the thermodynamic vibration effect, resulting in the dynamic transition between quasi-planar configuration and perpendicular configuration.

At each temperature, these two states are accompanied by small, sustained current fluctuations, reflecting the rotational activity of TPE benzene rings. As shown in Figs. 38(c) and 38(d), by analyzing the dwell time histograms and current distribution histograms, the average lifetimes of each conductive state and the proportions of the two states can be calculated. As the temperature increases, the average lifetimes of state 1 and state 2 both decrease. However, higher temperatures also promote the transition of molecules to quasi-planar conformations, as evidenced by the proportion of state 2 increasing significantly from

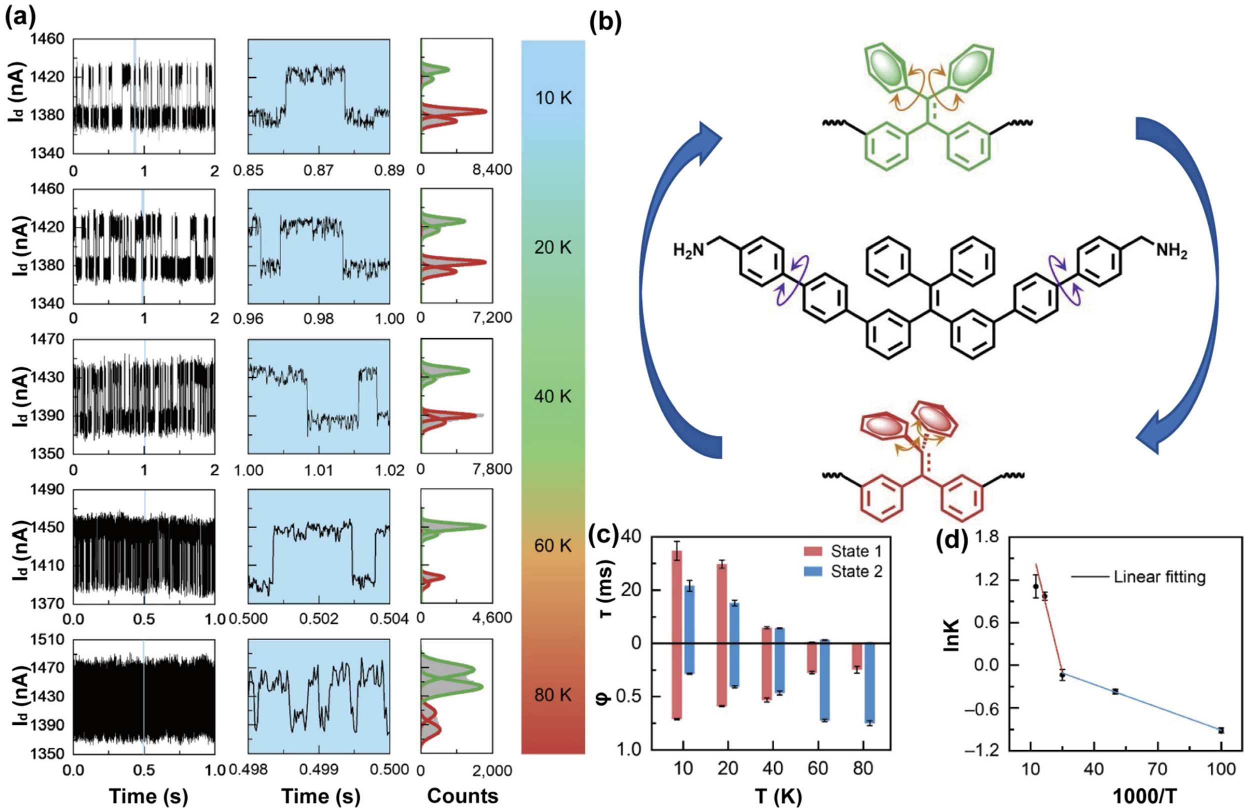

FIG. 38. (a) Effects of temperature on quasi-C=C bond twisting I − t curves, corresponding enlarged I − t curves marked in blue, and corresponding histograms of the device connected with TPE-2A at different temperatures. (b) Schematic diagram of the main transformation process. (c) Lifetime and occurrence proportion changes of State 1 (red) and State 2 (green) at different temperatures. (d) Plots of the thermodynamic parameters (ln*K* vs 1000/*T*) deduced from temperature-dependent measurements. Reproduced with permission from Yang *et al.*, Matter **5**, 1224 (2022). Copyright 2022 Elsevier.

28.6% to 75.2%, indicating that elevated temperatures favor the stabilization of quasi-planar conformations.

Transitioning from state 1 to state 2, two straight lines were obtained by linear fitting of the equilibrium constants ln*K* at different temperatures. The fundamental reason for the fitted two straight lines lies in the antagonistic and balanced relationship between double-bond twisting and benzene ring rotation. This study demonstrates that increasing temperature can enhance the vibrational effect of the tested molecule, reduce its activation energy, accelerate the isomerization process of the double bond, and promote the stabilization of the molecule in a planar configuration.

In addition to causing structural transitions by reducing the activation energy of molecules, thermodynamic vibration effects can also affect their charge transport mechanisms. Zhu *et al.*[504] successfully constructed graphene supramolecular structures based on dimers, combining cucurbituril as the host molecule with amino-terminated compounds M1, M2, and M3 as guest molecules as shown in Fig. 39(a). They not only extensively explored the influence of charge states and energy level distributions on charge transport in nanogap molecular junctions but also deeply verified the crucial role of thermally induced vibrations in the charge transport process.

When the temperature increased from 10 to 300 K, the currents of the three molecular junctions all exhibited significant growth in the high-temperature region while showing a slow upward trend in the low-temperature region [shown in Fig. 39(c)]. Particularly, for the positively charged SMJ-1, its conductance increases by approximately 6 times at 1 V within the 10–300 K range, whereas the conductivity of neutral SMJ-1 only increases by about three times. To further analyze the charge transport mechanisms within the molecular junctions, they conducted a detailed analysis of the I–V curves. The analysis results reveal that the presence of positive charges enhanced the dependence of the molecular junctions on bias, possibly because the charge transport process in the positively charged system was more sensitive to changes in bias. Using the Arrhenius formula, the researchers further elucidated the transition process of charge transport in the dimer system, transitioning from temperature-independent coherent transport at low temperatures to thermally activate incoherent transport at high temperatures. For the positively charged (SMJ-1), neutral (SMJ-2), and weakly conjugated (SMJ-3) cases, their transition temperatures were 92, 122, and 64 K, respectively, with these transition temperatures showing less dependence on bias as shown in Fig. 39(d). The calculated molecular vibrational energies in Fig. 39(e) are consistent with the thermal energies of the experimental transition temperatures.

As can be seen from the molecular rotation barrier depicted in Fig. 39(f), it not only reveals that thermal vibration effects have the ability to excite the rotation of pyridine rings even under

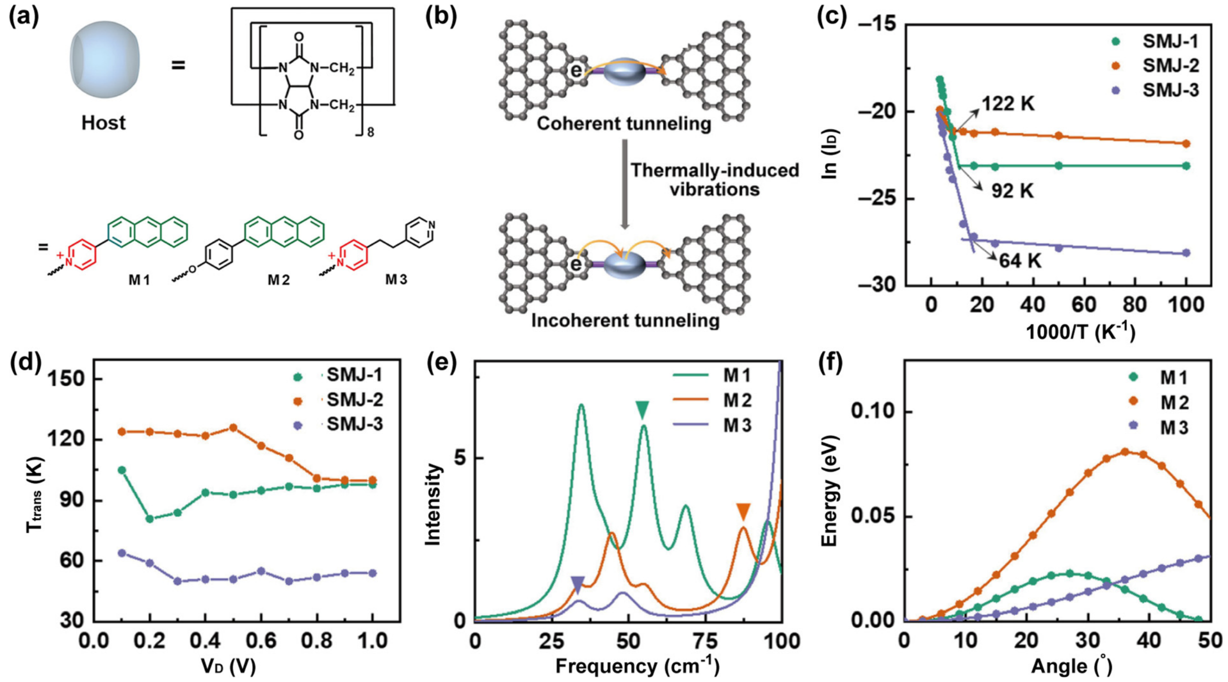

FIG. 39. (a) Structural formula of host and guest molecules. (b) Schematic mechanism of the charge transport transition. (c) Arrhenius plots of ln (I_D) vs 1/T at 0.1 V with marked transition temperatures. (d) Transition temperatures of the charge transport transition under different bias voltages. (e) Calculated vibration spectra of M1, M2, and M3. (f) Potential energy as a function of the rotation angle of the phenyl rings for M1, M2, and M3. Reproduced with permission Zhu *et al.*, from Angew. Chem., Int. Ed. **61**, e202210939 (2022). Copyright 2022 Wiley.

low-temperature conditions, but also further indicates that molecular rotation will lead to significant changes in charge transport mechanisms.

Whether it is the subtle transformation of molecular structure or the dynamic change in charge transport mechanism, they are closely linked to the flow and transformation of energy within molecular structures. An in-depth study of the thermodynamic vibration effect of single molecules helps us to better understand the mechanisms of energy storage and release at the molecular level, thus uncovering the core processes of energy conversion and optimizing energy conversion efficiency. This exploration lays a solid foundation for the research of novel nanomaterials.

C. Terahertz-induced vibrational effect

Due to its high penetrability, low energy, and strong spectral resolution, terahertz (THz) light has become a powerful tool for studying the vibrational dynamics of various molecules.[505–507] Due to the sub-nanometer gap separation between the source and drain, they can act as THz antennas, focusing THz radiation and even concentrating it on individual molecules. Additionally, due to the plasmonic effect of the metal electrodes, the THz field induced by THz light in the nanogap is enhanced tenfold. Therefore, single-molecule transistor-like structures are ideal platforms for studying THz light-induced vibrational dynamics. Du *et al.* obtained THz spectra related to single fullerene molecules and THz-induced molecular center-of-mass oscillations from time-domain THz autocorrelation measurements using a single-molecule transistor model, as shown in Fig. 40.[508]

The time-domain THz autocorrelation measurement,[509,510] as shown in the Fig. 40(a), refers to splitting the laser beam into two parts, generating femtosecond laser pulses, continuously pumping the InAs chip surface, thereby generating time-correlated THz double pulses. By recording the function relationship between the photocurrent induced by THz double pulses and the time interval between the two THz pulses, the photocurrent interference pattern induced by THz radiation in the single-molecule transistor can be obtained. Figure 40(b) shows the color-coded differential conductance map of the device, proving the successful capture of single molecules in the nanogap. The advantage of using a single-molecule transistor is that the molecular electrostatic potential and the number of electrons can be precisely controlled by gate voltage. As shown in Fig. 40(c), they irradiated the sample with THz pulses, measured the time-averaged THz-induced photocurrent, and obtained the photocurrent as a function of gate voltage V_G. When applying gate voltage with the same peak photocurrent, the interference pattern of the THz-induced photocurrent of C_{60}SMT can be obtained as shown in Figs. 40(d) and 40(e). By calculating the Fourier spectrum of the interference pattern, the THz spectrum of C_{60}SMT can be obtained. In Fig. 40(f), the waveform in the THz spectrum can be decomposed into two oscillation components: 2 meV (500 GHz) (blue curve) and 4 meV (1 THz) (green curve). The oscillation of the 4 meV component is clearly visible in the photocurrent waveform, especially around 1 ps. Similar characteristic peaks are also observed in the embedded fullerene Ce@C_{82} structure shown in Fig. 40(g). In the THz spectrum test, molecular vibrations

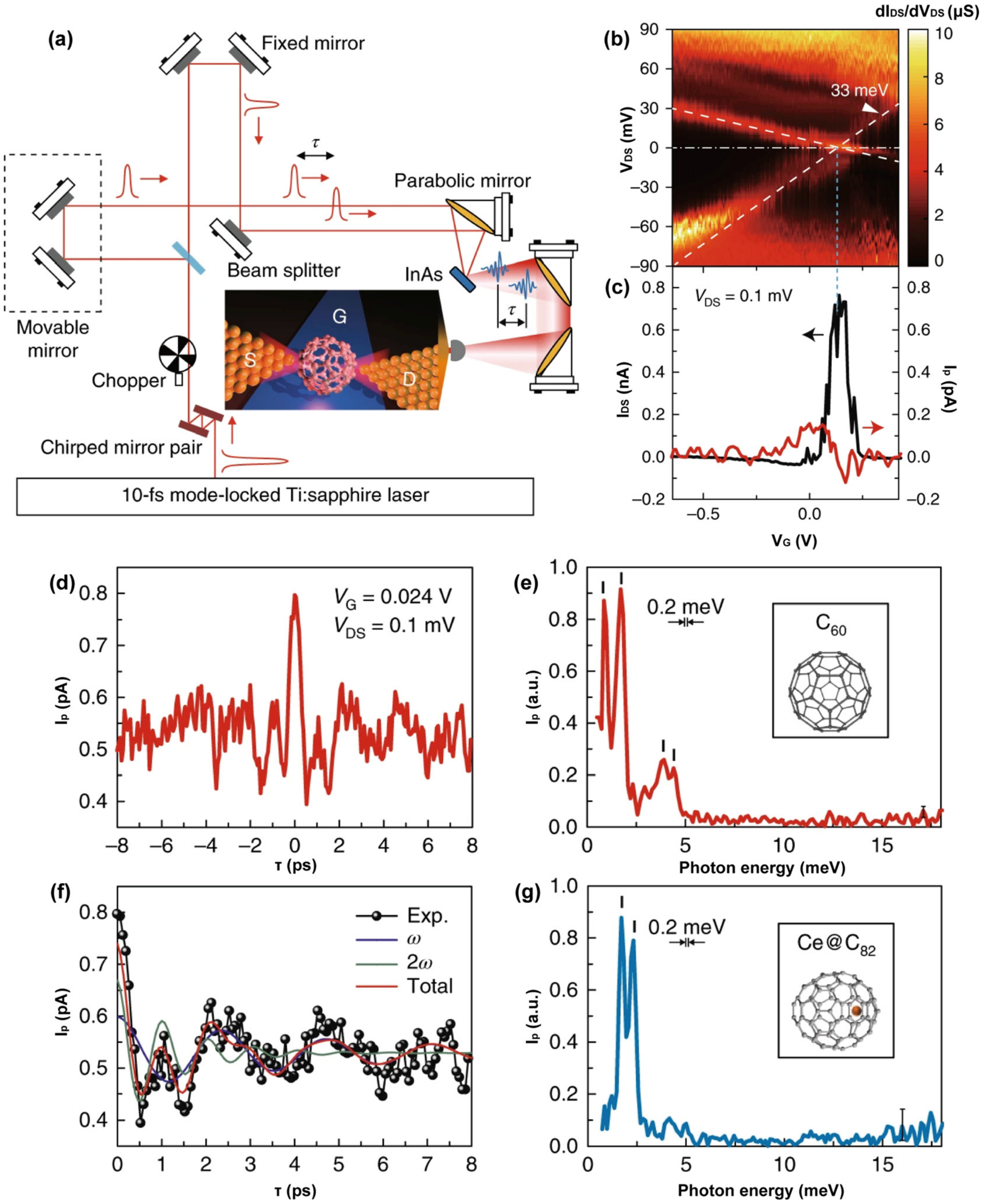

FIG. 40. (a) Schematic illustration of the experimental setup. (b) Coulomb stability diagram of a C_{60} SMT. (c) The single-electron tunneling current I_{DS} (black curve) and the THz-induced photocurrent IP (red curve) as a function of V_G measured at $V_{DS} = 0.1$ mV. (d) Quasi-autocorrelation trace (interferogram) of the THz-induced photocurrent measured at the peak of the photocurrent ($V_G = 0.024$, $V_{DS} = 0.1$ mV). (e) The Fourier spectrum of the interferogram is shown in c. (f) The interferogram for $\tau > 0$, replotted from d. The dots are the measured data points. (g) THz spectrum for a single-Ce@C_{82} SMT. Two sharply split peaks are observed at around 2 meV. Reproduced with permission from Du *et al.*, Nat. Photonics **12**, 608 (2018). Copyright 2018 Springer Nature.

can be induced not only by tunneling electron excitation but also by pulsed THz field excitation generated by femtosecond laser pulses.[14] The low-energy excitation observed in the C_{60}SMT structure originates from the center-of-mass oscillation of the C_{60} molecule induced by THz radiation. This oscillation creates new tunneling paths for electrons, namely, vibration-assisted tunneling.

To further understand the effects of the center-of-mass oscillation of C_{60} molecules, they theoretically simulated neutral and negatively charged C_{60} on the Au(111) surface. When C_{60} is negatively charged, the system becomes unstable, with an average distance extended by 0.011 nm and a decrease in vibration energy by 0.7 meV. The observed vibration energy matches the calculated vibration energy well. Du *et al.*'s study elucidates the vibration-assisted tunneling mechanism induced by center-of-mass oscillation, achieves ultra-sensitive detection of electron/vibration structures when single molecules are charged/discharged, and provides the foundation for further enhancing the energy conversion efficiency of future devices, such as batteries and sensors.

VII. CONCLUSION AND OUTLOOK

The past decade has seen remarkable advancements in experimental platforms for understanding energy conversion, dissipation, and transport in MSJs. As highlighted in this Review, recent research efforts have led to the discovery of a wide range of previously inaccessible physical and chemical properties, from atomic-scale luminescence and single-molecule heat conduction to plasmonic effects and the regulation of chemical reactions and spin states at the single-molecule level. These breakthroughs have profoundly deepened our understanding of MSJs and opened new avenues for controlling and manipulating electrical, optical, thermal, and magnetic energy at the molecular scale. It is reasonable to expect that continued experimental and theoretical efforts in these areas will unveil new potentials and pave the way for developing highly efficient molecular-scale devices for future computing, optoelectronics, energy conversion, energy harvesting, and sensing applications.

Despite recent progress, significant challenges remain in fully harnessing energy conversion and transport in MSJs. First, energy conversion processes often involve multiple, intertwined effects. For instance, light–matter interactions may involve optical, hot carrier, or thermal effects, complicating the interpretation of experimental data, such as the origin of plasmonic catalysis. To accurately understand these phenomena, it is crucial to develop experimental methods that can isolate the contributions of each effect through careful design and selection of molecular systems. Scrutinizing measured results and designing appropriate control systems are also essential for future investigations.

Second, energy conversion processes occur across distinct time scales, from femtoseconds for photoexcitation to milliseconds for thermal processes. Monitoring these dynamics and kinetics remains challenging but could be addressed by integrating MSJ platforms with advanced ultrafast techniques, such as pump-probe methods. In addition, for physical processes that occur at a longer timescale, the mechanical stability of a MSJ plays a pivotal role. The MSJ lifetimes are limited by the stochastic rupture of the weakest bond, often at the molecule–electrode interfaces. Therefore, enhancing the coupling at the junction contacts is essential. Promising results have been demonstrated in MSJs featuring graphene, silicon, and indium tin oxide electrodes coupled with custom-designed anchor groups.[511–513] Owing to their superb stability, graphene-based MSJs, in particular, have shown promise for real-time detection of single-molecule chemical reaction dynamics.

Third, our knowledge of thermal transport through single molecules has been largely limited to theoretical predictions due to technical challenges in detecting extremely small heat current ($\sim$ several picowatt) through a single molecule. This limitation hinders the characterization of the thermoelectric figure of merit (ZT) in single-molecule devices.[359,514] Recent advancements in ultra-sensitive temperature sensing techniques, such as scanning thermal probes and nanofabricated calorimetry,[351,353,515] have begun to enable direct quantification of heat conduction and ZT in single molecules. These tools will soon allow comprehensive interrogation of thermal transport properties in MSJs, verifying theoretical models and optimizing device performance. Insights from these studies will inform the design of high-efficiency thermoelectric and thermal management molecular devices. In contrast, the spin Seebeck effect remains inaccessible at the single-molecule level. Challenges include synthesizing reliable single-molecule magnets, conducting ultra-low temperature and high-vacuum characterizations, and efficiently converting spin currents to electrical currents. Similar technical challenges also remain for other energy processes. Addressing these issues will require close collaboration within the field.

The exploration of time-dependent modulated non-equilibrium energy transport reveals the vast potential for controlling and optimizing energy flow in nanoscale and advanced material systems. Through the strategic application of temperature oscillations, effective temperature pulses, and time-periodic driving forces, it is possible to enhance energy rectification and storage,[516] paving the way for more efficient energy harvesting and conversion technologies.[517] These approaches[518] capitalize on the intrinsic non-linearities and phase transitions within materials, enabling significant improvements in energy transfer efficiency. Several studies[519,520] demonstrate that precise temporal modulation can lead to novel mechanisms for directing energy flow, offering promising avenues for developing devices that operate far from equilibrium. Keeping the molecular bridge intrinsically non-equilibrium is helpful for applications in thermal-circuit systems (thermal rectifier, transistor, and diode). Here, traditional equilibrium methods fall short, emphasizing the importance of dynamic control in next-generation thermal and electronic systems.

In addition, several open questions remain regarding observed processes in MSJs. For instance, how can one use the single-molecule toolbox to tailor the reaction selectivity and specificity of favored reaction pathways and ultimately apply these molecular-scale insights to bulk reactions? The theoretical and experimental foundations that bridge the gap between single-molecule and bulk reactions remain elusive, particularly in mimicking homogeneous catalysis conditions. Additionally, puzzles persist around the CISS effect. The origins of experimentally measured CISS processes, such as photon transmission, electron transport, and chemical reactions, have remained elusive. Existing theories often yield effects that are many orders of magnitude lower than the measured results. To date, a comprehensive theoretical framework that interprets all experimental data has not been identified, leaving a significant gap between experimental observations and quantitative theoretical estimates.[521] In-depth investigations of simple model systems, where CISS can be studied both experimentally and theoretically in detail, are suggested by the research community as a promising starting point. While solving these puzzles is challenging, it offers rich opportunities in developing ambient condition quantum information sciences as a growing number of experiments report CISS effects at room temperature in various molecular systems.

The recent success of adopting artificial intelligence-powered approaches, such as machine learning methods, in materials discovery and life sciences has been inspiring.[522–525] We believe the field of molecular electronics (ME) could also greatly benefit from AI-assisted models and tools. AI-based methods could help in two significant ways. First, there is a clear shortage of suitable molecular candidates for various energy-related applications. Properly trained deep learning methods will enable high-throughput prediction and design of molecular systems that are readily synthesizable in the lab, addressing the issue of theoretically predicted molecules often being non-synthesizable in reality. This, in turn, could provide insights for improving existing theoretical models and synthetic approaches. Second, as demonstrated in several recent attempts,[526–529] machine learning-based methods can effectively identify hidden yet significant information from large and noisy data sets generated from MSJs. This capability will expedite data processing and prevent the loss or misinterpretation of valuable physical details in future studies, especially in challenging measurements with low signal-to-noise ratios.

What the future holds for the energy conversion and transport in MSJs in next decade relies on the creativity of researchers from multi-discipline and how collaborative works are managed today to make inroads in finding the missing puzzles at the molecular realm. The progress achieved in the past decade has laid solid groundwork for future developments. Although there is probably still a long way to go, we anticipate that with rapidly evolving molecular-scale characterization tools and theoretical frameworks, MSJ devices are poised to transition from research labs to more practical applications, offering solutions to key challenges in computing, optoelectronics, energy, and quantum sensing. From the application perspective, integrating MSJ devices into practical daily use hinges on overcoming the challenge of developing stable and high-quality devices. A critical factor in this endeavor is to ensure the stability of both the molecular core and the molecule–electrode coupling in an MSJ while maintaining a high fabrication yield. To this end, developing molecular materials and contact chemistry that are immune to certain external conditions (e.g., temperature, mechanical strain, electric/magnetic field, humidity, and light) are of pivotal importance. As the deterministic component whose failure could undermine device performance, the molecular core must be air-stable, chemically and structurally robust to maintain key functionality with good tolerance under varying conditions. Equally critical is the molecule–electrode contact chemistry. The Au–S contact (including Au–SH, Au–SMe, and Au–SAc), despite its widespread use in MSJ studies, presents challenges due to its multiple geometrical configurations with different conductance values.[530,531] Other anchor groups, such as pyridyl, amine, dimethylphosphine, and carbon, although beneficial for enhancing conductance or modifying frontier molecular orbitals, encounter issues in terms of interface resistance, contact stability, and coupling strength.[532,533] The instability of these interface connections is largely attributed to the flexible structural configurations and active chemical properties of metal electrodes. In contrast, according to MSJ experimental results reported to date, GMGJ has demonstrated exceptional device stability due to strong covalent coupling between organic molecule and graphene by amide linkages, maintaining its functions for more than one year, which makes such design strategy a suitable path for real-world applications.[55] While a clear solution for creating ideal contact chemistry remains elusive, this recent progress hints that all organic contact engineering is advantageous over metal-organic systems. Attempts to address the junction stability issues could also benefit from exploring new junction architectures by incorporating advanced on-surface nanofabrication. The ability to resolve the junction stability issues will ultimately transition MSJ devices from research labs to daily applications.

ACKNOWLEDGMENTS

K.W. acknowledges the financial support from the U.S. Department of Energy, Office of Science, Basic Energy Sciences (Award No. DE-SC0024924). L.C. acknowledges the support from National Science Foundation (NSF CAREER CBET-2239004) and Air Force Research Laboratory (No. AFRL FA8651-22-1-0012). C.J. acknowledges the supports from the National Key R&D Program of China (No. 2021YFA1200102) and the National Natural Science Foundation of China (No. 22173050). X.G. acknowledges the supports from the National Key R&D Program of China (Nos. 2021YFA1200101 and 2022YFE0128700), the National Natural Science Foundation of China (Nos. 22150013, 21727806, and 21933001), and the Natural Science Foundation of Beijing (No. 2222009).

AUTHOR DECLARATIONS

Conflict of Interest

The authors have no conflicts to disclose.

Author Contributions

Haixin Zhang, Yunxuan Zhu, and Ping Duan contributed equally to this work.

Haixin Zhang: Investigation (lead); Methodology (lead); Visualization (lead); Writing – original draft (lead); Writing – review & editing (lead). **Yunxuan Zhu:** Investigation (equal); Methodology (equal); Writing – original draft (equal); Writing – review & editing (equal). **Ping Duan:** Investigation (equal); Methodology (equal); Writing – original draft (equal); Writing – review & editing (equal). **Mehrdad Shiri:** Visualization (supporting); Writing – original draft (supporting); Writing – review & editing (supporting). **Sai Chandra Yelishala:** Writing – original draft (supporting); Writing – review & editing (supporting). **Shaocheng Shen:** Visualization (supporting); Writing – review & editing (supporting). **Ziqi Song:** Writing – original draft (supporting); Writing – review & editing (supporting). **Chuancheng Jia:** Conceptualization (equal); Funding acquisition (equal); Project administration (equal); Supervision (equal); Writing – review & editing (equal). **Xuefeng guo:** Funding acquisition (equal); Project administration (equal); Supervision (equal); Writing – review & editing (equal). **Longji Cui:** Conceptualization (equal); Funding acquisition (equal); Project administration (equal); Supervision (equal); Writing – original draft (equal); Writing – review & editing (equal). **Kun Wang:** Conceptualization (equal); Funding acquisition (equal); Project administration (equal); Supervision (equal); Writing – review & editing (equal).

DATA AVAILABILITY

Data sharing is not applicable to this article as no new data were created or analyzed in this study.

REFERENCES

[1] A. Aviram and M. A. Ratner, Chem. Phys. Lett. **29**, 277 (1974).
[2] B. Xu and N. J. Tao, Science **301**, 1221 (2003).
[3] C. Guo, K. Wang, E. Zerah-Harush, J. Hamill, B. Wang, Y. Dubi, and B. Xu, Nat. Chem. **8**, 484 (2016).

[4] H. Reddy, K. Wang, Z. Kudyshev, L. Zhu, S. Yan, A. Vezzoli, S. J. Higgins, V. Gavini, A. Boltasseva, P. Reddy, V. M. Shalaey, and E. Meyhofer, Science **369**, 423 (2020).

[5] A. K. Ismael, K. Wang, A. Vezzoli, M. K. Al-Khaykanee, H. E. Gallagher, I. M. Grace, C. J. Lambert, B. Xu, R. J. Nichols, and S. J. Higgins, Angew. Chem., Int. Ed. **56**, 15378 (2017).

[6] M. L. Perrin, R. Frisenda, M. Koole, J. S. Seldenthuis, J. A. C. Gil, H. Valkenier, J. C. Hummelen, N. Renaud, F. C. Grozema, J. M. Thijssen, D. Dulić, and H. S. J. van der Zant, Nat. Nanotechnol. **9**, 830 (2014).

[7] S. Caneva, P. Gehring, V. M. García-Suárez, A. García-Fuente, D. Stefani, I. J. Olavarria-Contreras, J. Ferrer, C. Dekker, and H. S. J. van der Zant, Nat. Nanotechnol. **13**, 1126 (2018).

[8] D. Xiang, H. Jeong, T. Lee, and D. Mayer, Adv. Mater. **25**, 4845 (2013).

[9] D. J. Wold and C. D. Frisbie, J. Am. Chem. Soc. **123**, 5549 (2001).

[10] T. Morita and S. Lindsay, J. Am. Chem. Soc. **129**, 7262 (2007).

[11] A. F. Morpurgo, C. M. Marcus, and D. B. Robinson, Appl. Phys. Lett. **74**, 2084 (1999).

[12] W. Liang, M. P. Shores, M. Bockrath, J. R. Long, and H. Park, Nature **417**, 725 (2002).

[13] K. I. Bolotin, F. Kuemmeth, A. N. Pasupathy, and D. C. Ralph, Appl. Phys. Lett. **84**, 3154 (2004).

[14] H. Park, J. Park, A. K. L. Lim, E. H. Anderson, A. P. Alivisatos, and P. L. McEuen, Nature **407**, 57 (2000).

[15] J. Park, A. N. Pasupathy, J. I. Goldsmith, C. Chang, Y. Yaish, J. R. Petta, M. Rinkoski, J. P. Sethna, H. D. Abruña, P. L. McEuen, and D. C. Ralph, Nature **417**, 722 (2002).

[16] C. Yang, C. Yang, Y. Guo, J. Feng, and X. Guo, Nat. Protoc. **18**, 1958 (2023).

[17] K. Ullmann, P. B. Coto, S. Leitherer, A. Molina-Ontoria, N. Martín, M. Thoss, and H. B. Weber, Nano Lett. **15**, 3512 (2015).

[18] C. Yang, A. Qin, B. Z. Tang, and X. Guo, J. Chem. Phys. **152**, 120902 (2020).

[19] Z. Chen, C. Ho, L. Wang, and W. Wong, Adv. Mater. **32**, 1903269 (2020).

[20] C. Wu, X. Qiao, C. M. Robertson, S. Higgins, C. Cai, R. Nichols, and A. Vezzoli, Angew. Chem. **132**, 12127 (2020).

[21] J. Bai, A. Daaoub, S. Sangtarash, X. Li, Y. Tang, Q. Zou, H. Sadeghi, S. Liu, X. Huang, Z. Tan, J. Liu, Y. Yang, J. Shi, G. Mészáros, W. Chen, C. Lambert, and W. Hong, Nat. Mater. **18**, 364 (2019).

[22] Z. Chen, I. M. Grace, S. L. Woltering, L. Chen, A. Gee, J. Baugh, G. A. D. Briggs, L. Bogani, J. A. Mol, C. J. Lambert, H. L. Anderson, and J. O. Thomas, Nat. Nanotechnol. **19**, 986 (2024).

[23] C. M. Holland, Y. Lu, and L. W. Cheuk, Science **382**, 1143 (2023).

[24] G. Schull, T. Frederiksen, A. Arnau, D. Sánchez-Portal, and R. Berndt, Nat. Nanotechnol. **6**, 23 (2011).

[25] X. Xie, P. Li, Y. Xu, L. Zhou, Y. Yan, L. Xie, C. Jia, and X. Guo, ACS Nano **16**, 3476 (2022).

[26] G. Ke, C. Duan, F. Huang, and X. Guo, InfoMat **2**, 92 (2020).

[27] M. A. Reed, C. Zhou, C. J. Muller, T. P. Burgin, and J. M. Tour, Science **278**, 252 (1997).

[28] H. Zhang, M. Shiri, R. T. Ayinla, Z. Qiang, and K. Wang, MRS. Commun. **12**, 495 (2022).

[29] P. Moreno-García, M. Gulcur, D. Z. Manrique, T. Pope, W. Hong, V. Kaliginedi, C. Huang, A. S. Batsanov, M. R. Bryce, C. Lambert, and T. Wandlowski, J. Am. Chem. Soc. **135**, 12228 (2013).

[30] A. D. Slepkov, F. A. Hegmann, S. Eisler, E. Elliott, and R. R. Tykwinski, J. Chem. Phys. **120**, 6807 (2004).

[31] S. Chakraborty and S. K. Maiti, ChemPhysChem **20**, 848 (2019).

[32] P. Li, C. Jia, and X. Guo, Chem. Rec. **21**, 1284 (2021).

[33] X. Huang and T. Li, J. Mater. Chem. C **8**, 821 (2020).

[34] L. H. Lee and R. M. Dickson, J. Phys. Chem. B **107**, 7387 (2003).

[35] J. Koch, F. Von Oppen, Y. Oreg, and E. Sela, Phys. Rev. B **70**, 195107 (2004).

[36] N. Nakpathomkun, H. Q. Xu, and H. Linke, Phys. Rev. B **82**, 235428 (2010).

[37] M. Leijnse, M. R. Wegewijs, and K. Flensberg, Phys. Rev. B **82**, 045412 (2010).

[38] C. M. Finch, V. M. García-Suárez, and C. J. Lambert, Phys. Rev. B **79**, 033405 (2009).

[39] M. Paulsson and S. Datta, Phys. Rev. B **67**, 241403 (2003).

[40] C. Li, Y. Cao, J. Ru, J. Dong, and M. Sun, Adv. Electron. Mater. **9**, 2300063 (2023).

[41] H. Miller, Z. Zhou, J. Shepherd, A. J. M. Wollman, and M. C. Leake, Rep. Prog. Phys. **81**, 024601 (2018).

[42] B. N. Miller, A. P. Ivanov, K. A. Wilson, F. Doğan, D. Japrung, and J. B. Edel, Chem. Soc. Rev. **42**, 15 (2013).

[43] L. Gerhard, K. Edelmann, J. Homberg, M. Valášek, S. G. Bahoosh, M. Lukas, F. Pauly, M. Mayor, and W. Wulfhekel, Nat. Commun. **8**, 14672 (2017).

[44] Y. Han, Y. C. Nickle, Z. Zhang, H. P. A. G. Astier, T. J. Duffin, D. Qi, Z. Wang, E. del Barco, D. Thompson, and C. A. Nijhuis, Nat. Mater. **19**, 843 (2020).

[45] C. Tang, J. Zheng, Y. Ye, J. Liu, L. Chen, Z. Yan, Z. Chen, L. Chen, X. Huang, J. Bai, Z. Chen, J. Shi, H. Xia, and W. Hong, iScience **23**, 100770 (2020).

[46] W. Zhang, H. Chen, and X. Guo, Adv. Mater. Technol. **4**, 1970025 (2019).

[47] S. Y. Quek, M. Kamenetska, M. L. Steigerwald, H. J. Choi, S. G. Louie, M. S. Hybertsen, J. B. Neaton, and L. Venkataraman, Nat. Nanotechnol. **4**, 230 (2009).

[48] J. Berson, M. Moosmann, S. Walheim, and T. Schimmel, Nano Lett. **19**, 816 (2019).

[49] Z. Yang, P. A. Cazade, J. L. Lin, Z. Cao, N. Chen, D. Zhang, L. Duan, C. A. Nijhuis, D. Thompson, and Y. Li, Nat. Commun. **14**, 5639 (2023).

[50] H. Chen, C. Jia, X. Zhu, C. Yang, X. Guo, and J. F. Stoddart, Nat. Rev. Mater. **8**, 165 (2022).

[51] R. T. Ayinla, M. Shiri, B. Song, M. Gangishetty, and K. Wang, Mater. Chem. Front. **7**, 3524 (2023).

[52] C. Jia, J. Wang, C. Yao, Y. Cao, Y. Zhang, Z. Liu, Z. Liu, and X. Guo, Angew. Chem., Int. Ed. **52**, 8666 (2013).

[53] Y. Kim, T. J. Hellmuth, D. Sysoiev, F. Pauly, T. Pietsch, J. Wolf, A. Erbe, T. Huhn, U. Groth, U. E. Steiner, and E. Scheer, Nano Lett. **12**, 3736 (2012).

[54] D. Kim, H. Jeong, W. Hwang, Y. Jang, D. Sysoiev, E. Scheer, T. Huhn, M. Min, H. Lee, and T. Lee, Adv. Funct. Mater. **25**, 5918 (2015).

[55] C. Jia, A. Migliore, N. Xin, J. Wang, Q. Yang, S. Wang, H. Chen, D. Wang, B. Feng, Z. Liu, G. Zhang, D. Qu, H. Tian, M. A. Ratner, H. Q. Xu, and X. Guo, Science **352**, 1443 (2016).

[56] G. Pace, G. V. Ferri, C. Grave, M. Elbing, C. von Hänisch, M. Zharnikov, M. Mayor, M. A. Rampi, and P. Samorì, Proc. Natl. Acad. Sci. U. S. A. **104**, 9937 (2007).

[57] M. J. Comstock, N. Levy, A. Kirakosian, J. Cho, F. Lauterwasser, J. H. Harvey, D. A. Strubbe, J. M. J. Fréchet, D. Trauner, S. G. Louie, and M. F. Crommie, Phys. Rev. Lett. **99**, 038301 (2007).

[58] A. S. Kumar, T. Ye, T. Takami, B. C. Yu, A. K. Flat, J. M. Tour, and P. S. Weiss, Nano. Lett. **8**, 1644 (2008).

[59] Y. Cao, S. Dong, S. Liu, Z. Liu, and X. Guo, Angew. Chem., Int. Ed. **52**, 3906 (2013).

[60] J. Harada, K. Ogawa, and S. Tomoda, Acta Crystallogr., Sect. B **53**, 662 (1997).

[61] D. Bléger, J. Schwarz, A. M. Brouwer, and S. Hecht, J. Am. Chem. Soc. **134**, 20597 (2012).

[62] C. E. Weston, R. D. Richardson, P. R. Haycock, A. J. P. White, and M. J. Fuchter, J. Am. Chem. Soc. **136**, 11878 (2014).

[63] Z. Li, P. Wang, B. Liu, Y. Wang, J. Zhang, Y. Yan, and Y. Ma, Soft. Matter **10**, 8758 (2014).

[64] L. Meng, N. Xin, C. Hu, J. Wang, B. Gui, J. Shi, C. Wang, C. Shen, G. Zhang, H. Guo, S. Meng, and X. Guo, Nat. Commun. **10**, 1450 (2019).

[65] N. Darwish, A. C. Aragonès, T. Darwish, S. Ciampi, and I. Díez-Pérez, Nano Lett. **14**, 7064 (2014).

[66] D. Roldan, V. Kaliginedi, S. Cobo, V. Kolivoska, C. Bucher, W. Hong, G. Royal, and T. Wandlowski, J. Am. Chem. Soc. **135**, 5974 (2013).

[67] C. Jia, B. Ma, N. Xin, and X. Guo, Acc. Chem. Res. **48**, 2565 (2015).

[68] E. D. Fung, O. Adak, G. Lovat, D. Scarabelli, and L. Venkataraman, Nano Lett. **17**, 1255 (2017).

[69] R. Arielly, A. Ofarim, G. Noy, and Y. Selzer, Nano Lett. **11**, 2968 (2011).

[70] M. Vadai, N. Nachman, M. Ben-Zion, M. Bürkle, F. Pauly, J. C. Cuevas, and Y. Selzer, J. Phys. Chem. Lett. **4**, 2811 (2013).

[71] M. Galperin and A. Nitzan, Phys. Chem. Chem. Phys. **14**, 9421 (2012).

[72] J. Zhou, K. Wang, B. Xu, and Y. Dubi, J. Am. Chem. Soc. **140**, 70 (2018).

[73] K. Kimura, K. Miwa, H. Imada, M. Imai-Imada, S. Kawahara, J. Takeya, M. Kawai, M. Galperin, and Y. Kim, Nature **570**, 210 (2019).

[74] J. L. O'Brien, Science **318**, 1567 (2007).

[75] B. Lounis and W. E. Moerner, Nature **407**, 491 (2000).

[76] A. Beveratos, R. Brouri, T. Gacoin, A. Villing, J. Poizat, and P. Grangier, Phys. Rev. Lett. **89**, 187901 (2002).

[77] J. Doležal, P. Mutombo, D. Nachtigallová, P. Jelínek, P. Merino, and M. Švec, ACS. Nano **14**, 8931 (2020).

[78] G. Chen, Y. Luo, H. Gao, J. Jiang, Y. Yu, L. Zhang, Y. Zhang, X. Li, Z. Zhang, and Z. Dong, Phys. Rev. Lett. **122**, 177401 (2019).

[79] Y. Zhang, Y. Luo, Y. Zhang, Y. Yu, Y. Kuang, L. Zhang, Q. Meng, Y. Luo, J. Yang, Z. Dong, and J. G. Hou, Nature **531**, 623 (2016).

[80] J. Doležal, S. Canola, P. Merino, and M. Švec, ACS. Nano **15**, 7694 (2021).

[81] J. Doležal, S. Canola, P. Hapala, R. C. de Campos Ferreira, P. Merino, and M. Švec, ACS. Nano **16**, 1082 (2022).

[82] K. H. Park, P. Kim, W. Kim, H. Shimizu, M. Han, E. Sim, M. Iyoda, and D. Kim, Angew. Chem., Int. Ed. **54**, 12711 (2015).

[83] M. Shiri, H. Zhang, and K. Wang, ACS. Appl. Electron. Mater. (published online, 2024).

[84] L. Ni, X. Li, Z. Zhao, J. Nam, P. Wu, Q. Wang, T. Lee, H. Liu, and D. Xiang, ACS Appl. Mater. Interfaces **13**, 29885 (2021).

[85] X. Sun, R. Liu, S. Kandapal, and B. Xu, Nanophotonics **13**, 1535 (2024).

[86] S. Guo, J. Hihath, I. Díez-Pérez, and N. Tao, J. Am. Chem. Soc. **133**, 19189 (2011).

[87] J. A. Malen, P. Doak, K. Baheti, T. D. Tilley, R. A. Segalman, and A. Majumdar, Nano Lett. **9**, 1164 (2009).

[88] J. R. Widawsky, W. Chen, H. Vázquez, T. Kim, R. Breslow, M. S. Hybertsen, and L. Venkataraman, Nano Lett. **13**, 2889 (2013).

[89] C. Huang, A. V. Rudnev, W. Hong, and T. Wandlowski, Chem. Soc. Rev. **44**, 889 (2015).

[90] H. Liu, L. Chen, H. Zhang, Z. Yang, J. Ye, P. Zhou, C. Fang, W. Xu, J. Shi, J. Liu, Y. Yang, and W. Hong, Nat. Mater. **22**, 1007 (2023).

[91] A. Vezzoli, R. J. Brooke, S. J. Higgins, W. Schwarzacher, and R. J. Nichols, Nano Lett. **17**, 6702 (2017).

[92] J. J. Baumberg, J. Aizpurua, M. H. Mikkelsen, and D. R. Smith, Nat. Mater. **18**, 668 (2019).

[93] H. A. Atwater and A. Polman, Nat. Mater. **9**, 205 (2010).

[94] J. Li, S. K. Cushing, F. Meng, T. R. Senty, A. D. Bristow, and N. Wu, Nat. Photonics **9**, 601 (2015).

[95] Y. Zhu, M. B. Raschke, D. Natelson, and L. Cui, Nanophotonics **13**, 2281 (2024).

[96] M. Kim, J.-H. Lee, and J.-M. Nam, Adv. Sci. **6**, 1900471 (2019).

[97] W. Ye, R. Long, H. Huang, and Y. Xiong, J. Mater. Chem. C **5**, 1008 (2017).

[98] S. Zeng, D. Baillargeat, H. P. Ho, and K. T. Yong, Chem. Soc. Rev. **43**, 3426 (2014).

[99] A. B. Zrimsek, N. Chiang, M. Mattei, S. Zaleski, M. O. McAnally, C. T. Chapman, A. I. Henry, G. C. Schatz, and R. P. Van Duyne, Chem. Rev. **117**, 7583 (2017).

[100] W. Du, T. Wang, H.-S. Chu, and C. A. Nijhuis, Nat. Photonics **11**, 623 (2017).

[101] M. Parzefall, P. Bharadwaj, A. Jain, T. Taniguchi, K. Watanabe, and L. Novotny, Nat. Nanotechnol. **10**, 1058 (2015).

[102] F. Benz, M. K. Schmidt, A. Dreismann, R. Chikkaraddy, Y. Zhang, A. Demetriadou, C. Carnegie, H. Ohadi, B. de Nijs, R. Esteban, J. Aizpurua, and J. J. Baumberg, Science **354**, 726 (2016).

[103] P. Nordlander, C. Oubre, E. Prodan, K. Li, and M. I. Stockman, Nano Lett. **4**, 899 (2004).

[104] R. Esteban, A. G. Borisov, P. Nordlander, and J. Aizpurua, Nat. Commun. **3**, 825 (2012).

[105] I. Romero, J. Aizpurua, G. W. Bryant, and F. J. García De Abajo, Opt. Express **14**, 9988 (2006).

[106] F. J. G. De Abajo, J. Phys. Chem. C **112**, 17983 (2008).

[107] S. Raza, S. I. Bozhevolnyi, M. Wubs, and N. Asger Mortensen, J. Phys. **27**, 183204 (2015).

[108] Q. Zhang, X. Cai, X. Yu, S. Carregal-Romero, W. J. Parak, R. Sachan, Y. Cai, N. Wang, Y. Zhu, and D. Y. Lei, Adv. Quantum Technol. **1**, 1800016 (2018).

[109] W. Zhu, R. Esteban, A. G. Borisov, J. J. Baumberg, P. Nordlander, H. J. Lezec, J. Aizpurua, and K. B. Crozier, Nat. Commun. **7**, 11495 (2016).

[110] V. Kulkarni and A. Manjavacas, ACS. Photonics **2**, 987 (2015).

[111] K. J. Savage, M. M. Hawkeye, R. Esteban, A. G. Borisov, J. Aizpurua, and J. J. Baumberg, Nature **491**, 574 (2012).

[112] J. A. Scholl, A. García-Etxarri, A. L. Koh, and J. A. Dionne, Nano Lett. **13**, 564 (2013).

[113] C. Ciracì, R. T. Hill, J. J. Mock, Y. Urzhumov, A. I. Fernández-Domínguez, S. A. Maier, J. B. Pendry, A. Chilkoti, and D. R. Smith, Science **337**, 1072 (2012).

[114] W. Zhu and K. B. Crozier, Nat. Commun. **5**, 5228 (2014).

[115] J. Lambe and S. L. McCarthy, Phys. Rev. Lett. **37**, 923 (1976).

[116] M. Büttiker, Phys. Rev. Lett. **65**, 2901 (1990).

[117] V. Kalathingal, P. Dawson, and J. Mitra, Sci. Rep. **7**, 3530 (2017).

[118] R. Pechou, R. Coratger, F. Ajustron, and J. Beauvillain, Appl. Phys. Lett. **72**, 671 (1998).

[119] F. Xu, C. Holmqvist, and W. Belzig, Phys. Rev. Lett. **113**, 066801 (2014).

[120] N. L. Schneider, P. Johansson, and R. Berndt, Phys. Rev. B **87**, 45409 (2013).

[121] G. Hoffmann, R. Berndt, and P. Johansson, Phys. Rev. Lett. **90**, 046803 (2003).

[122] P.-J. Peters, F. Xu, K. Kaasbjerg, G. Rastelli, W. Belzig, and R. Berndt, Phys. Rev. Lett. **119**, 066803 (2017).

[123] E. D. Fung and L. Venkataraman, Nano Lett. **20**, 8912 (2020).

[124] L. Cui, Y. Zhu, M. Abbasi, A. Ahmadivand, B. Gerislioglu, P. Nordlander, and D. Natelson, Nano Lett. **20**, 6067 (2020).

[125] Y. Zhu, L. Cui, M. Abbasi, and D. Natelson, Nano Lett. **22**, 8068 (2022).

[126] T. B. Hoang, G. M. Akselrod, and M. H. Mikkelsen, Nano Lett. **16**, 270 (2016).

[127] T. B. Hoang, G. M. Akselrod, C. Argyropoulos, J. Huang, D. R. Smith, and M. H. Mikkelsen, Nat. Commun. **6**, 7788 (2015).

[128] G. M. Akselrod, T. Ming, C. Argyropoulos, T. B. Hoang, Y. Lin, X. Ling, D. R. Smith, J. Kong, and M. H. Mikkelsen, Nano Lett. **15**, 3578 (2015).

[129] Y. Zhu, J. Yang, J. Abad-Arredondo, A. I. Fernández-Domínguez, F. J. Garcia-Vidal, and D. Natelson, Nano Lett. **24**, 525 (2024).

[130] J. Huang, G. M. Akselrod, T. Ming, J. Kong, and M. H. Mikkelsen, ACS. Photonics **5**, 552 (2018).

[131] G. M. Akselrod, C. Argyropoulos, T. B. Hoang, C. Ciracì, C. Fang, J. Huang, D. R. Smith, and M. H. Mikkelsen, Nat. Photonics **8**, 835 (2014).

[132] A. Rose, T. B. Hoang, F. McGuire, J. J. Mock, C. Ciracì, D. R. Smith, and M. H. Mikkelsen, Nano Lett. **14**, 4797 (2014).

[133] N. Hildebrandt, M. Lim, N. Kim, D. Y. Choi, and J. M. Nam, Chem. Commun. **59**, 2352 (2023).

[134] P. Anger, P. Bharadwaj, and L. Novotny, Phys. Rev. Lett. **96**, 113002 (2006).

[135] N. Kongsuwan, A. Demetriadou, R. Chikkaraddy, F. Benz, V. A. Turek, U. F. Keyser, J. J. Baumberg, and O. Hess, ACS. Photonics **5**, 186 (2018).

[136] M. Pelton, Nat. Photonics **9**, 427 (2015).

[137] R. Chikkaraddy, V. A. Turek, N. Kongsuwan, F. Benz, C. Carnegie, T. Van De Goor, B. De Nijs, A. Demetriadou, O. Hess, U. F. Keyser, and J. J. Baumberg, Nano Lett. **18**, 405 (2018).

[138] K. J. Russell, T. L. Liu, S. Cui, and E. L. Hu, Nat. Photonics **6**, 459 (2012).

[139] A. E. Schlather, N. Large, A. S. Urban, P. Nordlander, and N. J. Halas, Nano Lett. **13**, 3281 (2013).

[140] R. Chikkaraddy, B. de Nijs, F. Benz, S. J. Barrow, O. A. Scherman, E. Rosta, A. Demetriadou, P. Fox, O. Hess, and J. J. Baumberg, Nature **535**, 127 (2016).

[141] J. Dintinger, S. Klein, F. Bustos, W. L. Barnes, and T. W. Ebbesen, Phys. Rev. B **71**, 035424 (2005).

[142] P. Vasa, W. Wang, R. Pomraenke, M. Lammers, M. Maiuri, C. Manzoni, G. Cerullo, and C. Lienau, Nat. Photonics **7**, 128 (2013).

[143] Y. Sugawara, T. A. Kelf, J. J. Baumberg, M. E. Abdelsalam, and P. N. Bartlett, Phys. Rev. Lett. **97**, 266808 (2006).

[144] X. M. Qian and S. M. Nie, Chem. Soc. Rev. **37**, 912 (2008).

[145] D. O. Sigle, J. T. Hugall, S. Ithurria, B. Dubertret, and J. J. Baumberg, Phys. Rev. Lett. **113**, 087402 (2014).

[146] F. Benz, C. Tserkezis, L. O. Herrmann, B. De Nijs, A. Sanders, D. O. Sigle, L. Pukenas, S. D. Evans, J. Aizpurua, and J. J. Baumberg, Nano Lett. **15**, 669 (2015).

[147] R. W. Taylor, F. Benz, D. O. Sigle, R. W. Bowman, P. Bao, J. S. Roth, G. R. Heath, S. D. Evans, and J. J. Baumberg, Sci. Rep. **4**, 5940 (2014).

[148] M. D. Sonntag, D. Chulhai, T. Seideman, L. Jensen, and R. P. Van Duyne, J. Am. Chem. Soc. **135**, 17187 (2013).

[149] B. de Nijs, F. Benz, S. J. Barrow, D. O. Sigle, R. Chikkaraddy, A. Palma, C. Carnegie, M. Kamp, R. Sundararaman, P. Narang, O. A. Scherman, and J. J. Baumberg, Nat. Commun. **8**, 994 (2017).

[150] P. Roelli, C. Galland, N. Piro, and T. J. Kippenberg, Nat. Nanotechnol. **11**, 164 (2016).

[151] M. K. Schmidt, R. Esteban, F. Benz, J. J. Baumberg, and J. Aizpurua, Faraday Discuss. **205**, 31 (2017).

[152] A. Lombardi, M. K. Schmidt, L. Weller, W. M. Deacon, F. Benz, B. De Nijs, J. Aizpurua, and J. J. Baumberg, Phys. Rev. X. **8**, 011016 (2018).

[153] Y. Zhu, D. Natelson, and L. Cui, J. Phys. **33**, 134001 (2021).

[154] S. Liao, Y. Zhu, Q. Ye, S. Sanders, J. Yang, A. Alabastri, and D. Natelson, J. Phys. Chem. Lett. **14**, 7574 (2023).

[155] E. A. Muller, B. Pollard, and M. B. Raschke, J. Phys. Chem. Lett. **6**, 1275 (2015).

[156] B. Pollard, E. A. Muller, K. Hinrichs, and M. B. Raschke, Nat. Commun. **5**, 3587 (2014).

[157] S. A. Maier, P. G. Kik, H. A. Atwater, S. Meltzer, E. Harel, B. E. Koel, and A. A. G. Requicha, Nat. Mater. **2**, 229 (2003).

[158] M. L. Brongersma, N. J. Halas, and P. Nordlander, Nat. Nanotechnol. **10**, 25 (2015).

[159] P. Narang, R. Sundararaman, and H. A. Atwater, Nanophotonics **5**, 96 (2016).

[160] J. B. Khurgin, Nat. Nanotechnol. **10**, 2 (2015).

[161] J. B. Khurgin, Faraday Discuss. **214**, 35 (2019).

[162] R. Sundararaman, P. Narang, A. S. Jermyn, W. A. Goddard, and H. A. Atwater, Nat. Commun. **5**, 3935 (2014).

[163] A. Manjavacas, J. G. Liu, V. Kulkarni, and P. Nordlander, ACS. Nano **8**, 7630 (2014).

[164] A. M. Brown, R. Sundararaman, P. Narang, W. A. Goddard, and H. A. Atwater, ACS. Nano **10**, 957 (2016).

[165] C. Yannouleas and R. A. Broglia, Ann. Phys. **217**, 105 (1992).

[166] J. B. Khurgin, Faraday Discuss. **178**, 109 (2015).

[167] X. Li, D. Xiao, and Z. Zhang, New J. Phys. **15**, 023011 (2013).

[168] M. Lisowski, P. A. Loukakos, U. Bovensiepen, J. Stähler, C. Gahl, and M. Wolf, Appl. Phys. A **78**, 165 (2004).

[169] H. Inouye, K. Tanaka, and I. Tanahashi, Phys. Rev. B **57**, 11334 (1998).

[170] C. Frischorn and M. Wolf, Chem. Rev. **106**, 4207 (2006).

[171] M. Buret, A. V. Uskov, J. Dellinger, N. Cazier, M.-M. Mennemanteuil, J. Berthelot, I. V. Smetanin, I. E. Protsenko, G. Colas-des-Francs, and A. Bouhelier, Nano Lett. **15**, 5811 (2015).

[172] Y. Zhu, L. Cui, and D. Natelson, J. Appl. Phys. **128**, 233105 (2020).

[173] J.-L. Hou, A. Fischer, S.-C. Yang, J. Benduhn, J. Widmer, D. Kasemann, K. Vandewal, K. Leo, J. Hou, A. Fischer, J. Benduhn, J. Widmer, D. Kasemann, K. Vandewal, K. Leo, and S. Yang, Adv. Funct. Mater. **26**, 5741 (2016).

[174] M. Kang, Y. Park, H. Lee, C. Lee, and J. Y. Park, Nanotechnology **32**, 225203 (2021).

[175] P. Zolotavin, C. Evans, and D. Natelson, J. Phys. Chem. Lett. **8**, 1739 (2017).

[176] G. P. Szakmany, A. O. Orlov, G. H. Bernstein, and W. Porod, IEEE. Trans. Nanotechnol. **13**, 1234 (2014).

[177] L. Cui, Y. Zhu, P. Nordlander, M. Di Ventra, and D. Natelson, Nano Lett. **21**, 2658 (2021).

[178] M. Abbasi, S. Liao, Y. Zhu, and D. Natelson, Appl. Phys. Lett. **122**, 231103 (2023).

[179] C. I. Evans, R. Yang, L. T. Gan, M. Abbasi, X. Wang, R. Traylor, J. A. Fan, and D. Natelson, Proc. Natl. Acad. Sci. U. S. A. **117**, 23350 (2020).

[180] X. Wang, C. I. Evans, and D. Natelson, Nano Lett. **18**, 6557 (2018).

[181] M. Abbasi, C. I. Evans, L. Chen, and D. Natelson, ACS. Nano **14**, 17535 (2020).

[182] P. K. Jain, J. Phys. Chem. C **123**, 24347 (2019).

[183] L. Mascaretti and A. Naldoni, J. Appl. Phys. **128**, 41101 (2020).

[184] Y. Dubi and Y. Sivan, Light **8**, 89 (2019).

[185] P. V. Kamat, J. Phys. Chem. B **106**, 7729 (2002).

[186] S. Mukherjee, L. Zhou, A. M. Goodman, N. Large, C. Ayala-Orozco, Y. Zhang, P. Nordlander, and N. J. Halas, J. Am. Chem. Soc. **136**, 64 (2014).

[187] K. Sytwu, M. Vadai, F. Hayee, D. K. Angell, A. Dai, J. Dixon, and J. A. Dionne, Science **371**, 280 (2021).

[188] C. Zhang, H. Zhao, L. Zhou, A. E. Schlather, L. Dong, M. J. McClain, D. F. Swearer, P. Nordlander, and N. J. Halas, Nano Lett. **16**, 6677 (2016).

[189] P. Wang, M. E. Nasir, A. V. Krasavin, W. Dickson, and A. V. Zayats, Nano Lett. **20**, 1536 (2020).

[190] E. Kazuma, J. Jung, H. Ueba, M. Trenary, and Y. Kim, Science **360**, 521 (2018).

[191] S. Coe, W. K. Woo, M. Bawendi, and V. Bulović, Nature **420**, 800 (2002).

[192] M. Segal, M. Singh, K. Rivoire, S. Difley, T. Van Voorhis, and M. A. Baldo, Nat. Mater. **6**, 374 (2007).

[193] N. Christogiannis, N. Somaschi, P. Michetti, D. M. Coles, P. G. Savvidis, P. G. Lagoudakis, and D. G. Lidzey, Adv. Opt. Mater. **1**, 503 (2013).

[194] B. Yang, Y. Zhao, M. U. Ali, J. Ji, H. Yan, C. Zhao, Y. Cai, C. Zhang, and H. Meng, Adv. Mater. **34**, 2201342 (2022).

[195] H. Ohnishi, Annu. Rev. Mater. Res. **19**, 83 (1989).

[196] R. Polícia, N. Peřinka, C. Mendes-Felipe, P. Martins, D. M. Correia, and S. Lanceros-Méndez, Adv. Sustainable Syst. **8**, 2400140 (2024).

[197] G. H. Lee, M. G. Han, D. Leem, S. Lim, S. Yun, K. Lee, X. Bulliard, K. Park, T. Yagi, Y. S. Choi, Y. W. Jin, and S. Lee, J. Phys. Chem. C **120**, 10176 (2016).

[198] C. M. Hill, Y. Zhu, and S. Pan, ACS Nano **5**, 942 (2011).

[199] H. Cho, S. Jeong, M. Park, Y. Kim, C. Wolf, C. Lee, J. H. Heo, A. Sadhanala, N. Myoung, S. Yoo, S. H. Im, R. H. Friend, and T. Lee, Science **350**, 1222 (2015).

[200] A. Rosławska, P. Merino, C. Große, C. C. Leon, O. Gunnarsson, M. Etzkorn, K. Kuhnke, and K. Kern, Nano Lett. **18**, 4001 (2018).

[201] M. Mesta, M. Carvelli, R. J. de Vries, H. van Eersel, J. J. M. van der Holst, M. Schober, M. Furno, B. Lüssem, K. Leo, P. Loebl, R. Coehoorn, and P. A. Bobbert, Nat. Mater. **12**, 652 (2013).

[202] K. Kuhnke, C. Große, P. Merino, and K. Kern, Chem. Rev. **117**, 5174 (2017).

[203] T. H. Lee, J. I. Gonzalez, and R. M. Dickson, Proc. Natl. Acad. Sci. U. S. A. **99**, 10272 (2002).

[204] K. Miwa, S. Sakamoto, and A. Ishizaki, Nano Lett. **23**, 3231 (2023).

[205] R. Berndt, R. Gaisch, J. K. Gimzewski, R. R. Schlittler, W. D. Schneider, and M. Tschudy, Science **262**, 1425 (1993).

[206] X. H. Qiu, G. V. Nazin, and W. Hot, Science **299**, 542 (2003).

[207] H. Imada, K. Miwa, M. Imai-Imada, S. Kawahara, K. Kimura, and Y. Kim, Nature **538**, 364 (2016).

[208] M. A. Sillanpää, J. I. Park, and R. W. Simmonds, Nature **449**, 438 (2007).

[209] G. Zengin, M. Wersäll, S. Nilsson, T. J. Antosiewicz, M. Käll, and T. Shegai, Phys. Rev. Lett. **114**, 157401 (2015).

[210] K. Santhosh, O. Bitton, L. Chuntonov, and G. Haran, Nat. Commun. **7**, 11823 (2016).

[211] B. Luk'Yanchuk, N. I. Zheludev, S. A. Maier, N. J. Halas, P. Nordlander, H. Giessen, and C. T. Chong, Nat. Mater. **9**, 707 (2010).

[212] A. E. Miroshnichenko, S. Flach, and Y. S. Kivshar, Rev. Mod. Phys. **82**, 2257 (2010).

[213] Y. Vardi, E. Cohen-Hoshen, G. Shalem, and I. Bar-Joseph, Nano Lett. **16**, 748 (2016).

[214] C. Chen, P. Chu, C. A. Bobisch, D. L. Mills, and W. Ho, Phys. Rev. Lett. **105**, 217402 (2010).

[215] Y. Zhang, Q. Meng, L. Zhang, Y. Luo, Y. Yu, B. Yang, Y. Zhang, R. Esteban, J. Aizpurua, Y. Luo, J. Yang, Z. Dong, and J. G. Hou, Nat. Commun. **8**, 15225 (2017).

[216] J. Kröger, B. Doppagne, F. Scheurer, and G. Schull, Nano Lett. **18**, 3407 (2018).

[217] S. A. Svatek, J. Kerfoot, A. Summerfield, A. S. Nizovtsev, V. V. Korolkov, T. Taniguchi, K. Watanabe, E. Antolín, E. Besley, and P. H. Beton, Nano Lett. **20**, 278 (2020).

[218] T. Uemura, M. Furumoto, T. Nakano, M. Akai-Kasaya, A. Saito, M. Aono, and Y. Kuwahara, Chem. Phys. Lett. **448**, 232 (2007).

[219] A. Endo, K. Sato, K. Yoshimura, T. Kai, A. Kawada, H. Miyazaki, and C. Adachi, Appl. Phys. Lett. **98**, 083302 (2011).

[220] Y. Luo, F. Kong, X. Tian, Y. Yu, S. Jing, C. Zhang, G. Chen, Y. Zhang, Y. Zhang, X. Li, Z. Zhang, and Z. Dong, Nat. Commun. **15**, 1677 (2024).

[221] B. Doppagne, M. C. Chong, H. Bulou, A. Boeglin, F. Scheurer, and G. Schull, Science **361**, 251 (2018).

[222] M. C. Chong, N. Afshar-Imani, F. Scheurer, C. Cardoso, A. Ferretti, D. Prezzi, and G. Schull, Nano Lett. **18**, 175 (2018).

[223] M. C. Chong, L. Sosa-Vargas, H. Bulou, A. Boeglin, F. Scheurer, F. Mathevet, and G. Schull, Nano Lett. **16**, 6480 (2016).

[224] C. W. Marquardt, S. Grunder, A. Błaszczyk, S. Dehm, F. Hennrich, H. V. Löhneysen, M. Mayor, and R. Krupke, Nat. Nanotechnol. **5**, 863 (2010).

[225] S. Park, H. Kang, and H. J. Yoon, J. Mater. Chem. A **7**, 14419 (2019).

[226] Q. Zhang, Y. Sun, W. Xu, and D. Zhu, Adv. Mater. **26**, 6829 (2014).

[227] T. Markussen, J. Chem. Phys. **139**, 244101 (2013).

[228] S. V. Aradhya and L. Venkataraman, Nat. Nanotechnol. **8**, 399 (2013).

[229] B. Zhang, M. H. Garner, L. Li, L. M. Campos, G. C. Solomon, and L. Venkataraman, Chem. Sci. **12**, 10299 (2021).

[230] M. H. Garner, H. Li, Y. Chen, T. A. Su, Z. Shangguan, D. W. Paley, T. Liu, F. Ng, H. Li, S. Xiao, C. Nuckolls, L. Venkataraman, and G. C. Solomon, Nature **558**, 415 (2018).

[231] Y. Dubi and M. Di Ventra, Rev. Mod. Phys. **83**, 131 (2011).

[232] J. P. Bergfield, M. A. Solis, and C. A. Stafford, ACS. Nano **4**, 5314 (2010).

[233] J. Vacek, J. V. Chocholoušová, I. G. Stará, I. Starý, and Y. Dubi, Nanoscale **7**, 8793 (2015).

[234] H. D. Pandey and D. M. Leitner, J. Chem. Phys. **147**, 84701 (2017).

[235] S. H. Ke, W. Yang, S. Curtarolo, and H. U. Baranger, Nano Lett. **9**, 1011 (2009).

[236] N. Claughton and C. Lambert, Phys. Rev. B **53**, 6605 (1996).

[237] F. Hüser and G. C. Solomon, J. Phys. Chem. C **119**, 14056 (2015).

[238] M. Bürkle, L. A. Zotti, J. K. Viljas, D. Vonlanthen, A. Mishchenko, T. Wandlowski, M. Mayor, G. Schön, and F. Pauly, Phys. Rev. B **86**, 115304 (2012).

[239] L. A. Zotti, M. Bürkle, F. Pauly, W. Lee, K. Kim, W. Jeong, Y. Asai, P. Reddy, and J. C. Cuevas, New J. Phys. **16**, 015004 (2014).

[240] F. Pauly, J. K. Viljas, M. Bürkle, M. Dreher, P. Nielaba, and J. C. Cuevas, Phys. Rev. B **84**, 195420 (2011).

[241] M. Bürkle, T. J. Hellmuth, F. Pauly, and Y. Asai, Phys. Rev. B **91**, 165419 (2015).

[242] J. P. Bergfield and C. A. Stafford, Nano Lett. **9**, 3072 (2009).

[243] Z. Wang, J. A. Carter, A. Lagutchev, K. K. Yee, N. H. Seong, D. G. Cahilll, and D. D. Dlott, Science **317**, 787 (2007).

[244] A. A. Al-Jobory and M. D. Noori, J. Electron. Mater. **49**, 5455 (2020).

[245] C. J. Lambert, Chem. Soc. Rev. **44**, 875 (2015).

[246] S. H. Ke, Y. Weitao, and H. U. Baranger, Nano Lett. **8**, 3257 (2008).

[247] S. Ballmann, R. Härtle, P. B. Coto, M. Elbing, M. Mayor, M. R. Bryce, M. Thoss, and H. B. Weber, Phys. Rev. Lett. **109**, 056801 (2012).

[248] L. Huang, J. Wang, T. Chen, L. Xu, F. Ning, D. Wu, and K. Q. Chen, Appl. Phys. Lett. **124**, 102403 (2024).

[249] O. Sengul, A. Valli, and R. Stadler, Nanoscale **13**, 17011 (2021).

[250] O. Karlström, H. Linke, G. Karlström, and A. Wacker, Phys. Rev. B **84**, 113415 (2011).

[251] M. Bernien, D. Wiedemann, C. F. Hermanns, A. Kruüger, D. Rolf, W. Kroener, P. Muüller, A. Grohmann, and W. Kuch, J. Phys. Chem. Lett. **3**, 3431 (2012).

[252] D. Ghosh, P. Parida, and S. K. Pati, Appl. Phys. Lett. **106**, 193105 (2015).

[253] V. M. García-Suárez, C. J. Lambert, D. Z. Manrique, and T. Wandlowski, Nanotechnology **25**, 205402 (2014).

[254] H. Sadeghi, S. Sangtarash, and C. J. Lambert, Beilstein J. Nanotechnol. **6**, 1413 (2015).

[255] Q. H. Al-Galiby, H. Sadeghi, L. A. Algharagholy, I. Grace, and C. Lambert, Nanoscale **8**, 2428 (2016).

[256] M. A. Rivera Mateus, J. H. Ojeda, and D. Gallego, AIP. Adv. **10**, 65021 (2020).

[257] J. C. Klöckner, J. C. Cuevas, and F. Pauly, Phys. Rev. B **96**, 245419 (2017).

[258] C. M. Guédon, H. Valkenier, T. Markussen, K. S. Thygesen, J. C. Hummelen, and S. J. Van Der Molen, Nat. Nanotechnol. **7**, 305 (2012).

[259] T. Morikawa, A. Arima, M. Tsutsui, and M. Taniguchi, Nanoscale **6**, 8235 (2014).

[260] M. Tsutsui, T. Morikawa, Y. He, A. Arima, and M. Taniguchi, Sci. Rep. **5**, 11519 (2015).

[261] A. Aiba, F. Demir, S. Kaneko, S. Fujii, T. Nishino, K. Tsukagoshi, A. Saffarzadeh, G. Kirczenow, and M. Kiguchi, Sci. Rep. **7**, 7949 (2017).

[262] J. R. Widawsky, P. Darancet, J. B. Neaton, and L. Venkataraman, Nano Lett. **12**, 354 (2012).

[263] S. K. Yee, J. A. Malen, A. Majumdar, and R. A. Segalman, Nano Lett. **11**, 4089 (2011).

[264] A. Umeno and K. Hirakawa, Appl. Phys. Lett. **94**, 162103 (2009).

[265] C. Durkan, M. A. Schneider, and M. E. Welland, J. Appl. Phys. **86**, 1280 (1999).

[266] L. Rincón-García, C. Evangeli, G. Rubio-Bollinger, and N. Agraït, Chem. Soc. Rev. **45**, 4285 (2016).

[267] J. Hao, B. Wang, C. Zhao, Y. Huo, J. Wang, C. Jia, and X. Guo, Sci. China Mater. **67**, 1994 (2024).

[268] H. Ju, J. Wang, W. Liu, J. Hao, M. Li, Y. Xu, B. Wang, S. He, K. Mei, A. C.-H. Sue, K. Chen, C. Jia, and X. Guo, Chin. Chem. Soc. (published online, 2024).

[269] L. Zhou, M. Zhang, Y. Huo, L. Bai, S. He, J. Wang, C. Jia, and X. Guo, Green Energy Environ. (published online, 2024).

[270] B. Ludoph and J. M. Ruitenbeek, Phys. Rev. B **59**, 12290 (1999).

[271] S. Guo and G. Tao, Nano Lett. **13**, 4326 (2013).

[272] Y. Komoto, Y. Isshiki, S. Fujii, T. Nishino, and M. Kiguchi, Chem. Asian J. **12**, 440 (2017).

[273] P. Reddy, S.-Y. Jang, R. A. Segalman, and A. Majumdar, Science **315**, 1568 (2007).

[274] T. Fu, K. Frommer, C. Nuckolls, and L. Venkataraman, J. Phys. Chem. Lett. **12**, 10802 (2021).

[275] C. J. Lambert, H. Sadeghi, and Q. H. Al-Galiby, C. R. Phys. **17**, 1084 (2016).

[276] S. K. Lee, T. Ohto, R. Yamada, and H. Tada, Nano Lett. **14**, 5276 (2014).

[277] C. Evangeli, K. Gillemot, E. Leary, M. T. González, G. Rubio-Bollinger, C. J. Lambert, and N. Agraït, Nano Lett. **13**, 2141 (2013).

[278] J. A. Malen, P. Doak, K. Baheti, T. D. Tilley, A. Majumdar, and R. A. Segalman, Nano Lett. **9**, 3406 (2009).

[279] R. Miao, H. Xu, M. Skripnik, L. Cui, K. Wang, K. G. L. Pedersen, M. Leijnse, F. Pauly, K. Wärnmark, E. Meyhofer, P. Reddy, and H. Linke, Nano Lett. **18**, 5666 (2018).

[280] A. Tan, J. Balachandran, B. D. Dunietz, S. Y. Jang, V. Gavini, and P. Reddy, Appl. Phys. Lett. **101**, 243107 (2012).

[281] A. Tan, J. Balachandran, S. Sadat, V. Gavini, B. D. Dunietz, S. Y. Jang, and P. Reddy, J. Am. Chem. Soc. **133**, 8838 (2011).

[282] S. Park, J. W. Jo, J. Jang, T. Ohto, H. Tada, and H. J. Yoon, Nano Lett. **22**, 7682 (2022).

[283] E. J. Dell, B. Capozzi, J. Xia, L. Venkataraman, and L. M. Campos, Nat. Chem. **7**, 209 (2015).

[284] W. B. Chang, C. K. Mai, M. Kotiuga, J. B. Neaton, G. C. Bazan, and R. A. Segalman, Chem. Mater. **26**, 7229 (2014).

[285] Y. Li, L. Xiang, J. L. Palma, Y. Asai, and N. Tao, Nat. Commun. **7**, 11294 (2016).

[286] R. Panahinia and S. Behnia, Phys. Scr. **95**, 065004 (2020).

[287] S. Park, N. Cho, and H. J. Yoon, Chem. Mater. **31**, 5973 (2019).

[288] E. Maciá, Phys. Rev. B.**75**, 035130 (2007).

[289] X. D. Guo, X. R. Zhang, K. B. Zhang, M. D. He, M. Q. Long, S. H. Tan, and X. F. Peng, Results Phys. **51**, 106610 (2023).

[290] M. Alsaqer, A. H. S. Daaoub, S. Sangtarash, and H. Sadeghi, Nano Lett. **23**, 10719 (2023).

[291] L. Rincón-García, A. K. Ismael, C. Evangeli, I. Grace, G. Rubio-Bollinger, K. Porfyrakis, N. Agraït, and C. J. Lambert, Nat. Mater. **15**, 289 (2015).

[292] S. K. Lee, M. Buerkle, R. Yamada, Y. Asai, and H. Tada, Nanoscale **7**, 20497 (2015).

[293] L. Venkataraman, J. E. Klare, C. Nuckolls, M. S. Hybertsen, and M. L. Steigerwald, Nature **442**, 904 (2006).

[294] A. Mishchenko, D. Vonlanthen, V. Meded, M. Bürkle, C. Li, I. V. Pobelov, A. Bagrets, J. K. Viljas, F. Pauly, F. Evers, M. Mayor, and T. Wandlowski, Nano Lett. **10**, 156 (2010).

[295] S. Fujii, E. Montes, H. Cho, Y. Yue, M. Koike, T. Nishino, H. Vázquez, M. Kiguchi, S. Fujii, H. Cho, Y. Yue, M. Koike, T. Nishino, M. Kiguchi, E. Montes, and H. Vázquez, Adv. Electron. Mater. **8**, 2200700 (2022).

[296] J. Balachandran, P. Reddy, B. D. Dunietz, and V. Gavini, J. Phys. Chem. Lett. **4**, 3825 (2013).

[297] S. J. Youn, M. H. Fischer, S. H. Rhim, M. Sigrist, and D. F. Agterberg, Phys. Rev. B **85**, 220505 (2012).

[298] J. M. Hamill, A. Ismael, A. Al-Jobory, T. L. R. Bennett, M. Alshahrani, X. Wang, M. Akers-Douglas, L. A. Wilkinson, B. J. Robinson, N. J. Long, C. Lambert, and T. Albrecht, J. Phys. Chem. C **127**, 7484 (2023).

[299] N. Blankevoort, P. Bastante, R. J. Davidson, R. J. Salthouse, A. H. S. Daaoub, P. Cea, S. M. Solans, A. S. Batsanov, S. Sangtarash, M. R. Bryce, N. Agrait, and H. Sadeghi, ACS. Omega **9**, 8471 (2023).

[300] J. Balachandran, P. Reddy, B. D. Dunietz, and V. Gavini, J. Phys. Chem. Lett. **3**, 1962 (2012).

[301] K. Baheti, J. A. Malen, P. Doak, P. Reddy, S. Y. Jang, T. D. Tilley, A. Majumdar, and R. A. Segalman, Nano Lett. **8**, 715 (2008).

[302] S. Kang, S. Park, H. Kang, S. J. Cho, H. Song, and H. J. Yoon, Chem. Commun. **55**, 8780 (2019).

[303] J. Hurtado-Gallego, S. Sangtarash, R. Davidson, L. Rincón-García, A. Daaoub, G. Rubio-Bollinger, C. J. Lambert, V. S. Oganesyan, M. R. Bryce, N. Agraït, and H. Sadeghi, Nano Lett. **22**, 948 (2022).

[304] S. Park, S. Kang, and H. J. Yoon, Nano Lett. **22**, 3953 (2022).

[305] A. Ismael, X. Wang, T. L. R. Bennett, L. A. Wilkinson, B. J. Robinson, N. J. Long, L. F. Cohen, and C. J. Lambert, Chem. Sci. **11**, 6836 (2020).

[306] S. Ramezani Akbarabadi, H. R. Soleimani, and M. Bagheri Tagani, Sci. Rep. **11**, 8958 (2021).

[307] G. Yzambart, L. Rincón-García, A. A. Al-Jobory, A. K. Ismael, G. Rubio-Bollinger, C. J. Lambert, N. Agraït, and M. R. Bryce, J. Phys. Chem. C **122**, 27198 (2018).

[308] H. Chen, S. Sangtarash, G. Li, M. Gantenbein, W. Cao, A. Alqorashi, J. Liu, C. Zhang, Y. Zhang, L. Chen, Y. Chen, G. Olsen, H. Sadeghi, M. R. Bryce, C. J. Lambert, and W. Hong, Nanoscale **12**, 15150 (2020).

[309] H. Dekkiche, A. Gemma, F. Tabatabaei, A. S. Batsanov, T. Niehaus, B. Gotsmann, and M. R. Bryce, Nanoscale **12**, 18908 (2020).

[310] E. Zerah-Harush and Y. Dubi, Phys. Rev. Appl. **3**, 064017 (2015).

[311] C. Evangeli, M. Matt, L. Rincón-García, F. Pauly, P. Nielaba, G. Rubio-Bollinger, J. C. Cuevas, and N. Agraït, Nano Lett. **15**, 1006 (2015).

[312] D. Kim, P. S. Yoo, and T. Kim, J. Korean Phys. Soc. **66**, 602 (2015).

[313] K. Esfarjani, M. Zebarjadi, and Y. Kawazoe, Phys. Rev. B **73**, 085406 (2006).

[314] D. Nozaki, H. Sevinçli, W. Li, R. Gutiérrez, and G. Cuniberti, Phys. Rev. B **81**, 235406 (2010).

[315] D. Wu, X. H. Cao, P. Z. Jia, Y. J. Zeng, Y. X. Feng, L. M. Tang, W. X. Zhou, and K. Q. Chen, Sci. China Phys., Mech. Astron. **63**, 276811 (2020).

[316] Y. Kim, W. Jeong, K. Kim, W. Lee, and P. Reddy, Nat. Nanotechnol. **9**, 881 (2014).

[317] G. H. Kim, L. Shao, K. Zhang, and K. P. Pipe, Nat. Mater. **12**, 719 (2013).

[318] M. Famili, I. M. Grace, Q. Al-Galiby, H. Sadeghi, C. J. Lambert, M. Famili, I. M. Grace, H. Sadeghi, C. J. Lambert, and Q. Al-Galiby, Adv. Funct. Mater. **28**, 1703135 (2018).

[319] P. Gehring, J. K. Sowa, C. Hsu, J. de Bruijckere, M. van der Star, J. J. Le Roy, L. Bogani, E. M. Gauger, and H. S. J. van der Zant, Nat. Nanotechnol. **16**, 426 (2021).

[320] M. Li, H. Wu, E. M. Avery, Z. Qin, D. P. Goronzy, H. D. Nguyen, T. Liu, P. S. Weiss, and Y. Hu, Science **382**, 585 (2023).

[321] C. Fang, R. Almughathawi, Q. Wu, W. Cao, H. Chen, S. Hou, Y. Gu, H. Zhang, Y. Zhao, J. Zheng, G. Li, J. Shi, J. Liu, B.-W. Mao, Z. Liu, C. J. Lambert, and W. Hong, Natl. Sci. Open **2**, 20220039 (2023).

[322] J. Liu, X. Huang, F. Wang, and W. Hong, Acc. Chem. Res. **52**, 151 (2019).

[323] H. Chen, Y. Chen, H. Zhang, W. Cao, C. Fang, Y. Zhou, Z. Xiao, J. Shi, W. Chen, J. Liu, and W. Hong, Chin. Chem. Lett. **33**, 523 (2022).

[324] I. M. Grace, G. Olsen, J. Hurtado-Gallego, L. Rincón-Garciá, G. Rubio-Bollinger, M. R. Bryce, N. Agraït, and C. J. Lambert, Nanoscale **12**, 14682 (2020).

[325] T. Ghomian, O. Kizilkaya, L. K. Domulevicz, and J. Hihath, Nanoscale **14**, 6248 (2022).

[326] J. E. Greenwald, J. Cameron, N. J. Findlay, T. Fu, S. Gunasekaran, P. J. Skabara, and L. Venkataraman, Nat. Nanotechnol. **16**, 313 (2021).

[327] X. Wang, T. L. R. Bennett, A. Ismael, L. A. Wilkinson, J. Hamill, A. J. P. White, I. M. Grace, O. V. Kolosov, T. Albrecht, B. J. Robinson, N. J. Long, L. F. Cohen, and C. J. Lambert, J. Am. Chem. Soc. **142**, 8555 (2020).

[328] A. Henry and G. Chen, Phys. Rev. Lett. **101**, 235502 (2008).

[329] J. Liu and R. Yang, Phys. Rev. B **86**, 104307 (2012).

[330] Y. J. Zeng, D. Wu, X. H. Cao, Y. X. Feng, L. M. Tang, and K. Q. Chen, J. Mater. Chem. A **8**, 11884 (2020).

[331] A. Pecchia, G. Romano, and A. Di Carlo, Phys. Rev. B **75**, 035401 (2007).

[332] R. Landauer, IBM. J. Res. Dev. **1**, 223 (1957).

[333] E. Scheer and J. C. Cuevas, Molecular Electronics: An Introduction to Theory and Experiment (World Scientific, 2017), Vol. 15.

[334] M. Galperin, M. A. Ratner, and A. Nitzan, J. Chem. Phys. **121**, 11965 (2004).

[335] D. Segal and B. K. Agarwalla, Annu. Rev. Phys. Chem. **67**, 185 (2016).

[336] T. Yamamoto and K. Watanabe, Phys. Rev. Lett. **96**, 255503 (2006).

[337] M. Galperin, A. Nitzan, and M. A. Ratner, Phys. Rev. B **75**, 155312 (2007).

[338] J.-S. Wang, J. Wang, and J. T. Lü, Eur. Phys. J. B **62**, 381 (2008).

[339] R. Lake and S. Datta, Phys. Rev. B **46**, 4757 (1992).

[340] H. Sevinçli1, S. Roche, G. Cuniberti, M. Brandbyge, R. Gutierrez, and L. Medrano Sandonas, J. Phys. **31**, 273003 (2019).

[341] A. Dhar, K. Saito, and P. Hänggi, Phys. Rev. E **85**, 011126 (2012).

[342] A. Majumdar, Annu. Rev. Mater. Sci. **29**, 505 (1999).

[343] P. Jiang, X. Qian, and R. Yang, J. Appl. Phys. **124**, 161103 (2018).

[344] D. H. Olson, J. L. Braun, and P. E. Hopkins, J. Appl. Phys. **126**, 150901 (2019).

[345] T. Meier, F. Menges, P. Nirmalraj, H. Hölscher, H. Riel, and B. Gotsmann, Phys. Rev. Lett. **113**, 060801 (2014).

[346] A. Jain and K. E. Goodson, J. Heat. Transfer **130**, 102402 (2008).

[347] S. C. Yelishala, C. Murphy, and L. Cui, J. Mater. Chem. A **12**, 10614 (2024).

[348] L. Cui, W. Jeong, V. Fernández-Hurtado, J. Feist, F. J. García-Vidal, J. C. Cuevas, E. Meyhofer, and P. Reddy, Nat. Commun. **8**, 14479 (2017).

[349] F. Menges, P. Mensch, H. Schmid, H. Riel, A. Stemmer, and B. Gotsmann, Nat. Commun. **7**, 10874 (2016).

[350] K. Kim, W. Jeong, W. Lee, and P. Reddy, ACS. Nano **6**, 4248 (2012).

[351] L. Cui, W. Jeong, S. Hur, M. Matt, J. C. Klöckner, F. Pauly, P. Nielaba, J. C. Cuevas, E. Meyhofer, and P. Reddy, Science **355**, 1192 (2017).

[352] N. Mosso, U. Drechsler, F. Menges, P. Nirmalraj, S. Karg, H. Riel, and B. Gotsmann, Nat. Nanotechnol. **12**, 430 (2017).

[353] L. Cui, S. Hur, Z. A. Akbar, J. C. Klöckner, W. Jeong, F. Pauly, S.-Y. Jang, P. Reddy, and E. Meyhofer, Nature **572**, 628 (2019).

[354] W. Lee, K. Kim, W. Jeong, L. A. Zotti, F. Pauly, J. C. Cuevas, and P. Reddy, Nature **498**, 209 (2013).

[355] L. Cui, R. Miao, K. Wang, D. Thompson, L. A. Zotti, J. C. Cuevas, E. Meyhofer, and P. Reddy, Nat. Nanotechnol. **13**, 122 (2018).

[356] Q. Li, M. Strange, I. Duchemin, D. Donadio, and G. C. Solomon, J. Phys. Chem. C **121**, 7175 (2017).

[357] H. Sadeghi, J. Phys. Chem. C **123**, 12556 (2019).

[358] R. Chen, I. Sharony, A. Nitzan, and A. Nitzan, J. Phys. Chem. Lett. **11**, 4261 (2020).

[359] L. Cui, R. Miao, C. Jiang, E. Meyhofer, and P. Reddy, J. Chem. Phys. **146**, 092201 (2017).

[360] X.-D. Zhang, G. Yang, and B.-Y. Cao, Adv. Mater. Interfaces **9**, 2200078 (2022).

[361] M. Famili, I. Grace, H. Sadeghi, and C. J. Lambert, ChemPhysChem **18**, 1234 (2017).

[362] M. D. Noori, S. Sangtarash, and H. Sadeghi, Appl. Sci. **11**, 1066 (2021).

[363] E. Fermi, P. Pasta, S. Ulam, and M. Tsingou, Studies of the Nonlinear Problems (Los Alamos National Laboratory (LANL), Los Alamos, 1955), No. LA-1940.

[364] A. Dhar, Adv. Phys. **57**, 457 (2008).

[365] S. Lepri, R. Livi, and A. Politi, Phys. Rep. **377**, 1–80 (2003).

[366] D. Segal, A. Nitzan, and P. Hänggi, J. Chem. Phys. **119**, 68400 (2003).

[367] H. Sadeghi, S. Sangtarash, and C. J. Lambert, Nano Lett. **15**, 7467 (2015).

[368] J. C. Klöckner, M. Bürkle, J. C. Cuevas, and F. Pauly, Phys. Rev. B **94**, 205425 (2016).

[369] J. C. Duda, C. B. Saltonstall, P. M. Norris, and P. E. Hopkins, J. Chem. Phys. **134**, 94704 (2011).

[370] J. V. Goicochea, M. Hu, B. Michel, and D. Poulikakos, J. Heat. Transfer **133**, 082401 (2011).

[371] L. Hu, L. Zhang, M. Hu, J. S. Wang, B. Li, and P. Keblinski, Phys. Rev. B **81**, 235427 (2010).

[372] E. Díaz, R. Gutierrez, and G. Cuniberti, Phys. Rev. B **84**, 144302 (2011).

[373] D. Segal, Phys. Rev. B **73**, 205415 (2006).

[374] D. Segal and A. Nitzan, J. Chem. Phys. **122**, 194704 (2005).

[375] D. Segal and A. Nitzan, Phys. Rev. Lett. **94**, 034301 (2005).

[376] M. G. Menezes, A. Saraiva-Souza, J. Del Nero, and R. B. Capaz, Phys. Rev. B **81**, 012302 (2010).

[377] Q. Li, I. Duchemin, S. Xiong, G. C. Solomon, and D. Donadio, J. Phys. Chem. C **119**, 24636 (2015).

[378] F. Zhan, N. Li, S. Kohler, and P. Hänggi, Phys. Rev. E **80**, 061115 (2009).

[379] D. Segal and A. Nitzan, J. Chem. Phys. **117**, 3915 (2002).

[380] P. Carpio-Martínez and G. Hanna, J. Chem. Phys. **154**, 94108 (2021).

[381] R. D'Agosta, N. Sai, and M. Di Ventra, Nano Lett. **6**, 2935 (2006).

[382] R. Härtle and M. Thoss, Phys. Rev. B **83**, 115414 (2011).

[383] L. Simine and D. Segal, Phys. Chem. Chem. Phys. **14**, 13820 (2012).

[384] M. Tsutsui, S. Kurokawa, and A. Sakai, Nanotechnology **17**, 5334 (2006).

[385] M. Tsutsui, M. Taniguchi, and T. Kawai, Nano Lett. **8**, 3293 (2008).

[386] Z. Huang, F. Chen, R. D'Agosta, P. A. Bennett, M. Di Ventra, and N. Tao, Nat. Nanotechnol. **2**, 698 (2007).

[387] M. A. Reed, Mater. Today **11**, 46 (2008).

[388] D. R. Ward, D. A. Corley, J. M. Tour, and D. Natelson, Nat. Nanotechnol. **6**, 33 (2011).

[389] Q. Meng, J. Zhang, Y. Zhang, W. Chu, W. Mao, Y. Zhang, J. Yang, Y. Luo, Z. Dong, and J. G. Hou, Sci. Adv. **10**, 1015 (2024).

[390] L. Yang, Y. Tao, Y. Zhu, M. Akter, K. Wang, Z. Pan, Y. Zhao, Q. Zhang, Y.-Q. Xu, R. Chen, T. T. Xu, Y. Chen, Z. Mao, and D. Li, Nat. Nanotechnol. **16**, 764 (2021).

[391] C. L. Choy, Polymer **18**, 984 (1977).

[392] A. Henry and G. Chen, Phys. Rev. B **79**, 144305 (2009).

[393] J. J. Freeman, G. J. Morgan, and C. A. Cullen, Phys. Rev. B **35**, 7627 (1987).

[394] K. Sasikumar and P. Keblinski, J. Appl. Phys. **109**, 114307 (2011).

[395] R. Shrestha, P. Li, B. Chatterjee, T. Zheng, X. Wu, Z. Liu, T. Luo, S. Choi, K. Hippalgaonkar, M. P. De Boer, and S. Shen, Nat. Commun. **9**, 1664 (2018).

[396] C. Yang, S. Raza, X. Li, and J. Liu, J. Phys. Chem. B **127**, 6804 (2023).

[397] Z. Tian, A. Marconnet, and G. Chen, Appl. Phys. Lett. **106**, 211602 (2015).

[398] R. Y. Wang, R. A. Segalman, and A. Majumdar, Appl. Phys. Lett. **89**, 173113 (2006).

[399] A. Ota, M. Ohnishi, H. Oshima, T. Shiga, T. Kodama, and J. Shiomi, ACS. Appl. Mater. Interfaces **11**, 37295 (2019).

[400] W. A. Little, Can. J. Phys. **37**, 334 (1959).

[401] E. T. Swartz and R. O. Pohl, Appl. Phys. Lett. **51**, 2200 (1987).

[402] P. E. Hopkins, ISRN Mech. Eng. **2013**, 682586.

[403] P. E. Hopkins, J. C. Duda, C. W. Petz, and J. A. Floro, Phys. Rev. B **84**, 035438 (2011).

[404] H. Acharya, N. J. Mozdzierz, P. Keblinski, and S. Garde, Ind. Eng. Chem. Res. **51**, 1767 (2012).

[405] Y. Wang, Y. Cao, K. Zhou, and Z. Xu, Adv. Mater. Interfaces **4**, 1700355 (2017).

[406] J. Lu, K. Yuan, F. Sun, K. Zheng, Z. Zhang, J. Zhu, X. Wang, X. Zhang, Y. Zhuang, Y. Ma, X. Cao, J. Zhang, and D. Tang, ACS. Appl. Mater. Interfaces **11**, 42708 (2019).

[407] F. Sun, T. Zhang, M. M. Jobbins, Z. Guo, X. Zhang, Z. Zheng, D. Tang, S. Ptasinska, T. Luo, F. Sun, T. Zhang, Z. Guo, T. Luo, D. Tang, M. M. Jobbins, X. Zhang, Z. Guo, S. Ptasinska, and Z. Zheng, Adv. Mater. **26**, 6093 (2014).

[408] R. E. Peterson and A. C. Anderson, Phys. Lett. A **40**, 317 (1972).

[409] S. M. Lee and D. G. Cahill, J. Appl. Phys. **81**, 2590 (1997).

[410] R. B. Wilson, B. A. Apgar, W. P. Hsieh, L. W. Martin, and D. G. Cahill, Phys. Rev. B **91**, 115414 (2015).

[411] Y. Chalopin and S. Volz, Appl. Phys. Lett. **103**, 51602 (2013).

[412] G. T. Hohensee, R. B. Wilson, and D. G. Cahill, Nat. Commun. **6**, 6578 (2015).

[413] D. A. Young and H. J. Maris, Phys. Rev. B **40**, 3685 (1989).

[414] P. Singh, M. Seong, and S. Sinha, Appl. Phys. Lett. **102**, 181906 (2013).

[415] D. H. Olson, M. G. Sales, J. A. Tomko, T. F. Lu, O. V. Prezhdo, S. J. McDonnell, and P. E. Hopkins, Appl. Phys. Lett. **118**, 163503 (2021).

[416] M. Li, Y. Wang, J. Zhou, J. Ren, and B. Li, Eur. Phys. J. B **88**, 149 (2015).

[417] L. Medrano Sandonas, Á. Rodríguez Méndez, R. Gutierrez, J. M. Ugalde, V. Mujica, and G. Cuniberti, J. Phys. Chem. C **123**, 9680 (2019).

[418] M. D. Losego, M. E. Grady, N. R. Sottos, D. G. Cahill, and P. V. Braun, Nat. Mater. **11**, 502 (2012).

[419] P. J. O'Brien, S. Shenogin, J. Liu, P. K. Chow, D. Laurencin, P. H. Mutin, M. Yamaguchi, P. Keblinski, and G. Ramanath, Nat. Mater. **12**, 118 (2013).

[420] D. Huang, R. Ma, T. Zhang, and T. Luo, ACS. Appl. Mater. Interfaces **10**, 28159 (2018).

[421] J. Zhong, Q. Xi, Z. Wang, T. Nakayama, X. Li, J. Liu, and J. Zhou, J. Appl. Phys. **129**, 195102 (2021).

[422] Z. Zong, S. Deng, Y. Qin, X. Wan, J. Zhan, D. Ma, and N. Yang, Nanoscale **15**, 16472 (2023).

[423] S. Majumdar, J. A. Sierra-Suarez, S. N. Schiffres, W. L. Ong, C. F. Higgs, A. J. H. McGaughey, and J. A. Malen, Nano Lett. **15**, 2985 (2015).

[424] R. Prasher, Appl. Phys. Lett. **94**, 41905 (2009).

[425] T. Zhang, A. R. Gans-Forrest, E. Lee, X. Zhang, C. Qu, Y. Pang, F. Sun, and T. Luo, ACS Appl. Mater. Interfaces **8**, 33326 (2016).

[426] Z. Ge, D. G. Cahill, and P. V. Braun, Phys. Rev. Lett. **96**, 186101 (2006).

[427] L. Zhang, Z. Bai, L. Liu, L. Zhang, Z. Bai, and L. Liu, Adv. Mater. Interfaces **3**, 1600211 (2016).

[428] B. Lu, B. Wang, Y. Chen, A. Facchetti, T. J. Marks, and O. Balogun, ACS. Appl. Mater. Interfaces **12**, 34901 (2020).

[429] H. A. Patel, S. Garde, and P. Keblinski, Nano Lett. **5**, 2225 (2005).

[430] S. W. Hung, G. Kikugawa, and J. Shiomi, J. Phys. Chem. C **120**, 26678 (2016).

[431] A. Wisitsorasak and P. G. Wolynes, Proc. Natl. Acad. Sci. U. S. A. **109**, 16068 (2012).

[432] Y. Li, N. L. Haworth, L. Xiang, S. Ciampi, M. L. Coote, and N. Tao, J. Am. Chem. Soc. **139**, 14699 (2017).

[433] M. C. Walkey, C. R. Peiris, S. Ciampi, A. C. Aragonès, R. B. Domínguez-Espíndola, D. Jago, T. Pulbrook, B. W. Skelton, A. N. Sobolev, I. D. Pérez, M. J. Piggott, G. A. Koutsantonis, and N. Darwish, ACS Appl. Mater. Interfaces **11**, 36886 (2019).

[434] T. Michnowicz, B. Borca, R. Pétuya, V. Schendel, M. Pristl, I. Pentegov, U. Kraft, H. Klauk, P. Wahl, P. Mutombo, P. Jelínek, A. Arnau, U. Schlickum, and K. Kern, Angew. Chem., Int. Ed. **59**, 6207 (2020).

[435] Y. Zang, A. Pinkard, Z.-F. Liu, J. B. Neaton, M. L. Steigerwald, X. Roy, and L. Venkataraman, J. Am. Chem. Soc. **139**, 14845 (2017).

[436] T. A. Su, M. Neupane, M. L. Steigerwald, L. Venkataraman, and C. Nuckolls, Nat. Rev. Mater. **1**, 16002 (2016).

[437] A. C. Aragonès, N. L. Haworth, N. Darwish, S. Ciampi, N. J. Bloomfield, G. G. Wallace, I. Diez-Perez, and M. L. Coote, Nature **531**, 88 (2016).

[438] X. Huang, C. Tang, J. Li, L.-C. Chen, J. Zheng, P. Zhang, J. Le, R. Li, X. Li, J. Liu, Y. Yang, J. Shi, Z. Chen, M. Bai, H.-L. Zhang, H. Xia, J. Cheng, Z.-Q. Tian, and W. Hong, Sci. Adv. **5**, eaaw3072 (2019).

[439] C. Yang, Z. Liu, Y. Li, S. Zhou, C. Lu, Y. Guo, M. Ramirez, Q. Zhang, Y. Li, Z. Liu, K. N. Houk, D. Zhang, and X. Guo, Sci. Adv. **7**, eabf0689 (2021).

[440] H. Chen, F. Jiang, C. Hu, Y. Jiao, S. Chen, Y. Qiu, P. Zhou, L. Zhang, K. Cai, B. Song, X.-Y. Chen, X. Zhao, M. R. Wasielewski, H. Guo, W. Hong, and J. F. Stoddart, J. Am. Chem. Soc. **143**, 8476 (2021).

[441] Y. Echegoyen, I. Suelves, M. J. Lázaro, R. Moliner, and J. M. Palacios, J. Power. Sources **169**, 150 (2007).

[442] D. Wang, J. Zhang, J. B. Sun, W. M. Gao, and Y. B. Cui, Int. J. Hydrogen Energy **44**, 7205 (2019).

[443] S. Bekhouche, D. Trache, A. Abdelaziz, A. F. Tarchoun, S. Chelouche, A. Boudjellal, and A. Mezroua, Chem. Eng. J. **453**, 139845 (2023).

[444] P. Wu, X. J. Jin, Y. C. Qiu, and D. Q. Ye, Environ. Sci. Technol. **55**, 4268 (2021).

[445] Y. J. Lin, I. Khan, S. Saha, C. C. Wu, S. R. Barman, F. C. Kao, and Z. H. Lin, Nat. Commun. **12**, 180 (2021).

[446] C. Yang, Z. Chen, C. Yu, J. Cao, G. Ke, W. Zhu, W. Liang, J. Huang, W. Cai, C. Saha, M. A. Sabuj, N. Rai, X. Li, J. Yang, Y. Li, F. Huang, and X. Guo, Nat. Nanotechnol. **19**, 978 (2024).

[447] S. Chen, D. Su, C. Jia, Y. Li, X. Li, X. Guo, D. A. Leigh, and L. Zhang, Chem **8**, 243 (2022).

[448] Y. Guo, C. Yang, H. Li, L. Zhang, S. Zhou, X. Zhu, H. Fu, Z. Li, Z. Liu, C. Jia, Z. Liu, W. Zhu, F. Mo, D. Zhang, and X. Guo, J. Am. Chem. Soc. **144**, 3146 (2022).

[449] K. Uchida, S. Takahashi, K. Harii, J. Ieda, W. Koshibae, K. Ando, S. Maekawa, and E. Saitoh, Nature **455**, 778 (2008).

[450] K. Uchida, H. Adachi, T. An, T. Ota, M. Toda, B. Hillebrands, S. Maekawa, and E. Saitoh, Nat. Mater. **10**, 737 (2011).

[451] K. Uchida, T. Nonaka, T. Ota, and E. Saitoh, Appl. Phys. Lett. **97**, 262504 (2010).

[452] M. Erekhinsky, F. Casanova, I. K. Schuller, and A. Sharoni, Appl. Phys. Lett. **100**, 212401 (2012).

[453] C. M. Jaworski, R. C. Myers, E. Johnston-Halperin, and J. P. Heremans, Nature **487**, 210 (2012).

[454] R. Ramos, T. Kikkawa, K. Uchida, H. Adachi, I. Lucas, M. H. Aguirre, P. Algarabel, L. Morellón, S. Maekawa, E. Saitoh, and M. R. Ibarra, Appl. Phys. Lett. **102**, 072413 (2013).

[455] S. Pantke and G. R. Stewart, Solid State Commun. **108**, 221 (1998).

[456] D. Goldhaber-Gordon, H. Shtrikman, D. Mahalu, D. Abusch-Magder, U. Meirav, and M. A. Kastner, Nature **391**, 156 (1998).

[457] K. Chen and C. Jayaprakash, Phys. Rev. B **57**, 5225 (1998).

[458] S. M. Cronenwett, T. H. Oosterkamp, and L. P. Kouwenhoven, Science **281**, 540 (1998).

[459] S. Sasaki, S. De Franceschi, J. M. Elzerman, W. G. van der Wiel, M. Eto, S. Tarucha, and L. P. Kouwenhoven, Nature **405**, 764 (2000).

[460] R. Naaman, Abstr. Pap. Am. Chem. Soc. **249**, 1155 (2015).

[461] P. Hedegård, J. Chem. Phys. **159**, 104104 (2023).

[462] T. Gao, Q. P. Tian, M. Z. Du, L. L. Zhang, X. Liu, W. Qin, and S. J. Xie, Appl. Phys. Lett. **120**, 032405 (2022).

[463] H. Shishido, Y. Hosaka, K. Monden, A. Inui, T. Sayo, Y. Kousaka, and Y. Togawa, J. Chem. Phys. **159**, 064502 (2023).
[464] J. Chen and S. Hershfield, Phys. Rev. B **57**, 1097 (1998).
[465] F. Zuo, X. Su, P. Zhang, J. A. Schlueter, M. E. Kelly, and J. M. Williams, Phys. Rev. B **57**, R5610 (1998).
[466] H. Sato, S. Miya, Y. Kobayashi, Y. Aoki, H. Yamamoto, and M. Nakada, J. Appl. Phys. **83**, 5927 (1998).
[467] G. Neuttiens, J. Eom, C. Strunk, H. Pattyn, C. Van Haesendonck, Y. Bruynseraede, and V. Chandrasekhar, Europhys. Lett. **42**, 185 (1998).
[468] Z. P. Niu, Phys. Lett. A **375**, 3218 (2011).
[469] X. Y. Ye, H. Y. Xu, and M. Zhu, J. Phys. D **56**, 065001 (2023).
[470] I. Weymann and J. Barnás, Phys. Rev. B **88**, 085313 (2013).
[471] H. L. Wang, M. X. Wang, C. Qian, X. K. Hong, D. B. Zhang, Y. S. Liu, and X. F. Yang, Phys. Lett. A **381**, 1738 (2017).
[472] R.-Q. Wang, L. Sheng, R. Shen, B. Wang, and D. Y. Xing, Phys. Rev. Lett. **105**, 057202 (2010).
[473] P. S. Cornaglia, G. Usaj, and C. A. Balseiro, Phys. Rev. B **86**, 041107 (2012).
[474] Y. J. Hu, S. S. Liu, J. Huang, X. X. Li, and Q. X. Li, Nano Lett. **23**, 7890 (2023).
[475] J. F. Wang and Y. F. Yang, Phys. Rev. B **104**, 165120 (2021).
[476] I. Garate, Phys. Rev. B **84**, 085121 (2011).
[477] G. D. Scott and D. Natelson, ACS Nano **4**, 3560 (2010).
[478] R. Frisenda, R. Gaudenzi, C. Franco, M. Mas-Torrent, C. Rovira, J. Veciana, I. Alcon, S. T. Bromley, E. Burzurí, and H. S. J. van der Zant, Nano Lett. **15**, 3109 (2015).
[479] G. Mitra, J. Z. Low, S. J. Wei, K. R. Francisco, M. Definer, C. Herrmann, L. M. Campos, and E. Scheer, Nano Lett. **22**, 5773 (2022).
[480] M. Manso, M. Koole, M. Mulder, I. J. Olavarria-Contreras, C. L. Andersen, M. Jevric, S. L. Broman, A. Kadziola, O. Hammerich, H. S. J. van der Zant, and M. B. Nielsen, J. Org. Chem. **81**, 8406 (2016).
[481] H. J. Eckvahl, N. A. Tcyrulnikov, A. Chiesa, J. M. Bradley, R. M. Young, S. Carretta, M. D. Krzyaniak, and M. R. Wasielewski, Science **382**, 197 (2023).
[482] M. Z. Du, X. Liu, X. H. Liu, and S. J. Xie, Phys. Rev. B **108**, 125419 (2023).
[483] Y. Tiwari and V. S. Poonia, Phys. Rev. A **107**, 052406 (2023).
[484] T. P. Fay and D. T. Limmer, Nano Lett. **21**, 6696 (2021).
[485] Z. T. Xie, T. Z. Markus, S. R. Cohen, Z. Vager, R. Gutierrez, and R. Naaman, Nano Lett. **11**, 4652 (2011).
[486] A. C. Aragonès, E. Medina, M. Ferrer-Huerta, N. Gimeno, M. Teixidó, J. L. Palma, N. Tao, J. M. Ugalde, E. Giralt, I. Díez-Pérez, and V. Mujica, Small **13**, 1602519 (2016).
[487] H. Al-Bustami, G. Koplovitz, D. Primc, S. Yochelis, E. Capua, D. Porath, R. Naaman, and Y. Paltiel, Small **14**, 1801249 (2018).
[488] G. Koplovitz, D. Primc, O. B. Dor, S. Yochelis, D. Rotem, D. Porath, and Y. Paltiel, Adv. Mater. **29**, 1606748 (2017).
[489] A. C. Aragonès, D. Aravena, F. J. Valverde-Muñoz, J. A. Real, F. Sanz, I. Díez-Pérez, and E. Ruiz, J. Am. Chem. Soc. **139**, 5768 (2017).
[490] K. Yang, H. Chen, T. Pope, Y. B. Hu, L. W. Liu, D. F. Wang, L. Tao, W. D. Xiao, X. M. Fei, Y. Y. Zhang, H. G. Luo, S. X. Du, T. Xiang, W. A. Hofer, and H. J. Gao, Nat. Commun. **10**, 3599 (2019).
[491] J. Li, M. Bai, Z. Chen, X. Zhou, Z. Shi, M. Zhang, S. Ding, S. Hou, W. Schwarzacher, R. J. Nichols, and B. Mao, J. Am. Chem. Soc. **137**, 5923 (2015).
[492] J. Li, Z. Chen, Y. Wang, X. Zhou, L. Xie, Z. Shi, J. Liu, J. Yan, and B. Mao, Electrochim. Acta **389**, 138760 (2021).
[493] P. Li, L. Zhou, C. Zhao, H. Ju, Q. Gao, W. Si, L. Cheng, J. Hao, M. Li, Y. Chen, C. Jia, and X. Guo, Rep. Prog. Phys. **85**, 086401 (2022).
[494] C. Bosshard, R. Spreiter, L. Degiorgi, and P. Günter, Phys. Rev. B **66**, 205107 (2002).
[495] Z. C. Liu, X. S. Dong, Y. F. Liao, Y. P. Fan, and Y. J. Cao, Molecules **29**, 1034 (2024).
[496] T. Inagaki, M. Hatanaka, and S. Saito, J. Phys. Chem. B **127**, 5869 (2023).
[497] A. Niño and C. Muñoz-Caro, J. Phys. Chem. A **102**, 1177 (1998).
[498] A. van de Walle and G. Ceder, Rev. Mod. Phys. **74**, 11 (2002).
[499] B. Sohbi, A. Emtir, and M. Elgarni, Proc. World Acad. Sci. E **23**, 311 (2007).
[500] L. H. Yu, Z. K. Keane, J. W. Ciszek, L. Cheng, M. P. Stewart, J. M. Tour, and D. Natelson, Phys. Rev. Lett. **93**, 266802 (2004).
[501] J. Guo, D. Y. Cao, J. Chen, K. Bian, L. M. Xu, E. G. Wang, and Y. Jiang, J. Chem. Phys. **152**, 234301 (2020).
[502] T. Kumagai, F. Hanke, S. Gawinkowski, J. Sharp, K. Kotsis, J. Waluk, M. Persson, and L. Grill, Phys. Rev. Lett. **111**, 246101 (2013).
[503] C. Yang, P. Shen, Q. Ou, Q. Peng, S. Zhou, J. Li, Z. Liu, Z. Zhao, A. Qin, Z. Shuai, B. Z. Tang, and X. Guo, Matter **5**, 1224 (2022).
[504] X. Zhu, B. Wang, W. Xiong, S. Zhou, K. Qu, J. T. Lü, H. Chen, C. Jia, and X. Guo, Angew. Chem., Int. Ed. **61**, e202210939 (2022).
[505] Y. X. Wang, Z. R. Zhao, Z. Q. Chen, Y. Zhang, L. Zhang, and K. J. Kang, Opt. Lett. **33**, 1354 (2008).
[506] M. C. Beard, G. M. Turner, and C. A. Schmuttenmaer, J. Phys. Chem. A **106**, 878 (2002).
[507] P. U. Jepsen and S. J. Clark, Chem. Phys. Lett. **442**, 275 (2007).
[508] S. Du, K. Yoshida, Y. Zhang, I. Hamada, and K. Hirakawa, Nat. Photonics **12**, 608 (2018).
[509] T. L. Cocker, V. Jelic, M. Gupta, S. J. Molesky, J. A. J. Burgess, G. De Los Reyes, L. V. Titova, Y. Y. Tsui, M. R. Freeman, and F. A. Hegmann, Nat. Photonics **7**, 620 (2013).
[510] Y. Shimada, K. Hirakawa, M. Odnoblioudov, and K. A. Chao, Phys. Rev. Lett. **90**, 046806 (2003).
[511] H. Rascón-Ramos, J. M. Artés, Y. Li, and J. Hihath, Nat. Mater. **14**, 517 (2015).
[512] P. Pla-Vilanova, A. C. Aragonès, S. Ciampi, F. Sanz, N. Darwish, and I. Diez-Perez, Nanotechnology **26**, 381001 (2015).
[513] N. Darwish, P. K. Eggers, S. Ciampi, Y. Zhang, Y. Tong, S. Ye, M. N. Paddon-Row, and J. J. Gooding, Electrochem. Commun. **13**, 387 (2011).
[514] K. Wang, E. Meyhofer, and P. Reddy, Adv. Funct. Mater. **30**, 1904534 (2020).
[515] A. Gemma, F. Tabatabaei, U. Drechsler, A. Zulji, H. Dekkiche, N. Mosso, T. Niehaus, M. R. Bryce, S. Merabia, and B. Gotsmann, Nat. Commun. **14**, 3868 (2023).
[516] R. Chen and G. T. Graven, J. Phys. **36**, 405201 (2024).
[517] P. Lheritier, A. Torelló, T. Usui, Y. Nouchokgwe, A. Aravindhan, J. Li, U. Prah, V. Kovacova, O. Bouton, S. Hirose, and E. Defay, Nature **609**, 718 (2022).
[518] P. Portugal, F. Brange, and C. Flindt, Phys. Rev. Res. **4**, 043112 (2022).
[519] R. Chen, T. Gibson, and G. T. Craven, Phys. Rev. E. **108**, 024148 (2023).
[520] T. J. Shimokusu, Q. Zhu, N. Rivera, and G. Wehmeyer, Int. J. Heat Mass Transfer **182**, 122035 (2022).
[521] F. Evers, A. Aharony, N. Bar-Gill, O. Entin-Wohlman, P. Hedegård, O. Hod, P. Jelinek, G. Kamieniarz, M. Lemeshko, K. Michaeli, V. Mujica, R. Naaman, Y. Paltiel, S. Refaely-Abramson, O. Tal, J. Thijssen, M. Thoss, J. M. van Ruitenbeek, L. Venkataraman, D. H. Waldeck, B. Yan, and L. Kronik, Adv. Mater. **34**, 2106629 (2022).
[522] A. Merchant, S. Batzner, S. S. Schoenholz, M. Aykol, G. Cheon, and E. D. Cubuk, Nature **624**, 80 (2023).
[523] N. J. Szymanski, B. Rendy, Y. Fei, R. E. Kumar, T. He, D. Milsted, M. J. McDermott, M. Gallant, E. D. Cubuk, A. Merchant, H. Kim, A. Jain, C. J. Bartel, K. Persson, Y. Zeng, and G. Ceder, Nature **624**, 86 (2023).
[524] E. Callaway, Nature **588**, 203 (2020).
[525] J. Jumper, R. Evans, A. Pritzel, T. Green, M. Figurnov, O. Ronneberger, K. Tunyasuvunakool, R. Bates, A. Žídek, A. Potapenko, A. Bridgland, C. Meyer, S. A. A. Kohl, A. J. Ballard, A. Cowie, B. Romera-Paredes, S. Nikolov, R. Jain, J. Adler, T. Back, S. Petersen, D. Reiman, E. Clancy, M. Zielinski, M. Steinegger, M. Pacholska, T. Berghammer, S. Bodenstein, D. Silver, O. Vinyals, A. W. Senior, K. Kavukcuoglu, P. Kohli, and D. Hassabis, Nature **596**, 583 (2021).
[526] T. Fu, Y. Zang, Q. Zou, C. Nuckolls, and L. Venkataraman, Nano Lett. **20**, 3320 (2020).
[527] W. Bro-Jørgensen, J. M. Hamill, R. Brob, and G. C. Solomon, Chem. Soc. Rev. **51**, 6875 (2022).
[528] Y. Komoto, J. Ryu, and M. Taniguchi, Chem. Commun. **59**, 6796 (2023).
[529] M. Bürkle, U. Perera, F. Gimbert, H. Nakamura, M. Kawata, and Y. Asai, Phys. Rev. Lett. **126**, 177701 (2021).
[530] C. Li, I. Pobelov, T. Wandlowski, A. Bagrets, A. Arnold, and F. Evers, J. Am. Chem. Soc. **130**, 318 (2008).
[531] F. Demir and G. Kirczenow, J. Chem. Phys. **136**, 014703 (2012).
[532] C. Jia and X. Guo, Chem. Soc. Rev. **42**, 5642 (2013).
[533] R. Frisenda, S. Tarkuç, E. Galán, M. L. Perrin, R. Eelkema, F. C. Grozema, and H. S. J. van der Zant, Beilstein J. Nanotechnol. **6**, 1558 (2015).